

Front cover page: A system of channels (centered at 20.53°N, -118.49°E) emanated from the graben near to Jovis Tholus region, Mars. MRO-CTX stereo pair derived DTM draped over the CTX image. Presence of multiple channels, braided-like channel network at the downstream end, and terraces suggests their plausible fluvial origin. Lava flow into the channels termini hindered the real extent of the channel network, b) an example of a streamlined island formed within the channel and c) an example of a curvilinear island suggesting the possible flow direction.

Inside back cover pages: Events at PRL

Back cover page: Top Panel: Alpha Particle X-ray Spectrometer on-board Chandrayaan-2 rover [Mechanical Configuration]

Middle Panel: AMS Laboratory

Bottom Panels: Pre-monsoon and post-monsoon $\delta^{18}\text{O}$ & d-excess maps of shallow groundwater in India.

Compilation and Layout by:

Office of the Dean, PRL.

Published by:

Physical Research Laboratory, Ahmedabad.

Contact:

Physical Research Laboratory

Navrangpura

Ahmedabad - 380 009, India

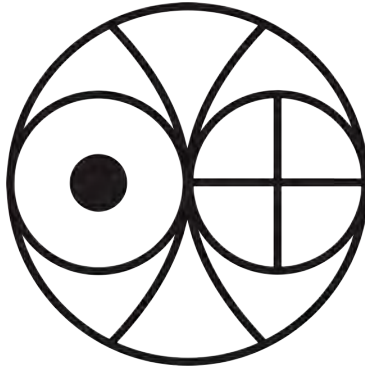
Phone: +91-79-2631 4000 / 4855

Fax: +91-79-2631 4900

Cable: RESEARCH

Email: info@prl.res.in

Website: <https://www.prl.res.in/>



PRL Annual Report
2016 – 2017

PRL Council of Management

Three nominees from Govt. of India

Professor U.R. Rao, Former Chairman, ISRO
Antariksh Bhavan, New BEL Road
Bengaluru-560231

Chairman

Shri A. S. Kiran Kumar, Secretary,
Department of Space, Govt. of India & Chairman, ISRO
Antariksh Bhavan, Bengaluru-560231

Member

Shri A. Vijay Anand, IRS, Additional Secretary & FA
Department of Space, Govt. of India
Antariksh Bhavan, Bengaluru-560231

Member
(Up to 31.08.2016)

Shri S. Kumaraswamy, Additional Secretary & FA
Department of Space, Govt. of India
Antariksh Bhavan, Bengaluru-560231

Member
(From 01.09.016 to 05.03.2017)

Mrs. Vandita Sharma, Additional Secretary & FA
Department of Space, Govt. of India
Antariksh Bhavan, Bengaluru-560231

Member
(From 06.03.2017)

A Nominee of Ahmedabad Education Society

Shri Sanjay S. Lalbhai
Ahmedabad-380009

Member

A Nominee of Karmakshetra Education Foundation

Shri Kartikeya V. Sarabhai, Director, Centre for Environment Education
Ahmedabad-380054

Member

A Nominee of Govt. of Gujarat, Gandhinagar-382010

Ms. Anju Sharma, I.A.S., Secretary, Higher and Technical Education
Department of Education

Member

Director, Physical Research Laboratory, Ahmedabad-380009

Professor Utpal Sarkar

Member (Ex-Officio, Up to 31.05.2016)

Shri Tapan Misra

Member (Ex-Officio, From 01.06.2016 to 09.02.2017)

Dr. Anil Bhardwaj

Member (Ex-Officio, From 10.02.2017)

Registrar, Physical Research Laboratory, Ahmedabad-380009

Wg. Cdr. (Retd.) Vibhas Gupta

Member Secretary (Ex-Officio, Up to 21.10.2016)

Professor Jyotiranjan S. Ray

Member Secretary (Ex-Officio, From 22.10.2016)

Contents

Director's Foreword	1
Science Highlights	3
Awards and Honours	8
Human Resource Development	11
Ph.D. Awarded [PRL students/project associates/employees]	12
Colloquia/Public Lectures by Visitors	13
Conferences / Symposia / Workshops by PRL	14
Invited Talks at Conferences / Symposia / Workshops	15
Lectures at Universities / Institutions	21
Science	24
Astronomy and Astrophysics	24
Solar Physics	41
Planetary Sciences	52
Space and Atmospheric Sciences	71
Geosciences	82
Theoretical Physics	100
Atomic, Molecular and Optical Physics	106
Publications	118
Journals	118
Proceedings of Conference/ Symposia/ Workshops	126
Books Edited / Review Articles / Other Publications	130
Promotion of Basic Sciences, Official Language and Outreach Activities	131
Facilities and Services	135
Honorary Fellows	143
Honorary Faculty	144
PRL Faculty	145
Audited Statement of Accounts	149

Director's Foreword

It's a privilege for me to be entrusted with the responsibility of leading the Physical Research Laboratory (PRL) as its Director in February 2017. PRL is one of the premier science laboratories of the country conducting cutting-edge research in many domains of Astronomy and Astrophysics, Solar Physics, Space and Atmospheric Sciences, Atomic, Molecular and Optical Physics, Geosciences, Planetary Sciences, and Theoretical Physics, as well as instrument design and mission payload development.

The mandate of the Laboratory is to carry out fundamental research, publish scientific papers in respective fields of expertise, and to design and develop appropriate instrumentation and experiments to enable realization of specific science goals. In the short time I have been here I can see that this mandate is being upheld, as is apparent from the over two hundred research publications in high impact peer-reviewed journals, and 12 PhD theses being produced in the last one year. PRL faculty members received invitations to give more than a hundred and seventy lectures at Conferences, Symposia, Workshops, Universities and other Academic Institutions.

Several new and vital scientific findings have been reported by PRL scientists in the frontier areas of research mentioned above, which are detailed in this report. Very significant progress has been made in the initiatives on the large projects, like the Multi-Application Solar Telescope (MAST) at Udaipur Solar Observatory, which is now operational. A low-order adaptive optics system and stokes polarimeter has been successfully developed in-house. The PARAS spectrograph has now produced significant science that includes the discovery of a very rare three-body Eclipsing Binary system with the third body being a planet of 10 Jupiter mass orbiting at a separation of 1 Astronomical Unit.

The establishment of a new 2.5m telescope facility at Mt. Abu is well underway, along with the development of back-end instruments. A 1 MeV Accelerator Mass Spectrometer (AMS) for the detection of C, Al and Be isotopes has been installed in Thaltej campus of PRL, enhancing the capability to contribute to the geochronological research. Work on establishing a facility for hard X-ray focusing optics has been initiated. Technology Development Program has been initiated to advance and support the new scientific ideas. The development of payloads XSM, APXS, ChaSTE for the upcoming Chandrayaan-2 Orbiter, Rover and Lander missions, and ASPeX payload on the Aditya-L1 mission, are progressing well. The work on design and development of payloads for the future planetary and space missions is also on-going.

Other large programmes, like the GEOTRACES, an international programme which aims to improve the understanding of biogeochemical cycles and large-scale distribution of trace elements and their isotopes in the marine environment, and IWIN a National Programme aimed at oxygen and hydrogen isotopic characterization of water sources to better understand hydrological processes in atmospheric, surface and sub-surface domain are also making good progress. The optics group has successfully generated high power, airy beams, having peculiar properties such as self-acceleration, self-healing and non-divergence, tunable in the near-IR wavelength range.

Observations using Astrosat and analysis of scientific data from a variety of ground- and space-based telescopes and planetary, solar and astronomy missions are being vigorously pursued in PRL. Field expeditions for collection of geological samples as well as scientific ship-cruises for obtaining crucial marine samples are continuously undertaken by PRL scientists. The samples undergo controlled-preparation and then analysed using different techniques and sophisticated experiments in the Laboratory. Research in theoretical physics is focused on cosmology, matter under extreme conditions, quark-gluon plasma, condensed matter and neutrino physics. Measurements are made using photometers, spectrometers, radars, lidars, and other ground-based experiments to understand the unique processes in the lower, middle, and upper atmosphere, and combining with the solar and interplanetary medium data to study the space weather phenomena.

PRL coordinates the PLANEX and RESPOND programmes of the Department of Space and currently more than thirty research groups at various universities and research institutions are conducting scientific investigations through these programmes. PRL hosted about half-a-dozen national meetings in different disciplines of its research for scientific interactions and discussion. Research students of PRL have also organised conferences aimed at young researchers and students with a good number of participation.

As a part of societal commitment and capacity building, PRL contributes by providing highly skilled researchers through its strong Doctoral and Post-Doctoral programmes. In addition, PRL conducts a Visiting Scientist programme for university teachers, and project training for graduate and post graduate students in both engineering and science to conduct long-term project work. PRL organizes intensive summer programmes for students as well as college and University teachers every year and also partake through its association with similar programmes conducted by the Indian Science

Academies.

More than fifty graduate and undergraduate students have participated this year in the PRL summer programme. PRL is entrusted with the responsibility of conducting UN CSSTEAP course on Space and Atmospheric Sciences for the Asia-Pacific region. The tenth course with 12 students is getting completed on 30 April 2017. PRL continues its academic association with many universities and institutes in Gujarat and in the country.

PRL scientists continue to get recognized at both national and international academic fora. This year the recognitions include two national civilian awards, the Padma Vibhushan and the Padma Shri, Shanti Swarup Bhatnagar Award, ISRO's Prof. Satish Dhawan Professorship, J.C. Bose Fellowship, ISRO's Performance Excellence, Merit and Team Excellence awards, Fellowship of Indian Academy of Science, Hari Om Ashram prerit Dr. Vikram Sarabhai Award and INSA young scientist medal. PRL faculty members serve on the Editorial Board of various leading national and International journals, as well as in Council and Advisory Committees of several academic and research institutions, and government departments, such as SERB, DST, CSIR and MoES. Several PRL research scholars have also received awards for their presentation in national and international scientific meetings.

Significant steps have been taken to ensure use of Hindi in all areas of administration and official communications. The new bilingual website of PRL with enhanced security features is operational now. Work done at PRL in implementation of Hindi in various domains has been recognized by the Town Official Language Committee and DOS. PRL also has a vibrant outreach programmes, including a three-day long open house in February 2017, which attracted over 6000 children, young school, college, and university students and a host of other visitors across almost every social background and profession.

I am indebted to all the members of the PRL Council for their constant encouragement, invaluable advice and whole-hearted support for all the scientific activities pursued at PRL. In particular, I am grateful to Prof. U. R. Rao, Chairman, PRL Council, and Shri A. S. Kiran Kumar, Chairman, ISRO for their sage advices, unstinted support and encouragement.

Anil Bhardwaj

Director

Science Highlights

Astronomy and Astrophysics

- Using the technique of radio occultation of the strong radio source 3C144 (Crab nebula) we obtained a comprehensive palette of results concerning the heliocentric dependence of the density turbulence spectral amplitude (C_N^2) and the density modulation index ($\epsilon_N = \Delta N/N$) for $10R_\odot < R < 45R_\odot$, where R_\odot is the solar radius. This is a distance range that is typically not covered by either IPS or interferometric techniques. Since the spatial scales used are small enough to possibly be comparable to the inner/dissipation scale, we used the general structure function (GSF) to model the observed radio visibilities rather than asymptotic approximations. The heliocentric dependence of the density turbulence amplitude as $C_N^2(R) = AR^{-\gamma}$ were parameterized to get an idea of the range of possibilities for the behavior of C_N^2 using currently prevalent ideas. To the best of our knowledge, this is the most extensive characterization of the density turbulence spectral amplitude to date.
- The evolution of highly reddened Nova V1831 Aquila in near Infrared (NIR) and optical wavelength domains have been studied. Based solely on the nature of NIR spectrum we are able to classify the nova to be of the Fe II class. The distance and extinction to the nova are estimated to be 6.1 ± 0.5 kpc and $A_v \sim 9.02$ respectively. V1831 Aql formed dust around 18 days after discovery, one of the earliest dust producing events seen in a nova. While the dust temperature is seen to gradually decrease from 1400K to 950K, the dust mass and mean grain radius remained fairly constant with values in the range $(1 - 2) \times 10^{-8} M_\odot$ and $1.5 - 3.0 \mu m$ respectively.
- Near-infrared regime of the spectrum is most suitable to study cool dwarf star in a binary system. J and H band light curves of DO Draconis was investigated to understand the cool component of the binary and the system parameters. A coherent modulation at 1.96 hr period was detected which was interpreted as a first harmonic of the orbital period. Modelling the phase curve inferred the inclination of the orbital period to be $43^\circ \pm 5^\circ$. The spectral type and temperature of the secondary was estimated to be $M3V \pm 1$ and 3400 K, respectively. The shift in the time of inferior conjunction with respect to previously estimated time was observed which can be useful in estimating the accretion rate of the system.
- The star-forming region, IRAS 17599-2148 is part of an elongated filamentary structure (extension ~ 21 pc), which also contains at least six star-forming massive clumps. We found that the most massive clump contains two O-type stars and a massive protostar candidate prior to an ultracompact HII phase.
- In the molecular cloud G35.20-0.74, an observational signature of the cloud-cloud collision (CCC) process has been investigated based on the ^{13}CO line data. We find that G35.20-0.74 is a site of triggered star formation, where the CCC has influenced the birth of massive stars and clusters of young stellar objects.
- Broad-band spectral studies of X-ray pulsars provide important information regarding the geometry, magnetic field and emission mechanism of the neutron star in the binary systems. Spectral properties of X-ray pulsar SMC X-2 were investigated by using three simultaneous NuSTAR and Swift/XRT observations during its 2015 outburst. The most important feature discovered in our study was the detection of cyclotron resonance scattering feature at 27 keV. Corresponding magnetic field of the neutron star was estimated to be $\sim 2.3 \times 10^{12}$ G. The cyclotron line energy showed a marginal negative dependence on the pulsar luminosity. The cyclotron line parameters were found to be variable with pulse phase and interpreted as due to the effect of emission geometry or complicated structure of the pulsar magnetic field.
- Active galactic nuclei feedback plays an important role in the

evolution of non-thermal radio jets and lobes ejected from the central supermassive black hole. These jets and lobes interact with the surrounding environment releasing a large amount of energy. With an objective to investigate signatures of the interactions between the radio jets/lobes and the surrounding intra-cluster medium, we tried to find association between the X-ray cavities and the radio emission maps by using data from Chandra and GMRT observations of cool core cluster ZwCl 2701. These observations showed the presence of an extensive pair of ellipsoidal cavities within the central region <20 kpc. Detection of bright rims around the cavities suggested that the radio lobes displaced X-ray emitting hot gas forming shell-like structures.

- A deep Chandra observation the bright FRII radio galaxy 3C 444 in Abell 3847 cluster showed a pair of huge X-ray cavities along North and South directions from the centre of the galaxy. X-ray and radio images of the cluster revealed peculiar positioning of the cavities and radio bubbles with a physical offset of ~ 61 and ~ 77 kpc from the center. A detailed analysis of the temperature and density profiles showed the presence of a rarely detected elliptical shock in the cluster. The cooling luminosity of the cluster was estimated to be $\sim 8.30 \times 10^{43}$ erg s^{-1} , which confirms that the AGN power is sufficient to quench the cooling.
- Timing and spectral properties of the accretion powered X-ray pulsar GX 1+4 were investigated by using a long Suzaku observation in 2010 October. Iron K-shell (K_{α} and K_{β}) emission lines from nearly neutral iron ions were detected in the pulsar spectrum. A significant K_{α} emission line from neutral Ni atoms was detected for the first time in this pulsar. Using the *Suzaku* observation, we estimated an iron abundance of $\sim 80\%$ of the solar value and an Ni/Fe abundance ratio of about two times the solar value.
- Using deep radio, optical, and near-IR observations in the two deep fields named as the Subaru X-ray Deep Field (SXDF) and the Very Large Array VIMOS VLT Deep Survey (VLA-VVDS) field, we have discovered a new population of obscured AGN at high-redshifts. These AGN are identified by studying an unusual class of objects called Infrared-Faint Radio Sources (IFRSs) that are relatively bright at radio wavelengths but have faint or undetected infrared counterparts even in deep surveys. The use of one of the most sensitive data allows us to find, for the first time, IFRSs with measured redshift > 3.0 , and also, IFRSs in the faintest flux regime i.e., $S_{3.6\mu m} < 1.3 \mu Jy$. Radio properties such as high radio luminosity ($L_{1.4 GHz} > 10^{24}$ W Hz^{-1}), extended double-lobe morphology of many sources, and steep radio spectra confirm IFRSs to be AGN. The non-detection of all but one IFRSs in the X-ray band and the optical-to-MIR colour suggest that a significant fraction of these are AGN hosted in dusty obscured galaxies.
- In a multi-wavelength study of flaring activity in blazar 1ES 1959+650 during 2015 January-2016 June, two major outbursts (March 2015 and October 2015) with significant flux enhancements across whole electromagnetic spectrum were detected. The data from Fermi-LAT, Swift-XRT & UVOT and optical data from our Mt. Abu InfraRed Observatory reveal correlated variations with diverse flare durations indicating co-spatial origin of these emissions. Local magnetic field was estimated to be about 1.2 Gauss using synchrotron cooling time scale.
- Broadband spectral and temporal properties of the FSRQ PKS

1510-089 during a high gamma-ray state were studied using VHE gamma-ray observations from MAGIC, radio, UV, X-ray and GeV gamma-ray from other sources and optical and NIR band data from Mt Abu IR Observatory led to detection of intra-night variability in near-infrared which was accompanied by a rotation of the optical polarization angle and the emission of a new jet component observed in radio. The observed flux variability sets, for the first time, constraints on the VHE-emission region size for this source.

- We, at PRL, have discovered a very rare Eclipsing Binary (EB) system of 1.68 days, which is a three-body system and the third body is a planet. The EB pair is a F+M system which is orbited by a 10 MJ mass planet. Despite its short orbital period, the system has a considerable eccentricity of 0.3 (determined by PRL HR spectrograph PARAS). Transit time variation (TTV) photometric data over a decade in combination with PARAS RV data points have revealed the existence of the body a 10 Jupiter mass planet orbiting at a separation of 1AU and e of 0.7.

Solar Physics

- GOLF aboard SOHO observations reveal that global velocity oscillations in the Sun (or the p-modes) show significant variations in their power during the solar minimum. This indicates substantial changes in the internal structure and dynamics of the Sun even during the phase of minimum solar activity.
- Investigation of photospheric magnetic imprints of several major flares produced by the largest active region NOAA 12192 of solar cycle 24 shows that large, abrupt, downward vertical Lorentz force change occur during flares. These changes are larger for eruptive events as compared to the non-eruptive ones in the same AR.
- The study of confined and eruptive events of the largest AR 12192 of solar cycle 24 studied using Ca K observations shows that for similar GOES X-ray class, the eruptive flares have lesser reconnection flux compared to confined flares.
- Various phases of an eruptive filament studied using multi-wavelength data set revealed complex, multi-step phenomenon which provided evidence for magnetic reconnection supporting the fast ejection of prominence in the lower corona.
- Study of several cases of interacting CMEs reveals that the pre-collision parameters dictate the type of collision such as the relative approaching speed, expansion speed of the following CME over the preceding one, and the time duration of collision phase.
- Observations of two partial filament eruptions obtained from MAST telescope shows that the eruption initiated due to the flux emergence in and around the filament. This flux emergence was followed by converging/shearing motions which further stressed the overlying fields, leading to eruption.
- Magnetohydrodynamic simulations assert the importance of successive magnetic reconnections in creation and activation of three dimensional flux ropes. The reconnections being localized below the created rope, drives its ascent; a scenario which agrees with the standard flare model.

Planetary Sciences and PLANEX Program

- Model calculations explaining the effect of solar X-ray flares on ionosphere and human exploration show that flares increase the electron densities of D and E peaks by one to two orders of magnitude. The X-class flare, X14.4 has been found to have the highest biological dose and is thus lethal for humans.
- PRL ion-dust model to study the effect of high altitude (20km) dust layer on the subtropical ionosphere shows that smaller sized dust particles reduce ion densities by an order of magnitude.
- Retrieval of four years of columnar ozone over entire Mars from SPICAM raw data on board Mars Express shows that the photolytic processes play important role in the observed hemispheric anti-symmetry in Ozone-CO correlation.
- A power law size distribution has been suggested for incoming dust at Mars using the MAVEN observations. It has been found that interplanetary dust flux at Mars is two orders higher than the dust flux from Phobos/Deimos and the incoming dust at Mars is expected to be interplanetary in nature.
- A correlation analysis is suggested to study the effect of lunar surface material on microwave brightness temperature. Our results show that major contribution in brightness is from density driven component and ~14 % contribution is made by iron and titanium oxides. Further, results do not agree with the existing permittivity model which is based on local Apollo lunar samples and in this regard, a modified permittivity model is suggested for the lunar surface based on global coverage.
- Remote sensing study of an undocumented outflow channels system within Jovis Tholus region on Mars revealed geomorphic evidence for streamlined/curvilinear islands, terraces, divide crossing and crossover channels suggesting plausible fluvial origin of channels during the past 3.4 Ga, Amazonian epoch.
- Recent meteorite fall (2012) in India, Katol L6-7, has been studied to understand the Asteroidal process. The high pressure polymorphs and microstructural study suggest that the rare occurrence of troilite-metal nodule in Katol chondrite was formed due to an independent, localised event by a high energy impact.
- Raghunathpura meteorite, Fall 1986, is discussed as an early crystallised IIAB iron with low Ni, low P, low S and high Ir. Metallographic cooling rate of this type of magmatic iron group vis-a-vis the asteroidal core has been estimated as extremely slow, 7C/Ma.
- Best match for the nature of impactor in Lonar crater, India has been found to be EH type impactor with 6 wt % impactor component in the impact spherule. Our study further suggests that neither the pre-impact crater soil nor the Achaean crust was source component for impactite. Further, the alterations at basaltic environment in Lonar imply the soil formation process at Mars.

Space and Atmospheric Sciences

- Black carbon measurements over a remote, free troposphere site exhibit a high during afternoon hours due to heating of the Earth's surface which increases the boundary layer height resulting in the transport of pollutants from the foothills to the free troposphere.

- An inter-comparison of black carbon mass concentrations performed using two aethalometers revealed that the black carbon mass concentrations measured by a dual spot aethalometer is higher than a single spot aethalometer which has significant implications in estimating the single scattering albedo of aerosols and radiative forcing.
- Despite predominant emission from anthropogenic sources, biogenic emissions of Volatile Organic Compounds (VOCs) at an urban site in India show significant contributions to ambient air during winter to summer transition period.
- Response to the variations of solar flux in the thermosphere is expected, however, based on over three years of mesospheric OH and O₂ optical nightglow emission data from Gurushikhar, Mt Abu, it is shown that mesosphere too is affected by the variation in solar flux. This solar influence on OH and O₂ emissions emanates from the requirement of O and O₃ concentrations as reactants for their production, which are known to be solar activity dependent.
- Imprint of equatorial electric field variation in the optical neutral dayglow diurnal behaviour has been revealed. To augment this finding, data that exists in the published literature for over 25 years have been made use of, to show that the diurnal emission pattern of dayglow shows solar cycle dependence. This reveals the existence of a strong coupling of diverse drivers in the solar terrestrial environment.

Geosciences Division

- To determine the effect of future climate change on ocean ecosystems, a mesocosm experiment was done by growing marine plankton under controlled conditions of salinity and temperature. The reduced salinity treatment had the most considerable influence manifested as significantly lower primary production, and the most dissimilar phytoplankton species community.
- New observations of nitrogen isotope ratio of marine particulate organic matter in the eastern and central Arabian Sea indicate significant spatial variability in the $\delta^{15}\text{N}$ as a result of the upper ocean response to the monsoonal forcing that triggers upwelling and thus supplies sub surface nitrate to the surface. An increasing trend has been found in the $\delta^{15}\text{N}$ (PON) from the upwelling zone to the open ocean, which tracks the progressive utilization of advected nitrate from the coast.
- Measurement of dissolved Zn, though a challenging task, was done in the Indian Ocean. Dissolved Zn seems to be lost partially in the Oxygen Minimum Zone (OMZ, dissolved oxygen is less than 50 μM) in the northern Indian Ocean. The plausible reason for the observed loss of Zn in the OMZ could be due to the formation of Zinc Sulfides.
- A study on sediment cores retrieved from the western Arabian Sea and equatorial region showed changes in past productivity variations attributable to changed upwelling conditions. During the last glacial period, equatorial region had high productivity, in contrast to which western Arabian sea was a low productivity region. Presumably, the southward migration of the Intertropical Convergence Zone caused weakening of the Indian summer monsoon and strengthening of the North-East monsoon.

- Paleoclimate record reconstructed from mudflats of Diu Island showed warm and wet condition between $\sim 4,000$ year to present, interspersed by an arid climate at $\sim 2,100$ year and by a cool and wet phase around 600 years ago.
- A 1 MV Accelerator Mass Spectrometer (AMS) for the detection of ^{14}C , ^{26}Al and ^{10}Be isotopes has been installed in Thaltej campus of PRL. AMS would contribute to the geochronological needs and will provide a major thrust to research in the field of earth and planetary sciences.

Theoretical Physics

- In an post Higgs discovery era, our main focus into beyond the Standard Model of particle physics as well as precise determination on Higgs measurements. Neutrino oscillation data profoundly established the necessity for going beyond. Different seesaw mechanisms naturally explain the scenario with tiny neutrino mass. Here we investigate the LHC phenomenology for TeV scale seesaw mechanisms at the Large Hadron Collider (LHC) calculating at the Next to Leading Order (NLO).

Discovery of Higgs opened up the opportunity to explore different properties and couplings of Higgs, also, to find out important hints of new physics. We devise some methodology to reconstruct the semi-invisible event modes (such as through Tau pair production) uniquely, together with a significant enhancement in terms of efficiency over the existing methods. Non-commutative(NC) space-time, if realized in nature, can introduce a fundamental length scale in the model. This unknown scale can be rather high and possible explored at the high energy collider like LHC. We explored such possibility which is one of the first few in this direction.

- We studied the effect of non-standard interactions (NSI) on the propagation of neutrinos through matter and how it affects the hierarchy sensitivity of the DUNE experiment. We emphasize on the special case when the diagonal NSI parameter $\varepsilon_{ee} = -1$ and nullifies the standard matter effect. We show that, if in addition, there is maximal CP violation then this gives rise to an exact intrinsic hierarchy degeneracy, in the appearance channel, irrespective of the baseline and energy. Introduction of off-diagonal NSI parameter, $\varepsilon_{e\tau}$, shifts the position of intrinsic degeneracy to a different ε_{ee} . Moreover the unknown magnitude and phases of the off-diagonal NSI parameters can give additional degeneracies. Overall, given the current model independent limits on NSI parameters, no hierarchy sensitivity can be observed in the DUNE experiment if NSIs exist in nature. A signal of neutrino mass hierarchy at DUNE will therefore be able to rule out certain ranges of the NSI parameters.

The right-handed neutrinos within the type-I seesaw mechanism can induce large radiative corrections to the Higgs mass, and naturalness arguments can then be used to set limits on their mass scale and Yukawa couplings. Driven by minimality, we consider the presence of two degenerate right-handed neutrinos. We compare the limits from naturalness with the ones from the stability of the electroweak vacuum and from lepton flavor violation implications from neutrinoless double beta decay are also discussed and renormalization effects for the light neutrino parameters are presented. Adding small perturbations to the degenerate heavy neutrino spectrum allows for successful leptogenesis.

There are experimental evidences in support of existence of light sterile neutrinos from neutrino oscillation experiments. We study the zero textures of the Yukawa matrices in the minimal extended type-I seesaw (MES) model which can give rise to eV scale sterile neutrinos. The MES model leads to some extra correlations which disallow some of the Yukawa textures allowed from three generation analysis. We show that the allowed textures in our study can be realized in a simple way in a model based on MES mechanism with a discrete Abelian flavor symmetry group.

- The Moris projection method, known as the memory function method, is an important theoretical formalism to study various transport coefficients. In a recent work, we calculate the dynamical thermal conductivity in the case of metals using the memory function formalism. We introduce thermal memory functions for the first time and discuss the behaviour of thermal conductivity in both the zero frequency limit and in the case of nonzero frequencies. We compare our results for the zero frequency case with the results obtained by the Bloch-Boltzmann kinetic approach and find that both approaches agree with each other. Motivated by some recent experimental advancements, we obtain several new results for the ac or the dynamical thermal conductivity.
- Submillimeter astronomy with a South Pole Telescope: A proposal for a 10 meter class telescope for 1-0.1 mm EM waves which can be installed in the Antarctic Station Bharti is being developed. A detailed science case for such a telescope for studying dark matter, dark energy and M-dwarf exoplanets. The design will be implemented in partnership with Space Application Center, Ahmedabad.
GMAP : A detailed proposal for making a Gravity Map of the underground features of Indian terrain (like water, oil and mineral deposits) using satellite borne atomic clocks is being developed. The design of the system with the algorithm for signal processing is being developed in PRL and the implementation will be carried out in collaboration with Space Application Centre, Ahmedabad.

Atomic, Molecular and Optical Physics

- We have demonstrated on both theoretical and experimental basis, a method to recover the topological structure of a monochromatic optical field that has suffered diffuse transmission.
- A new program for estimation of exhumation rates in Himalayas using luminescence thermochronology.
- A generic trapping scheme for atoms at the magic wavelengths that are independent of vector and tensor components of the interactions of the atoms with the external electric field is presented. Many highly charged ions have been analyzed for their suitability to provide very high precision atomic clocks. Atomic structures of the plasma embedded aluminium, magnesium and iron ions are investigated accounting screening effects in the electron-electron interactions. Limits on the electric dipole moments (EDMs) of neutron and proton are inferred as $d_n < 2.2 \times 10^{-26}$ e-cm and $d_p < 2.1 \times 10^{-25}$ e-cm, respectively, from atomic studies on ^{199}Hg . These values give limits on the quantum chromodynamics parameter and the combined up- and down- quark chromo-EDMs as 1.1×10^{-10} and 5.5×10^{-27} e-cm, respectively, which

are several orders larger than the standard model of particle physics predicted values. This also constraints the tensor-pseudotensor electron-nucleus coupling coefficient with the mass of a possible dark matter candidate.

- Photons with orbital angular momentum (OAM), an important degree of freedom, are of great importance in both classical and quantum optics. Typically, optical vortex beams carry photons with OAM. Using optical vortex beam, we have demonstrated controlled switching of OAM among the interacting beams in optical parametric oscillators. Such study can be useful in quantum entanglement and quantum communication.
- Calibration of the recently installed LIBS setup was completed using deuterium-halogen source. The optimum conditions for recording the emission spectra based on the response of the instrument has been obtained.
- We have introduced an interesting quantum state, the perfect quantum optical vortex state which exhibits a highly localized distribution along a ring in the quadrature space.
- Efforts to date millennia old samples using PIR-IR luminescence technique and its comparison with existing luminescence methodologies.
- Steps towards automation of spatially resolved luminescence (SRL) system.
- We have demonstrated that the OAM of two photons can be annihilated in nonlinear interaction. Using two optical vortices of same order but in opposite sign in a second order nonlinear crystal we have produced hollow Gaussian beam with photons of no OAM.
- We have generated high power, Airy beam, having peculiar properties such as self-acceleration, self-healing and non-divergence, tunable in the near-IR wavelength range using optical parametric oscillators in all time scales (continuous-wave, picosecond and femtosecond). Such beams are of great importance in both basic and applied sciences.
- We generated ultrafast vortex beams in the deep ultraviolet (DUV) wavelength range at 266 nm. Using second order nonlinear interaction of near-IR ultrafast laser we have produced optical vortex of order as high as 6 with output power in excess of 350 mW.
- PDR of SWIS instrument was completed in Dec, 2016. Field simulations to understand magnetic field leakages and performance of the instrument was performed and validated using field tests at LEOS, Bangalore.
- Reversible phase change from amorphous to crystalline and back to amorphous is seen for the first time in astrochemical ices. Ethanethiol molecules prepared under astrochemical conditions and probed using IR revealed the reversible phase change to occur even at such low temperatures. The ice was also found to repeatedly switch phases upon temperature cycling.
- A unique photoabsorption band for carbonic acid is identified in the vacuum ultraviolet wavelength region, 180 nm -210 nm. This will help identify, to-date evasive, carbonic acid molecule in water-carbon dioxide rich irradiated icy satellite surfaces.
- S-H stretching region of propanethiol ices is found to be the indicator for its identification in interstellar ices. Though there is an overlap with the S-H stretching region of the other lower order thiols such as methanethiol and ethanethiol, the shoulder band that appears in the propanethiol molecule is a unique indicator.
- Deuterated Formaldehyde molecule (HDCO) has been reported for the first time in the low mass protostellar system HH212. Using the ALMA interferometric image it has been seen that this emission is from hot region near the central source and emission is affected by disc-wind and bipolar jets.
- Chemical Diagnostics of the Massive Star Clusters-Forming Cloud G33.92+0.11 has been described using DCN, HDCS and $\text{H}_2\text{C}^{34}\text{S}$ molecular line from ALMA observation. This is first ever use of these deuterated molecular lines along with isotopomer of H_2CS to understand the chemical and physical property of different star forming regions of the Star Clusters-Forming Cloud G33.92+0.11.
- Hydrogen is widespread either in atomic or in molecular form in the interstellar medium (ISM). Considering the typical dust (amorphous carbon, silicate) in the ISM, we have considered benzene, water-cluster $(\text{H}_2\text{O})_6$, silica $(\text{SiO}_2)_3$ as adsorbents and discussed the H_2 formation in ISM. Using quantum-chemical analysis we have calculated variation of adsorption energies

Awards and Honours

Faculty

U.R. Rao

1. Padma Vibhushan Award- 2017, Government of India.

J.N. Goswami

2. Padma Shri Award - 2017, Government of India.

A. Bhardwaj

3. Infosys Prize in Physical Sciences, 2016.
4. Member, Governing Council, Indian Institute of Geomagnetism, Mumbai, 2017.
5. Member, Governing Council, National Centre for Earth Science Studies, Trivandrum, 2017.
6. Member of INSA Sectional Committee IV: Earth & Planetary Sciences for 2017-2019.

A.K. Singhvi

7. Honoured as Subject-Editor, Earth Sciences for the Proceedings of Indian National Science Academy 2017
8. Honoured as on the Editorial Board of Quaternary International, Elsevier Press.
9. Chaired the Program Advisory and Monitoring Committee, Geosciences, Ministry of Earth Sciences 2016
10. Honoured as Leader of Indian Delegation, 35th International Geological Congress 2016 in Capetown.
11. Chaired the Science Program Committee of 36th International Geological Congress -2020

12. Chaired the Research Advisory Committee of the Institute of Seismological Research, 2016
13. Honoured by the Department of Science and Technology.
14. Chaired the Review Committee of National Facility for National Facility on Low Temperature Thermo-chronology Kuruskehtra University.
15. Honoured as Member, Ministry of Earth Sciences' Independent Review Committee for Autonomous Institution-Indian National Centre for Ocean Information Services (INCOIS), Hyderabad.

R. Ramesh

16. Member, 'Ministry of Earth Sciences' Independent Review Committee for Autonomous Institution-National Centre for Antarctic and Ocean Research (NCAOR), Goa.
17. Member, CSIR Review Committee for Niti Ayog Projects-National Geophysical Research Institute (NGRI), Hyderabad.
18. Member, CSIR Review Committee for Niti Ayog Projects-National Institute of Oceanography, (NIO), Goa.
19. Member, Research Advisory Council, NGRI, Hyderabad.
20. Chairman, Research Advisory Council, CMLRE, Kochi.
21. Conferred with National J.C. Bose Fellowship.
22. Conferred with ISRO Performance Excellence Award, 2016.
23. Member, Review committee for the project on biogeochemical processes of mud banks-National Institute of Oceanography, RC,Kochi.
24. Guest Professorship at Sardar Patel University, Anand.
25. Conferred with ISRO's Prof. Satish Dhawan Professorship.

M.M. Sarin

26. Co-Chair, MoES-DBT (India)-NERC-MRC (UK) Expert Panel Meeting on "Atmospheric Pollution and Human Health", Medical Research Council (London), April 4-5, 2016.
27. Co-Convener, Special Session on "Air-sea exchanges: Impacts on Biogeochemistry and Climate", EGU-2016, Vienna, (Austria), April 19, 2016,
28. Co-Chair, GESAMP Annual Session hosted by United Nations Environmental Programme (UNEP), Nairobi (Kenya), November 14-17, 2016.
29. Co-Chair, GESAMP Working Group Workshop on "Changing Atmospheric Acidity and Oceanic Solubility of Nutrients", University of East Anglia, Norwich (UK), 27 Feb - 2 March 2017.

P. Janardhan

30. Awarded the - ISRO Merit Award 2015. The award conferred annually is given for outstanding performance and high productivity.

S.A. Haider

31. J. C. Bose National Fellowship
32. Member of INSA Sectional Committee IV: Earth & Planetary Sciences for 2017-2019

S. Goswami

33. Elected as the Fellow of Indian Academy of Sciences, 2017.
34. Received the C. V. Raman Mahila Vijnana Puraskara from Swadeshi Vijnana Andolana, Karnataka in 2016.

S. K. Singh

35. Awarded Shanti Swarup Bhatnagar Prize 2016.

D. Pallamraju

36. Chair, Session IVa of the 9th IAGA - ICMA/IAMAS - ROSMIC/VarSITI/SCOSTEP workshop on Long-Term Changes and Trends in the Atmosphere held at K hlungsborn, Germany during 19 - 23 September, 2016.

V. Sheel

37. Main Convenor, Science and Exploration of Mars and Venus, 13th annual meeting of the Asia Oceania Geosciences Society (AOGS), Beijing, China, 31 July-5 August 2016

B. K. Sahoo

38. Awarded as an Outstanding Reviewer for 2016 by J. Phys. B: Atomic, Mol. and Opt. Physics; PIFI Fellowship from Chinese Academy of Sciences (CAS) for 2017-2018; selected for Indo-Australia EMCR fellowship by INSA for 2016-2017.

D. Chakrabarty

39. Received the Hari Om Ashram Prerit Vikram Sarabhai Research Award (2015) for significant contributions in Space Sciences.

G. K. Samanta

40. International Commission of Optics and ICTP Gallieno Denardo award for optics, 2017.

B. Sivaraman

41. INSA Medal for Young Scientist - 2016, Indian National Science Academy, New Delhi, India.

MAST Team

42. ISRO team excellence award - 2015 for Multi Application Solar Telescope (MAST)

A. B. Sarbadhikari

43. Section Editor for Encyclopedia of Lunar Science, Springer Publishing

Research Scholars and Post Doctoral Fellows**P. Chaturvedi**

44. Best Thesis Presentation Award, ASI, March 2017.

R. Yadav

45. International Global Atmosphere Chemistry (IGAC) travel grant award for the work Emission ratios of C₂-C₇ non-methane hydrocarbons at an urban site of western India presented in Science Conference, Breckenridge, Colorado, USA, 26 - 30 September, 2016.

A. Aadhi

46. Honored by European Physical Society grant for young scientist for the paper, High repetition rate Airy beam pulses in higher-harmonic fractional cavity, in 7th EPS-QEOD Europhoton Conference, Vienna, Austria, August 21-26, 2016.

A. Chaitanya N.

47. Best poster award in International Conference on Fiber Optics and Photonics - PHOTONICS 2016, IIT Kanpur, during December 4-8, 2016.
48. Honored by Optical Society of America student travel grant for the paper, Nonlinear generation of high power and higher order hollow Gaussian beam, in Frontier in Optics Conference, University of Rochester, USA, October 17-21, 2016.
49. Best poster award for the paper, Nonlinear generation of perfect vortex beam, in RAOS-2016 conference, Hyderabad University, May 6-7, 2016.

A. Patel

50. Second prize for the presentation entitled "Oxidative potential of ambient fine aerosols over the Indo-Gangetic Plain during winter", in the conference of Indian Aerosol Science and Technology Association (IASTA-2016) on Aerosol and Climate Change: Insights and Challenges held at Physical Research Laboratory, Ahmedabad during December 6-8, 2016.

N. Kaur

51. A fully funded Integrated Activities in the High Energy Astrophysics Domain (AHEAD) grant, European Horizon 2020-program, to learn high-energy astrophysics data analysis, Istituto Nazionale di Astrofisica, Bologna, Italy, 20 January - 3 February, 2017.

Jabir M. V

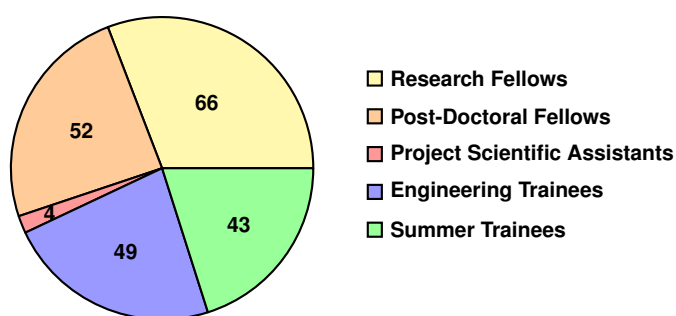
52. Best poster award for the paper, Structuring of entangled photons using structured classical pump beam, in 25th DAE BRNS National Laser Symposium, KIIT University, Bhubaneswar during December 20-23, 2016.
53. Honored by European Physical Society grant for young scientist for the paper, Generation of laser beam in variable sized perfect vortex spatial structure and its interaction with nonlinear crystal, in 7th EPS-QEOD Europhoton Conference, Vienna, Austria, August 21-26, 2016.

N. Tripathi

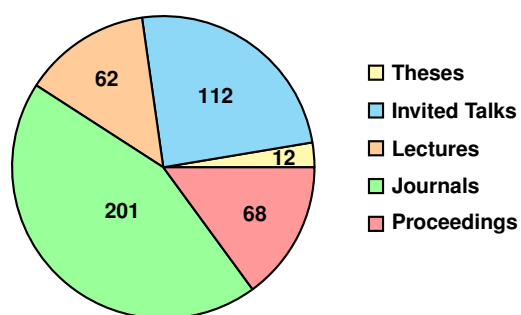
54. European Research Course on Atmospheres (ERCA) travel grant for the work Measurement of VOCs in an urban site of India: Application of PTR-TOF-MS instruments, Grenoble, France, 11 January - 9 February, 2017.

Human Resource Development

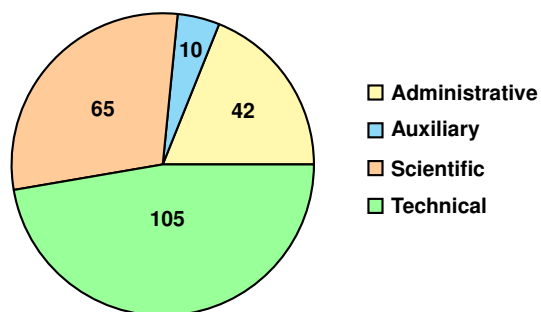
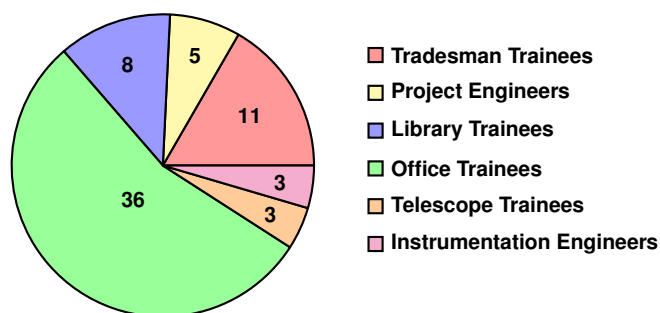
Research and Internship Programmes



Scientific Contributions



Administrative and Auxiliary staff structure



The laboratory has a strong Human Resource Development (HRD) component with Doctoral, Post-Doctoral, visiting Scientist programs. In addition we have an Associate program for university teachers and project training for graduate and post graduate students in both engineering and computer applications. PRL organizes intensive summer programmes for students as well as college teachers every

year. The purpose is to provide them an insight into current research activities being pursued at PRL which they can continue even after returning back to their colleges. It is also aimed at motivating them to take up research in basic sciences. The scientific output and staff details in numbers during the reporting year are presented in the above pie charts.

Ph.D. Awarded

[PRL students/project associates/employees]

Research Scholars

P. Chithrabhanu

1. "Polarization And Orbital Angular Momentum Entanglement With Classical And Quantum Sources: Implications And Applications", Mohanlal Sukhadia University, Udaipur, July, 2016 [Supervisor: Dr. R. P. Singh].

Apurv Chaitanya N.

2. "Non-linear interaction of structured optical beams", Indian Institute of Technology, Gandhinagar, July, 2016 [Supervisor: Dr. G. K. Samanta].

Sanjay Kumar

3. "Magnetohydrodynamic Relaxation in Astrophysical Plasmas", Mohanlal Sukhadia University, Udaipur, July, 2016 [Supervisor: Dr. R. Bhattacharyya].

Shraddha Band

4. "Multiproxy-paleoclimate studies in the Indian region for the past 200ka;A synthesis", Maharaja Sayajirao University of Baroda, Vadodara, July, 2016 [Supervisor: Dr. R. Ramesh].

Guruprasad Prakash Kadam

5. "Phenomenological studies of strongly interacting matter under extreme conditions", Mohanlal Sukhadia University, Udaipur, August, 2016 [Supervisor: Dr. H. Mishra].

Girish Kumar

6. "Decays of Hadrons Probes of the Standard Model and Beyond", Indian Institute of Technology, Gandhinagar, September, 2016 [Supervisor: Dr. N. Mahajan].

Tanmoy Mondal

7. "Constraining Physics Beyond the Standard Model in Post-Higgs Era", IIT Gandhinagar, October, 2016 [Supervisor: Dr. P. Konar].

Kuldeep Suthar

8. "Binary Mixtures of Ultracold Quantum Gases in Optical Lattices", IIT Gandhinagar, December, 2016 [Supervisor: Dr. D. Angom].

K. Damodara Rao

9. "Geochemical and Isotopic studies of Waters and sediments of Arabian and Andaman Seas", Mohanlal Sukhadia University, Udaipur, December, 2016 [Supervisor: Dr. S. K. Singh].

Gaurava Kumar Jaisawal

10. "Timing and Spectral Studies of Accretion-powered X-ray Pulsars", Mohanlal Sukhadia University, Udaipur, January, 2017 [Supervisor: Dr. S. Naik].

Project Associate

Upasana S. Banerji

1. "Holocene Climatic Variability using Mudflats from Saurashtra, Western India", Maharaja Sayajirao University of Baroda, Vadodara, April, 2016 [Supervisor: Dr. R. Bhushan].

Employee

Md. Nurul Alam

1. "Growth of Space Science Research Publications in India since 1960 A Scientometric Study", Indira Gandhi National Open University, New Delhi, August, 2016 [Supervisor: Dr. Archana Shukla, IGNOU].

Colloquia/Public Lectures by Visitors

1. **Prof. Ganapathy Baskaran**
The Institute of Mathematical Sciences, Chennai
Superconductivity at Crossroads
11.04.2016
2. **Prof. Subir Sachdev**
Department of Physics, Harvard University, Massachusetts
Quantum entanglement and the phases of matter
13.04.2016
3. **Prof. A. J. Timothy Jull**
NSF-AMS Laboratory, University of Arizona, USA
Using ^{14}C and ^{129}I as tracers of cosmogenic events and environmental processes
19.04.2016
4. **Dr. Scott E. Parazynski**
Arizona State University, USA
Human Destiny in Space Current and Future Prospects
21.04.2016
5. **Dr. Henry Throop**
Planetary Science Institute, Arizona, USA
New Horizons Mission to Pluto and Beyond
01.06.2016
6. **Prof. Samir Mathur**
Ohio State University, USA
Resolution of the black hole information paradox
05.07.2016
7. **Dr. Mausumi Goswami**
School of Natural Sciences, Shiv Nadar University, UP
Fourier Transform Microwave Spectroscopy the ultimate structural tool for molecular science and astronomy
20.07.2016
8. **Prof. Majid Ebrahim-Zadeh**
The Institute of Photonic Sciences (ICFO), Spain
A Brief History of Light
02.09.2016
9. **Dr. Bidya Binay Karak**
National Centre for Atmospheric Research, USA
Solar Magnetic Fields and Cycles Understanding the Dynamo Mechanism
29.09.2016
10. **Dr. Amitava Sen Gupta**
The NorthCap University, Gurgaon
From Sundials to Atomic Clocks A glimpse into the amazing journey 28.12.2016
11. **Prof. Arnab Rai Choudhuri**
Indian Institute of Science, Bangalore
The Mysterious Magnetic Personality of Our Sun
05.01.2017
12. **Dr. Murthy S. Gudipati**
NASA Jet Propulsion Laboratory, California Institute of Technology, USA
Astrophysics, Astrochemistry, and Astrobiology Exploring the Universe in Search of Life Beyond Earth
14.03.2017

Conferences/Symposia/Workshops by PRL

Geosciences

1. Workshop on "Recent Trends in Isotope Geochemistry", Physical Research Laboratory, Ahmedabad, 16-17 June, 2016.

Space and Atmospheric Sciences

2. IASTA - 2016, Conference of Indian Aerosol Science and Technology Association (IASTA) on Aerosols and Climate Change: Challenges and Insights, Physical Research Laboratory, Ahmedabad, 6-8 December 2016..

Theoretical Physics

3. "PRL Conference on Condensed Matter Physics", PRL-Ahmedabad, 11-13 April 2016.

Atomic, Molecular and Optical Physics

4. 21st National Conference on "Atomic and Molecular Physics", NCAMP-XXI, PRL, Ahmedabad, 03-06 January 2017. .
5. SCOP - The Students Conference in "Optics and Photonics", PRL Ahmedabad, 2-3 Sep 2016.

Invited Talks at Conference / Symposia / Workshops

Astronomy and Astrophysics

A. Chakraborty

1. "High Resolution Spectroscopy and Radial Velocity", IIA-ISAC National Symposium on Exoplanets at Kodaikanal Observatory, Tamil Nadu, 7-8 October 2016."

A. S. Rajpurohit

2. "Very Low Mass Stars and Exoplanets", IIA-ISAC National Symposium on Exoplanets, Kodaikanal Observatory, Kodaikanal, 7-8 October 2016.

A. Sarkar

3. "Solar Wind & Space weather", IUCAA workshop for graduate and undergraduate students, M A College of Arts & Science, Kothamangalam, Kerala, 30 Nov - 2 Dec, 2016.
4. "Science with ASPEX", 35th Meeting of Astronomical Society of India, Jaipur, Rajasthan, 6 Mar - 10 Mar, 2017

L. K. Dewangan

5. "A multi-scale, multi-wavelength study of massive star-forming region W42", 34th meeting of Astronomical Society of India, University of Kashmir, Srinagar, 10 May - 13 May, 2016
6. "A multi-wavelength study of star formation activity in the S235 complex", Russian-Indian seminar on radio astronomy and star formation (2016), Institute of Applied Physics, Russian Academy of Sciences, Nizhny Novgorod, Russia (via Skype), 10 Oct - 12 Oct, 2016

7. "Observational study of massive star-forming regions W42 and IRAS 17599-2148", Star and Planet Formation Insights and Intricacies, IIST, Thiruvananthapuram, 5 Dec - 7 Dec, 2016
8. "The Physical Environment around IRAS 17599-22148 Infrared Dark Cloud and Bipolar Nebula", URSI Regional Conference on Radio Science 2017, Tirupati, 1 Mar - 4 Mar, 2017

M. K. Srivastava

9. "Introduction to Integral Field Units (IFUs) and Science with IFUs", Two Lectures in the Training School in Optical Astronomy with Large Telescopes, IUCAA, Pune, 16 Jan - 27 Jan, 2017

S. Naik

10. "Cyclotron Resonance Scattering Features in High Mass X-ray Binary Pulsars", Wide band spectral and timing studies of cosmic sources, TIFR, Mumbai, 10 Jan - 13 Jan, 2017
11. "Recent Results on Cyclotron Resonance Scattering Features in Accretion Powered X-ray Pulsars", 35th meeting of Astronomical Society of India, Jaipur, Rajasthan, 6 Mar - 10 Mar, 2017

G. K. Jaisawal

12. "Cyclotron absorption lines in the era of *Suzaku* and *NuSTAR*", the 7 years of MAXI monitoring X-ray transients, RIKEN, Wako, Japan, 5 Dec - 7 Dec, 2016
13. "Time resolved spectroscopy of high mass X-ray binaries", Wide band spectral and timing studies of cosmic sources, TIFR, Mumbai, 10 Jan - 13 Jan, 2017

14. "First detection of cyclotron absorption resonance scattering feature in high mass X-ray binary pulsar SMC X-2 with *NuSTAR*", 35th meeting of Astronomical Society of India, Jaipur, Rajasthan, 06 Mar - 10 Mar, 2017

P. Epili

15. "Timing and spectral studies of the transient X-ray binary pulsar KS 1947+300", Wide band spectral and timing studies of cosmic sources, TIFR, Mumbai, 10-13 Jan, 2017

S. Gupta

16. "Spectral Properties of High Mass X-ray Binary Cen X-3", Wide band spectral and timing studies of cosmic sources, TIFR, Mumbai, 10-13 Jan, 2017

S. V. Vadawale

17. "In-orbit performance of AstroSat-CZTI", SPIE Astronomical Telescopes & Instrumentation, Edinburgh, UK, 26 Jun - 1 Jul, 2016
18. "Hard X-ray polarimetry with AstroSat-CZTI", 2nd CORE-U International Conference Cosmic Polarimetry from Micro to Macro Scale, Hiroshima, Japan, 17-18 Feb, 2017
19. "Hard X-ray Polarimetry with AstroSat CZTI", 35th meeting of Astronomical Society of India, Jaipur, Rajasthan, 6-10 Mar, 2017
20. "Inflight calibration of AstroSat CZT Imager", 12nd meeting of International Astronomical Consortium for High Energy Calibration (IACHEC), Lake Arrowhead, California, US (Remote presentation), 27-30 Mar 2017.

Mithun N. P. S.

21. "AstroSat Proposal Preparation and Submission A Walkthrough", AstroSat AO-1 workshop, IUCAA, Pune, 13 Jul - 14 Jul, 2016
22. "In-flight Spectral Calibration of AstroSat CZT Imager", 35th meeting of Astronomical Society of India, Jaipur, Rajasthan, 6-10 Mar, 2017

V. Singh

23. "Distant AGN via radio continuum surveys and uGMRT", uGMRT Science Workshop, National Centre for Radio Astrophysics, Pune, 15-17 Jun, 2016
24. "Unveiling the nature of Infrared-faint Radio Sources in deep fields", SKA Pathfinder Radio Continuum Survey (SPARCS) conference, International centre Goa, 3-5 Nov, 2016.
25. "Discovery of three episodes of AGN-jet activity in a radio galaxy and role of new radio telescopes", URSI-RCRS conference, National Atmospheric Research Laboratory, Tirupati, 1-4 Mar, 2017

V. Joshi

26. "Near-infrared studies of Novae Highlights of recent results", 35th meeting of Astronomical Society of India, Jaipur, Rajasthan, 06-10 Mar, 2017

P. Janardhan

27. "A 20 year Decline in Solar Magnetic Fields and Solar Wind Micro-turbulence Are we Headed towards a Maunder-like Solar Minimum?", the URSI Asia Pacific Radio Science Conference, Seoul, South Korea, 21-25 Aug, 2016

S. Ganesh

28. "Solar system astronomy with the 3.6m DOT and 4m LMT", 1st Belgo-Indian Network for Astronomy & Astrophysics(BINA) workshop, ARIES, Nainital, 15-18 Nov, 2016

P. Chaturvedi

29. "Radial Velocity Studies of Eclipsing Binary Systems", ASI meeting, Jaipur, 6-10 March, 2017."

N. Kaur

30. "Multi-wavelength study of variability in blazars", Conference on Wide Band Spectral and Timing Studies of Cosmic X-ray Sources, TIFR-Mumbai, India, 10-13 Jan, 2017.

Aarthy E.

31. "GRB Polarization using AstroSat CZTI", 35th meeting of Astronomical Society of India, Jaipur, Rajasthan, 6-10 Mar, 2017.

Solar Physics

B. Joshi

32. "Active and eruptive Sun", UN-CSSTEAP Course on Space Weather, PRL, Ahmedabad, 9 May-8 Jun, 2016.
33. "HEL1OS and its science objectives", Science with Aditya L1 mission, 35th Annual Meeting of Astronomical Society of India, Jaipur, 6-10 Mar, 2017

B. Kumar

34. "Solar Internal Structure and Dynamics & Solar Oscillations", UN-CSSTEAP Course on Space Weather, PRL, Ahmedabad, 9 May-8 Jun, 2016.

Nandita Srivastava

35. "CMEs & Space weather", UN-CSSTEAP Course on Space Weather, PRL, Ahmedabad, 9 May-8 Jun, 2016.
36. "Solar Instrumentation", UN-CSSTEAP Course on Space Weather, PRL, Ahmedabad, 9 May-8 Jun, 2016.
37. "Multi-Application Solar Telescope: Study of solar activity using recent observations", Technical Seminar in Hindi, PRL, Ahmedabad, 29 Apr, 2016
38. "Preliminary observations with Multi-Application Solar Telescope (MAST) at Udaipur Solar Observatory", 35th Annual Meeting of Astronomical Society of India, Jaipur, 6-10 Mar, 2017.
39. "STEREO observations of Coronal mass ejections", COSTEP/ISWI school, Sangli, 10 Nov, 2016
40. "Solar Activity", IUCAA Solar Physics Workshop, Kothamanglam, 30 Nov – 2 Dec, 2016
41. "Recent Observations from the Multi-Application Solar Telescope (MAST) at Udaipur Solar Observatory", XIV Astrophysical Colloquium, Hvar Observatory, Croatia, 26-30 Sept, 2016.

Planetary Sciences and PLANEX Program**A. Bhardwaj**

42. "A New View on Solar Wind - Moon Interaction from SARA/Chandrayaan-1" International Conference on Frontiers in Theoretical and Applied Physics, American University of Sharjah, Sharjah, UAE, 22 Feb, 2017.
43. "In-situ observation of Martian neutral exosphere: Results from MENCA aboard Indian Mars Orbiter Mission (MOM)", International Conference on Frontiers in Theoretical and Applied Physics, American University of Sharjah, Sharjah, UAE, 23 Feb, 2017.

J. P. Pabari

44. "Research Avenues in Wireless Sensor Network", An Invited Talk during Research Week 2016, Gujarat Technological University, Chandkheda, Ahmedabad, 21 Apr, 2016.
45. "Recent Advances in Microwave Remote Sensing for Planetary Surface Study", STTP on "Recent Advances in RF and Microwave Engineering", Lalbhai Dalpatbhai College of Engineering, Ahmedabad, 23 Nov, 2016.

K. Durga Prasad

46. "A 3D Thermal Model for Lunar Surface using COMSOL - Validation and Results", COMSOL International Conference-2016, Bangalore, 20-21 Oct, 2016.

S. A. Haider

47. "Effect of X-Ray Flares on the Ionosphere and Human Exploration to Mars", International Conference on Frontiers in Theoretical and Applied Physics, Sharjah, UAE, 22-25 Feb. 2017.

S. K. Goyal

48. "Supra Thermal & Energetic Particle Spectrometer, subsystems of ASPEX payload (onboard Aditya L1 mission)", 35th Meeting of Astronomical Society of India, Jaipur, Rajasthan, 6-10 Mar, 2017.

V. Sheel

49. "Variability of Trace Gases in the Atmosphere of Mars", International Conference on Frontiers in Theoretical and Applied Physics, Sharjah, UAE, 22-25 Feb. 2017.

Space and Atmospheric Sciences**A. Guharay**

50. "Investigation of lower atmospheric wave dynamics", User scientist workshop on ST wind profiler radar, Cochin University of Science and Technology, Kochi, 09-10 Feb, 2017.

D. Pallamraju

51. "9th IAGA - ICMA/IAMAS - ROSMIC/VarSITI/SCOSTEP workshop on Long-Term Changes and Trends in the Atmosphere", The changes in ionospheric-thermospheric behaviour during varying solar activity levels, Kühlungsborn, Germany, 19-23 Sep, 2016.

H. Gadhave

52. "Biomass burning aerosol emissions over India: Implication for climate", Indo-Dutch bilateral conference on climate, Atmospheric Sciences and Applications, IIT-Delhi, New Delhi, 20-21 Feb, 2017.

L. K. Sahu

53. "Volatile organic compounds at urban sites of India: Recent results from PTR-TOF-MS measurements", US Embassy Workshops on Combating Air Pollution in North India, Jaipur, 23-24 May, 2016.

S. Lal

54. "Atmospheric chemistry in the Indian region", Japan Agency for Marine-Earth Science and Technology (JAMSTEC), Yokohama, Japan, 9 Sep, 2016.
55. "Ozone and trace gases in the Indian region", Workshop on Major Challenges and Opportunities to Air Pollution Research in South Asia, Kathmandu, Nepal, 28-29 Nov, 2016.

S. Ramachandran

56. "Aerosol simulations: Challenges", US Embassy Workshops on Combating Air Pollution in North India, Jaipur, May 23-24, 2016.
57. "Aerosols: Role in regional climate", Workshop on Climate Change and Regional Impacts over South Asia, Indian Institute of Tropical Meteorology, Pune, 28-29 Jul, 2016.
58. "Aerosols and Climate: Challenges", Conference of Indian Aerosol Science and Technology Association, Physical Research Laboratory, Ahmedabad, 6-8 Dec, 2016.
59. "Aerosols, and Climate Change", Seminar on Climate Change and its Impact, Dharmasinh Desai University, Nadiad, 19 Jan, 2017.
60. "Aerosols and Climate Change: Challenges", Indo-Dutch International Conference on Atmospheric & Climate Science, Indian Institute of Technology, Delhi, 20-21 Feb, 2017.

S. K. Sharma

61. "Multi-instrumental Study of Aerosols and Clouds: Future Perspective", ARFI Review meeting, Space Physics Laboratory (VSSC, ISRO), Thiruvananthapuram, 21 Mar, 2016.

Geosciences Division**J. S. Ray**

62. "Learning from Volcanoes: story of India's only active volcano", Kalinga Institute of Industrial Technology University, Bhubaneswar, 17 Nov, 2016.
63. "The Proterozoic Earth: a geochemical insight from rocks of India", 6th Dr. Venkatachala Memorial Lecture, Birbal Sahni Institute of Palaeosciences, Lucknow, 02 Jan, 2017.

S. K. Singh

64. "Tectonic - Weathering - Climate coupling in the Himalayan Orogenic Belt in 1st triennial convention on "Geosciences for Sustainability", Federation of Indian Geosciences Associations, Indian Institute of Technology (ISM), Dhanbad, 8-10 Nov, 2016.

R. D. Deshpande

65. "Enigma of large ice-stones falling from clear sky without any pre-indication", Popular Lecture in the Conference of Indian Aerosol Science and Technology Association (IASTA-2016), PRL, Ahmedabad, 6 Dec, 2016.
66. "Application of isotopes in Aquifer Mapping", Bhujal Manthan-2, Section on Aquifer Mapping & Ground Water Management, by CGWB, Ministry of Water Resources, Vigyan Bhavan, New Delhi, 29 Nov, 2016.
67. "Importance of Interdisciplinary Sciences: Curiosity and Necessity", Seminar on Emerging Trends and Opportunities in Interdisciplinary Sciences, Centre for Interdisciplinary Studies in Science and Technology, S.P University, Vallabh Vidyanagar, 3 Feb, 2017.

M. G. Yadava

68. "Paleoclimate reconstruction from speleothems", Symposium on Advances in Modern Earth System Sciences, Indian Institute of Science Education and Research (IISER), Kolkata, 25-26 Mar, 2017.

S. Kumar

69. "Nitrogen cycling in terrestrial ecosystems", Symposium on Advances in Modern Earth System Sciences, Indian Institute of Science Education and Research (IISER), Kolkata, 25 Mar, 2017

N. Rastogi

70. "Oxidative Potential of Ambient Aerosols: Impacts on Human Health", Centre for Environmental Science and Engineering (CESE), Indian Institute of Technology, Kanpur, 14 Dec, 2016.

A. Singh

71. "Cellular isotopic composition of marine microorganisms", Conference on Recent Trends in Isotope Geochemistry, Physical Research Laboratory (PRL), Ahmedabad, 16 Jun, 2016
72. "Timeseries analysis of dissolved oxygen and inorganic nutrients in the eastern Arabian Sea", International Symposium on Microbial Responses to Ocean Deoxygenation, National Institute of Oceanography, Goa, 2-6 Dec, 2016.
73. "Impacts of Ocean Acidification on Ocean Biogeochemical Cycles", Climate Change and its impact, Dharmasinh Desai University, Nadiad, 19 Jan, 2017.

M. M. Sarin

74. Atmospheric organic aerosols in the Indo-Gangetic Plain session on "Atmospheric pollution in the Hindu-Kush-Himalaya (HKH) and Indo-Gangetic Plain (IGP) region", EGU-2016, Vienna (Austria), 17-22 Apr, 2016.

R. Ramesh

75. "Quantifying climate change by innovative use of isotopes", in Mini-Symposium on Earth and Planetary Sciences, National Institute of Science Education and Research, Bhubaneswar, 5 May, 2016.
76. "Problems related to climate change in the Anthropocene", International Seminar on 'Environmental Security and sustainable development in South Asia', South Asia, 19 Oct, 2016.
77. "Long term climate variability", at the 2nd Brain storming meeting on MoES strategic Vision document, Indian Institute of Tropical Meteorology, Pune, 9 May, 2016.
78. "Problems pertaining to climate change and Oceans", at the 'Brainstorming Session on Future Earth', Divecha Centre for Climate Change, Indian Institute of Science, Bengaluru, 9 Jul, 2017.

79. "My adventure with stable isotopes in earth Sciences", at Scientific Interaction meeting on 'Recent trends in isotope geochemistry', PRL, Ahmedabad, 16-17 Jun, 2016.
80. "Sun and Climate", SCOSTEP/ISWI International School on Space Science, Sangli, Maharashtra, 17 Nov, 2016.
81. "Past monsoon reconstruction from speleothems", 104th Indian Science Congress, S.V. University, Tirupati, 6 Jan, 2017.

Theoretical Physics

S. Mohanty

82. "Detection of dark matter with gravitational waves", Plenary talk, in the conference "Dark Side of the Universe" 2016, Bergen, Norway, 25-29 Jul, 2016.

H. Mishra

83. "Matter under extreme conditions", 34th Annual convention of Odisha Physical Society, Berhampur University, 11-12 Feb, 2017.
84. "Viscosity coefficients in quark matter", Theory Conference- ten Years of IISER Kolkata, IISER Kolkata, 20-21 Jan, 2017.
85. "Transport coefficients of hot and dense quark matter", International Nuclear Physics Conference, (INPC 2016), Adelaide, Australia, 11-16 Sep, 2016.

Angom D. K. Singh

86. "Properties of two-component Bose-Einstein condensates", Plenary talk, National Conference on Atomic and Molecular Physics XXI (NCAMP-XXI), PRL, Ahmedabad, 3-6 Jan, 2017.

R. Rangarajan

87. "Constraints on just enough inflation preceded by a thermal era", COSMO-16, University of Michigan, Ann Arbor, 7-12 Aug, 2016.

P. Konar

88. "Kinematic variables - important instrumental for event selection Collider Physics", Analysis and QCD, at Department of Physics, IIT Guwahati, 27-31 Mar, 2017.
89. "Kinematic variables for BSM search", CHEP meet at Indian Institute of Science, IISc, Bangalore, 20-22 Dec, 2016.
90. "Boosted objects - Jet substructure and New kinetic variables at the LHC", XXII DAE-BRNS HEP Symposium, University of Delhi, 12-16 Dec, 2016.
91. "T-cup and beyond: some recent developments", PHENO Workshop on Beyond Standard Model Physics, IISER Mohali, 6-9 Apr, 2016.

S. Goswami

92. "Status of INO", Invited Planery talk, Neutrino 2016, London, UK, London, UK, 3-9 Jul, 2016.
93. "Neutrinoless double beta decay", Invited talk, Pheno1, IISER Mohali, 6-9 Apr, 2016.

Atomic, Molecular and Optical Physics

R. P. Singh

94. "Vortex scattering through random media", International Workshop on Complex Photonics, TIFR, Mumbai, 22-24 Jan, 2017.

B. K. Sahoo

95. "Relativistic Theory for Atomic Electric Dipole Moments.", Recent Advances in Many-Electron Theory (RAMET 2017), Hotel Bogmallo Beach Resort, Goa, India, 9-12 Feb, 2017.
96. "Atomic Calculations for Frequency Standards.", 21st National Conference on Atomic and Molecular Physics (NCAMP 2017), PRL, Ahmedabad, 3-6 Jan, 2017.
97. "Relativistic Many-body Methods for Electric Dipole Moments of Closed-shell Atoms Current Trends and Future Directions Relativistic Many Electron Theories", (RMET-2016), Tokyo Institute of Technology (TIT), Japan, 26-28 Sep, 2016.

B. Sivaraman

98. "Synthesizing the basic PAH unit.", NCAMP-XXI, PRL 21st National Conference on Atomic and Molecular Physics, PRL, Ahmedabad, 3-6 Jan, 2017.
99. "Astrochemistry and Chemical Engineering.", Department of Chemical Engineering, VIT University, Vellore, 7 Feb, 2017.
100. "Laboratory Astrochemistry", Department of Physics, Ethiraj college, Chennai. 8-10 Feb, 2017.

D. Sahu

101. "The Molecular Universe: study by means of modelling, experiment and observation", IISc Physics Department, Bengaluru, 4 Apr, 2017.

G. K. Samanta

102. "ICO/ICTP Gallieno Denardo Award for Optics", Winter College on Optics, ICTP, Trieste, Italy, 21 Feb, 2017.
103. "Nonlinear frequency conversion of structured beams and Airy beam optical parametric oscillator", Photonics West, San Francisco, USA, 28 Jan-2 Feb, 2017.
104. "Structured beam parametric sources and optical parametric oscillators", 25th DAE BRNS National Laser Symposium (NLS-25), KIIT University, Bhubaneswar, 20-23 Dec, 2016.
105. "Structured laser beams and novel applications", 7th EPS-QEOD Europhoton Conference, Vienna, Austria, 21-26 Aug, 2016.

106. "Structured beam optical parametric oscillators", Recent Advances in Optical Sciences-II, School of Physics, University of Hyderabad, Hyderabad, 6-7 May, 2016.

Prashant Kumar

107. "Ratio based algorithm to quantitatively determine elemental composition using CF-LIBS", 9th International Conference on Laser-Induced Breakdown Spectroscopy (LIBS), Chamonix-Mont-Blanc, France, 12-16 Sep, 2016.
108. "Improvements to the CF-LIBS algorithm for elemental analysis", 21st National Conference on Atomic and Molecular Physics (NCAMP-XXI), PRL, Ahmedabad, 3-6 Jan, 2017.
109. "Solar Wind Ion Spectrometer (SWIS) on-board Aditya-L1 Mission", 35th Annual Meeting of the Astronomical Society of India (ASI), BISR, Jaipur, 6-10 Mar, 2017.

K. P. Subramanian

110. "Rainbow Effects in Atomic Scattering", National Seminar on Theoretical Physics, University of Calicut, Thenhipalam, 24-25 Mar, 2017.

R. K. Kushawaha

111. "Structure and dynamics of molecular ions: Probing the wave packet dynamics", 21st National Conference on Atomic and Molecular Physics, PRL, Ahmedabad, 3-6 Jan, 2017.
112. "Mapping of evolution Dynamics and Structure of molecular systems: Towards Molecular Movies", National Workshop on LASER TECHNIQUES, GJUS&T Hisar, 2-3 Mar, 2017.

Lectures at Universities / Institutions

Astronomy and Astrophysics

M. K. Srivastava

1. "Advanced Instrumentation in Optical Astronomy", Centre for Basic Sciences, Pt. Ravishankar Shukla University Raipur, January 16, 2017

G. K. Jaisawal

2. "Cyclotron resonance scattering feature and magnetic field of pulsars", Saitama University, Saitama, Japan, December 08, 2016
3. "Probing the magnetic field of accretion powered X-ray pulsars", Rikkyo University, Tokyo, Japan, December 10, 2016

S. V. Vadawale

4. "Solar X-ray Monitor (XSM) experiment on board Chandrayaan-2", Department of Applied Mathematics and Theoretical Physics, Cambridge University, UK, July 6, 2016
5. "Aditya Solar-wind and Particle Experiment (ASPEX) on board Aditya-L1 mission", Department of Applied Mathematics and Theoretical Physics, Cambridge University, UK, July 7, 2016
6. "Early results from Astrosat-CZTI", School of Physics and Astronomy, University of Southampton, UK, July 13, 2016

Solar Physics

A. Ambastha

7. "The Active and Explosive Sun", DST-Inspire Camp, Shrinathji Institute of Technology and Engineering, Nathdwara, Rajsamand, August 10, 2016

8. "The Invisible Sun", DST-Inspire Camp, Sir Padampat Singhan University, Bhatewar, Udaipur, October 21, 2016
9. "A Cosmic Voyage: Space-time scales and structures", DST-Inspire Camp, Shrinathji Institute of Technology and Engineering, Nathdwara, Rajsamand, February 21, 2017
10. "Elements of Solar Physics", Series of 10 lectures at 10th Post Graduate Course in Space and Atmospheric Sciences, Centre for Space Science and Technology Education in Asia and the Pacific, Bopal Campus, Ahmedabad, December 19 – 23, 2016

B. Joshi

11. "Multi-wavelength signatures of magnetic reconnection and energy release processes in solar eruptive phenomena", Astrophysics Colloquium, Institute of Physics, University of Graz, Graz, Austria, August 1, 2016
12. "Lectures on Solar structure and processes", Kadi Sarva Vishwavidyalaya, Gandhinagar, Gujarat, April 4 – 5, 2016

B. Kumar

13. "Helioseismology and GONG Program: A tool for sounding the solar interior", Department of Physics, B.N. University, Udaipur, April 7, 2016

Nandita Srivastava

14. "Current Research and facilities at Udaipur Solar Observatory", IGAM, University of Graz, Austria, June 24, 2016

Planetary Sciences and PLANEX Program

J. P. Pabari

15. "Planetary Surface Study using Microwave Remote Sensing", Parul Institute of Engineering and Technology, Waghodia, July 25, 2016.

K. Achyra

16. "Molecular Complexity in Magellanic Clouds", Leiden observatory, The Netherlands, 19th April, 2016.

Space and Atmospheric Sciences**A. Guharay**

17. "Characteristics of atmospheric waves and their impact on ambient atmosphere", Pt. Ravishankar Shukla University, Raipur, Chhattisgarh, October 03, 2016.

S. K. Sharma

18. "Remote Sensing of the Earth's Atmosphere: Research and Societal Outlook", Council of Science and Technology of UP, Lucknow, July 25, 2016.
19. "Lidar and Radar Studies of the Earth's Atmosphere", DST INSPIRE Program, Christ College, Rajkot, Gujarat, April 29, 2016.
20. "LIDAR Observed Atmospheric Temperature Characteristics and its Association with Ozone over Western Indian Region", Max-Planck-Institut für Chemie (MPIC), Mainz, Germany, September 15, 2016.
21. "Earth's Lower and Middle Atmospheres: Uniqueness and Importance for Society", DST INSPIRE Program, Christ College, Rajkot, Gujarat, October 24, 2016.

S. Ramachandran

22. "Aerosol characteristics: Observations and model simulations", National Atmospheric Research Laboratory, Gadanki, April 13, 2016.
23. "Aerosols: Observations and model simulations", SRM University, Chennai, April 26, 2016.
24. "Aerosols, and Climate Change", World Environment Day, Science City, Ahmedabad, June 5, 2016.

D. Pallamraju

25. "Space Weather: Science and Applications", UN School on Space Weather, held at PRL during 9 May to 4 June 2016, 2 lectures, May 16, 2016.
26. "Optical Techniques for Space Weather Studies", UN School on Space Weather, held at PRL during 9 May to 4 June 2016, 1 Lecture., May 25, 2016.
27. "Influence of equatorial electrodynamics on low-latitude neutral optical dayglow emissions", Indian Institute of Geomagnetism, Navi Mumbai, March 10, 2017.

T. A. Rajesh

28. "Earth's atmosphere and Radiation budget", 10 Lectures for M.Sc. (Earth Science), Sardar Patel University, Vallabh Vidyanagar, Anand, September- November 2016.

H. Chandra

29. "UN Course (short) on Space weather", 10 Lectures on Ionosphere- Thermosphere, May-June 2016.
30. "UN Course on space science", 36 Lectures on ionosphere and radio techniques, August-September 2016.

S. Lal

31. "Atmospheric structure", Eight lectures to the students of Space science course of CSSTEAP conducted by PRL, Ahmedabad, August 3-23, 2016.
32. "Ozone and other trace gases and atmospheric Chemistry", Three lectures to the students of the Satellite Meteorology and Global Climate (SATMET) course of CSSTEAP conducted by SAC, Ahmedabad, January 4-6, 2017.

Geosciences Division**S. K. Singh**

33. "Organized a theme, "Weathering and Erosion", Goldschmidt Conference 2016", Yokohama, Japan, June 26 - July 1, 2016

A. Singh

34. "Hydrosphere and Earth Systems", International Earth Science Olympiad (IESO) - 2016 students at Anna University, May 25-29, 2016 (10 lectures).
35. "Pre-departure camp of IESO 2016 students at Anna University", Anna University, September 16-18, 2016. (9 lectures).
36. "Monitoring Structure & Function of Pelagic Ecosystem at Regional Sectors: Relevance for fisheries", Marine Nitrogen Cycle in the NICRA sponsored training programme, CMFRI, Cochin, December 29, 2016 (3 invited lectures).
37. "Climate Modelling", II semester M.Sc. students at Gujarat University, Ahmedabad, Jan-April 2017 (10 lectures).
38. "Oceanography and climate change", UGC Refresher Course, Orientation Programme, S P University, Anand, February 18, 2017 (2 lectures).

R. Ramesh

39. "DST-INSPIRE lectures", K.R. Rangasamy College, Thiruchengodu, July 31; Sep 03; & Oct 22, 2016 (4 Lectures).
40. "DST-INSPIRE lecture", M.S. University of Baroda, Vadodara, Aug 12, 2016.
41. "Climate Change", M.Sc. students at the Gujarat University, Ahmedabad, Feb-Dec, 2016 (20 Lectures).
42. "Advanced Statistics", IIT, Kharagpur, Sep 21-26, 2016 (10 Lectures)
43. "Oceanography", Sardar Patel University, Anand, Oct 7-12, 2016 (10 Lectures).
44. "Tenth Post-Graduate Course on Space and Atmospheric Science", CSSTEAP, October 13-14, 2016 (2 Lectures).

Theoretical Physics**R. Rangarajan**

45. "Gravitinos, Reheating and the Matter-Antimatter Asymmetry of the Universe", University of Pittsburgh, August 15, 2016
46. "Exploring the Pre-Inflationary Universe", University of Pennsylvania, Philadelphia, August 16, 2016

P. Konar

47. "Review on optimum variable in search at LHC", Harish-Chandra Research Institute, Allahabad, February 4 - 17, 2017
48. "Statistical Methods in Physics", SERC Preparatory School in THEP lecture and tutorials at IIT-Gandhinagar, September 12-17, 2016

N. Singh

49. "Non-equilibrium electron relaxation: memory function approach", Physics Department, PU Chandigarh, November 3, 2016

S. Goswami

50. "Guest Faculty for the Group Theory Course", 6 tutorial sessions in SERC school held at IIT Gandhinagar, 4 Sept – 9 Sept, 2016.

N. Mahajan

51. "Guest Faculty for Scattering Amplitudes course, XXXI Main SERC School in Theoretical High Energy Physics, University of Kalyani, 9 January- 18 January, 2017.

Atomic, Molecular and Optical Physics**A. K. Singhvi**

52. "Land Sea Correlations: Pitfalls and Remedies", National workshop on Holocene and Anthropocene, Emerging trends

Birbal Sahni Institute of Paleobotany, February 21-23, 2017

53. "Thermochronology and Himalayan Tectonics", Inaugural talk at the National Brainstorming seminar, March 27-28, 2017
54. "Inaugural lecture", Annual Convention of Indian Association of Sedimentologists BSIP, Department of Geology, Banaras, November 12, 2016.
55. "University of Salzburg on Societal Relevance of- and Scientific Challenges for-Geosciences as Services", Invited Geoscience Colloquium, Departments of Geosciences and Geography, March 14, 2017

N. Chauhan

56. "Spatially Resolved Luminescence System", Oral Presentation in NCAMP-2017, January 3-6, 2017
57. "Luminescence Dating: Developments and Applications", Colloquium lecture, March 8, 2017
58. "Luminescence Thermochronology", Invited lecture in a workshop in Kurukshetra University., March 28, 2017

B. K. Sahoo

59. "Modern atomic clocks for testing fundamental physics and other applications", Department of Physics, IIT Roorkee, Roorkee, May 12, 2016
60. "Atomic Clocks as time keeping devices to probing new physics", Time and Frequency Division-CSIR, National Physical Laboratory, New Delhi, April 4, 2016
61. "Electron correlation trends in Ca^+ ion", Wuhan Institute of Physics and Mathematics (WIPM), Wuhan, China, April 1, 2016

R. P. Singh

62. "Optical Vortices: Making Whirlpools in Light", IIT Madras Colloquium, October 5, 2016

Science

Astronomy and Astrophysics

Simulation of dynamic solar active region

Various modern space based observations have shown that when an active region of the solar corona is hit by a flare like explosive event, it goes through various complicated dynamics. Understanding such dynamics require detailed numerical simulation. We have simulated such a flare hitting an active region.

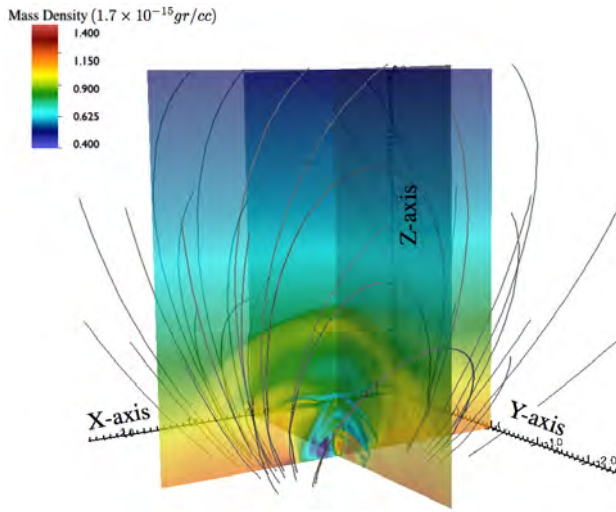


Figure 1: A snapshot taken from the simulated active region which is hit by a flare. Figure showing density colour contour and magnetic field lines.

We show that the loop structures of this active region develop magnetohydrodynamic wave modes, which were theoretically

predicted for a much simpler geometry. Our simulations also reveal complicated dynamics of the loop behavior. Such a simulated active region is shown in the figure 1.

This work is done in collaboration with Bhargav Vaidya of IIT - Indore and Soumitra Hazra of IISER - Kolkata.

(A. Sarkar)

Amplitude of solar wind density turbulence from 10 to 45 R_s .

Turbulent density inhomogeneities in the solar corona are typically characterized by their spatial power spectrum

$$P_{\delta N}(k) = C_N^2(R) k^{-\alpha} e^{-(kl_i(R)/2\pi)^2}, \quad (1)$$

where k is the (isotropic) wave number, and $l_i(R)$ is the inner (dissipation) scale, where the spectrum steepens. The quantity C_N^2 is the amplitude of density fluctuations, and has dimensions of $\text{cm}^{-\alpha-3}$. Here, k is the (isotropic) wave number, and $l_i(R)$ is the inner (dissipation) scale, where the spectrum steepens. Density fluctuations are an important and relatively ill-understood facet of the phenomenon of solar wind turbulence. Most studies of solar wind turbulence in general, and density fluctuations in particular, concentrate on the spectral slope (α , Eq 1) and not so much on its spectral amplitude C_N^2 .

The amplitude of the density turbulence spectrum is the key to several important problems such as extended solar wind heating and angular broadening of radio sources. Our knowledge of C_N^2 and its heliocentric

dependence in particular, is currently limited to the investigations using VLBI observations made 2 years past the maximum of cycle 19 to probe scale sizes ≥ 200 km and using the Kolmogorov scaling ($\alpha = 11/3$) and without considering an inner/dissipation scale. The density modulation index ϵ_N is given by:

$$\epsilon_N(R) \equiv \frac{\delta N_{k_i}(R)}{N(R)} \quad (2)$$

where, N is the solar wind background density is somewhat better studied. However, most of these studies have rather sparse coverage, with only one comprehensive study of this, in the literature, only for heliocentric distances $> 40R_\odot$.

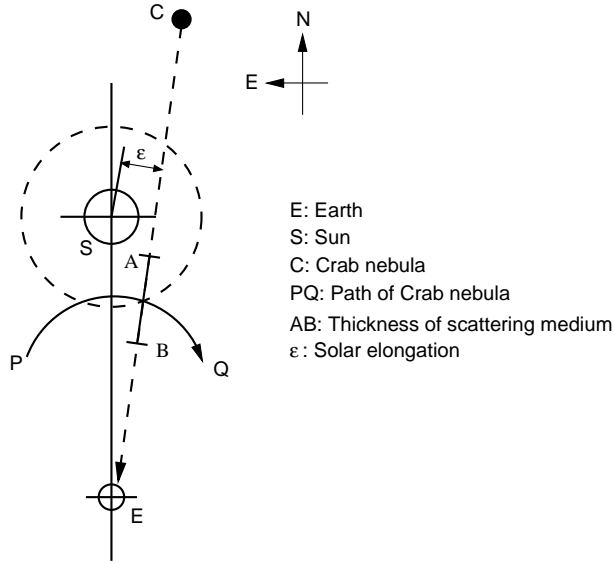


Figure 2: The schematic diagram shows the geometry of Crab nebula occultation; 'PQ' indicates the projected path of the Crab nebula during the month of June. The closest point of 'PQ' to 'S' is $\approx 5 R_\odot$. The radiation from the 'C' passes through the effective turbulent medium 'AB' at a solar elongation of ' ϵ ' as viewed from 'E'.

We use results from the standard technique of Crab nebula occultation to obtain a comprehensive palette of results concerning the heliocentric dependence of the density turbulence spectral amplitude (C_N^2) and the density modulation index (ϵ_N) for $10R_\odot < R < 45R_\odot$. This is a distance range that is typically not covered by either IPS or interferometric techniques. We include the effects of the inner scale using currently prevalent models for it. Since the spatial scales used are small enough to possibly be comparable to the inner/dissipation scale, we use the general structure function (GSF) to model the observed visibilities rather than asymptotic approximations. Since there is evidence for flattening of the spectrum near the inner scale, we quote results for $\alpha = 11/3$ as well as a flatter value of 3. We parametrize the heliocentric dependence of the density turbulence amplitude as $C_N^2(R) = AR^{-\gamma}$ to get an idea of the range of possibilities for the behavior of C_N^2 using currently prevalent ideas. To the best of our knowledge, this is the most extensive characterization of the density turbulence spectral amplitude to date.

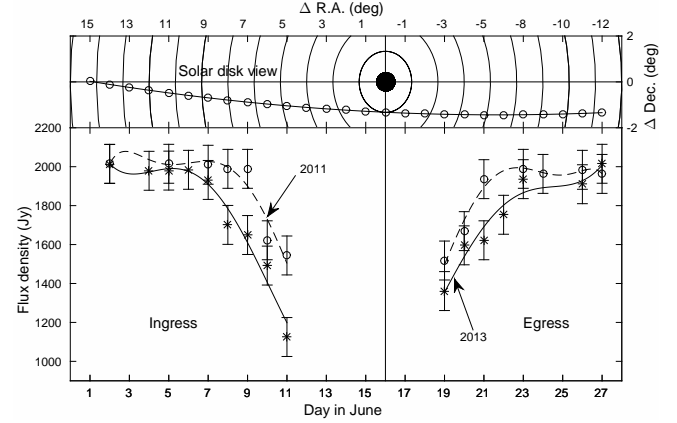


Figure 3: The upper panel shows solar disk view of the Crab nebula occultation. The filled circle indicates the Sun and open circles represent the position of Crab nebula with respect to the Sun on different dates; $\Delta R.A.$ and $\Delta Dec.$ are the offset distances of Crab nebula from the Sun in right ascension and declination respectively. The concentric circles around the Sun are drawn in steps of $5 R_\odot$ from the sun. The bottom panel shows the observed flux densities at 80 MHz, of the Crab nebula on different days during its occultation by the solar corona. The periods before and after June 16th correspond to the ingress and egress, respectively. The plots marked 'o' and '*' correspond to measurements during June 2011 and June 2013, respectively.

For example, for the proton inertial length prescription for the inner scale and $\alpha = 3$, 'A' ranges from 2.2×10^3 to $1.2 \times 10^8 \text{ cm}^{-6}$ and γ ranges from -2.1 to -4.9 . With the same inner scale prescription, with $\alpha = 11/3$, 'A' varies between 1.3 and $5.3 \times 10^4 \text{ m}^{-20/3}$ and γ ranges from -2.7 to -5.6 . With the proton gyroradius inner scale model and $\alpha = 3$, 'A' ranges from 4×10^2 to $2.3 \times 10^6 \text{ cm}^{-6}$ and γ ranges from -1.7 to -4.4 . With the proton gyroradius inner scale model and $\alpha = 11/3$, 'A' ranges from 0.74 to $1.4 \times 10^4 \text{ cm}^{-20/3}$ and γ varies from -2.6 to -5.4 . Given the widely different observational and theoretical interpretation techniques we use, and the fact that the observations we are using for comparison are from a different solar cycle, this is remarkable.

This work was done in collaboration with IIA, Bangalore and IISER, Pune.

(M. Ingale and P. Janardhan)

Spectroscopic follow-up of short and long period comets

Optical low resolution spectra of various comets (long and short period) were obtained with the LISA (Long slit Intermediate resolution Spectrograph for Astronomy) spectrograph mounted on 0.5m and 1.2m telescopes at Mt. Abu IR Observatory (MIRO). Comets C/2015 V2 (Johnson), C/2015 ER61 (PanSTARRS), C/2013 X1 (PanSTARRS) and C/2013 US10 (Catalina) are the long period comets observed during the period October 2016 to Feb 2017. Comets 41P/Tuttle-Giacobini-Kresak and 45P/Honda-Mrkos-Pajdusakova are the two short period comets observed during December 2016 to Feb 2017.

The comets showed a lot of molecular emissions with varying C2 to CN ratio. This variation could be because of the intrinsic heterogeneity in the composition of the comets. Even when comets are from

the same family, their age, number of perihelion passes, the orbital inclination, the perihelion distance, all play a very important role in determining the molecular content and the production rates. Hence it is important to study the evolution of the molecular emissions of different comets as they approach perihelion and then move away in their orbit.

(K. Venkataramani, S. Ganesh and K. S. Baliyan)

High resolution optical spectroscopy to probe the evolution of cometary volatiles

Comets show a plethora of molecular emissions in their optical spectra. The spectra of the comets in the optical region obtained by using the PRL 0.5m telescope at Mount Abu Infra-Red Observatory (MIRO) show many molecular emission lines from species like C2 (Swan Bands), C3, CN, CH, OH, NH₂. Many of these emissions appear as bands and are blended. To unblend and study these emission lines in detail requires high resolution spectroscopy. Studying these different molecular emissions and their isotopic abundances as a function of cometary orbital parameters would significantly help our understanding of cometary volatiles and their evolution.

Therefore, in an attempt to study the comets with high spectral resolution, we had obtained time on the high resolution Hanle Echelle Spectrograph (HESP) mounted on the 2m Himalayan Chandra Telescope, at Hanle. This spectrograph has two resolution modes(30000 and 60000), of which the 30000 resolution mode was used to observe the comets C/2015 V2 and comet 41P/Tuttle-Giacobini-Kresak. The spectra of comet C/2015 V2(Johnson) clearly showed the atomic oxygen lines at 6300, 6360 and green line 5770. Further analysis of the spectra obtained during February and March 2017 is in progress. Both these comets are brightening further as they approach perihelion later this year. In order to study them at varying epochs (and hence, varying heliocentric distances), we plan to follow them with more HESP time in the coming cycle of HCT observations.

This work is done in collaboration with B.C.Bhatt, D.K.Sahu, T. Sivarani and A. Surya of Indian Institute of Astrophysics, Bengaluru.

(K. Venkataramani, S. Ganesh and K. S. Baliyan)

Near-infrared and optical studies of the highly obscured nova V1831 Aquilae (Nova Aquilae 2015)

The evolution of Nova V1831 Aquila in near Infrared (NIR) and optical wavelength domains have been studied using photometry and spectroscopy. It was a highly reddened nova. Our studies covered the early decline and dust forming phases during the first ~ 90 days after its discovery. Based solely on the nature of NIR spectrum we are able to classify the nova to be of the Fe II class. The distance and extinction to the nova are estimated to be 6.1 ± 0.5 kpc and $A_v \sim 9.02$ respectively. Estimates of the electron density, emission measure and ionized ejecta mass are made from a Case B analysis

of the NIR Brackett lines while the neutral gas mass is estimated from the optical [OI] lines. We discuss the cause for a rapid strengthening of the He I 1.0830 μm line during the early stages. V1831 Aql formed dust around 18 days after discovery, one of the earliest dust producing events seen in a nova. The dust was not substantial enough for the shell to be optically thick. Estimates are made of the dust parameters viz. temperature, dust mass and grain sizes; the evolution of these parameters is studied. While the dust temperature is seen to gradually decrease from 1400K to 950K over the course of our observations, the dust mass and mean grain radius remained fairly constant with values in the range $(1 - 2) \times 10^{-8} M_\odot$ and $1.5 - 3.0 \mu\text{m}$ respectively.

This work has been done in collaboration with Prof. U. Munari of the INAF Astronomical Observatory of Padova, Italy and other collaborators.

(D. P. K. Banerjee, M. K. Srivastava and N. M. Ashok)

Multi-wavelength study of intermediate age open cluster NGC 5617

In this work we have studied an intermediate age open star cluster NGC 5617 towards, longitude (l)= -45 deg in the Galactic plane. For this purpose we have used the CCD BVRI, PPMXL, 2MASS, VVV survey, WISE and GLIMPSE data. Stellar density distribution and color-magnitude diagrams are used to estimate the geometrical structural parameters (cluster center, cluster radius, core and tidal radii, the distance from the Sun, Galactocentric distance and the perpendicular distance from the Galactic plane). Also, the main astrophysical parameters of the cluster i.e. age, color excesses, total mass, relaxation time, dynamical evolution parameter, luminosity function, mass function and mass-segregation are also derived.

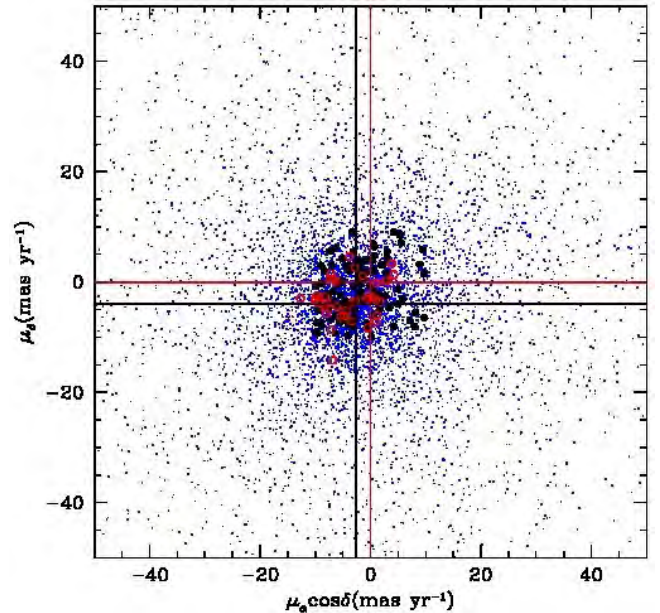


Figure 4: The distribution of stars in the $\mu_\alpha \cos(\delta) - \mu_\delta$ plane, for which proper motion values are determined. Solid black line shows the mean proper motion in RA and DEC directions.

The mean proper motion of a cluster is defined as the average angular displacement of the cluster, per year, by which it has changed its position over the sky. We have used the PPMXL catalogue which provides the absolute proper-motion with an accuracy of 4-10 mas yr⁻¹ for about 900 million stars. The proper motion values in RA and DEC directions for NGC 5617 is estimated by fitting a Gaussian function. Distribution of stars in the cluster NGC 5617 is shown in Figure 4. We have thus found the mean-proper motion as -2.68 ± 0.29 mas yr⁻¹ and -4.04 ± 0.23 mas yr⁻¹ in RA and DEC directions, respectively. Using these proper motion values we have determined membership probabilities (spatial and kinematical) for this cluster. We find 38 stars as most likely members of NGC 5617 cluster. These are shown in Figure 5 as red dots. We have fitted theoretical isochrones to our observed colour-magnitude diagrams as shown in Figure 5 to estimate the age and distance. In the kinematical studies of the cluster, we have estimated the total velocity, space velocity and elements of solar motion of the cluster NGC 5617.

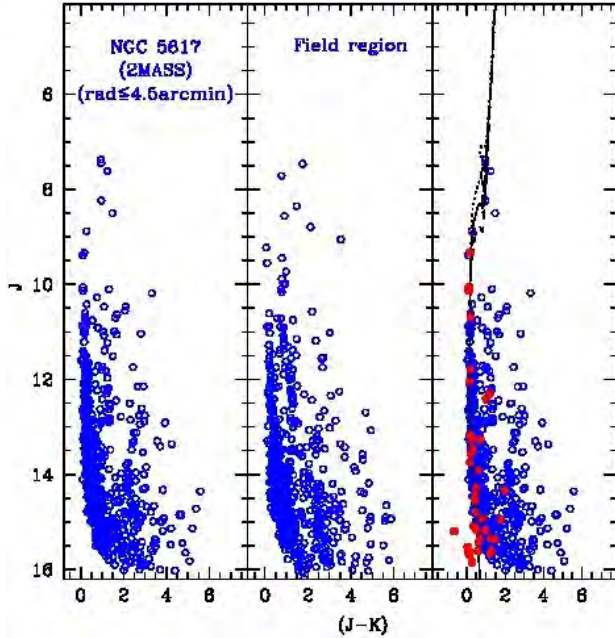


Figure 5: The colour-magnitude diagram of open cluster NGC 5617. The curves are the isochrones of $(\log(\text{age}) = 7.80, 7.90 \text{ and } 8.00)$. These isochrones are taken from Girardi et al. (2000).

(D. Bisht, A. Rai, S. Ganesh and K. S. Baliyan)

Comprehensive study of open clusters Berkeley 24 and Czernik 27

We present the astrophysical parameters of two less studied open star clusters Berkeley 24 and Czernik 27 using UBV_I CCD and 2MASS JHK_s photometric data. These clusters are located in the third Galactic quadrant. Radial density profile, colour-magnitude diagram and colour-colour diagram are used for the estimation of fundamental parameters. Stellar surface density profile indicates that the cluster extent are 2.5 and 2.2 arcmin for clusters Be 24 and Cz 27 respectively. Their reddening $E(B - V)$ are 0.45 ± 0.05

mag and 0.15 ± 0.05 mag and their distances, from main sequence fitting are 4.4 ± 0.5 kpc and 5.6 ± 0.2 kpc. We have estimated $E(J - K) = 0.23 \pm 0.03$ mag and $E(V - K) = 1.23 \pm 0.02$ for Be 24, while $E(J - K) = 0.06 \pm 0.02$ mag and $E(V - K) = 0.33 \pm 0.01$ mag for Cz 27. Colour-excess ratio indicates normal interstellar extinction law towards the cluster region for both the clusters. From the ultraviolet excess measurement, we derived the metallicity to be $[\text{Fe}/\text{H}] = -0.025 \pm 0.01$ dex and -0.042 ± 0.01 dex for clusters Be 24 and Cz 27 respectively. Comparison with $Z = 0.008$ isochrones leads to an age of 2.0 ± 0.2 Gyr and 0.6 ± 0.1 Gyr for Be 24 and Cz 27, respectively, as shown in Figure 6 and Figure 7.

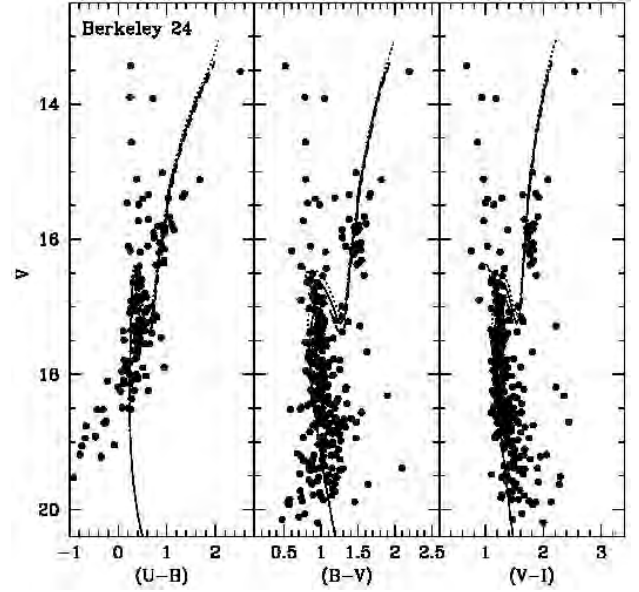


Figure 6: The colour-magnitude diagram of the clusters under study. The curves are the isochrones of $(\log(\text{age}) = 9.25, 9.30 \text{ and } 9.35)$ for the cluster Berkeley 24. These isochrones are taken from Girardi et al. (2000).

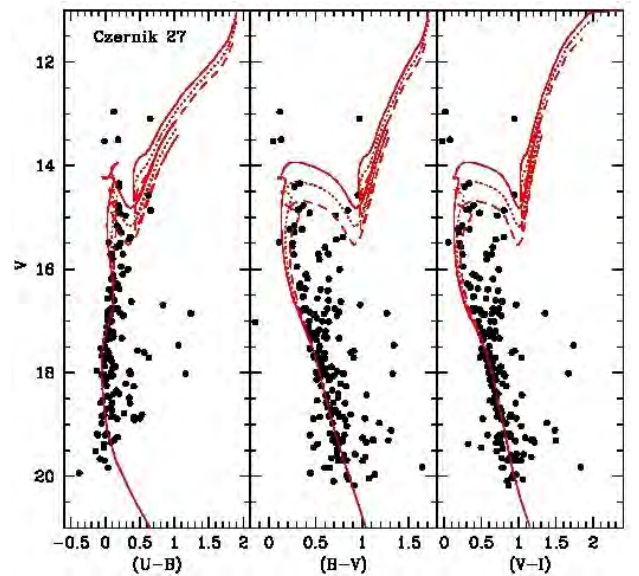


Figure 7: Same as Fig 6 for open cluster Czernik 27

We have redetermined the age and distance using $V/(V-K)$, $J/(J-H)$ and $K/(J-K)$ colour magnitude diagrams and got values consistent with what we have obtained using optical CMDs. On combining UBV optical data with 2MASS JHKs data, we found reddening law in the direction of clusters to be normal. Mass function slopes of $x = 1.64 \pm 0.30$ and 1.62 ± 0.31 are derived for the clusters, which is in good agreement with the Salpeter IMF ($x=1.35$) within errors. Mass function slopes in the core, halo and overall region leads to the effect of mass-segregation. Our study indicates that both clusters are dynamically relaxed. This may be due to the dynamical evolution or star formation process itself.

This work has been done in collaboration with R. K. S. Yadav (ARIES, Nainital, India) and Alok Durgapal (Kumaun University, Nainital, India.)

(D. Bisht and S. Ganesh)

Detection of a 10 Jupiter Mass exoplanet in a circumbinary system

We, at PRL, have discovered a very rare Eclipsing Binary (EB) system which is a three-body system and the third body is a planet. The EB pair is a F+M system which is orbited by a $\sim 10 M_J$ mass planet. HD 23765 was shortlisted as an EB candidate having a low mass companion from the *STEREO* catalogue. It has a visual magnitude of 9.5 and a spectral type of F6. In addition to *STEREO*, this source was also observed by SuperWasp (SW) and K2 (Kepler2).

HD 23765 was first followed up with PARAS in the months between October to November 2013. A set of 14 RV observations of this source were obtained. The spectra were taken in the simultaneous Thorium-Argon reference mode of PARAS at a resolving power of 67,000. The exposure times for each RV observation were kept at 1200 s resulting in SNR between 14 to 20 per pixel at peak of blaze wavelength of each order. A similar set of RV measurements were repeated between November 2016 to February 2017.

For systems, which have no additional component, can be simultaneously fitted for their spectroscopy and photometry measurements with a single orbital solution independent of time. However, if there are additional forces on the system due to the presence of third body the solution for the system becomes a function of time. The two RV datasets observed in 2013 and 2016-17 showed a periastron advance as the system was perturbed by a distant third body. Similarly, this signature in transit was inferred by the advance of the central transit time. The different datasets for photometry, two observed from SuperWasp, many observed from Kepler (K2) and one from Las Campanas, Chile confirmed the variations in the transit times. The TTvs as seen over time indicate a periodicity of 24 y.

This system is a short period EB having a period of 1.6866 d (F+M system). Despite its short orbital period, the system has a considerable eccentricity of ~ 0.3 . Simulations were performed on the EB system to understand the dynamics and mass of the third body (Ford et. al. 2000, Omer et. al. 2002, Mardling et. al. 2007). The mass of the primary component is $1.3 M_\odot$ and that for the secondary is $0.35 M_\odot$ as derived from the photometry and spectroscopy measurements of the system.

The third body, in this model, starts off in an orbit that is 88 degrees tilted from the plane of the inner system. It oscillates back and forth by about 30 degrees, hitting minimum inclination when inner binary is at maximum eccentricity. Tidal damping is not included in this model. Tidal heating of the secondary might be significant. The mass of the third body derived from here is $10 M_J$ at an orbital separation of 1.0 AU and e of 0.7.

The mass of the secondary M dwarf derived from the combined RV and photometry measurements is $0.305^{+0.014}_{-0.013} M_\odot$ and the radius is $0.39 \pm 0.025 R_\odot$. The formal errors on the measurements for secondary mass and radius are $\sim 7-8\%$. As derived from photometry, the system has an inclination angle of $87.2^\circ_{-2.9}^{+2.0}$, transit depth of 0.039 ± 0.001 mag and transit duration of 266 ± 6 min. We estimate the age of EB HD 23765 to be between 0.7 to 1 Gyr based on its rotational velocity of 32 km s^{-1} .

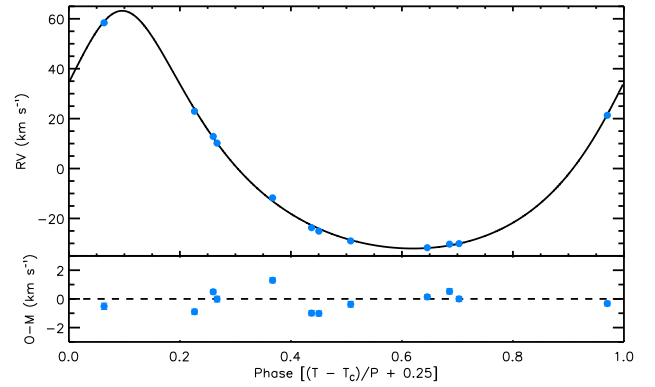


Figure 8: (Top panel) RV model curve for star HD 23765 obtained from EXOFAST for 2016-17 RV dataset is plotted against orbital phase. PARAS, Mount Abu (solid blue circles) observed data points for the year 2016 along with the estimated errors are overplotted on the curve. (Bottom panel) The residuals from best-fitting are plotted below the RV plot. For better visual representation, the x axis (Phase) is shifted by 0.25 so that the central primary transit crossing point (T_c) occurs at phase 0.25 instead of 0.

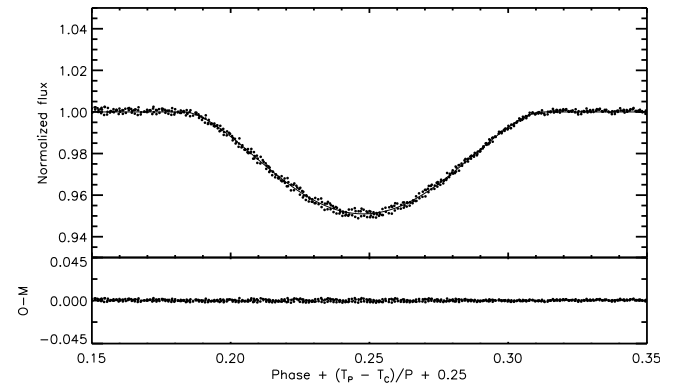


Figure 9: (Top panel) Transit curve for HD 23765 obtained from K2 data in the year 2015 is plotted based on the parameters from EXOFAST. (Bottom panel) Observed-Fit residuals are plotted. For better visual representation, the x axis (Phase) is shifted by 0.25 so that the central primary transit crossing point (T_c) occurs at phase 0.25 instead of 0.

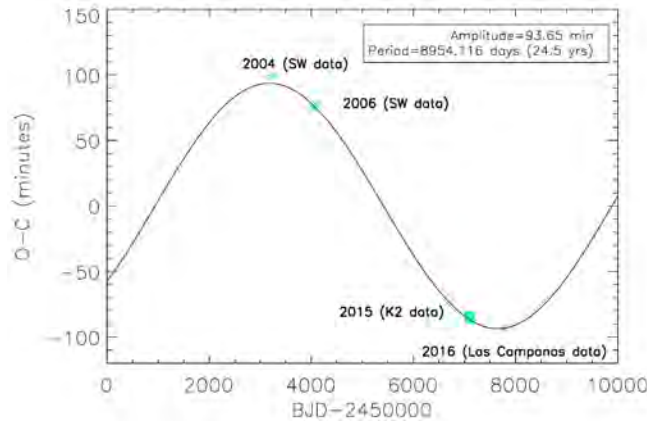


Figure 10: Transit time variation (of the central transit time) observed for HD 23765 for a period between 2004-2016. The 2004 and 2006 data are taken from SuperWasp (SW), 2015 data are from K2(Kepler) and 2016 data are observed from Las Campanas, Chile. The O-C TTV plot across the elapsed days (BJD) are plotted, x axis is days in BJD and y axis is O-C in minutes. The best fit sinusoidal curve yields an amplitude of 93 minutes and a time duration of ~ 24 y.

(A. Chakraborty, P. Chaturvedi, R. Sharma, P. Neelam and B.G. Anandarao)

Multi-wavelength study of the star-formation in the S237 Hii region

The feedback processes of massive stars ($\gtrsim 8 M_{\odot}$) in their vicinity are still poorly understood. The role of filaments in the formation of dense massive star-forming clumps and clusters is still a matter of debate. A detailed multi-wavelength study of observations from X-ray, near-infrared to centimeter wavelengths was carried out to probe the star formation processes in the S237 region. Multi-wavelength images trace an almost sphere-like shell morphology of the region, which is filled with the 0.5–2 keV X-ray emission. The region contains two distinct environments - a bell-shaped cavity-like structure containing the peak of 1.4 GHz emission at center, and elongated filamentary features without any radio detection at edges of the sphere-like shell - where *Herschel* clumps are detected. Using the 1.4 GHz continuum and ^{12}CO line data, the S237 region is found to be excited by a radio spectral type of B0.5V star and is associated with an expanding Hii region. The photoionized gas appears to be responsible for the origin of the bell-shaped structure. The majority of molecular gas is distributed toward a massive *Herschel* clump ($M_{\text{clump}} \sim 260 M_{\odot}$), which contains the filamentary features and has a noticeable velocity gradient (Figure 11). The photometric analysis traces the clusters of young stellar objects (YSOs) mainly toward the bell-shaped structure and the filamentary features. Considering the lower dynamical age of the Hii region (i.e. 0.2-0.8 Myr), these clusters are unlikely to be formed by the expansion of the Hii region. An interesting outcome of this work is the existence of a cluster of YSOs and a massive clump at the intersection of filamentary features, indirectly illustrating that the collisions of these features may have triggered cluster formation, similar to those seen in the Serpens South star-forming region (see Figure 11).

This work was done in collaboration with D.K. Ojha (TIFR, India), I. Zinchenko (IAPRAS, Russia) and A. Luna (INAOE, México).

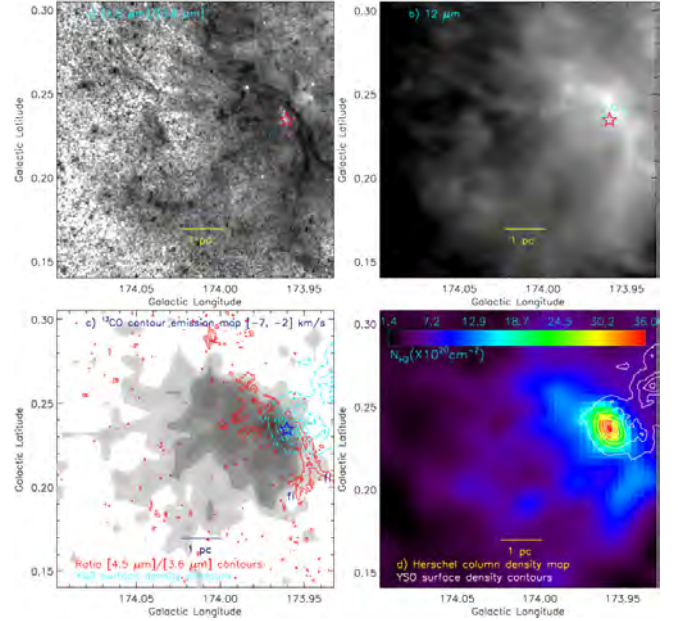


Figure 11: Zoomed-in view toward the filamentary features embedded in the molecular condensation linked with the S237 site. a) *Spitzer*-IRAC ratio map of $4.5 \mu\text{m}/3.6 \mu\text{m}$ emission traces the filamentary features. b) *WISE* image at $12 \mu\text{m}$ also depicts the filamentary features. c) The integrated $^{13}\text{CO}(J=1-0)$ emission map of the molecular condensation, cond1. The ^{13}CO contours are shown with levels of 10, 18, 25, 30, 40, 55, 70, 80, 90, and 99% of the peak value (i.e. $8.251 \text{ K km s}^{-1}$). The YSO surface density contours (dotted dashed; in cyan color) and filamentary features (in red) are also shown in the map. Two filamentary features are highlighted by labels "f1". d) *Herschel* column density map is overlaid with the YSO surface density contours, revealing a physical connection between a cluster of YSOs and a massive clump. In the last two panels, the contours are shown at 3, 5, 7, 10, 15, and 20 YSOs/pc², from the outer to the inner side. In the first three panels, the position of the *Herschel* column density peak is marked by a star symbol. Figures exhibit the presence of a cluster of YSOs and a massive clump at the intersection of filamentary features. A scale bar corresponding to 1 pc (at a distance of 2.3 kpc) is shown in all the panels.

(L. K. Dewangan and P. Janardhan)

The physical environment around IRAS 17599-2148: IRDC and bipolar nebula

The formation mechanisms of massive stars ($\gtrsim 8 M_{\odot}$) and young stellar clusters are still poorly understood. Furthermore, we do not have much knowledge of the physical processes of their interaction and feedback on the surrounding molecular environment. A multi-scale and multi-wavelength study was carried out to investigate the star formation process around IRAS 17599-2148 that is part of an elongated filamentary structure (EFS) (extension ~ 21 pc) seen in the *Herschel* maps (Figure 12). Using the *Herschel* data analysis, at least six massive clumps ($M_{\text{clump}} \sim 777 - 7024 M_{\odot}$) are found in the EFS with a range of temperature and column density of $\sim 16-39 \text{ K}$ and $\sim 0.6-11 \times 10^{22} \text{ cm}^{-2}$ ($A_V \sim 7-117$ mag), respectively. The EFS hosts cold gas regions (i.e. infrared dark cloud) without any radio detection and a bipolar nebula (BN) linked with the Hii region IRAS 17599-2148, tracing two distinct environments inferred through the temperature distribution and ionized emission. Based on virial analysis and higher values of self-gravitating pressure, the clumps are found unstable against gravitational collapse. We find 474 young stellar objects (YSOs) in the selected region and $\sim 72\%$ of these YSOs are

found in the clusters distributed mainly toward the clumps in the EFS. These YSOs might have spontaneously formed due to processes not related to the expanding H ii region. At the edges of BN, four additional clumps are also associated with YSOs clusters, which appear to be influenced by the expanding H ii region. The most massive clump in the EFS contains two compact radio sources traced in the GMRT 1.28 GHz map and a massive protostar candidate, IRS 1 prior to an ultracompact H ii phase. Using the Very Large Telescope (VLT)/NACO adaptive optics near-infrared images, IRS 1 is resolved with a jet-like feature within a 4200 AU scale.

This work was done in collaboration with D.K. Ojha (TIFR, India), I. Zinchenko (IAPRAS, Russia), S.K. Ghosh (NCRA, India) and A. Luna (INAOE, México).

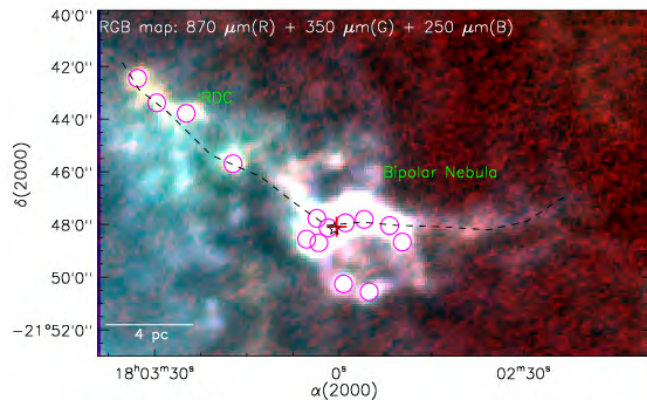


Figure no. 12: Three-color composite image (red, ATLASGAL 870 μm ; green, *Herschel* 350 μm ; blue, *Herschel* 250 μm ; in linear scale) of the region around IRAS 17599–2148, which clearly traces the cold dust emission. An elongated filamentary structure (EFS) is highlighted by a dashed curve. The ATLASGAL clumps at 870 μm are also marked by magenta circles. The positions of IRAS 17599–2148 and Class II 6.7 GHz methanol maser emission are marked by plus and star symbols, respectively. The scale bar at the bottom-left corner corresponds to 4 pc (at a distance of 4.2 kpc).

(L. K. Dewangan and P. Janardhan)

Star Formation Activity in the molecular cloud G35.20-0.74: onset of cloud-cloud collision

Obtaining observational proof of triggered star formation is a very challenging task. We present results of an analysis of the molecular cloud G35.20-0.74 (hereafter MCG35.2) using multi-frequency observations covering from optical- $\text{H}\alpha$, near-infrared, and radio wavelengths. The molecular gas emission in the direction of the MCG35.2 is traced in a velocity range of 30–40 km s^{-1} . An almost horseshoe-like structure embedded within the MCG35.2 is evident in the infrared and millimeter images and harbors the previously known sites, ultra-compact/hyper-compact G35.20–0.74N H ii region, Ap2-1, and Mercer 14 at its base (see Figure 13a). The site, Ap2-1 is found to be excited by a radio spectral type of B0.5V star where the distribution of 20 cm and $\text{H}\alpha$ emission is surrounded by the extended molecular hydrogen emission. Using the *Herschel* 160–500 μm and photometric 1–24 μm data analysis, several embedded clumps and clusters of young stellar objects (YSOs) are investigated within the MCG35.2, revealing the star formation activities. A majority of the YSOs clusters and massive clumps (500–4250 M_{\odot}) are seen toward

the horseshoe-like structure. The position-velocity analysis of ^{13}CO emission shows a blue-shifted peak (at 33 km s^{-1}) and a red-shifted peak (at 37 km s^{-1}) interconnected by a lower intensity intermediate velocity emission, tracing a broad bridge feature (see Figures 13b and 13c). The presence of such broad bridge feature suggests the onset of a collision between molecular components. The clusters of YSOs and massive stars are evident at the intersection of these molecular components (see Figure 13). A noticeable change in the H-band starlight mean polarization angles has also been observed in the MCG35.2, probably tracing the interaction between molecular components. Based on all our observational findings, we conclude that the star formation activities in the MCG35.2 are influenced by the cloud-cloud collision process.

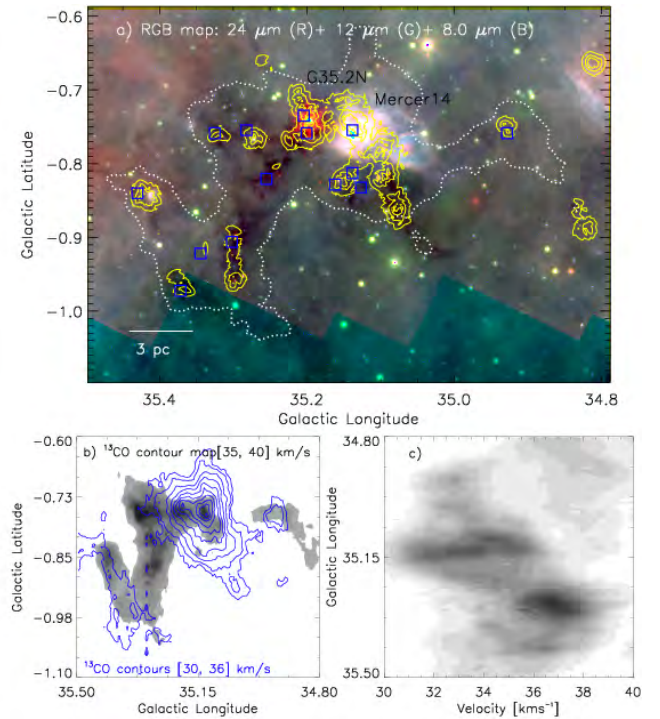


Figure 13: A multi-wavelength view of the star-forming complex, G35.20-0.74. a) A *Spitzer-WISE* color-composite image is overlaid with surface density contours (in yellow) of all the identified YSOs. The surface density contours are shown at 5, 10, and 20 YSOs/ pc^2 , increasing from the outer to the inner regions. The *Herschel* clumps are also marked by squares (in blue). A CO contour (dotted white) is also shown with a level of 12.356 K km s^{-1} . The scale bar at the bottom-left corner corresponds to 3 pc (at a distance of 2.0 kpc). b) The ^{13}CO emission contours from 30 to 36 km s^{-1} are overlaid on the ^{13}CO emission map. The background ^{13}CO emission map (from 35 to 40 km s^{-1}) is shown with levels of 25.133 $\text{K km s}^{-1} \times (0.35, 0.42, 0.5, 0.6, 0.7, 0.8, \text{ and } 0.9)$. The ^{13}CO contours (in blue) are shown with levels of 55.165 $\text{K km s}^{-1} \times (0.15, 0.2, 0.3, 0.4, 0.5, 0.6, 0.7, 0.8, 0.9, \text{ and } 0.98)$. c) Longitude-velocity distribution of ^{13}CO . The CO emission is integrated over the latitude from -0.6 degree to -1.1 degree. This position-velocity map traces two peaks (a red-shifted and a blue-shifted) which are separated by a lower intensity intermediate velocity emission (i.e., a broad bridge feature).

(L. K. Dewangan)

Probing the periodicity and physical parameters of the cool star in binary system DO Draconis

Cool Dwarf stars are most common stars in our universe. An estimation says that almost 90% of all stars in our galaxy are such

stars. Studying a cool dwarf star is easy if it is in a binary system and interacting with the other component. Cataclysmic Variable stars (CVs) are such a compact binary system comprising a cool dwarf star and a white dwarf interacting with each other. This is why CVs are known as a natural laboratory to study cool dwarf stars. We obtained time resolved near-infrared photometry of DO Draconis (DO Dra), one such Cataclysmic Variable, using 1.2 meter Mount Abu telescope with Near Infrared Camera/Spectrograph (NICS) as a back end instrument. Near-infrared J and H band Light curves of DO Dra have shown variability at various time scales from few minutes to few days. Lomb-Scargle periodogram of combined light curve clearly indicates the presence of a coherent modulation at 1.96 hr period. We interpret this period as a first harmonic of the orbital period occurring due to the non-spherical shape of the cool star. Phase curve folded at orbital period shows quasi-sinusoidal profile. We used Wilson-Devinney binary simulation code to model phase curve which inferred the inclination of the system and temperature of the cool star to be $43^\circ \pm 5^\circ$ and 3400 ± 100 K, respectively. This corresponds to the spectral type of the cool star as $M3V \pm 1$. The phase curve was found shifted in phase zero compared to the previously known ephemeris. This may be due to a small change in orbital period of the system which is probably due to the mass transfer from the cool star to the white dwarf. We have also detected Transient Periodic Oscillation (TPO) in one night observations. A possible origin of this TPO may be a reflection from a rotating blob (local in-homogeneity in density) in the accretion disc which moves with Keplerian velocity within the disc.

(V. Joshi)

NIR spectroscopy of M-dwarfs: Their fundamental parameters and atmospheric properties

Very Low-Mass stars in particular M dwarfs are an important source of information for probing the low mass end of the main sequence, down to the hydrogen burning limit.

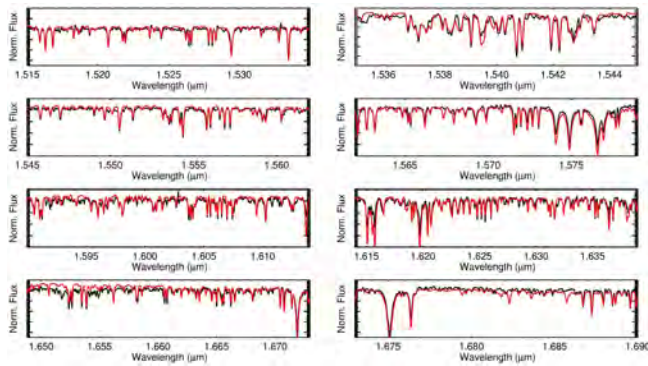


Figure 14: APOGEE spectra of 2M11091225-0436249 (black) of spectral type M1.0 is compared with the best-fit BT-Settl (red). The best fit parameter is $3900 / 4.0 / -0.3$.

The presence first of molecules and then of condensed particulates greatly complicates the understanding of their physical properties, and thus makes the determination of their fundamental stellar parameters challenging. Accurate knowledge of their atmospheric parameters and especially their composition is essential for understanding the chemical history of our Galaxy. The purpose of this work is to

perform a detailed study of the high-resolution H-band spectra of M dwarfs. The determination of atmospheric parameters of late-type stars is difficult because the spectra of these cool stars contain many overlapping absorption lines, preventing the determination of atmospheric parameters. This study also allows us to perform a more detailed analysis of the atmospheric composition in order to determine the stellar parameters and to constrain the atmospheric models. Further, this study will help us to understand physical and chemical processes such as increasing condensation of gas into dust, to point out the missing continuum opacities, and to see how the main band features are reproduced by the models. The high spectral resolution in H-band provide a unique opportunity to constrain the processes that occur in a cool atmosphere. The high-resolution APOGEE spectra, covering the entire H-band, provides the opportunity to measure physical stellar atmospheric parameters of M dwarfs. We performed a spectral synthesis analysis using a full grid of synthetic spectra computed from BT-Settl models and obtained stellar parameters such as effective temperature, surface gravity, and metallicity. We determine the fundamental parameters such as effective temperature, surface gravity, and metallicity for 45 M dwarfs using high-resolution H-band spectra. The derived effective temperature for the sample range from 3100-3900 K. The resulting metallicities lie between $-0.5 \leq [M/H] \leq +0.5$ whereas the surface gravity is between $4.5 \leq \log g \leq 5.5$. We explore systematic differences between effective temperature and metallicity calibrations with other studies using the same M dwarfs catalogs. We have also validated that stellar parameters determined using BT-Settl model are more accurate and reliable as compared to other comparative studies using other models.

This work has been done in collaboration with Prof. F. Allard (ENS, Lyon France), G. D. C. Teixeira (Instituto de Astrofísica e Ciências do Espaço, Porto, Portugal), D. Homeier (University of Heidelberg, Germany), Prof. O. Mousis (Laboratoire d'Astrophysique de Marseille, France).

(A. S. Rajpurohit)

An Infrared Photometric and Spectroscopic Study of Post-AGB Stars

A selection of post-Asymptotic Giant Branch (PAGB) stars have been studied using their mid-infrared (IR) spectra and by modeling their spectral energy distribution (SED). Based on the mid-infrared spectral features the sample stars can be classified into five distinct types namely those having strong/weak polycyclic aromatic hydrocarbons (PAHs), silicate emission, in some cases along with PAH feature, silicate absorption, prominent broad bump around $11 \mu\text{m}$ and nearly featureless dust continuum. The physical and circumstellar parameters for these sample stars were derived from the SED modeling. Our results from SED modeling showed interesting trends of dependency between the photospheric and circumstellar parameters. Correlations were noticed between the ratios of equivalent widths (EWs) of various vibrational modes of PAHs and the photospheric temperature T_* and model derived circumstellar parameters for the sample stars. The PAGB mass loss rates derived from the SED models are found to be higher than those for the AGB stars.

In a few objects, low and high excitation fine structure emission lines were identified, indicating their advanced stage of evolution. Further,

IR vibration modes of fullerene (C_{60}) were detected for the first time in the PAGB star IRAS 21546+4721.

This work has been done in collaboration with Prof. Rajesh Pandey of MLSU, Udaipur.

(V.Venkataraman, B.G.Anandarao and P.Janardhan)

Modeling of the Unidentified infrared features at 21 & 30 μm and crystalline silicates in a sample of PAGB candidates

The unidentified infrared (UIR) features at 21 & 30 μm and the crystalline silicates have been identified and modeled in a sample of post-Asymptotic Giant Branch (PAGB) sources. The mid-infrared spectra of a few oxygen-rich sources displayed the presence of crystalline olivines whereas the 21 and 30 μm feature was observed in a few sources with carbon rich circumstellar environments. These observed spectral features were modeled using DUSTY software. Our study revealed two sources displaying different spectral morphologies at 21 μm compared to the others exhibiting similar feature. Among these the source IRAS 18533+0523 is reported for the first time displaying these features. We propose a core-mantle type configuration to explain the observed spectral morphologies with SiC and SiO_2 as the core and mantle materials. Modeling of 30 μm feature using a SiC core and MgS mantle showed an shift in the broad feature towards the shorter wavelength with the increase of dust grain temperature. Modeling of these spectral features show a shift in the peak wavelength towards the red that may be attributed to size and temperature of the dust grains and the amount of Fe content.

(V.Venkataraman and B.G.Anandarao)

High resolution imaging of molecular line emission in PAGB stars

An investigation of the physical mechanism responsible for the shaping of asymptotic giant branch (AGB) stars and their circumstellar envelopes (CSEs) is crucial for understanding the various aspherical morphologies observed during the planetary nebulae (PNe) phase of evolution. As PAGB stars evolve into their early planetary nebulae (PNe) phase of evolution, part of the shell formed during the mass-loss processes during the AGB phase begins to get ionized by the central star. These ionization fronts act as a shaping agent and could heavily influence the observed morphology. The interaction of fast wind during the PAGB phase with the molecular AGB envelopes can be detected by observing molecular hydrogen at 2.121 and 2.248 μm in the near-IR (NIR) wavelengths. Narrow band imaging of a sample of PAGB sources at these wavelengths were carried out using an near-infrared imaging Fabry-Perot spectrometer (NIFS) coupled to the Near-infrared camera and Spectrograph (NICS). NIFS was used as a tunable narrow band filter in the K band and it offers an accurate method for subtracting the continuum.

(V.Venkataraman and B.G.Anandarao)

Detection of Cyclotron Resonance Scattering Feature in High Mass X-ray Binary Pulsar SMC X-2

Accretion powered X-ray pulsars are known to be highly magnetized rotating neutron stars. These sources are powered by the accretion of matter from the binary companion either through Roche lobe overflow or capture of stellar wind. The broadband spectrum of the pulsars show several important features such as fluorescence emission lines, soft X-ray excess, broad absorption like features known as cyclotron resonance scattering features (CRSFs) etc. CRSFs are generally detected in the hard X-ray spectrum of pulsars with magnetic field in the order of 10^{12} G. These line-like features are formed due to the resonant scattering of photons with electrons in quantized Landau levels. The energy difference between these levels depends on the strength of magnetic field and expressed through the relation $E_{\text{cyc}} = 11.6 B_{12} \times (1+z)^{-1}$ keV (without relativistic correction), where B_{12} is the magnetic field in the unit of 10^{12} G and z is the gravitational redshift. Detection of CRSFs in the pulsar spectrum, therefore, is a powerful tool for the direct estimation of neutron star magnetic field.

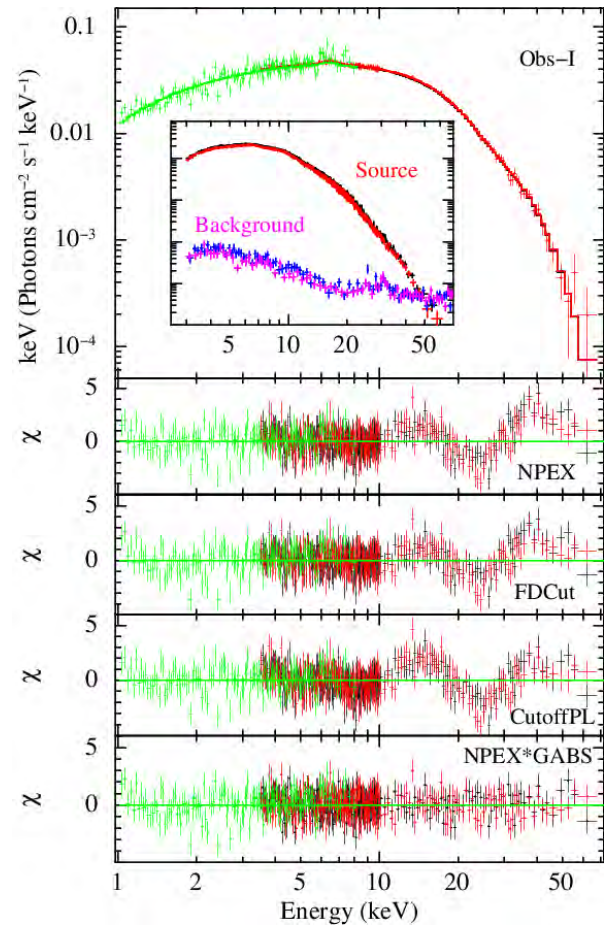


Figure 15: The energy spectrum of SMC X-2 in 1-70 keV range obtained from *NuSTAR* and *Swift*/XRT data during the first observation along with the best-fitted models. A cyclotron line at ~ 27 keV is clearly detected in the residuals when fitted with all three models separately. A Gaussian absorption feature (GABS) was used to model the cyclotron line.

We have studied one of the poorly known high mass X-ray binary pulsars SMC X-2 by using three simultaneous *NuSTAR* and *Swift*/XRT observations during its 2015 outburst. The pulsar was

significantly bright ($\sim 5.5 \times 10^{38}$ ergs s $^{-1}$) during these observations, accreting above the Eddington luminosity of a canonical neutron star. Spin period of the pulsar was estimated to be 2.37 s. Pulse profiles were found to be strongly luminosity dependent. The 1-70 keV energy spectrum of the pulsar was well described with three different phenomenological continuum models such as (i) negative and positive power-law with exponential cutoff, (ii) Fermi-Dirac cutoff power-law and (iii) cutoff power-law models. Apart from the presence of an iron line at ~ 6.4 keV, a model independent absorption like feature at ~ 27 keV was detected in the pulsar spectrum (see Figure 15). This feature was identified as a cyclotron absorption line and detected for the first time in this pulsar. Based on the '12-B-12' rule the corresponding magnetic field of the neutron star was estimated to be $\sim 2.3 \times 10^{12}$ G. The cyclotron line energy showed a marginal negative dependence on the luminosity. The cyclotron line parameters were found to be variable with pulse phase and interpreted as due to the effect of emission geometry or complex structure of the pulsar magnetic field.

(G. K. Jaisawal and S. Naik)

Detection of a pair of prominent X-ray cavities in Abell 3847

We present results obtained from a detailed analysis of a deep *Chandra* observation of the bright FR II radio galaxy 3C 444 in Abell 3847 cluster. A pair of huge X-ray cavities are detected along North and South directions from the centre of 3C 444. X-ray and radio images of the cluster reveal peculiar positioning of the cavities and radio bubbles (see Figure 16).

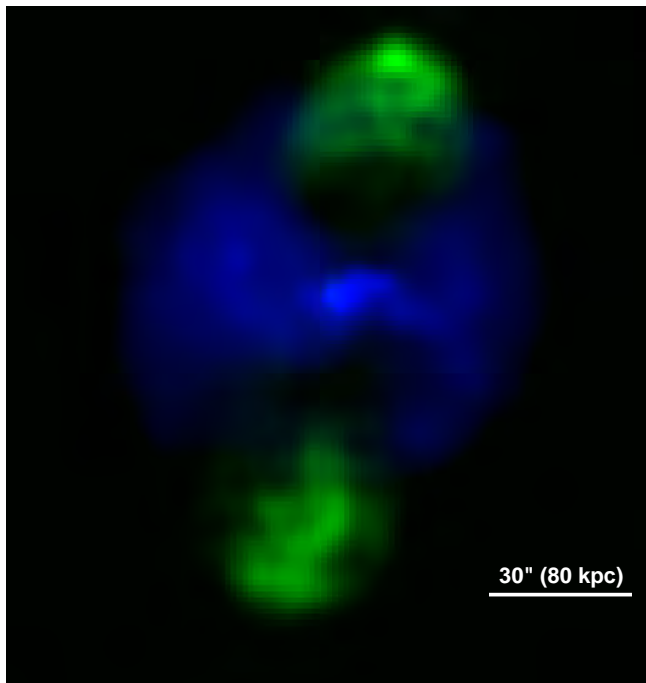


Figure 16: A composite false colour *Chandra* X-ray and VLA radio emission from Abell 3847. Blue and green colours represent the distribution of hot diffuse gas (0.3-3 keV range) and 4.89 GHz radio emission map, respectively.

The radio lobes and X-ray cavities are apparently not spatially coincident and exhibit offsets by ~ 61 kpc and 77 kpc from each other along the North and South directions, respectively. Radial temperature and density profiles reveal the presence of a cool core in the cluster. Imaging and spectral studies showed the removal of substantial amount of matter from the core of the cluster by the radio jets. A detailed analysis of the temperature and density profiles showed the presence of a rarely detected elliptical shock in the cluster. Detection of inflating cavities at an average distance of ~ 55 kpc from the centre implies that the central engine feeds a remarkable amount of radio power ($\sim 6.3 \times 10^{44}$ erg/s) into the intra-cluster medium over $\sim 10^8$ yr, the estimated age of cavity. The cooling luminosity of the cluster was estimated to be $\sim 8.30 \times 10^{43}$ erg/s, which confirms that the AGN power is sufficient to quench the cooling. Ratios of mass accretion rate to Eddington and Bondi rates were estimated to be ~ 0.08 and 3.5×10^{-4} , respectively. This indicates that the black hole in the core of the cluster accretes matter through chaotic cold accretion.

This work was done in collaboration with M. K. Patil of SRTM University, Nanded, Maharashtra, India.

(N. Vagshette and S. Naik)

A *Suzaku* View of Accretion Powered X-ray Pulsar GX 1+4

Accretion powered X-ray pulsars are the constituents of binary systems that contain a magnetized neutron star and an evolving companion star. The surface magnetic field of these neutron stars is typically in an order of 10^{12} G. The accreted matter from the companion star flows along the magnetic field lines and falls on the poles of the neutron stars forming column like structures known as accretion columns. Photons emitted from the magnetic poles of the neutron star get reprocessed at various places around the neutron star before being collected at the detectors.

Therefore, a detailed and thorough analysis of the observations of these source provide important information regarding the characteristic properties of the neutron star, its companion and the surrounding regions. We carried out a detailed study of a low mass X-ray binary pulsar GX 1+4 by using a long observation of the pulsar with the Japanese X-ray observatory *Suzaku*. GX 1+4, with a spin period of more than 2 minutes, has had a very interesting pulse-period history since its discovery. Spin-downs observed in GX 1+4, in spite of a large accretion rate corresponding to a persistent X-ray luminosity of a few times 10^{37} erg s $^{-1}$, suggest a very high magnetic field strength of the neutron star, 10^{13} - 10^{14} G, which is yet to be confirmed from spectroscopic measurements. A low-mass companion star and the possibility of a very wide orbit with orbital period of about 300 days or more also make GX 1+4 somewhat unique among the X-ray binaries.

We used a *Suzaku* observation of the accretion-powered X-ray pulsar GX 1+4 to investigate the spectral and timing properties of the pulsar. A broadband continuum spectrum of the pulsar was found to be better described by a simple model consisting of a blackbody component and an exponential cutoff power law than the previously used compTT continuum model. Though the pulse profile had a sharp dip in soft X-rays (< 10 keV), phase-resolved spectroscopy confirmed that the dimming was not due to an increase in photoelectric absorption. Phase-sliced spectral analysis showed the presence of a significant spectral modulation beyond 10 keV except for the dip phase. A search

for the presence of a cyclotron resonance scattering feature in the Suzaku spectra yielded a negative result. Iron K-shell (K_α and K_β) emission lines from nearly neutral iron ions ($<Fe\ III$) were clearly detected in the source spectrum.

A significant K_α emission line from almost neutral Ni atoms was detected for the first time in this source. We estimated an iron abundance of $\sim 80\%$ of the solar value and an Ni/Fe abundance ratio of about two times the solar value. We searched for an iron Ly_α emission line and found a significant improvement in the spectral fitting by inclusion of this line. We found a clear intensity modulation of the iron K_α line with the pulse phase with an amplitude of 7%. This finding favored an inhomogeneous fluorescent region with a radius much smaller than the size ($\sim 3 \times 10^{12}$ cm) estimated by an assumption of homogeneous matter.

This work was done in collaboration with Yuki Yoshida, Shunji Kitamoto, Hiroo Suzuki and Akio Hoshino of Rikkyo University, Tokyo, Japan.

(S. Naik and G. K. Jaisawal)

AGN-driven perturbations in the intracluster medium of the cool-core cluster ZwCl 2701

AGN feedback plays an important role in the evolution of non-thermal radio jets and lobes ejected from the central supermassive black holes. The brightest cluster galaxy at the core of the cool core clusters is found to be radio loud galaxy where jets from the AGN in the galaxy extend outwards in a bipolar flow and inflate the lobes. These lobes push the X-ray emitting hot gas in the Intra-cluster Medium (ICM) and create X-ray deficiency regions called as “cavities”. The availability of high angular resolution X-ray imaging detectors onboard *Chandra* observatory made it possible to detect such cavities in several of the clusters. It is believed that these cavities are filled with non-thermal radio lobes consisting of relativistic particles and magnetic field. This has been supported by the observations of radio lobes that spatially match with the X-ray cavities in many clusters. There are several possible sources of ICM heating viz. AGN feedback, merger, conduction, supernovae, cosmic ray heating etc. It is understood that several clusters are being formed because of merging of smaller mass concentrations through gravitational infall of matter. During merger process large amount of energy is carried by the gas which is being dissipated in the form of shocks and turbulence. The energy dissipated through shock and turbulence enhances the temperature of the ICM. Supernova explosions also act as a heating source and can cause delay in the formation of cooling flow. Another mechanism of ICM heating is known to be due to the cosmic rays. Relativistic electrons form a minihalo in the core of the cluster and produce hard X-ray photons due to inverse Compton scattering. These relativistic electrons and hard X-ray photons heat the gas in the ICM. We selected one galaxy cluster, ZwCl 2701 which is located at a redshift of 0.214 to carry out a detailed and systematic study with an emphasis on the comparison of the X-ray and radio properties by using deep *Chandra* X-ray data and 1.4 GHz *GMRT* observations.

We used a total of 123 ks X-ray (*Chandra*) and 8 hrs of 1.4 GHz radio (*GMRT*) observations of ZwCl 2701 for our study. These observations of ZwCl 2701 showed the presence

of an extensive pair of ellipsoidal cavities along the East and West directions within the central region <20 kpc (Figure 17).

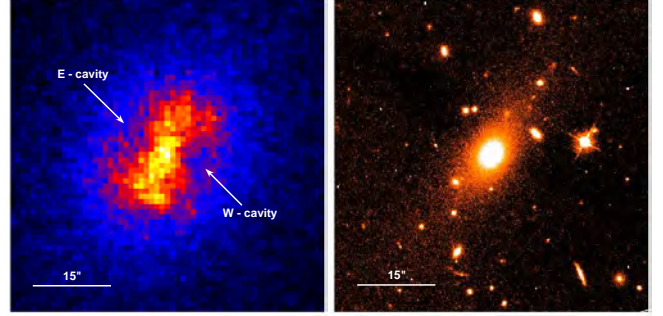


Figure 17: Background subtracted exposure corrected $1' \times 1'$ *Chandra* image of ZwCl 2701 and wide band 606 nm *HST* $1' \times 1'$ image are shown in the left and right panels, respectively. The arrows in the *Chandra* image indicate the presence of X-ray deficiency regions in the cluster.

Detection of bright rims around the cavities suggested that the radio lobes displaced X-ray emitting hot gas forming shell-like structures. The total cavity power that directly heated the surrounding gas and cooling luminosity of the cluster were estimated to be $\sim 2.27 \times 10^{45}$ erg/s and 3.5×10^{44} erg/s, respectively. Comparable values of cavity power and cooling luminosity of ZwCL 2701 suggested that the mechanical power of the AGN outburst is large enough to balance the radiative cooling in the system. The star formation rate derived from the H_α luminosity was found to be $\sim 0.60 M_\odot \text{ yr}^{-1}$ which is about three orders of magnitude lower than the cooling rate of $\sim 196 M_\odot \text{ yr}^{-1}$. Lower value of the ratio ($\sim 10^{-2}$) between black hole mass accretion rate and Eddington mass accretion rate suggested that launching of jet from the super massive black hole is efficient in ZwCl 2701.

This work was done in collaboration with S. S. Sonkamble and M. K. Patil of SRTM University, Nanded, Maharashtra, India.

(N. Vagshette and S. Naik)

Detection of hard X-ray polarization of Crab nebula and pulsar

Our group had conceived the new capability of AstroSat-CZTI to measure hard X-ray polarization for bright X-ray sources. Earlier, we had experimentally established this capability with both polarized and unpolarized X-rays on ground, as well as verified it with observations of Crab nebula. Now with more than one year of Crab observations with CZTI, we have made the most sensitive measurements of hard X-ray polarization of the Crab nebula and pulsar in the 100 – 300 keV energy range. Using 550 ks of observations of Crab the measured polarization fraction and angle are $33.4 \pm 5.8\%$ and $143.0^\circ \pm 2.8^\circ$ NE.

Pulsars are rapidly spinning strongly magnetized neutron stars that produces beamed emission across the entire electromagnetic spectrum due to acceleration of charged particles to very high energies. Crab pulsar and its nebula is the brightest source in hard X-rays and hence it has been studied in great detail by all high energy astronomy missions using spectroscopy and timing. However, the details of the acceleration process, the emission

mechanism and geometry of emission location remains poorly understood despite five decades of investigations. Measurement of X-ray polarization as a function of the pulse phase is considered as essential for understanding these aspects. With the proven capability of CZTI and availability of sufficient exposure, we have, for the first time, accurately measured the X-ray polarization during the off-pulse phase of the Crab pulse profile. We find that this off-pulse component shows a higher degree of polarization of $50.4 \pm 12.0\%$ compared to the phase integrated polarization with polarization angle of $139.5^\circ \pm 3.2^\circ$. (Figure 18) shows the modulation curves for phase integrated crab and off-pulse emission and the confidence contours for polarization fraction and angle.

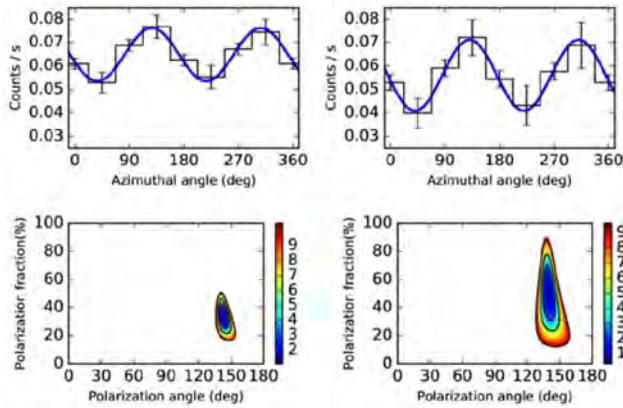


Figure 18: Hard X-ray polarization of the Crab nebula and pulsar: Top panel shows the modulation curves for total crab emission and emission only during the off-pulse phase. Bottom panel show the confidence contours for the polarization fraction and polarization angle for these measurements. These are the most sensitive hard X-ray polarization measurements for the Crab available so far.

The polarization properties of the pulsed component during rest of the pulse phase are currently under investigation and the initial results show highly interesting results.

(Mithun N. P. S. and S. V. Vadawale)

GRB monitoring with CZTI and AstroSat mass model

Gamma ray bursts (GRB) are one of the most energetic events in the universe. GRBs are observed at random time and location all over the sky with a typical rate of approximately one GRB per day. CZTI, due to the transparency of collimators beyond 100 keV and high efficiency of 5mm thick CZT detectors, acts as an excellent detector for hard X-ray transients like Gamma Ray Bursts (GRB). In 1.5 years of operation of CZTI, it has detected over 100 GRBs (in CZT or veto detectors) all except one outside its primary field of view. Joint spectral fits of GRB spectrum observed by CZTI with that of other instruments like Fermi-GBM and Swift-BAT will provide new insights to prompt emission mechanism in Gamma Ray Bursts. To provide accurate spectral response for such studies it is important to consider the interaction of source photons with CZTI instrument and rest of the satellite structure. For this purpose, We have developed AstroSat mass model using Geant4, a monte-carlo based toolkit for simulation of interaction of photons and particles. The mass model includes all instruments of AstroSat and other satellite structures with necessary approximations. Figure 19 shows the AstroSat

geometry as incorporated in Geant4 mass model. Simulations using this mass model is used for generation of off-axis response matrix for CZTI as well as to obtain modulation factor for 100% polarized beam as required for polarization measurement of GRBs.

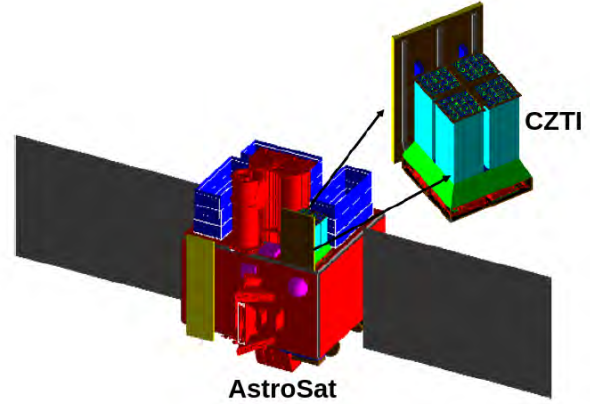


Figure 19: The mass model of the AstroSat depicting the overall material characteristics of the spacecraft and various sub-systems including the scientific instruments. Such mass model is essential to achieve accurate results from the Monte-Carlo simulations.

(Aarth E., Mithun N. P. S., and S. V. Vadawale)

Hard X-ray polarization measurement of Gamma Ray Bursts

Since their discovery four decades ago, GRBs have been extensively studied with spectral analysis of prompt emission and the afterglow. However, the emission mechanism during the prompt emission of GRB is still not completely understood. There are several competing models that can explain all the observed spectral properties of the GRBs. The polarization measurement of the GRB prompt emission is expected to break this degeneracy and provide new insights into the emission mechanism of the GRBs. However, the polarization measurements at these energies are extremely difficult. So far far polarization measurements are reported only for 10 GRBs and out of them many are controversial. Hence any new polarization measurements for GRBs are vital to increase the overall sample with firm polarization measurements so as to improve our understanding of these enigmatic phenomena. With the now well established new capabilities of CZTI, namely hard X-ray polarization measurement and hard X-ray transient monitoring, it is possible to measure polarization for bright GRBs.

During the first year of AstroSat operations, CZTI detected 47 GRBs and amongst this 11 GRBs were bright enough for measurement of polarization. In CZTI, azimuthal distribution of Compton scattered double pixel events are used for polarization measurement. Figure 20 shows the light curve for double events for GRB160821A and figure 21 shows the azimuthal distribution showing clear sinusoidal variation and thus indicating the polarized emission, for the same GRB. Modulation amplitude of azimuthal distribution along with the modulation factor for 100 % polarized beam in the same direction obtained from the mass model simulations provide measurement of the polarization fraction and the angle of polarization. We have measured polarization of 11 GRBs, thus doubling the sample of polarization measurements available. Given this rate of polarization

measurement throughout its mission life time, CZTI will provide good sample of GRB polarization measurements which would help in drawing conclusions on the prompt emission mechanism.

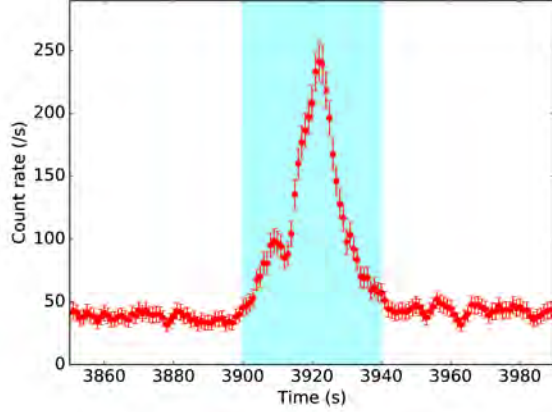


Figure 20: Compton double event light curve for GRB160821A showing the clear detection of the GRB in the events selected for the polarization analysis.

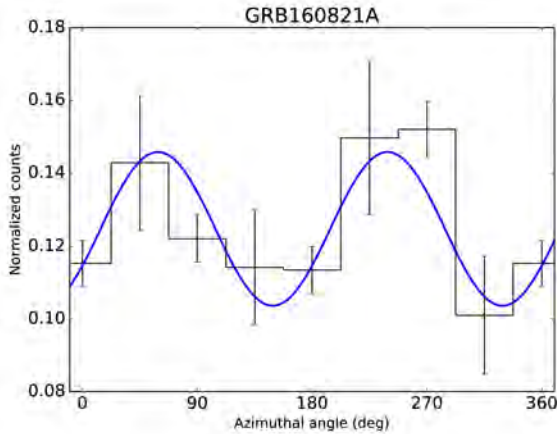


Figure 21: Modulation curve for GRB160821A. The presence of clear sinusoidal modulation indicate the presence of the polarized emission.

(Aarthi E., Mithun N. P. S., and S. V. Vadawale)

Post-maximum Near-infrared Spectra of supernova SN 2014J: A Search for Interaction Signatures

We present near-infrared (NIR) spectroscopic and photometric observations of the nearby Type Ia SN 2014J. A large fraction of this data was obtained from Mt. Abu. The 17 NIR spectra span epochs from +15.3 to +92.5 days after B-band maximum light, while the JHK photometry include epochs from -10 to +71 days. These data are used to constrain the progenitor system of SN 2014J utilizing the hydrogen Paschen beta line, following recent suggestions that this phase period and the NIR in particular are excellent for constraining the amount of swept-up hydrogen-rich material associated with a non-degenerate companion star. We find no evidence for Paschen beta emission lines

in our post-maximum spectra, with a rough hydrogen mass limit of less than or equal to $0.1 M_{\odot}$ which is consistent with previous limits in SN 2014J from late-time optical spectra of the H line. Nonetheless, the growing data set of high-quality NIR spectra holds the promise of very useful hydrogen constraints.

This work has been done in collaboration with Dr David Sand of the Texas Technical University, USA and other collaborators.

(D. P. K. Banerjee, V. Joshi and V. Venkataraman)

On the nature of infrared-faint radio sources in deep extragalactic fields

Infrared-Faint Radio Sources (IFRSs) are an unusual class of objects that are relatively bright at radio wavelengths but have faint or undetected infrared counterparts even in deep surveys. We identify and investigate the nature of IFRSs using deep radio (flux density limit at $5\sigma \simeq 100 \mu\text{Jy}$), optical (r-band magnitude limit $\sim 26 - 27.7$), and near-IR ($3.6 \mu\text{m}$ flux limit at $5\sigma \sim 1.3 - 2.0 \mu\text{Jy}$) data available in the Subaru X-ray Deep Field (SXDF) and the Very Large Array VIMOS VLT Deep Survey (VLA-VVDS) field. In 1.8 square degree area of the two fields we find a total of nine confirmed and ten candidate IFRSs, where IFRSs are defined as sources with high flux ratio of radio-to-IR ($S_{1.4 \text{ GHz}}/S_{3.6 \mu\text{m}} > 500$) and low $3.6 \mu\text{m}$ flux ($S_{3.6 \mu\text{m}} < 30 \mu\text{Jy}$). Our IFRSs are found to be high-redshift radio-loud AGN with 12/19 sources distributed over $z \sim 1.7 - 4.3$, and a lower limit of $z > 2.0$ is placed for rest of the seven sources. We note that our study finds, for the first time, IFRSs with measured redshift > 3.0 , and also, IFRSs with redshift estimates in the faintest flux regime i.e., $S_{3.6 \mu\text{m}} < 1.3 \mu\text{Jy}$. Radio properties such as high radio luminosities, steep radio spectra and extended double-lobe morphology of several sources, confirm IFRSs to be AGN. The non-detection of all but one IFRSs in the X-ray band and the optical-to-MIR colour suggest that a significant fraction of these IFRSs are likely to be AGN hosted in dusty obscured galaxies.

This work is done in collaboration with Dr. Yogesh Wadadekar and Prof. Ishwara-Chandra from NCRA-TIFR, Pune.

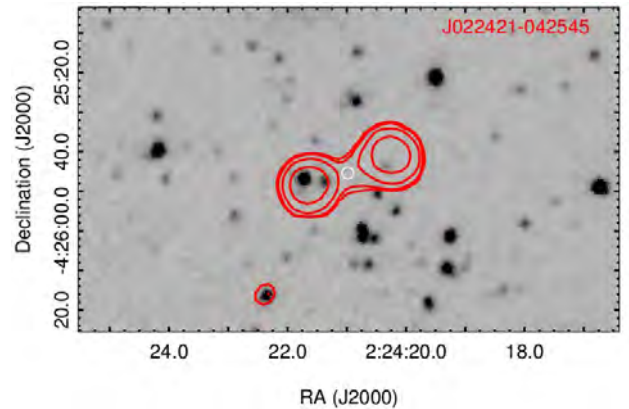


Figure 22: 1.4 GHz VLA radio contours of an Infrared-Faint Radio Source (IFRS) overlaid on a $3.6 \mu\text{m}$ Spitzer image. This IFRS is identified as a radio galaxy having no detected $3.6 \mu\text{m}$ counterpart with estimated redshift > 2 .

(V. Singh)

Understanding the evolution of AGN and galaxies across the cosmic epochs using deep surveys

Understanding the formation and evolution of galaxies is one of the fundamental problems in astrophysics. Observations have shown that almost all galaxies host a supermassive black hole (SMBH) in their centres and accretion of ambient matter on to the SMBH is manifested as Active Galactic Nuclei (AGN). It has been found that the mass of SMBH is correlated with the bulge mass and total luminosity of galaxy, and therefore, suggesting that galaxies and their SMBHs grow together possibly via AGN feedback mechanisms. Furthermore, the comoving luminosity density of both star-formation as well as of AGN peaks at the redshift (z) 2, and hence inferring that both starformation and AGN activity in galaxies are interlinked. In order to understand the evolution of starformation and AGN activity in galaxies across all cosmic epochs we are carrying our deep GMRT radio surveys of extragalactic fields in which deep multi-wavelength data exist. Our radio observations at centimeter wavelengths are unaffected by the dust obscuration, and therefore, deep radio surveys are apt to detect the population of both star forming galaxies and AGN at large redshifts. With our recent 1.4 GHz uGMRT survey in ELAIS-N1 field we cover 0.5 square degree with an unprecedented depth of $10 \mu\text{Jy}$.

This work is being done in collaboration with Prof. Ishwara-Chandra and Dr. Yogesh Wadadekar from NCRA-TIFR, Pune, India.

(V. Singh)

Investigating variability in radio-loud Narrow-Line Seyfert 1 galaxies

Narrow line Seyfert 1 galaxies (NLS1s) are low-luminosity AGN with relatively narrower width of emission lines ($\text{FWHM of } H_{\beta} < 2000 \text{ km s}^{-1}$) than that are found in Broad-Line AGN (BL-AGN). In comparison to BL-AGN, NLS1s host relatively smaller SuperMassive Black Holes (SMBHs; $10^5 - 10^7 M_{\odot}$) with relatively higher accretion rates. A small fraction of NLS1s are found to be radio-loud ($F_{5 \text{ GHz}}/F_{B\text{-band}} > 100$). Indeed, it is intriguing to find radio-loud AGN with relatively smaller SMBHs. Recent discovery of some of the radio-loud NLS1s detected in gamma-ray with space-based Fermi telescope, invoked the idea of the presence of relativistic jets oriented close to the line-of-sight in NLS1s. We are investigating variability in radio-loud NLS1s using optical, IR and X-ray observations. Preliminary results based on the monitoring of few RL-NLS1s in r-band using 1.2m Mt. Abu telescope show that some NLS1s exhibit variability on day times-scales.

(V. Singh, K. S. Baliyan and S. Ganesh)

Multiple outbursts in HBL 1ES 1959+650 during 2015: A Multi-wavelength study

As is known, blazars, a subclass of AGN, are highly variable and this property is useful to study the emission processes and structure of AGN as these remain un-resolve even by best available facility at our disposal. In a multi-wavelength study of flaring activity in high energy peaked BL Lac objects (HBL) 1ES 1959+650 during January–December 2015, we used light curves to obtain signatures of emission processes. The source underwent two major outbursts (March 2015 and October 2015) with significant flux enhancement

in optical, ultraviolet, X-rays and γ -rays. Normally, HBLs are not very active but 1ES 1959+650 has shown exceptional outburst activity in frequency domains discussed here. We used Fermi-LAT, Swift-XRT & UVOT data from space borne facilities and optical data from our Mt. Abu InfraRed Observatory (MIRO) along with archival data from other ground-based facilities to look for possible connections between emissions at different energies and the nature of variability during flaring state. The source showed no intra-night variability (INV) in optical flux during the whole observation campaign, but a short-term variability resulting in two peaks was recorded during MJD 57318 to MJD 57370. Within thirteen nights of follow-up optical observations, the brightest and faintest R-magnitudes recorded, averaged over a night, were 13.99 ± 0.03 and 14.39 ± 0.02 , respectively. Multi-wavelength study suggests the flaring activity at all frequencies to be correlated with diverse flare durations. The simultaneous flux enhancement in radio at 15GHz and VHE γ -rays indicates to the activity in the accretion disk leading to a fresh injection of plasma into the jet that interacts with a standing sub-mm core giving rise to the enhanced, co-spatial emissions in all the energy bands.

This work is done in collaboration with S Chandra of TIFR.

(N. Kaur, K. S. Baliyan and S. Ganesh)

Very high energy (VHE) flare in FSRQ PKS 1510-089: Observations with multi-wavelength facilities

PKS 1510-089 is a bright quasar at low redshift ($z=0.36$) and one of only a few flat spectrum radio quasars detected in the VHE (very-high-energy, $> 100 \text{ GeV}$) gamma-ray band. We study the broadband spectral and temporal properties of the PKS 1510-089 emissions during a high gamma-ray state. We performed VHE gamma-ray observations of PKS 1510-089 with two Cherenkov telescopes (MAGIC, La Palma) during a long high gamma-ray outburst in May 2015. In order to perform broadband modelling of the source, we have also obtained contemporaneous multi-wavelength data in radio, UV, X-ray and GeV gamma-ray ranges while observations in optical and near infrared bands were carried out from Mt Abu IR Observatory (MIRO). We construct a broadband spectral energy distribution (SED) in two periods, selected according to VHE gamma-ray state. PKS 1510-089 has been detected by MAGIC during a few day-long observations performed in the middle of a long, high optical and gamma-ray state, showing for the first time a significant VHE gamma-ray variability. The source was seen to have intra-night variability in near-infrared with significant amplitude of variation. Similar to the optical and gamma-ray high state of the source detected in 2012, it was accompanied by a rotation of the optical polarization angle and the emission of a new jet component observed in radio. However, due to large uncertainty on the knot separation time, the association with the VHE gamma-ray emission cannot be firmly established. The spectral shape in the VHE band during the flare is similar to the ones obtained during previous measurements of the source. The observed flux variability sets, for the first time, constraints the size of the region from which VHE gamma rays are emitted. The multi-wavelength emissions in PKS 1510-089 lead to the broadband SED which can be explained in the framework of the external Compton scenario.

This work is carried out in collaboration with MAGIC Collaboration team.

(N. Kaur, Sameer and K. S. Baliyan)

PRL optical photo-polarimeter (PRLPOL)

PRL had developed India's first astronomical optical photopolarimeter during the mid 1980s. This instrument has been extensively used on various telescopes in the country for the first decade and exclusively on the 1.2m telescope at Mount Abu during the last two decades. The control system of the instrument has been regularly updated with keeping pace with the temporal evolution of computer technology and miniaturization of electronics. However, now not much change had been made as regards the detectors used in this instrument. Recently we have found that Multi-pixel photon counters (MPPC) are very good substitute for the photo-multiplier tubes that had been employed so far. They are compact and have better sensitivity with built in power supplies and cooling units. After qualifying these new detectors in the lab, we have now modified the photo-polarimeter by removing the old, bulky, cooling unit + PMT system and replacing it with a very compact unit developed in PRL workshop to hold the very compact MPPC detectors. Two MPPC detectors have been employed to detect the ordinary and extra-ordinary rays and thence measure the degree of polarization and position angle. Laboratory tests have been carried out and we expect to begin observations with this instrument in the next months.

(S. Ganesh, A. B. Shah, K. S. Baliyan, G. P. Ubale and R. Kaila)

Near-infrared Imaging Spectro-Polarimeter (NISP): Backend instrument for the new 2.5 mt Telescope

NISP is being designed and developed at PRL as facility-class focal plane instrument for the upcoming 2.5 mt telescope. It will be a multi-function instrument having capability of near-infrared imaging, spectroscopy and polarimetry. It will be possible to study several class of astronomical objects such as transients (Novae, Supernovae, optical companions in X-ray binaries etc.), comets, star forming regions, Milky Way survey, galaxies, AGNs etc. All optical, mechanical and electrical sub-systems are being designed at PRL.

NISP will encompass 0.8 to 2.5 μm spectral range, imaging area of 36x36 mm² (2048 x 2048 pixels, 18 μm pixel size) at a spectroscopic resolution of 2000 and 0.3% minimum detectable polarization. In order to achieve 2.5 μm cut-off, IR optics and focal plane array (detector) will be cooled to 77 K. Both, the optics and detector, will be encapsulated into custom designed cryo-cooled vacuum Dewar. The imaging, spectroscopic and polarimetric optics will consist of long slit, collimator, refractive lens, filter wheels (broadband filters, narrow-band filters, half-wave plate) and focal-reducer.

HAWAII 2Kx2K pixels, CMOS HgCdTe will be used as focal plane array detector. To provide clocks and precision biases to the detector and to get noise free digitization of analog output signals, traditionally extensive external focal plane electronics (FPE) is being employed. Normally FPE is mounted at some distance from the Dewar which requires bulky harness hence limits noise performance. We plan to mount FPA and FPE side-by-side in the Dewar. FPE will be realized using System for Image digitization, Enhancement, Control And Retrieval (SIDEAR) Application Specific Integrated Circuit (ASIC) developed by Teledyne Imaging Sensors, California. SIDEAR is very complex programmable ASIC which requires high speed digital interface for commanding and data readout. Figure-23 depicts block-schematic of NISP using SIDEAR ASIC. FPGA based

controller will be developed to program SIDEAR for all various operating modes required for NISP. To control all the subsystems of NISP, Graphical User Interface (GUI) software based on MS Windows and/or Linux platforms will be developed. Room Temperature and Cryo-cooled setups of Space Application Center, Ahmedabad are being used to obtain experience for SIDEAR development.

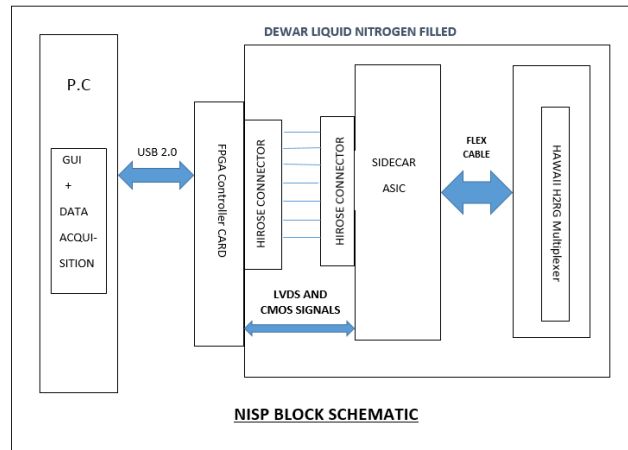


Figure 23: NISP SIDEAR ASIC based Block schematic

As a parallel approach discrete electronics based clock driver (Figure 24), bias supply and digitization boards are designed and being tested. The multi-boards based front-end electronics (FEE) will be controlled by low cost general purpose FPGA board (figure-24). Firmware for FPGA is being developed in VHDL. The GUI will have all on-line diagnostic features for on-site fault finding.

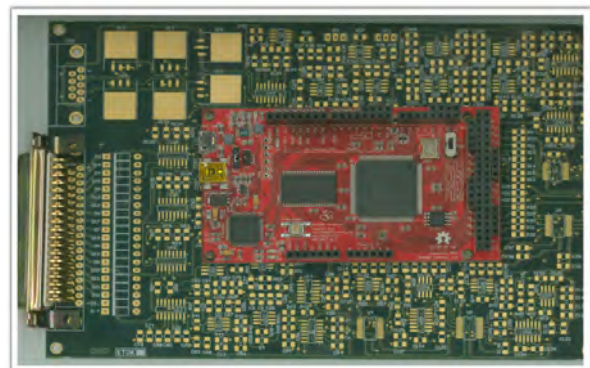


Figure 24: NISP discrete electronics based clock driver (green) and FPGA board (red)

(A. B. Shah, D. Sarkar, P. S. Patwal, K. S. Baliyan, S. Ganesh, S. Naik, S. N. Mathur, H. Adalja and A. Rai)

Development of MFOSC-P : An Optical Imager-Spectrograph for Mt. Abu 1.2m Telescope - The Opto-Mechanical Design

Mt. Abu Faint Object Spectrograph and Camera-Pathfinder (MFOSC-P) is an imager-spectrograph currently under development. Based on focal reducer design, MFOSC-P would provide imaging

over $\sim 6 \times 6 \text{ arc-min}^2$ on a $1\text{K} \times 1\text{K}$ Andor CCD detector, with the sampling of 3 pixels per arc-seconds. Two modes of slit limited spectroscopy with gratings would achieve the resolution of ~ 2000 and ~ 1000 around ~ 6500 and ~ 5500 angstroms. The base specifications and optical design were described in the last annual report. The procurement of various optical components are currently in progress. Here we report on the mechanical system development of the instrument. The opto-mechanical system of MFOSC-P (shown in Figure 25) is developed using a modular approach.

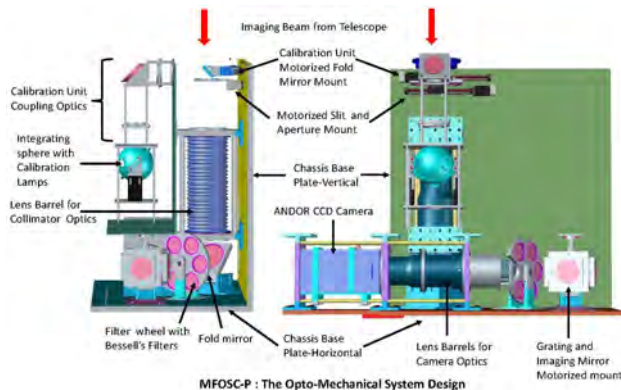


Figure 25: Opto-Mechanical System Design of MFOSC-P

Imaging beam from the telescope would be focused through an optical glass window on to the designed aperture masks. Three masks for two modes of spectroscopy (with 75 and 150 microns width of slit opening) and one for imaging would be mounted on a linear translation stage driven by stepper motor. The masks would be moved in and out of the beam path as per imaging or spectroscopy mode selection. Mechanical mounts have been designed for each of the elements of the optical chain. The mounted lenses for both the collimator and camera optics are to be first aligned in respective barrels and then within a cage rod structure to ensure required opto-mechanical tolerances. Bessel's filters for broadband imaging and grating are kept in the parallel beam space between collimator and camera optics, with pupil at the grating position. These components are mounted on two stepper motor based mechanism to automate the observing sequence on the telescope. Off-the-shelf ANDOR CCD imaging camera with read out electronics is being used as the detector.

A calibration unit with standard spectral lamps coupled to an integrating sphere has been designed. A set of two achromatic lenses and a movable fold mirror would feed the light from integrating sphere in to the main optical chain of the instrument through slit aperture. The calibration unit fold mirror is mounted on a stepper motor driven linear stage and can be moved to block telescope beam during the spectral calibration of the instrument. Various moving components (filter wheel, grating wheel etc.) are driven by stepper motors with encoder feedbacks. The entire opto-mechanical structure would be fixed on a aluminum chassis and sealed for dust contamination etc. Assembly, integration and tests (AIT) plans of the instrument, first on the optical bench and then within the instrument has been development. Fabrication of the various mechanical parts are currently in process.

(M. K. Srivastava and M. Jangra)

Design and Development of a general purpose Electronic Instrument Control System (ECS)

A general purpose electronic instrument control system (ECS) for the instrumentation needs of Mt. Abu observatory is currently under development. The system has been designed around off-the shelf Arduino Mega 2560 micro-controller board. A controller card includes the necessary circuitry for the closed loop operation of three stepper motors, switching circuitry for six lamps modules using three on board relays and three external relay driving circuits. The motion control module for a stepper motor uses an off-the-shelf motor driver card, a optical quadrature encoder readout IC, and readout circuits for limit sensors. A closed loop control algorithm within the micro controller would then be responsible for the motion of stepper motor based on inputs from external limit sensors and the encoder. A PC based command line interface and a communication protocol between PC to ECS cards has been developed. Based on master-slave architecture an USB-RS485 based communication link is used to transfer commands from PC to various cards. Data parsing algorithm and command execution algorithms for various tasks have been developed. Algorithms and codes for various stepper motor's motion profiles and controls are currently under development and electronic testing of the cards are underway (Figure 26).

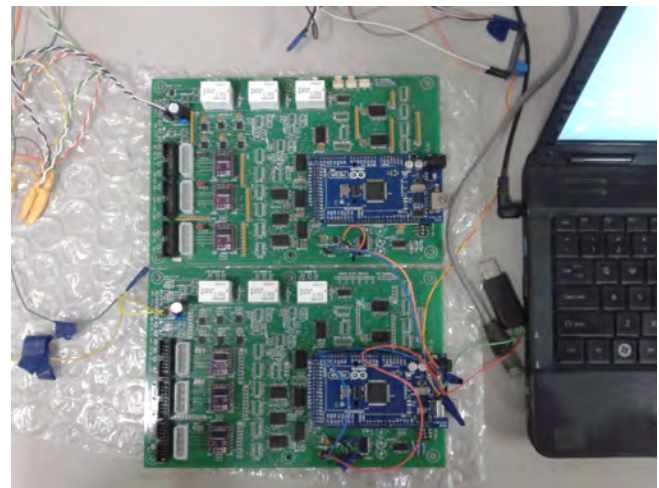


Figure 26: Controller Cards of ECS currently under development

(M. K. Srivastava, N. Ahmed, A. B. Shah and S. Ganesh)

AstroSat: Indian Multi-wavelength Astronomy Mission

AstroSat, India's first dedicated astronomy mission launched on 28th September 2015, is successfully continuing its operations. After the completion of first year of operations in October 2016, AstroSat is open for observations by Indian proposers through Announcement of Opportunity (AO). The AO proposals and the Guranteed Time (GT) proposals are reviewed for scientific merit and technical feasibility of observations by the AstroSat Time Allocation Committee and the AstroSat Technical Committee respectively and the successful proposals are scheduled for observations in each observation cycle.

Our group is closely involved in all steps of the planning of the AstroSat observations, including scientific review of the proposals, verifying their technical feasibility with various instrument as well as scheduling constraints. Our group has also contributed to familiarizing Indian astronomy community to AstroSat proposal submission process as well as analysis of the AstroSat data.

(Mithun N. P. S. and S. V. Vadawale)

In-flight calibration of AstroSat CZT Imager

Cadmium Zinc Telluride Imager (CZTI) is the hard X-ray coded mask telescope on-board AstroSat for imaging and spectroscopy in 20-200 keV. Extensive ground calibration was carried out to characterize the instrument response prior to the launch. Further improvements on the instrument response is made by analyzing the in-flight data. Various aspects of the imaging and spectral calibration like detector gain, instrument boresight, mask-alignment, non-uniformity in background were analyzed using data from in-flight calibration observations.

We developed a modified mask-weighting technique to account for some of the peculiarities of the instrument observed post-launch, such as slight mis-alignment of the four quadrants, so as to measure accurate hard X-ray spectrum of the source. These modifications are incorporated into the spectral response matrix as well as the data processing software for CZTI. Spectrum of the standard calibration source obtained in multiple observations with CZTI are fitted with the canonical power law model to verify the response matrix. We obtain power law index of 2.08 which is consistent with the observations

by other instruments. Quasi-simultaneous observations with CZTI and NuSTAR of Crab nebula is used for simultaneous fitting of spectrum to establish cross calibration. Figure 27 shows the joint CZTI NuSTAR fit to the crab spectrum that demonstrates consistency of CZTI observations with NuSTAR.

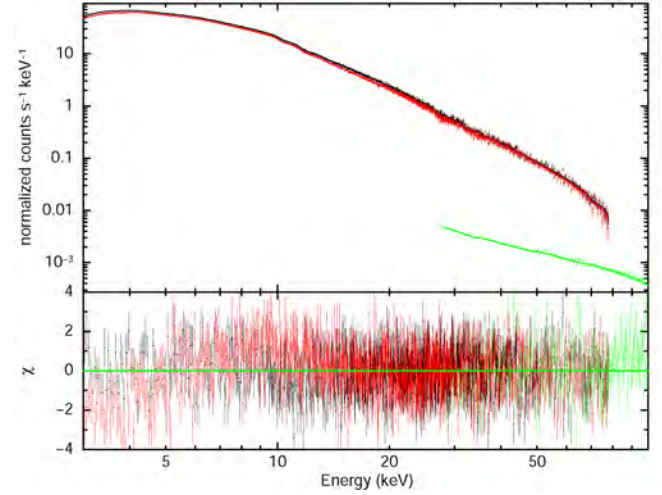


Figure 27: Joint fit of the power-law model to the Crab spectrum measured by CZTI and NuSTAR. The best fit parameters are very close to the canonical spectral parameter for the Crab

(Mithun N. P. S. and S. V. Vadawale)

Science

Solar Physics

Study of stochastic variation in the global velocity oscillations in the Sun during the phase of minimum solar activity

The global velocity oscillations in the Sun, known as p -modes, are stochastically excited due to high turbulence in the convection zone just beneath the solar surface. The incoherent superposition of these p -modes peak in the 2–5 mHz frequency band, corresponding to the acoustic cut-off frequency of nearly 5.3 mHz of the solar photosphere.

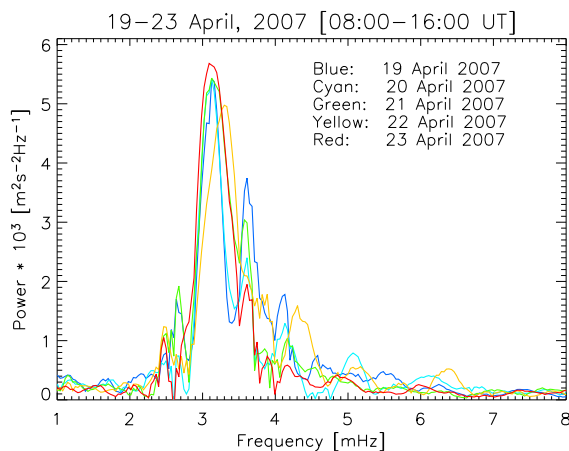


Figure 1: Plots showing the comparison of Fourier Power Spectra obtained from Sun-as-a-star disk-integrated GOLF velocity observations onboard SOHO space mission for the period from 19 April 2007 to 23 April 2007 during the minimum phase of solar activity in the Solar Cycle 23. It is observed that the power of global modes of oscillations in the Sun show a significant variation in different frequency regimes even during the epoch of minimum solar activity.

The amplitudes and frequencies of these global p -modes have shown correlation with the solar activity indicators over the solar cycle. The changes in the characteristics of these p -modes with the solar cycle

appear to be connected with the structural and magnetic changes in the sub-surface layers of the Sun with the increase and decrease of the solar activity. In this work, we have studied the variation in the power of these p -modes on short time-scales during the phase of minimum solar activity in order to examine the short-term changes in the stochastic processes in the solar convection zone that excite the global modes of oscillations in the Sun. We have used the Sun-as-a-star disk-integrated velocity observations obtained by the GOLF instrument onboard SOHO space mission for several days during the minimum phase of Solar Cycle 23. In the Figure 1, we show the comparison of the Fourier Power Spectra obtained for each of the days during the period from 19 April 2007 to 23 April 2007. We find that the power of the p -modes change significantly in the different frequency regimes even during the minimum phase of solar activity, which has minimum influence of the solar magnetic fields. These results indicate that there are significant changes in the internal dynamics of the Sun even during the phase of minimum solar activity.

This work has been done in collaboration with Savita Mathur of Space Science Institute, Boulder (USA), Rafael A. Garica of CEA/DSM-CNRS, IRFU/Sap, Saclay (France), and Antonio Jimenez of IAC, Tenerife (Spain).

(B. Kumar)

Study of acoustic and magnetohydrodynamic wave modes over the flaring active region NOAA 12634 using the MAST observations

Heliaseismic waves (p -modes) and the by-products of their interaction with magnetic fields, both in sunspots and magnetic network, in the form of magnetohydrodynamic (MHD) wave modes (slow and fast magneto-acoustic wave modes) provide very useful diagnostics of the magnetic and thermal structure of sunspots. These are also useful for understanding the atmospheric wave energetics and heating. In this work, we have obtained two-height

high-resolution and high-cadence simultaneous observations of the flaring active region NOAA 12634 on 9 February, 2017 during the period 04:00-08:00 UT covering the photosphere (G-band) and the upper chromosphere (H_α) to image the oscillatory signals in intensity measurements (Figure 2) with the MAST facility at USO.

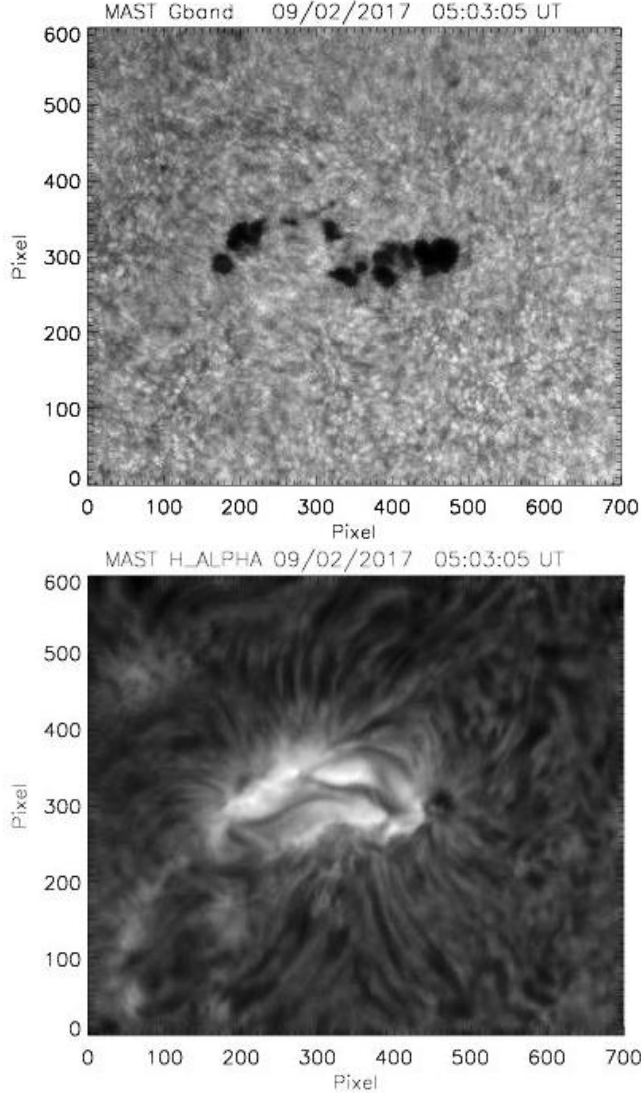


Figure 2: The images show the snapshots of flaring active region NOAA 12634 obtained by the MAST facility on 9 February 2017 in G-band (top), and H_α (bottom) wavelengths corresponding to the solar photosphere and chromosphere, respectively. The spatial scale is about 0.2 arc-sec per pixel.

The observations from HMI and AIA instruments onboard SDO space mission are also being used in conjunction with the MAST observations in order to sample the different other layers of the solar atmosphere. From these observations, our objective is to study the following: (1) p -mode to MHD wave mode conversion mechanisms, (2) contributions of MHD wave modes to local helioseismic observables, (3) height evolution of wave modes, (4) any sudden variations in the solar magnetic fields in the active region during the flare, and (5) the role of impulsive Lorentz force changes in energizing the localized oscillations in the active region.

This work is being done in collaboration with S.P. Rajaguru of Indian Institute of Astrophysics, Bengaluru (India).

(B. Kumar, S. Dhara, S. K. Mathew, A. Raja Bayanna, and B. Ramya)

Photospheric magnetic imprints of several major flares produced by the largest active region of solar cycle 24

In order to understand the changes in photospheric magnetic field related to flares, several studies have been made (Sudol and Harvey, 2005 and Wang, 2006 and references therein). Wang and Liu (2010) found an increase of transverse field at the Polarity Inversion Line (PIL) for 11 X Class flares. Petrie (2012) found an increase in strength of the field vector at the neutral line at the time of the flare, particularly in its horizontal component parallel near the PIL. This was accompanied by a large, abrupt, downward vertical Lorentz force change. The detailed explanation of these was first time given by Fletcher and Hudson (2008). AR 12192, is the largest active region of the solar cycle 24, which produced 6 X class flares, 22 M class flares, and 53 C class flares in the course of its disc passage from October 19-27, 2014. Interestingly, all the major flares produced by this AR were non-eruptive except one M4.0 class flare which produced one CME. The goal of this work is to make a comparative study of the flare related photospheric magnetic field changes for both the eruptive and non-eruptive flares produced by AR12192.

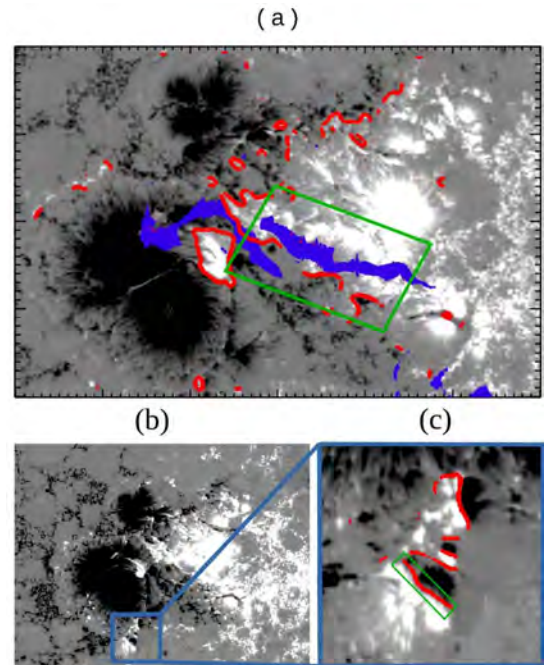


Figure 3: Panel (a) and (b) show the line of sight component of photospheric magnetic field obtained from HMI vector magnetogram data during non-eruptive X3.1 class flare on 2014 October 24 and eruptive M4.0 class flare on the same date respectively. Panel (c) shows the line of sight component of photospheric magnetic field zoomed in from the selected region (source region of M4.0 class flare) shown in panel (b). Blue regions are the overplotted flare brightening and red lines are the magnetic polarity inversion line. The green rectangles specify the selected area within which all the analysis has been done.

In this work, we analyzed five 6 hr series of HMI 12 minute cadence vector magnetograms covering four non-eruptive major flares

occurring near the core region of AR 12192 and one eruptive flare occurring away from the core region. We found that near the main polarity inversion line in between the observed flare ribbons (Figure 3), the magnetic field vectors become more horizontal during all the five flares.

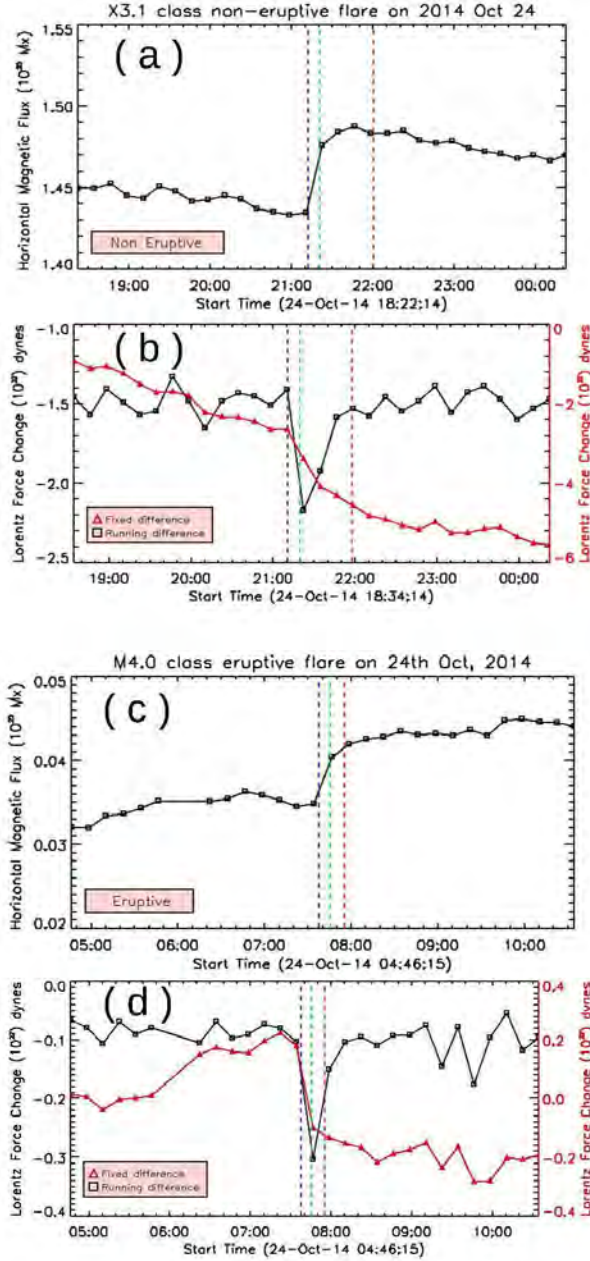


Figure 4: In the panels (a) and (b) the horizontal magnetic flux and vertical component of Lorentz force changes for non-eruptive X3.1 class flare are plotted as functions of time respectively. The downward component of the Lorentz force changes computed from running difference method are represented by the black solid lines. The changes of the total vertical Lorentz force with respect to the first image are represented by the solid red lines. In the panels (c) and (d) the horizontal magnetic flux and vertical component of Lorentz force changes for eruptive M4.0 class flare are plotted as functions of time respectively. The areas of integration are indicated by the green rectangles in Figure 3. The vertical blue, green and red dotted lines represent the GOES flare start, peak, and end times.

The changes in horizontal magnetic field, during all of these flares,

last more than two hours. During each of the flares, the vertical Lorentz force shows a large, abrupt downward change (Figure 4). The magnitude of these force changes, ranging from about 0.2×10^{22} dynes to about 4×10^{22} dynes, are comparable to those found in the previous estimates of flare related Lorentz force changes. These large abrupt changes in Lorentz force are consistent with the loop collapse scenario. For the four non-eruptive flares, the changes in Lorentz force per unit area ranges from about 180 dynes/cm² to about 1410 dynes/cm². Whereas, the changes in Lorentz force per unit area for the eruptive flare is about 2700 dynes/cm², which is almost two times larger than the maximum changes found in the four non-eruptive cases.

(R. Sarkar, Nandita Srivastava)

Pre-flare blowout coronal jet and evolutionary phases of a solar eruptive prominence

We investigate the triggering, activation, and ejection of a solar eruptive prominence that occurred in a multi-polar flux system of active region NOAA 11548 on 2012 August 18 by analyzing data from the Atmospheric Imaging Assembly (AIA) on board the Solar Dynamics Observatory (SDO), the Reuven Ramaty High Energy Solar Spectroscopic Imager (RHESSI), and the Extreme Ultraviolet Imager/Sun Earth Connection Coronal and Heliospheric Investigation (EUVI/SECCHI) on board the Solar Terrestrial Relation Observatory (STEREO). Prior to the prominence activation, we observed striking coronal activities in the form of a blowout jet, which is associated with the rapid eruption of a cool flux rope (see Figure 5).

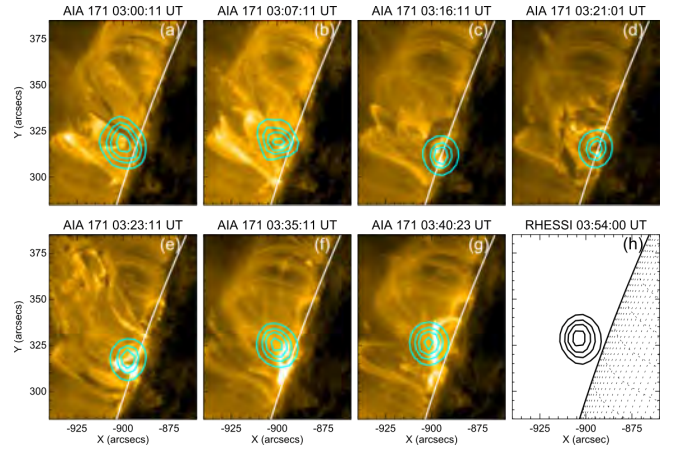


Figure 5: Few representative images showing the evolution of X-ray 6–12 keV source from the early pre-flare stages to the decay phase of M1.8 flare. To show the spatial association between the prominence evolution and the thermal X-ray source, AIA 171 images are plotted in the background (panels (a)–(g)).

Furthermore, the jet-associated flux rope eruption undergoes splitting and rotation during its outward expansion. These coronal activities are followed by the prominence activation during which it slowly rises with a speed of ~ 12 km s⁻¹ while the region below the prominence emits gradually varying EUV and thermal X-ray emissions (cf. Figures 5 and 6). From these observations, we propose that the prominence eruption is a complex, multi-step phenomenon in which a combination of internal (tether-cutting reconnection) and external

(i.e., pre-eruption coronal activities) processes are involved. The prominence exhibits catastrophic loss of equilibrium with the onset of the impulsive phase of an M1.8 flare, suggesting large-scale energy release by coronal magnetic reconnection. We obtain signatures of particle acceleration in the form of power-law spectra with hard electron spectral index ($\delta \sim 3$) and strong HXR footpoint sources. During the impulsive phase, a hot EUV plasmoid was observed below the apex of the erupting prominence that ejected in the direction of the prominence with a speed of $\sim 177 \text{ km s}^{-1}$. The temporal, spatial, and kinematic correlations between the erupting prominence and the plasmoid imply that the magnetic reconnection supported the fast ejection of prominence in the lower corona.

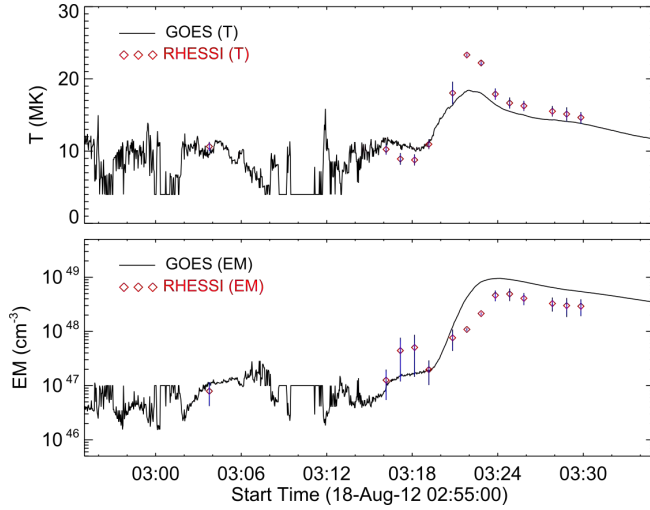


Figure 6: Top : Evolution of temperature (T) and emission measure (EM), bottom: from solar source region during various stages of prominence eruption (shown in Figure 5) derived from GOES and RHESSI X-ray measurements. The error bars are plotted on each T and EM values derived from RHESSI spectra.

(B. Joshi)

Study of confined and eruptive solar events observed in Ca-K images

There are two kinds of major energetic phenomena called eruptive and confined events. The former describes flares with associated coronal mass ejections (CMEs), while the latter denotes flares without associated CMEs. One of the methods to understand the mechanism of the two types of events is to derive the magnetic-reconnection rates and fluxes from the flare-ribbon evolution of the active region. For this purpose the high cadence Ca-K time series data and low-noise 720-second HMI LOS magnetogram data were used to measure the reconnection rate, total reconnection flux. From the past studies it is understood that the surface magnetic flux swept by the flare ribbons relates to a global reconnection rate. Therefore in order to measure the abovesaid parameters, the observables like the newly brightened area and magnetic field of the area inside this, are calculated. Figure 7 shows the estimated parameters for AR12320 using Ca-K filtergrams. This study is conducted both on confined and eruptive events and the difference between the two are studied. The difference is expected since in the eruptive flares, part of the energy is converted into the magnetic reconnection process into acceleration and escape of

the CME, whereas in the confined flares all of the magnetic energy released is available for the flare.

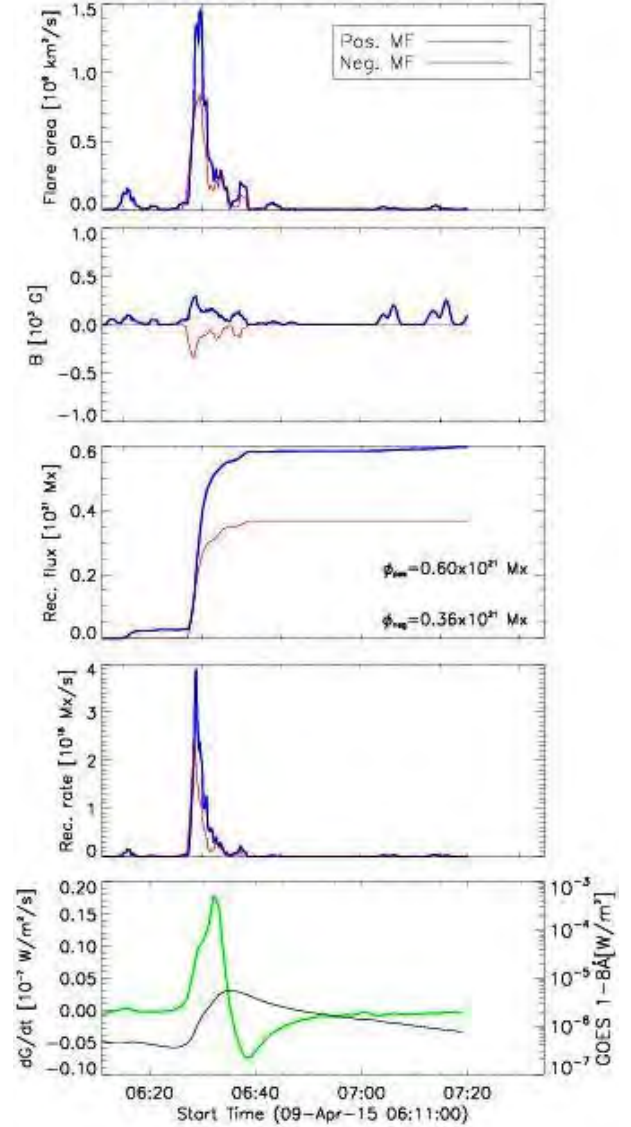


Figure 7: Parameters derived for AR 12320 a confined flare observed using KSO Ca-K filtergram. From Top to bottom: Panels show evolution of the newly brightened flare pixels, mean magnetic field [B], reconnected magnetic flux [$\phi(t)$], magnetic reconnection rate [$\dot{\phi}(t)$], (blue indicates positive polarity and red indicates negative polarity), and the GOES 1-8 Å soft X-ray flux (black) together with its time derivative (green).

(G. Sindhuja, Nandita Srivastava)

Study of evolution and eruption of filaments using MAST and AIA/SDO observations

We studied two partial filament eruptions that occurred in the vicinity of the active region NOAA 12525 and NOAA 12612, respectively. First event occurred on 17 March, 2016 associated with AR NOAA 12525 and second event occurred on 28 November, 2016 associated

with AR NOAA 12612. For first event, we obtained MAST $H\alpha$ data before and after the eruption, while for the second event, we were able to take $H\alpha$ data during eruption. General appearance of these filaments before the eruption are shown in Figure 8.

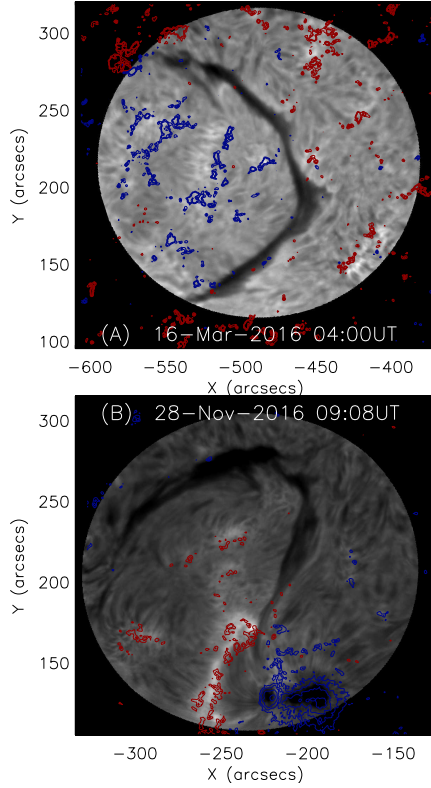


Figure 8: Filaments observed in $H\alpha$ in different active regions. Isocontours of the SDO/HMI magnetic strength values are overlaid on the images. The red and blue contours represent the positive and negative polarities with magnetic field strength values of ± 20 , 50 , 150 , and 200 G, respectively.

The barbs of the filament are clearly visible. For first event, the filament appeared on the solar disk on 14 March, 2016 and it has a circular shape. We matched the MAST $H\alpha$ image with GONG $H\alpha$ image using heliographic coordinate and the same field-of-view matched with line-of-sight magnetogram from HMI. From the direction of barbs of filament and magnetic polarity signs on both side of filament, we can infer that the filament is right-bearing for an observer looking at the filament from north polarity region of magnetic field and hence the filament is dextral with negative helicity sign, which follows the hemispheric chirality rule. For the second event, the filament was located outside the active region NOAA 12612 at a latitude of $\sim 18^\circ$ in the northern hemisphere. The dark thread like structure of the filament bifurcates into two parts before the activation of the filament on 28 November 2016. After the partial eruption, the filament forms back again. From the Figure 8(B), it is also clear that the filament has the right-handed twist with the negative helicity sign.

The filament experienced twice partial eruptions on 17 March, 2016 at 04:00 UT and 05:30 UT. The filament channel still exists after both eruptions. The main objective of this work is to understand the trigger and instability mechanism of filament eruptions by thoroughly analyzing the sequence of pre-eruption activities occurring in filament surrounding region. From HMI line-of-sight magnetogram, we

calculated the evolution of the magnetic field for the AR for same field-of-view of Figure 8(A). We observed the emergence of magnetic field in the AR (Figure 9(top)).

We also observed that there is a continuous converging motion near the barb and footpoint locations of the filament (as shown in Figure 9(bottom)). The disappearance of barb is also observed before the filament activation (as shown in Figure 10). Figure 11 shows the sequence of $H\alpha$ images obtained from MAST before and during activation of filament on 28 November 2016. Filament started to bifurcate in two parts before the activation and then it experienced a partial eruption. Before the eruption, we observed a brightening below the spine of the filament.

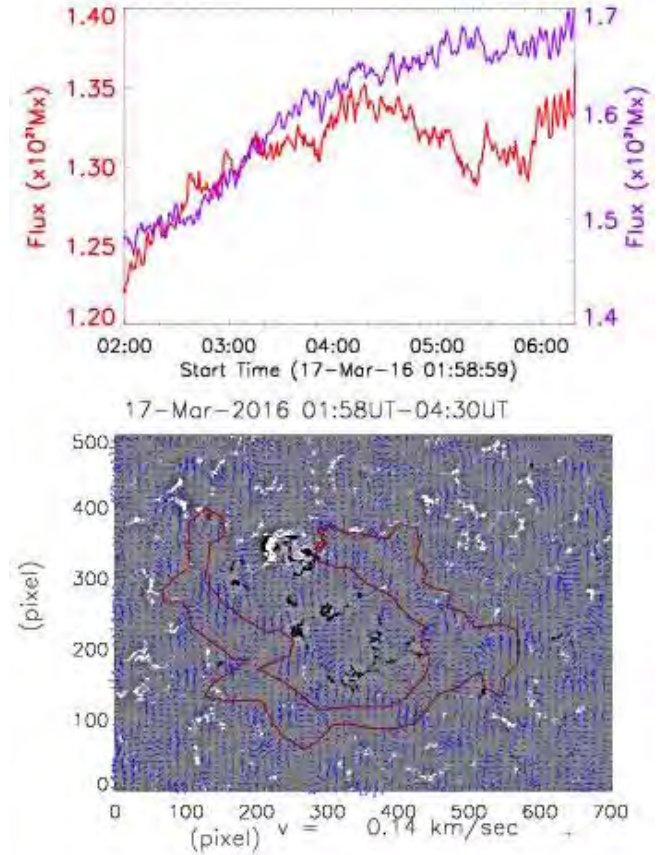


Figure 9: Top: Evolution of magnetic flux are plotted with respect to time for the same FOV of Figure 8 (Top). Bottom: Averaged horizontal velocity vectors shown in arrows are overlaid upon an averaged magnetogram. The contour of the filament, extracted from the 304 Å image.

In summary, both filament eruptions initiated during the flux emergence in and around the filament. This kind of flux emergence followed by converging/shearing motions will stress overlying fields and hence builds up energy in the corona. In such condition, a small perturbation can trigger the filament eruption.

From MAST $H\alpha$ data, we obtained that the helicity sign of the filament follow the hemispheric rule before the eruption. After partial eruption, the filament reforms in the same channel and maintained its helicity sign.

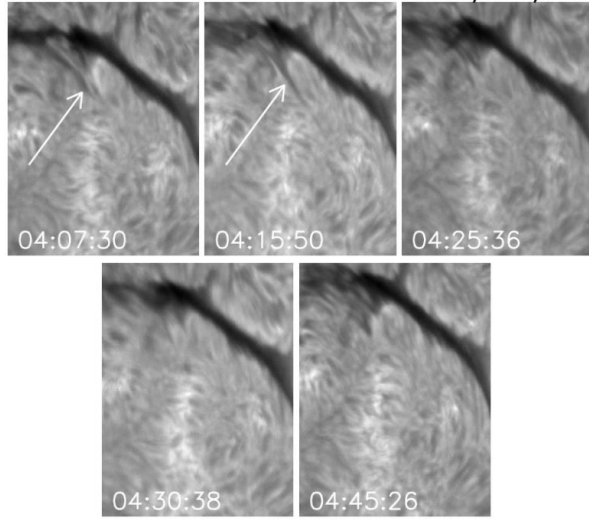


Figure 10: Sequence of $H\alpha$ images obtained from MAST shows the disappearance of barb of the filament on 16 March 2016. The barb locations are shown by white arrows.

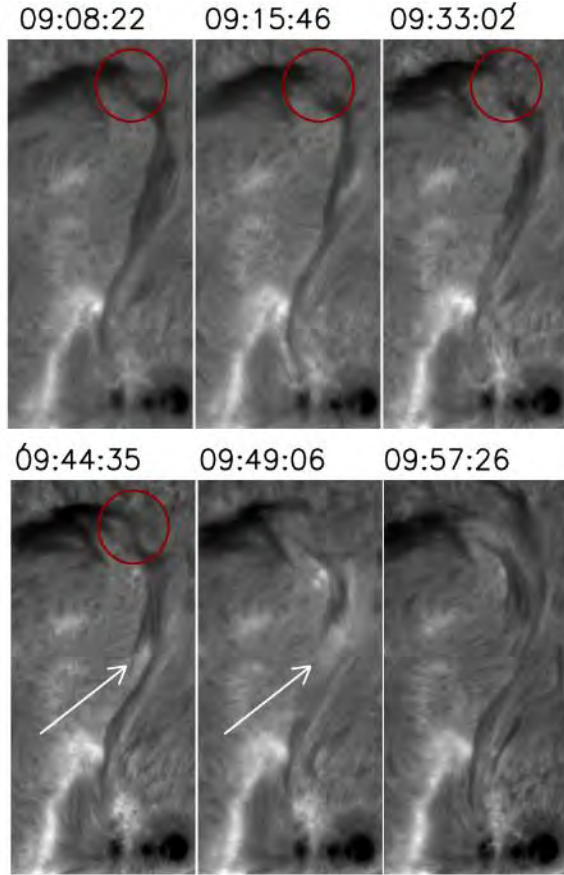


Figure 11: Sequence of $H\alpha$ images obtained from MAST shows the activation of the filament on 28 November 2016. The activation location of the filament are shown by white arrows. The red circled regions show the bifurcation of filament before its activation.

Assessing the collision nature of coronal mass ejections in the inner heliosphere

Coronal Mass Ejection (CME) is an episodic expulsion of magnetized plasma from the Sun into the Heliosphere. Realizing the importance of studying the CME-CME interaction, almost a dozen cases of interacting CMEs have been reported in the literature in the last 5 years, based on observations recorded by Heliospheric Imager aboard STEREO mission. These studies were based on simple scenario of head-on collision and real scenarios of oblique collision in three-dimension (3D), expansion speeds, and angular widths of the CMEs were not considered. In the present study, we examine the role of CME characteristics in deciding the nature of their collision viz, elastic, inelastic or superelastic. We determine the CMEs characteristics using STEREO and SOHO imaging observations and assess how a reasonable uncertainty in the measured parameters changes the probability of one type of collision to the other. We selected a total of 8 cases of interacting CMEs and have determined the nature of collision using their observed characteristics in oblique collision. Among the cases studied, two cases (CMEs of 2012 June 13-14 and 2011 August 3-4) the collision is found to be inelastic and two cases (CMEs of 2012 March 4-5 and 2012 November 9-10) show perfectly inelastic collision nature.

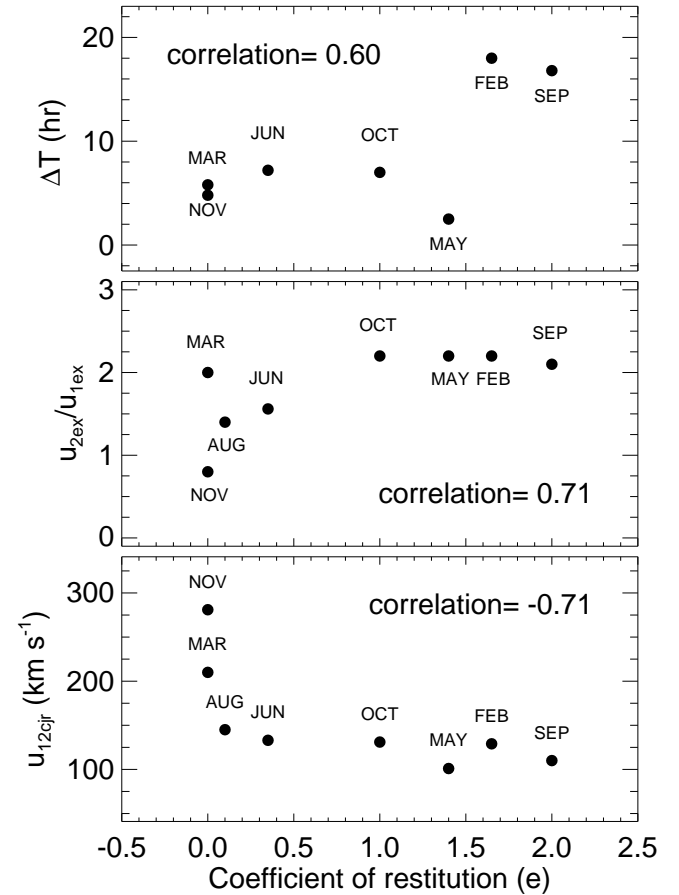


Figure 12: The correlation coefficient between the values of coefficient of restitution (e) and measured CME characteristics is shown for the selected cases of the CMEs. The values of e are plotted on the X-axis. The collision duration, ratio of pre-collision expansion speed of CME2 to CME1 and relative approaching speed of the CMEs along the line joining their centroids are shown on the Y-axis of top, middle and bottom panels, respectively.

One case (CMEs of 2013 October 25) show elastic nature of collision and other three cases (CMEs of 2011 February 14-15, 2010 May 23-24 and 2012 September 25-28) show super-elastic nature of collisions. Our study reveals that the crucial pre-collision parameters that dictate the nature of collision of CMEs, in descending order of priority, are their relative approaching speed, expansion speed of the following CME over the preceding one, and the time duration of collision phase (Figure 12). We note that direction of impact, distance of a collision site from the Sun, and mass ratio of the CMEs do not favor a particular type of collision. On taking the uncertainties into account, the nature of collision of 3 cases among the 8 cases of the CMEs, could not be ascertained decisively. Such an uncertainty is not obviously noticed while considering the head-on collision scenario where the value of coefficient of restitution, e is often underestimated. We highlight the uncertainties involved in such studies and suggest to ascertain only a finite probability for a specific type of collision.

This work is done in collaboration with Wageesh Mishra, Yuming Wang and Chenglong Shen of USTC, China

(Nandita Srivastava)

On the role of repetitive magnetic reconnections in evolution of magnetic flux ropes in solar corona

The presented magnetohydrodynamics simulations aim to explore a scenario in which the repeated magnetic reconnections (MRs) provide an autonomous mechanism governing emergence of coherent structures like magnetic flux rope in solar corona. For the purpose, we consider the magnetic initial field line (MFL) topologies identical to observed coronal loops and simulate viscous relaxation of an incompressible, thermally homogeneous high magnetic Reynolds number plasma maintaining the condition of flux-freezing. During the relaxation, sharpening of magnetic field gradient is unbounded, ultimately leading to MRs at locations where separation of non-parallel field lines approaches grid resolution.

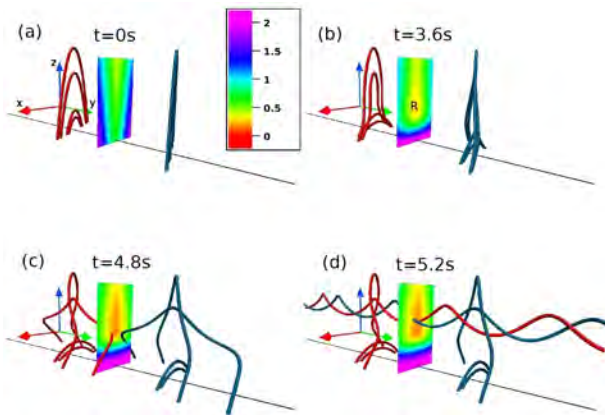


Figure 13: Panel (a) shows the MFLs geometry of initial field with translational symmetry. The polarity inversion line is the solid black line. The figure is overlaid with contours of magnetic pressure a y -constant plane. Panel (b) documents the implosion of MFLs situated at lower height along with an increase in their footpoint separation which results in depletion of magnetic pressure (symbolized by R) in the y -constant plane. Parts of MFLs are dragged into this pressure depleted region R from both sides of PIL, which sharpens up the gradient in \mathbf{B} (panel (c)). Subsequent reconnection leads to the generation of rope which is made of helical MFLs (panel (d)).

The MR process per se is under resolved, but effectively regularized by locally adaptive dissipation of non-oscillatory numerics, in the spirit of implicit large eddy simulations. In effect, the post-reconnection condition of flux-freezing is restored, and field lines tied to the reconnection outflow push other sets of MFLs, leading to secondary MRs. The whole process is replicated in time to realize repetitive reconnections. The simulations are performed with initial magnetic field (panel a, Figure 13) congruent to a gauge-invariant form of linear force-free field having translational symmetry. The results show that initial unbalanced forces deform initial field lines such that the field gradient sharpens in a direction (herein x). Further push eventuates in reconnection and development of a detached flux rope (Figure 13). Notably, the projection of the rope on a y -constant plane corresponds to a magnetic island.

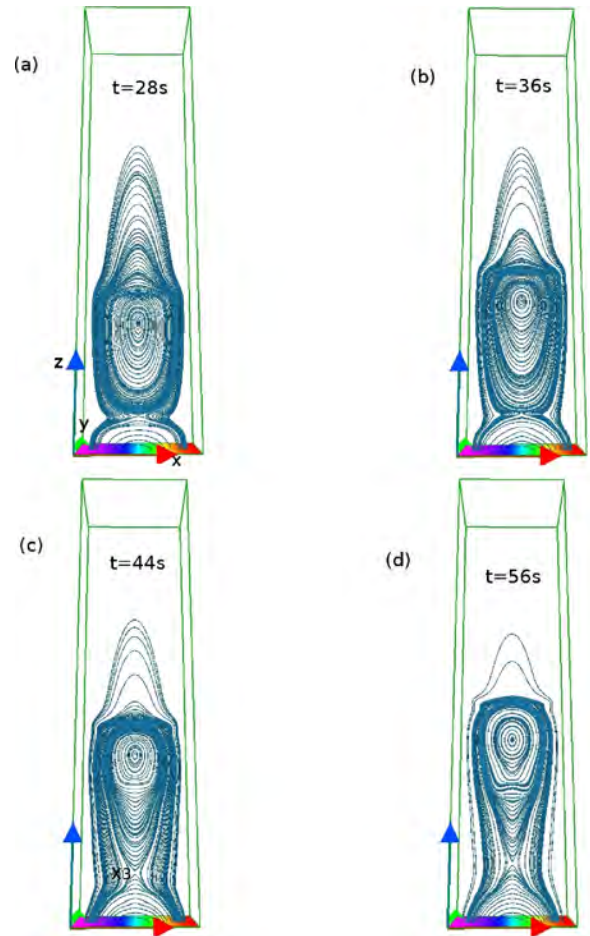


Figure 14: Evolution of MFLs projected on a y -constant plane where the rope corresponds to an island. The repeated MRs increase MFLs in the rope and enable its rise. Important is the onset of a X-type null (illustrated by X3) while the bottom portion of the rope develops a dip (panel (c)). Also, the X-point moves upward along with the rope (panel (d)).

In Figure 14 we plot the evolution of the island for time instances $t = 30s$, $t = 40s$, $t = 50s$, and $t = 55s$. Notably, the MRs beneath the island increase the number of MFLs constituting the island. Also, the outflow generated by these repeated MRs lifts the island center along the vertical. Noticeably, the repeated reconnections reduce the pressure beneath the rope. The neighbouring MFLs are then stretched into this pressure depleted region, from all sides, rendering the rope to be dipped at the bottom portion. In

addition, fully three dimensional (3D) simulation is also performed to verify the robustness of repeated spontaneous MRs in creation and ascent of a rope accordant to a more realistic evolution (Figure 15).

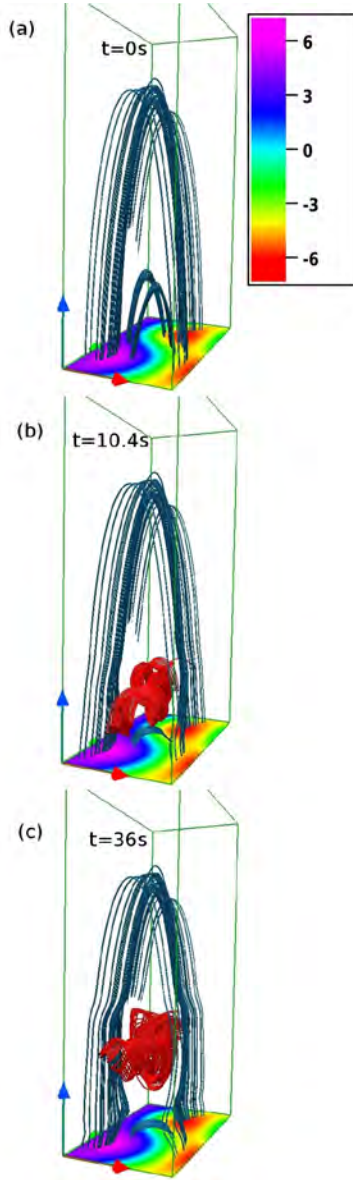


Figure 15: Panel (a) depicts the MFLs of the 3D field. Notable is the curved PIL. The evolution of MFLs (panel (b)) shows the formation of the rope via repeated MRs. The lines in red marks the rope. Noticeable is the ascent of the rope (panel (c)).

With the ascending flux ropes having underlying reconnections in agreement with the standard flare model, the reported simulations identify spontaneous repeated MRs as the initial driver for the rope formation and triggering its ascent. Further, the simulations underline that MRs play an active role in the feedback mechanism between flux rope dynamics and reconnections, central to the standard flare model. This is in harmony with contemporary observations.

This work is being done in collaboration with P. K. Smolarkiewicz.

(S. Kumar, R. Bhattacharyya, and B. Joshi)

A viable non-axisymmetric non-force-free field to represent solar active regions

A combination of analytical calculations and vector magnetogram data are utilized to develop a non-axisymmetric non-force-free magnetic field and assess its viability in describing solar active regions. For the purpose, we construct a local spherical shell where a planar surface, tangential to the inner sphere, represents a Cartesian cutout of an active region. The magnetic field defined on the surface is then correlated with magnetograms. The analysis shows that the non-axisymmetric non-force-free magnetic field, obtained by a superposition of two linear-force-free fields, correlates reasonably well with magnetograms.

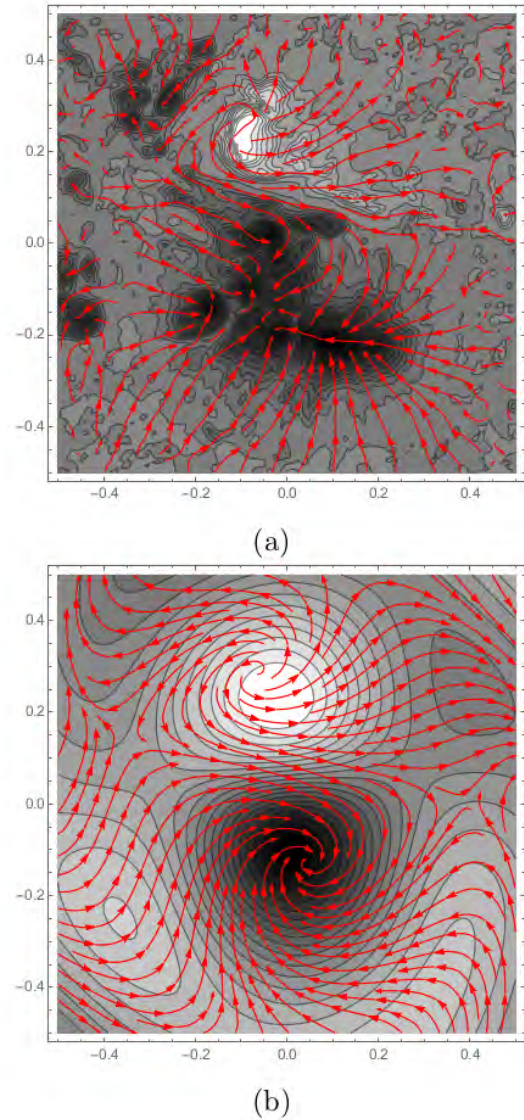


Figure 16: Vector magnetogram for AR 11283 on September 7, 2011 at 02:00 hours represented using (a) observational data from SDO/HMI and (b) the best-fit non-axisymmetric non-force-free case.

A representative case, the vector magnetogram of active region (AR) 11283 as observed on September 7, 2011 at 02:00 hours represented

using data from SDO/HMI and the best-fit non-axisymmetric non-force-free case are shown in Figure 16, where the contours represent the strength of the vertical magnetic field and the streamlines depict the horizontal components.

(A. Prasad, R. Bhattacharyya)

Magnetohydrodynamic modeling of solar coronal dynamics with an initial non-force-free magnetic field

The magnetic fields in the solar corona are generally neither force-free nor axisymmetric and have complex dynamics which are difficult to characterize. Here we simulate the topological evolution of solar coronal magnetic field lines using a magnetohydrodynamic model. The simulation is initialized with a non-axisymmetric non-force-free magnetic field that best correlates with observed vector magnetogram of solar active regions. To focus on the ideas, simulations are performed for a flaring AR 11283 noted for its complexity and well documented dynamics. The magnetic field lines (MFLs) for the best-fit non-axisymmetric non-force-free case are shown in Figure 17.

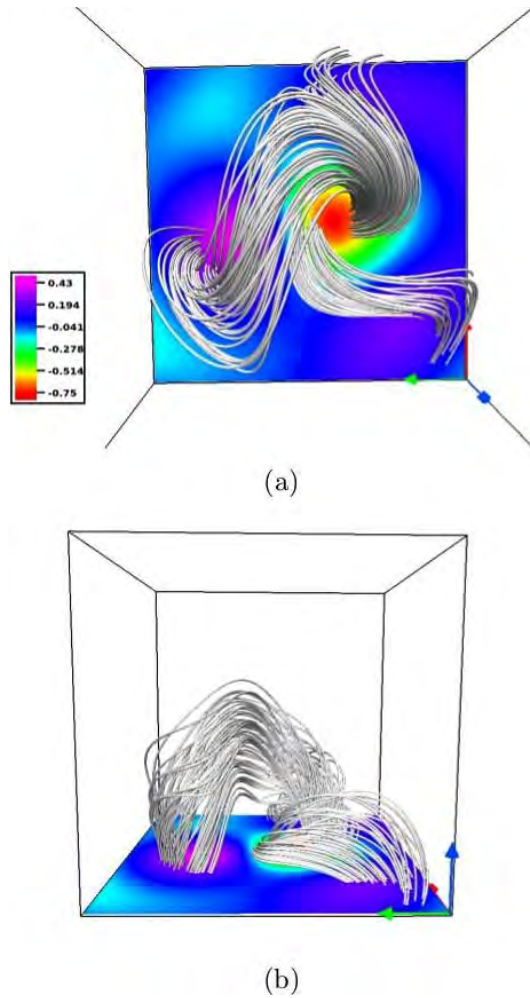


Figure 17: The initial field line topology. Panel (a) and (b) show top and side views respectively. The plots are overlaid with contours of B_z at the $z = 0$ plane. Notable are the presence of two strong opposite polarity regions (located in the central part) along with weak polarity regions (situated at the corners), leading to a complex field line topology. Also, twisted nature of magnetic field lines is evident.

The MFLs connecting the strong polarity regions are twisted loops, having the appearance of a forward S which resemble the sigmoid emission in AR 11283. The simulated dynamics develops as the initial Lorentz force pushes the plasma and facilitates successive magnetic reconnections at the two X type null lines present in the initial field.

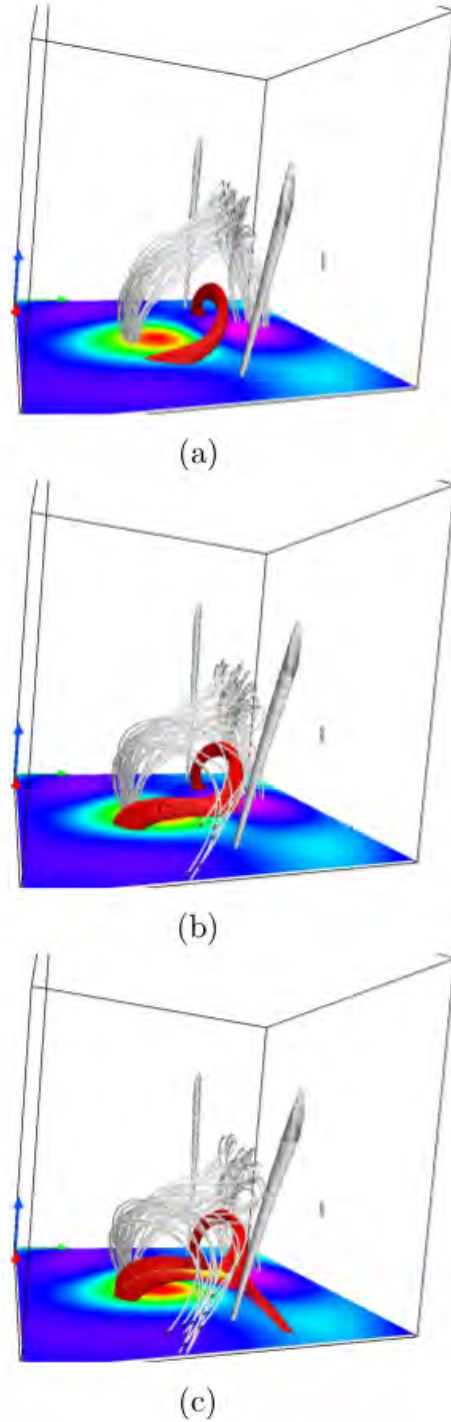


Figure 18: Side view of the evolution and subsequent bifurcation of the flux rope located over the polarity-inversion-line shown at (a) $t = 0$, (b) $t = 1.6$ and (c) $t = 2.2$. We also overlay the figure with overlying MFLs (in color white) and magnetic nulls (in color grey). Important is the reconnections of the overlying MFLs, allowing the ascent of the structures.

Importantly, the simulation allows for a spontaneous development of mass flow, unique among contemporary works, that preferentially reconnects field lines at one of the X type null lines. Consequently, a flux rope consisting of low lying twisted magnetic field lines which approximately traces the major polarity inversion line, undergoes an asymmetric monotonic rise (see Figure 18). The rise is attributed to a reduction in magnetic pressure at the region overlying the rope as resulted by the reconnection. A monotonic rise of the rope is in conformity with standard scenario of flares. Importantly, the simulated dynamics leads to bifurcations of the flux rope, which being akin to the observed filament bifurcation in AR 11283, establishes appropriateness of the initial field in describing active regions.

(A. Prasad, R. Bhattacharyya, S. Kumar)

Estimation of order parameter of a Liquid crystal variable retarder using Haller's approximation

A polarimeter consisting of liquid crystal variable retarder (LCVR) is developed for the measurement of solar magnetic fields using Multi-Application Solar Telescope (MAST). It is known that the retardance (δ) of LCVR depends on the voltage and temperature. Voltage at a constant temperature is used for fast modulation. However, fluctuations in the temperature reduces the accuracy in the polarimetric measurements. In order to improve the polarimetric accuracy, we studied the temperature sensitivity of the instrument. Order parameter (S), which describes various physical properties of the liquid crystals is also estimated using the temperature sensitivity measurements of the LCVRs using Haller's equation i.e., $\delta = \delta_0 S = \delta_0 (1 - T/T_C)^\beta$; where, β is a critical exponent related to the phase transition, δ_0 is the retardance for $S=1$ and T_C is transition temperature.

Using an experimental setup, voltage dependence of retardance of a LCVR is obtained at four different temperatures, i.e., 28°C, 30°C, 35°C, and 40°C. Figure 19 depicts the temperature dependence of the retardance at a fixed voltage 3.967 V (voltage corresponding to quarter wave retardance). The data (temperature Vs. retardance) is fitted to Haller's equation in two ways: one, in which T_C is fixed at a known value of 368 K (provided by the manufacturer of LCVR, M/s Meadowlark optics) for this particular LCVR (fit A) and another in which all the parameters are (fit B) obtained from the fit. Fit A produces larger errors in the estimated parameters (i.e., δ_0 , β). However, Fit B produces better results. Using the derived value of T_C (339.9 K) and the Haller's equation, data shown in the Figure 19 is extrapolated for retardance as a function of temperature at different voltages. As the polarimeter uses voltages in the range of 0-4 V for achieving required retardance, we have shown only these five voltages in the plot.

Critical exponent (β) and maximum retardance δ_0 are also obtained for the voltage range 0-8 V using the Haller's equation with T_C at 340 K. Figure 20 depicts the change in β (top left panel) and δ_0 (top right panel) with voltage along with the 1- σ error bars. Change in β shows larger error at higher voltages. This could be due to the temperature sensitivity of retardance, which is very low at higher voltages. Also β and δ_0 are almost constant in the low voltage regime (0-2 V). Lower panel of the Figure 20 shows the variation of order parameter at different temperatures and voltages and also change in the order parameter with respect to change in temperature.

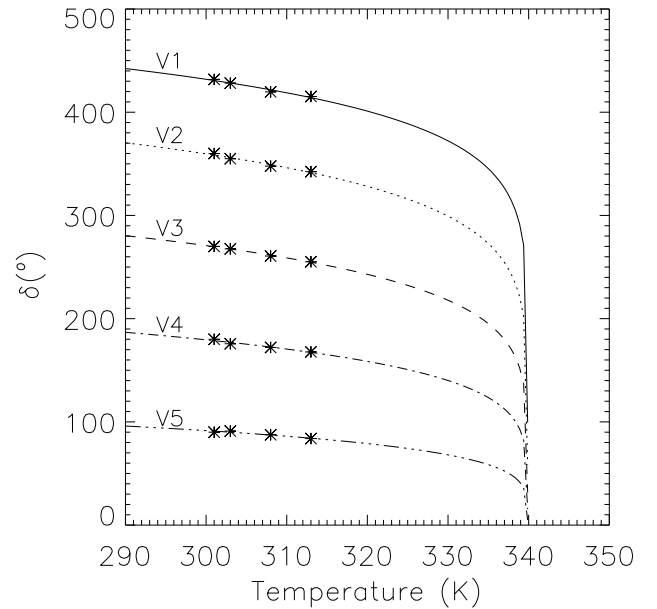
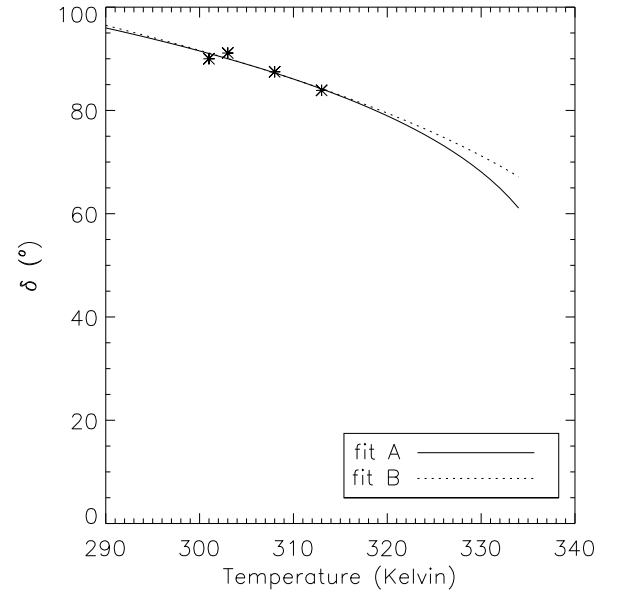


Figure 19: **Top:** Temperature Vs. retardance keeping the LCVRs at a voltage corresponding to quarter wave plate ($V=3.967$ V). Asterisk symbols shows the experimental data and the curves show the corresponding fits using the two methods (Fit A and Fit B). For Fit A, temperature is fixed at 368 K. For Fit B, all the three parameters are varied to fit the Haller's equation. **Bottom:** Retardance versus temperature for different voltages: $V_1=0.0$, $V_2=1.861$, $V_3=2.318$, $V_4=2.918$, and $V_5=3.967$ V at a constant $T_C=352$ K. These voltages corresponds to retardance of maximum, λ , $3\lambda/4$, $\lambda/2$, and $\lambda/4$, respectively.

The estimated order parameter varies between 0.45 and 0.8 for different combination of voltage and temperature and it decreases with increase in temperature as well with the increase in voltage.

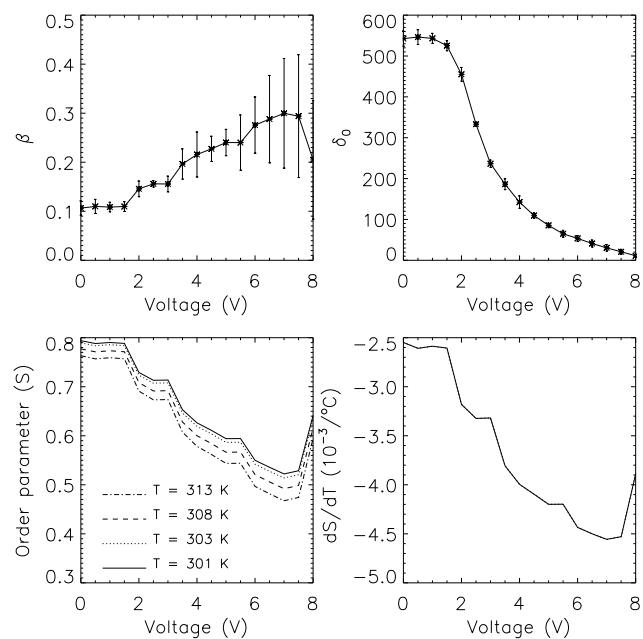


Figure 20: Top Left: Change in critical exponent (β) with voltage. Right: Change in δ_0 with voltage. The error bars corresponding to $1-\sigma$ error. Bottom: Left Change in order parameter (S) with voltage at different temperatures. Right: Change in order parameter (S) with respect to change in temperature.

It also shows that order parameter is more sensitive to voltage or the applied electric field than the temperature. Estimated δ_0 varies from 540 to 0 degrees with increase in voltage. This could be the reason for the peaks observed in the estimated values of the order parameter.

(A.R. Tiwary, A. Raja Bayanna, and S. K. Mathew)

Science

Planetary Sciences

Meteorite studies Oxygen Isotopic composition of presolar grain

Oxygen isotopic composition within the meteorite section allows identifying of presolar grains and inferring the abundance of the same. Respective isotope anomalies further help in elucidating the stellar origin of the individual presolar grains. In-situ search for oxygen anomalous presolar grains were carried out in two different sessions, using NanoSIMS in non-hydrated lithic clasts in Isheyevo CB/CH carbonaceous chondrite.

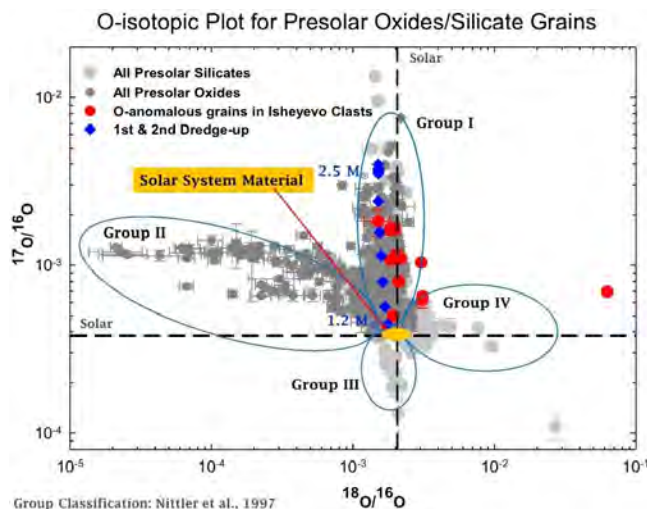


Figure 1: Oxygen three isotope plot of oxygen rich presolar grains (red) found in present study along with silicate grains (light grey) and presolar oxide grains (dark grey) from literature. Grains following group I pattern can be explained with the 1st and 2nd dredge up events of 2.5 M AGB star (blue).

A total of 13 grains were found, indicating a total abundance of presolar oxygen rich anomalous grains (silicate/oxide) of about 38

ppm in the 3 lithic clasts in Isheyevo. Oxygen anomalies can be divided in four distinct groups in the 3-isotope oxygen plot. These groups have characteristic oxygen composition and falls in line with processes taking place in stellar objects. Most of the grains fall in group I that might have condensed in the outer envelopes of RGB/AGB stars. 1st and 2nd dredged up events of an AGB stars are able to explain the present ¹⁷O anomalies indicating a very small change in ¹⁸O for a 2.5 Mstar. Whereas, few grains, have both ¹⁷O and ¹⁸O excesses (group 4). The origin of these grains are kind of uncertain and have been debate to be either (1) low-mass AGB stars in which ¹⁸O produced by helium burning of ¹⁴N during early pulses was mixed into the envelope by third dredge-up or (2) from low AGB mass stars with high metallicity or (3) for the grains with the largest ¹⁸O excesses could be an SN origin if ¹⁸O-rich material produced from partial He burning in the He/C zone can be mixed to material from oxygen-rich zones. Further isotopic measurements could delineate between these three options.

(Marhas K. K and Sanghani M.)

Temperature effects on ion implantation in Supernovae environment

The effects of temperature and relative velocities on Cr and Zn ions' implantation in presolar SiC grains generated in the outer envelopes of supernova from the time they condense (~800-1500 days after explosion) till the onset of Rayleigh Taylor phase (few hundred years) have been investigated. We also estimate the concentrations of stable isotopes of these elements implanted into a micron sized grain by constructing an ion implantation model using nucleosynthesis data from KEPLER hydrodynamic code and taking into account the explosion (explosive energy 10⁵¹⁻⁵² J) of type II core collapse supernovae of various stellar masses. Model together with a high accuracy ion target simulator SDTrimSP was used to calculate the amount of Cr and Zn ions implanted at various

depths for a micron sized grain at temperatures of 300K, 1200K and 1600K. This model provides the flexibility of taking RT mixing and differential zonal velocities as free parameters which are important criteria of supernovae ejecta characteristics. Our calculations indicate central concentrations (in ppm) of 2.8 and 0.2 for ^{52}Cr and ^{64}Zn (relative velocity $\sim 1000 \text{ km s}^{-1}$) for a grain condensed in the mid-He zone of $15.2M_{\odot}$ star, while assuming penultimate zonal mixing as 1% and differential zonal velocity as 2000 km s^{-1} . This is in agreement with the extremely low concentrations observed for trace elements in presolar grains embedded in meteorites. We also find implantation remains fairly independent of temperature (provided $T < 2000\text{K}$) for slow moving ions (velocities $< 2500 \text{ km s}^{-1}$), however, it decreases by as high as 90% for fast moving ions. Interestingly, higher concentrations of these ions are noted for $20.1M_{\odot}$ than for $25.2M_{\odot}$ star, which is a direct consequence of nucleosynthesis yields of the isotopes in question. This hint towards 15-20 M_{\odot} stars being majorly responsible for trace elements generation, however, more massive stars must be studied to strongly support this hypothesis.

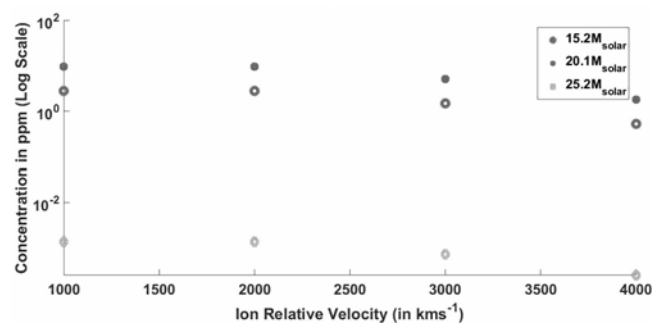


Figure 2: Concentrations of ^{52}Cr (in ppm) at room temperature for $15.2M_{\odot}$, $20.1M_{\odot}$ and $25.2M_{\odot}$ at different ion velocities. A similar, scaled down pattern is obtained for ^{64}Zn as well.

(K. K. Marhas and P. Sharda)

Petrographical and mineralogical diversity between fresh and impact-melted domains in Martian meteorites

Martian meteorites are the only lab-based tool to understand about the impact-related geochemical, mineralogical and structural transformations that could happen on a rock mass at the Martian surface. In this study, two Martian meteorites are used. Tissint, an olivine-phyric shergottite, suffered a prolonged and intense history of impact melting and subsequent re-crystallization, forming high-pressure neo-mineralization and chemical diversity within dominant phases. Shergotty is a basaltic shergottite, which was affected by a severe shock event, causing plagioclase to be converted to dense maskelynite without melting. Foliated texture has been observed in Shergotty. In both cases megacrystic grains are pervaded by fractures. Shock-induced melt pockets are present as patches with the obscured grain boundaries (Fig. 3).

Analyses of major-element compositions of the mineral phases were conducted using a Cameca SX100 electron microprobe at PRL. A few olivine phenocrysts of Tissint preserve an overgrowth boundary (Fig. 3), which separates the inner core and mantle of olivine

(Fo_{80-56}), containing micron to submicron chromite inclusions, to the outer inclusion free Fe-rich (Fo_{55-45}) rim. The most Fe-rich olivines, which occur in impact-melt domains and at the rim of the phenocrystic olivine, range in composition of Fo_{50-18} . The core and inner rim of the phenocrystic olivine (Fo_{80-56}) is devoid of phosphorus zoning, but rims ($\text{Fo}_{\leq 55}$) of the olivine in the shock-induced domains consist of prominent, multiple, oscillatory P-rich bands of 10-15 μm width (Fig. 3). There was heterogeneous distribution of a severe impact pulse, forming features of planar deformation to melting in Tissint. The partial melting perhaps takes into account the contribution of the numerous micron to submicron chromite inclusions in olivine, which re-crystallized more Fe-rich olivine and pyroxene. The Fe-rich rim of the olivine, which consists of a primary magmatic boundary, is not in equilibrium with the Tissint bulk at any stage of crystallization. Minimum cooling-rate estimate yielded values of $< 0.1 ^\circ\text{C/h}$ for the olivine core to inner rim concentration profiles, while that range is $\sim 1.0-5.0 ^\circ\text{C/h}$ for the outer rim overgrowth. These values indicate a significant difference in the time-scale of cooling at three different stages of olivine growth. The oscillatory P-zoning near the rim of the olivine phenocrysts, which cannot be correlated to the Fe/Mg zoning, also reflects a more rapid cooling rate at the late-stage of crystallization for Tissint.

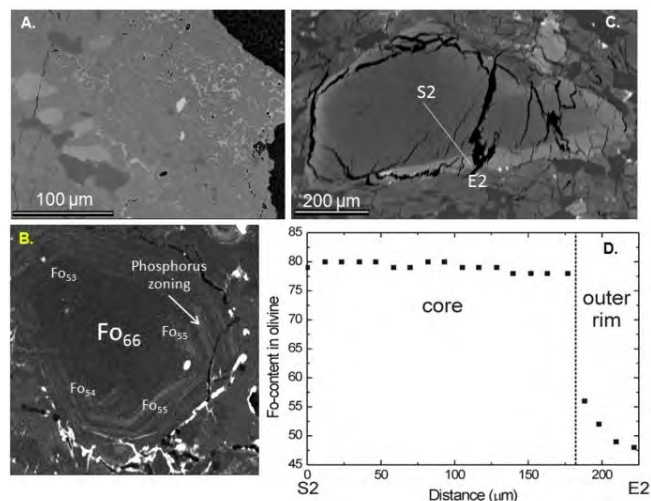


Figure 3: (a) BSE image of impact-induced deformation texture, displaying dendrites of spinel and clinopyroxene; (b) phosphorus X-ray image; (c) Olivine BSE image with prominent overgrowth against core; (d) traverse profile of Fo-content across the olivine in (c).

(A. Basu Sarbadhikari, P. Das, G. Arora)

Bhuka, an ungrouped IAB iron - metallography, noble gas and nitrogen isotopes

We report the chemical, petrological and isotopic studies of the Bhuka iron meteorite that fell in Rajasthan, India in 2005. Numerous silicate and graphite inclusions are visible on the surface of the hand specimen (Fig. 4a). Under BSE images, irregular patches of graphite appear to be the most dominant inclusion type commonly associated with pure corundum (Al_2O_3 95 wt%), spinel, feldspar and often Si-rich phases (Fig. 4b). Apart from typical Widmānstätten pattern,

taenites are also commonly found to occur as a rim of the graphite inclusions. P-rich (up to 10 wt%) taenites are also found locally within the recrystallised kamacite matrix. Based on mineralogy, texture and bulk composition, Bhuka resembles the low-Ni IAB subgroup (ungrouped). Noble gas isotope studies suggest He, Ne and Ar are mostly cosmogenic origin, while Kr and Xe represent mixture of cosmogenic, radiogenic and trapped components. A pre-atmospheric radius of 10 ± 1 cm and a cosmic ray exposure age of 346 ± 52 Ma are derived based on depth dependant $(^3\text{He}/^4\text{He})_c$ and $^{38}\text{Ar}_c$ respectively, following production systematic of cosmogenic noble gas isotopes (Figs. 2c,d). Cosmogenic ^{83}Kr and ^{126}Xe yield production rates of 12 and 0.335 (in 10^{-15} ccSTP/g Ma) for ^{83}Kr and ^{126}Xe respectively. Presence of trapped Kr and Xe, with $(^{84}\text{Kr}/^{132}\text{Xe})_t=2$ and radiogenic $^{129}\text{Xe}=120 \times 10^{-12}$ ccSTP/g are due to presence of graphite/silicate inclusions in the analysed sample. Over 150% excess $^{131}\text{Xe}_c$ than expected from spallation suggests contribution from (n,) reactions from Ba from inclusions and suggests irradiation of pre atmospheric object in a larger body, indicative of complex irradiation. Trapped N of 24 ppm, with $\delta^{15}\text{N} = -10.7 \pm 0.8\%$ of Bhuka, is heavier than the expected range for IAB irons.

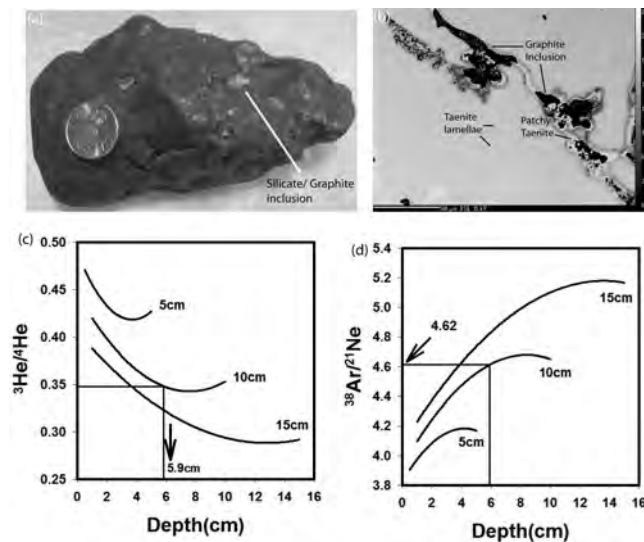


Figure 4: (a) Hand Specimen of Bhuka iron with several inclusions. Diameter of coin is 2.2 cm; (b) BSE image of graphite inclusions with P-rich taenite rim. (c): Depth profiles of cosmogenic ratio $(^3\text{He}/^4\text{He})_c$ have been plotted for objects of radii 5, 10, 15 cm, with Fe, Ni composition of Bhuka. The measured ratio in Bhuka sample, corresponds to a sample at depth of 6 cm, in 10 cm radius object. (d): Depth profiles of cosmogenic ratio $(^{38}\text{Ar}/^{21}\text{Ne})_c$ have been plotted for objects of radii 5, 10, 15 cm, with Fe, Ni composition of Bhuka. The calculated ratio at 6 cm is lower than the measured ratio in Bhuka sample, suggesting partial loss of ^{21}Ne .

(S.V.S. Murty, P.M. Ranjith, D. Ray and S. Ghosh)

Noble gas study in Annama chondrite, a recent fall in Russia

Annama, an ordinary chondrite, is a recent fall in Russia (April 19, 2014). The meteorite fragments were collected immediately after the fall. Noble gases and nitrogen were studied in this meteorite with the objective of finding cosmic ray exposure age, as well as to look for pre-atmospheric size. The sample was analysed by stepwise pyrolysis in order to better recognise and decouple trapped and in situ produced

components. Isotopic measurements were done in 'Noblesse' multicollector noble gas mass spectrometer facility at Thaltej campus. No solar-wind-derived He and Ne was found; therefore, Annama is not a regolith breccia (about 15% of all H chondrites are regolith breccias), nor are there other trapped components present for He and Ne. As regards Ar, a small contribution from a trapped component (perhaps Ar-Q) is present. Kr and Xe are dominated by the Q component (Fig. 5), with a concentration in the typical range of an equilibrated ordinary chondrite. Besides Q gases, there is also a contribution of cosmogenic Kr. A small excess of ^{82}Kr by neutron-induced reactions on Br is visible in the. The neutron-induced Kr excess is very small, either due to very shallow shielding, or the meteorite is a fragment from inside portion of a large parent object (>2 m) before impact on Earth. The second interpretation is in agreement with the high shielding conditions derived from the low $^{22}\text{Ne}/^{21}\text{Ne}$ ratio. The ratio $^{129}\text{Xe}/^{132}\text{Xe}$ of 1.144 indicates excess ^{129}Xe from the decay of now extinct ^{129}I ($t_{1/2} = 15$ Ma) is present in this chondrite.

This work was carried out in collaboration with Dr. T. Kohout of University of Helsinki, Finland.

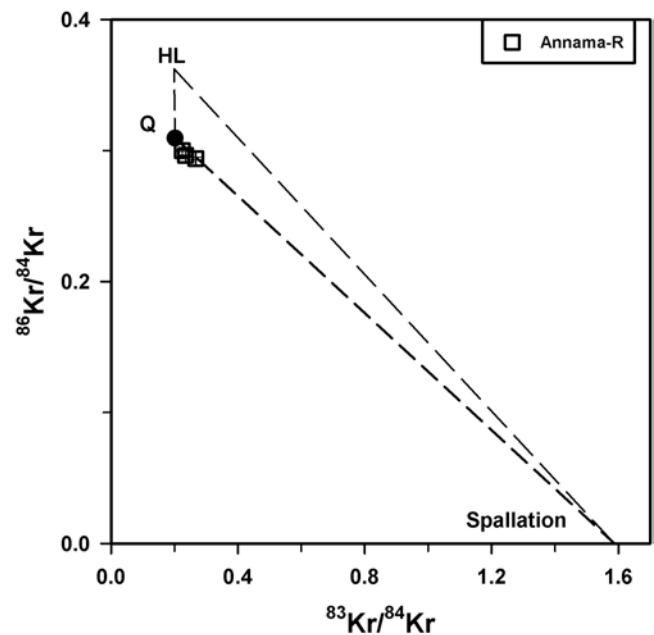


Figure 5: Krypton three-isotope plot for Annama chondrite.

(R. R. Mahajan and Sekhar Naik)

Chondritic impactors on asteroid Vesta: an integrated noble gas and nitrogen study in the Lohawat howardite

We studied nitrogen and noble gases in howardite Lohawat to understand the impactor and interior components of Vesta. Various specific samples like individual grains (impact melt, spherule, and pyroxene), matrix and bulk aliquot are studied for isotopes of nitrogen, noble gas and chemical composition. This helps us to understand the volatile budget of differentiated asteroid Vesta. The nitrogen concentration various samples range from 0.3 to 11 ppm. We obtain trapped nitrogen ($\delta^{15}\text{N}_t$) of +72.5 to -419 ‰ in the grains; -111 ‰ in

matrix-1 and -94.4 ‰ in bulk. The light nitrogen isotopic signature, observed in Lohawat is implanted solar wind or adsorb/intrinsic HL gas component. However, the observed heavy nitrogen isotopic signature can only be explained by a contribution of ^{15}N -rich non-solar nitrogen. A diagram of $\delta^{15}\text{N}$ versus $^{20}\text{Ne}/^{132}\text{Xe}$ ratio is plotted (Fig. 6) to gain further insight into the exact nature of non-solar ^{15}N rich contributor(s). In this figure the end-member components, SW, Q and HL, are also plotted. The areas representing chondrites and achondrites type impactors are shown. Due to the specific ratios of nitrogen in meteorites/impactors, the combined nitrogen and noble gases is used for the identification of the type of impactor(s). Data for various Lohawat samples plot between the regions of chondrites (overlapped area of CM, CV, H, L and LL) and achondrites (angrites, aubrites and IIE), while few data points tend towards solar wind (Fig. 6). Few grains have light nitrogen and plot towards SW indicating presence of trapped solar wind. Some of the grains show having heavy nitrogen composition, therefore they must have been derived from an impactor or the gas has been trapped. The trapped gas was released from an impactor during impact degassing/melting, as Vesta is depleted in ^{15}N . In contrast, ureilites, CO, CR, CI, IAB irons cannot be the impactors of the Lohawat parent mass, as no signature of the noble and nitrogen gases of these chondrites and achondrites are observed in this study. The achondrites, angrites, aubrites and IIE irons can also be excluded because the gas abundance in them is very little than in the chondrites and ureilites. It can therefore be inferred that nitrogen trapped in the Lohawat grains represents a mixture of solar wind (light N signature) and N delivered by impactors (heavy N signature). Therefore, it is suggested that the impactors were mostly CM, CV, H, L and LL type.

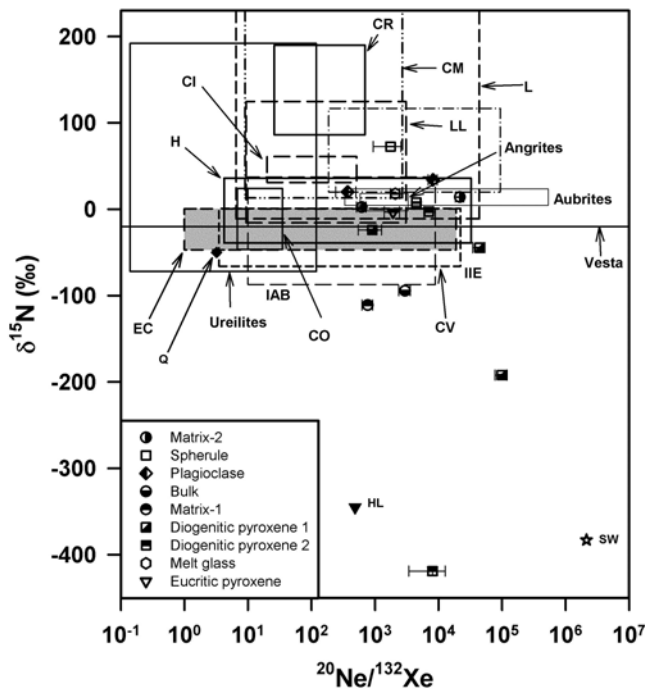


Figure 6: Diagram ^{15}N vs $^{20}\text{Ne}/^{132}\text{Xe}$ depicting data plots of different types of trapped components, and ranges of bulk composition in chondrites and achondrites. Totals of the measurements are plotted for Lohawat samples.

(R.R. Mahajan, A. Basu Sarbadhikari)

Studies on effects of preheating effects prior to IRSL signal measurement in feldspars

Determination of luminescence ages of feldspar grains has been the research focus of several recent studies, particularly since the luminescence signal from feldspar has potential for measuring large doses (kGy). We investigate the source of the IRSL signal in two feldspars obtained from NIST, viz., Standard Reference Material (SRM) 99b (soda feldspar) and K-feldspar SRM 607. For SRM 607, the TL glow curve consists of a several peaks at 95°C , 160°C , 260°C and 340°C . In the soda feldspar SRM 99b, a broad TL peak is observed at temperatures between 140°C - 190°C ; this TL signal is absent in the preheated SRM 99b aliquot, and a TL peak at 300°C is observed in the glow curve. Although IRSL signals from the soda-feldspar SRM 99b indicate no significant depletion at temperatures below 200°C , the pulse anneal data for the K-feldspar sample SRM 607 does show a 30% loss in IRSL while heating upto 200°C . For the natural feldspar extracts considered here (SUN-1-GR and SHRD-1), the equivalent dose value remains constant for preheat temperatures between 80°C - 320°C . It has been previously argued that a single trap (around 410°C) may be primarily responsible for the IRSL signal.

The preheat plateaus from natural feldspar extracts presented here support the conclusion that low temperature TL peaks do not make a significant contribution to IRSL in several feldspar samples. Assuming a water content of 10%, and an alpha efficiency factor of 0.1, the dose-rates for SHRD-1 and SUN-1-GR are estimated to be 3.86 and 5.2 mGy a^{-1} . We observed that the fading-uncorrected IRSL age for SHRD-1 is 19 ka, and is more than twice than the quartz age ($8.5 \pm 0.7 \text{ ka}$) obtained using a modified SAR procedure from this sample. However, the quartz extracts exhibited large IR intensities after laboratory irradiation; hence further work, including a fading test on the quartz extracts used in the previous study is necessary to confirm the validity of the existing ages.

(D. Banerjee, D K Panda and S Sharma)

Modelling of Planetary Atmospheres

Characteristics of solar- X-ray flares and their effects on the ionosphere and human exploration to Mars: MGS Radio Science Observations

Responses of solar X-ray flares were observed in a layer of the Martian ionosphere at altitudes of $\sim 110 \text{ km}$ from 35 electron density profiles obtained by radio science experiment onboard Mars Global Surveyor during solar cycle 23. Of the 35 profiles recorded during flare periods, 10 were associated with X-class flares, 13 with M class, 10 with C class, and 2 with B class flares. Their flare E-peak densities vary with solar X-ray flux, Solar Zenith Angle (SZA), Solar Longitude (Ls), Universal Time (UT) and latitude. Ionospheric Electron Content (IEC) and E-peak electron production rates of these flare profiles are estimated in the E region ionosphere. We found a maximum increase of $\sim 200\%$, $\sim 140\%$, $\sim 90\%$ and $\sim 20\%$ in the time series of IEC for X, M, C and B-class flares respectively. These increases are compared with the percentage increases in GOES flux (see Figure 7a-f). The IEC of flare profiles also increase at high latitude region.

The peak altitudes and peak densities of flare profiles behave like a Chapman layer at high SZA. The dependence of flare E-peak electron production rate with L_s is fitted by a sinusoidal function. We have also calculated biological doses $\sim 0.1 - 1.0 \times 10^{-1}$, $1 - 8 \times 10^{-3}$, $1 - 6 \times 10^{-4}$ and $0.4 - 1 \times 10^{-4}$ Gy for X, M, C and B-class flares respectively to study the human risk for exploration to Mars. Among 10 X-class flares X14.4 is a strong solar flare that gives highest dose, which is potentially lethal for humans.

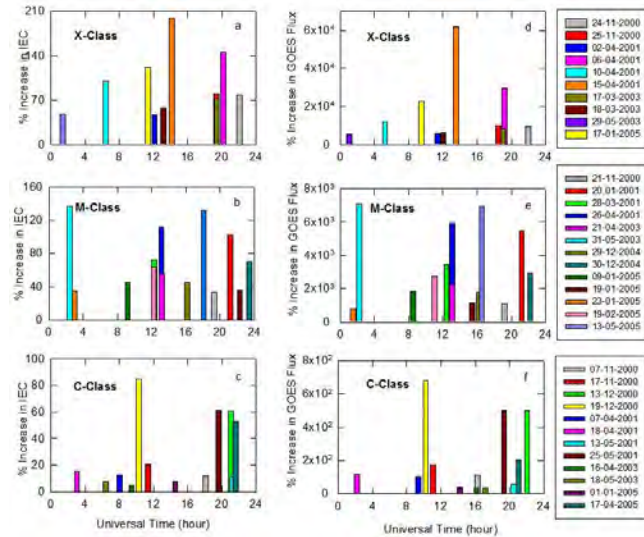


Figure 7: Left panel: The % increase in IEC at different UT for 10 X-class(a), 13-M class(b) and 12-C class (c) flare profiles as observed by MGS at peak flare time. Right panel: The % increase in Solar X-ray fluxes at different UT for 10 X-class(d), 13-M class(e) and 12-C class (f) flares as observed by GOES 10 at peak flare time.

(P. Thirupathaiah, Siddhi Y. Shah and S.A. Haider)

STANDARD and Flare Electron Density Profiles in the D and E region Ionosphere of Mars: Comparison of X-ray flare responses on Earth and Mars Ionosphere

Solar X-ray flare responses in E region of Mars' ionosphere were observed from Mars Global Surveyor on 6 April, 2001 and 17 March, 2003. Responses of these flares were also recorded in D and E regions of Earth's ionosphere at College AK (64.9°N, 212°E). We have estimated D and E flare peaks in the ionosphere of Mars for a short time due to hard X-rays (0.5-3Å) and soft X-rays (3-90Å) at 30 km and 100 km with electron densities $4 \times 10^4 \text{ cm}^{-3}$ and $1 \times 10^5 \text{ cm}^{-3}$ respectively.

In STANDARD profile D and E peaks are formed permanently due to absorption of Galactic Cosmic Rays (GCR) and soft X-rays (1-90Å) at 25 km and 110 km with electron densities $1.5 \times 10^2 \text{ cm}^{-3}$ and $8 \times 10^3 \text{ cm}^{-3}$ respectively. D and E peaks of flare profiles increased 1-2 orders of magnitudes than that produced by STANDARD profile. In Figures 6a-d, the flare profiles of electron density, positive and negative ion densities of 6 April, 2001 are compared with the STANDARD profiles of electron density, positive and negative ion densities.

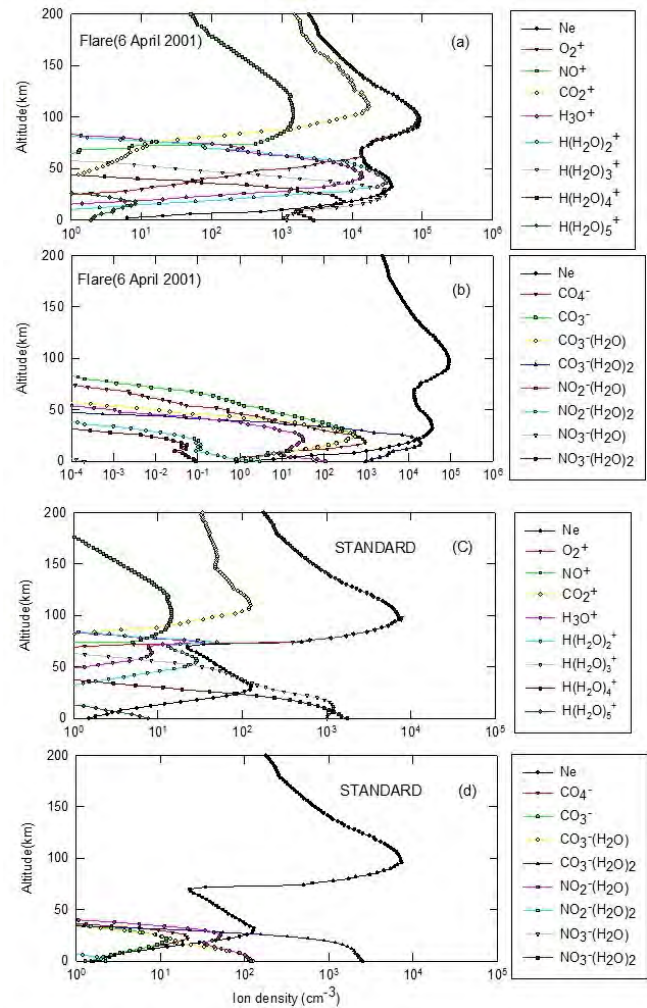


Figure 8: Flare induced positive and negative ion densities for 6 April, 2001 is shown in figures a and b respectively. The estimated altitude profile of electron density at flare time is also shown in these figures. STANDARD positive and negative ion density profiles are plotted in figures c and d respectively. STANDARD electron density profiles are also plotted in these figures.

(S.A. Haider and Siddhi Y. Shah)

Modeling and causative mechanism of OI 630.0 nm nightglow on Earth at Cachoeira Paulista (22.7°S, 45°W) - Brazil: Comparison with OI 630.0 nm nightglow at Mars

The OI 630.0 nm nightglow was observed at Cachoeira Paulista (22.7°S, 45°W) in Brazil by multichannel photometer during the year 2015. The seasonal variation of OI 630.0 nm nightglow is studied. It is found that temporal variation of OI 630.0 nm nightglow intensity shows a peak at post-midnight hours (~ 01.00 hrs) during the summer. During autumn, this peak is shifted towards pre-midnight hours (~ 22.00 hrs). It is noticed that this peak again shifted towards post-midnight hours, 02:30 hrs and 01:50 hrs during winter and spring, respectively. The intensity values increases by a factor of 4 in summer than that observed in other three seasons.

We have also developed a 4-Dimensional Yield Spectrum (4-DYS) model based on Monte Carlo method to compute excitation, loss, emission rates and intensity of OI 630.0 nm nightglow on Earth and Mars at low latitude (22.7°S, 45°W). The estimated intensities are compared with a ground based measurements of OI 630.0 nm carried out at Cachoeira Paulista, Brazil from a nightglow photometer (The nightglow intensity of OI 630.0 nm is not observed on Mars). It has been found that model intensities at Cachoeira Paulista are reasonably in good agreement with the measurements for all four seasons and model reproduces the features of peak intensities very well. The nightglow intensity of OI 630.0 nm on Mars is lower by a factor of 5-8 than that observed by at Cachoeira Paulista, Brazil by a nightglow photometer.

(S. A. Haider and P. Thirupathiah)

Effect of detached dust layers on subtropical lower ionosphere

This southern subtropical region (25–35°S) on Mars is important as many dust storms originate in this region. We study long term variability of dust in this region for 15 years (1999-2014, based on observations by Mars Global Surveyor and Mars Odyssey, and identify three typical seasons with (i) major global dust storms (ii) regional dust storms and (iii) absence of dust storms. For these seasons, we construct altitude profiles of dust aerosols based on recent observations made by Mars Climate Sounder (MCS) on board the Mars Reconnaissance Orbiter (MRO). These observations show an elevated maximum in the dust profiles above 20 km (detached dust layers) in most seasons of southern tropics. We have considered a modified gamma size distribution of dust with r_{eff} and variance ν_{eff} taken as 1.8 μm and 0.3 respectively. Calculations with our PRL one-dimensional ion-dust model show that smaller dust particles have larger effect on the ion densities, which reduce by order of magnitude near the surface in the presence of major dust storms. This is due to the fact that ion loss due to the attachment with dust is large for the particle of small radius. Our model also shows that the conductivity is strongly affected by the dust loading in the Martian atmosphere. ExoMars mission in 2020 will provide an opportunity to observe the Martian environment during dust storms and test our predictions.

(Varun Sheel and S. A. Haider)

Seasonal variation of ozone on Mars and its relation to H₂O, CO and dust

Ozone (O₃) is important in the stabilization of CO₂ in the Martian atmosphere. As hydroxyl (OH) radicals are a sink for both carbon monoxide (CO) and O₃, their correlation is an indicator of the oxidizing capacity of the Martian atmosphere. It is thus important to study the spatio-temporal variability of O₃ and its correlation with H₂O and CO. We retrieve four years of total columnar O₃ from raw spectral data provided by the SPICAM instrument onboard the Mars Express. The seasonal variability is studied in tropical, mid and high latitudes. The high latitudes exhibit the largest seasonal variations in O₃, with a winter high and a summer low. A pronounced anti-correlation with H₂O is seen in the high latitudes. The O₃-CO correlation shows

a hemispheric anti-symmetry, reflecting the importance of photolytic processes. We have used dust optical depth observations by Mars Odyssey to study the correlation of dust with ozone observations from SPICAM. The high correlation observed in southern tropical latitudes in the dust storm year MY 28 during L_s=240° to L_s=300°, indicate towards the radiative impact of dust on ozone or triboelectrical production of ozone.

(Varun Sheel and Ashimananda Modak)

Effect of convection on CO and O₃ during normal and extreme events

Carbon monoxide (CO) and ozone (O₃) are trace gases that play a very important role in the Earth's atmospheric chemistry through their effect on radiative forcing. Their seasonal and vertical distribution is strongly affected by local dynamics. We study the variability of the vertical profiles of these species over Hyderabad, during 2006-2010 using aircraft (MOZAIC) and satellite (TES) observations. Observed profiles that are anomalous with respect to the monthly mean are compared with simulations from the WRF-Chem model run at PRL. The observed profile in winter months is well reproduced by the convection schemes of the model, compared to monsoon. We have also studied the effect of extreme events of thunderstorm and heavy rainfall on CO and O₃ distribution. We identify the convective events through Meteosat-7 observations and various meteorological indices. For these cases of deep convection, we compared WRF-Chem model simulated CO and O₃ with satellite observations. As an example, for the Kedarnath extreme event on June 2013, model results show that the anthropogenic emissions from the Kedarnath basin region contributed significantly to the precipitation. The deep convection has found to rapidly transport high amounts of CO amount in the free troposphere.

(Varun Sheel and Jagat Bisht)

Modelling of High Altitude Dust at Mars

Recently, MAVEN observed dust around Mars from ~ 150 km to ~ 1000 km and it is a puzzling question to the space scientists about the presence of dust at orbital altitudes and about its source. A continuous supply of dust from various sources could cause existence of dust around Mars and it is expected that the dust could mainly be from either the interplanetary source or the Phobos/Deimos. We have studied incident projectiles or micrometeorites at Mars using the existing model. Comparison of results with the MAVEN results gives a new power law size distribution for the incoming dust at Mars.

In addition, the secondary ejecta from natural satellites of Mars can cause a dust ring or torus around Mars and remain present for its lifetime. The dust particles whose paths are altered by the solar wind over its lifetime, could present a second plausible source of dust around Mars. We have investigated escaping particles from natural satellites of Mars and compared with the interplanetary dust flux estimation. It has been found that flux rate at Mars is dominated (~ 2 orders of magnitude higher) by interplanetary particles in comparison

with the satellite originated dust. It is inferred that the dust at high altitudes of Mars could be interplanetary in nature and our expectation is in agreement with the MAVEN observation. As a corollary, the mass loss from Martian natural satellites is computed based on the surface erosion by incident projectiles. Figure 9 illustrates incident projectiles or interplanetary dust coming to Mars.

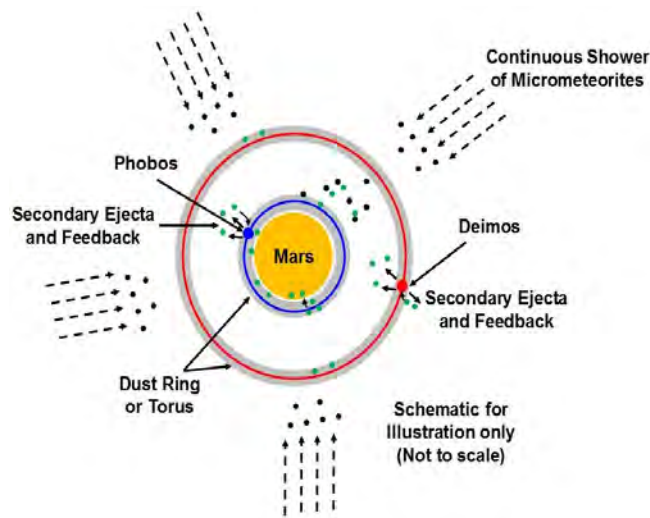


Figure 9: Illustration of incident projectiles or interplanetary dust coming to Mars

(J. P. Pabari and P. J. Bhalodi)

Understanding the Surface Modifications at Landing Site Due To Spacecraft (Soft) Landing on The Moon

In view of the upcoming Indian mission to moon, Chandrayaan-2 which is a soft landing mission, a numerical investigation has been carried out to understand the surface modifications at landing site due to spacecraft soft landing on the lunar surface. This understanding has several implications not only on various mission aspects but also effects science output. The bulk properties of the landing site, especially the upper layer of its regolith, and its physical interaction with the supersonic jet plumes principally determines the possible modifications to the surface. The resulted cratering and consequently ejected particle kinematics provide clues to the physical affects that might have caused to its surroundings. Also, for carrying out in situ measurements, it is important to know beforehand the extent to which the landing site might get altered by the jet plumes. This information is also necessary for planning and properly interpreting the science data from in situ experiments. In the present study, the process of pit formation, its dimensions i.e. depth, volume and area as a function of average grain size, hardness of the dust particles and the ejected dust velocity and mass flux density are derived to understand the surface modifications during lunar landings. The actual engine parameters of Chandrayaan-2 lander and the soil mechanical properties from literature were used in this study. Models of dust ejection from lunar surface were taken from literature and the calculations were carried out using those models. Since, viscous erosion is main mechanism of jet induced crater formation, the resulting dust particle will eject at a very acute angle with respect to lunar surface. The extent of

modification was found to be a function of hovering time. Variation of dust eject velocity and its mass flux density as a function of grain size was also obtained for the simplest case and it has been found that micron size particles can attain eject velocities of 3500 m/s. For large particles with size more than 1 mm, the eject velocity was found to decrease monotonically. The mass flux density for particles with grain sizes in the range of microns is found to be $5.5 \times 10^{-2} \text{ g/(cm}^2\text{-s)}$. The pit profile, i.e. depth, area and volume as a function of particle hardness were also obtained. Further work is needed to account for the assumptions close to realistic conditions which would consequently enhance our understanding of surface modifications during spacecraft landing on lunar surface.

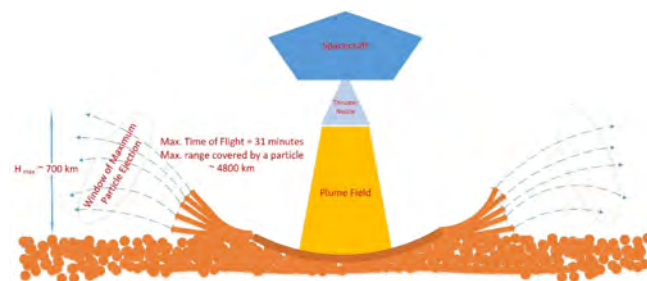


Figure 10: Illustration of dust ejection from lunar surface during spacecraft landing [Not to Scale].

(Sanjeev Mishra, K. Durga Prasad)

Astrochemistry

Sticking of molecules on non-porous amorphous water ice

More than 200 molecules are detected in the interstellar medium (ISM). Many of these molecules are believed to be formed on the surface of interstellar grains, including molecular hydrogen, which is the simplest and the most abundant molecule in the Universe. The accretion rate (R_{acc}) of a given neutral gas phase species i on an interstellar dust grain is given by,

$$R_{acc} = S_i \sigma v_i n_i n_d,$$

Where S_i is the sticking coefficient, a number between 0 and 1, σ , v_i , n_i and n_d is the grain cross-section, thermal velocity, the concentration of the incoming species, and the grain number density respectively. Since the availability of atoms/molecules on the grain surface is dependent on the sticking coefficient of gas-phase species onto the grain surface, it has a profound effect in the synthesis of molecules on the grain surface. In a series of laboratory experiments, the determination of the sticking coefficient of H_2 , D_2 , N_2 , O_2 , CO , CH_4 , and CO_2 on non-porous amorphous solid water (np-ASW) for a wide range of surface temperatures are made using a highly collimated molecular beam. It is found that the following formula for sticking coefficient as a function of grain temperature (T_s) and binding energy is able to fit the experimental data well:

$$S(T_s, E_{LC,i}) = \alpha (1 - \tanh(\beta(T_s - \gamma E_{LC,i}))).$$

Where, α , β and γ are three fitting parameters. $E_{LC,i}$ is the binding energy of a given species i at low surface coverages ($\sim 0.001 \text{ ML}$).

We then used this formula in a simulation code to study its effect on the formation of molecules in the dense interstellar medium. Simulation results using the new data are compared to the results of the simulation using the standard value for the sticking coefficient, 0.5. We find that CO, N₂, and O₂ abundances versus time behave similarly. There is a greater gas-phase depletion of these molecules in the new model than in the traditional one; as a result, their abundance is less in the gas phase. The enhanced freezing of ammonia on grains in the new model due to greater sticking leads to a delay in its destruction when released in the gas phase during the warm-up period. A similar trend is observed for water. Finally, most radicals (especially, CH₃, NH, and NH₂) required for the synthesis of complex organic molecules during the hot core/corino phase have enhanced abundance in the model with the sticking formula.

(This work is done in collaboration with Dr. Jiao He and Prof. Gianfranco Vidali of University of Syracuse)

(Kinsuk Acharyya)

Molecular Complexity in the Magellanic Clouds

Large and Small Magellanic clouds are dwarf irregular satellite galaxies of the Milky Way. Their metallicity is lower by a factor 2 and 5 for Large Magellanic Cloud (LMC) and Small Magellanic Cloud (SMC) respectively. Study of molecular complexity in these clouds, especially, SMC can help us to understand the role of metallicity on the formation of building block molecules like H₂O, CH₄, NH₃, etc. Physical parameters such as, dust temperature, gas to dust ratio, cosmic ray fluxes are also different than our Galaxy which can have a profound effect on the synthesis of molecules in these galaxies. Our simulations show that the cold, dense regions of the LMC and SMC can have a rich chemistry. Most of the major gas-phase species observed in our Galaxy are also produced in both the LMC and SMC although in lower quantities. With our simulations, we are able to explain observed gas-phase abundances reasonably. We have also compared our calculated abundances for selected ices (e.g., H₂O, CO₂) with limited observations in dense regions in front of young stellar objects and found good agreement. We found that for molecules like CO and N₂, which are predominantly formed in the gas phase, their abundances are consistent with the reduced elemental abundances of their constituent elements above 25 K; however, for species that are produced fully (e.g., CH₃OH) or partially on the grain surface (e.g., H₂CO, NH₃), the dependence on metallicity can be complex.

(This work is done in collaboration with Prof. Eric Herbst of University of Virginia)

(Kinsuk Acharyya)

Remote Sensing Data Analysis

Lunar Passive Microwave Remote Sensing Data Analysis

The Moon is known to radiate microwave emission as a grey body, depending on its surface emissivity and physical temperature.

Measurement of lunar brightness temperature can reveal surface properties and thermal behavior, as it is dependent on the surficial material. To understand possible correlation and compare the results obtained from the measured data with those obtained from the theory, we have used the amount of lunar surface material (iron and titanium), measured by the lunar prospector mission, as a first quantity in the analysis. The lunar brightness temperature, measured by a microwave radiometer on Changé-1 mission, serves as the other variable in our analysis. The global maps of lunar surface materials have been generated from the lunar prospector data sets and one such plot for lunar iron and titanium oxides is depicted in Figure 11. A conditional coefficient, representing the correlation between microwave brightness temperature and lunar surface material has been defined, and its analysis has been carried out for the lunar Mare region. Results show that major contribution in brightness temperature comes from lunar regolith density driven component, while a small contribution is made by the lunar surface material. The correlation results disagree with the existing theoretical model used to describe the brightness temperature dependence with surface material. In this connection, a modified permittivity model is suggested for the Mare region, based on our correlation analysis.

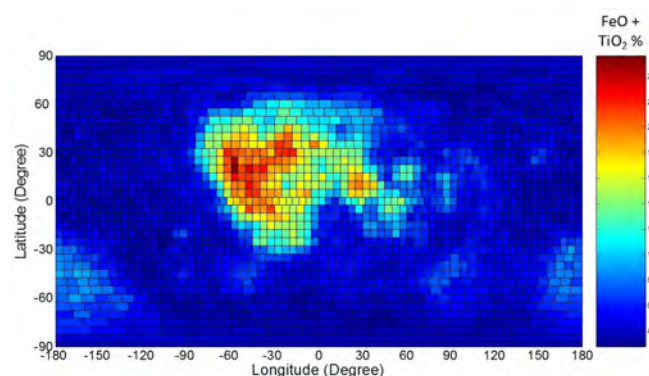


Figure 11: Lunar FeO + TiO₂ cylindrical projection map using lunar prospector data

(J. P. Pabari)

Young Volcanism on the Moon

Our understanding of the volcanic history of the Moon in space and time is undergoing major revisions in view of the recent studies indicating possibilities of very recent volcanism (< 100 Ma ago) in widely distributed areas across the Moon. These include a recently built volcanic field inside the Lowell crater on the far side of the Moon (Srivastava et al., 2011, 2013; Gupta et al., 2014) and several small anomalously fresh mare patches on the near-side of the Moon (Braden et al., 2014). These new findings are hotly debated since their occurrence is not amicably explained by the existing thermal models for the evolution of the Moon. In this study, surface topography and morphology of the Lowell crater formation using Kaguya DTM and LROC-NAC data have provided new evidences supporting the multiple source volcanic proposition for the formation of the unit, as proposed by Srivastava et al., 2013. It has been observed that subsequent to descending down the steeper portions on the Lowell crater wall, the

fluids have covered substantial distances on flat surfaces / surfaces with negligible down-slope on the Lowell crater floor, before moving significant up-slope towards the terminus of the formation (Fig 10). Such a motion of fluids is not possible according to the laws of fluid dynamics therefore the viscous flows present on these topographic highs have to be locally produced volcanic flows.

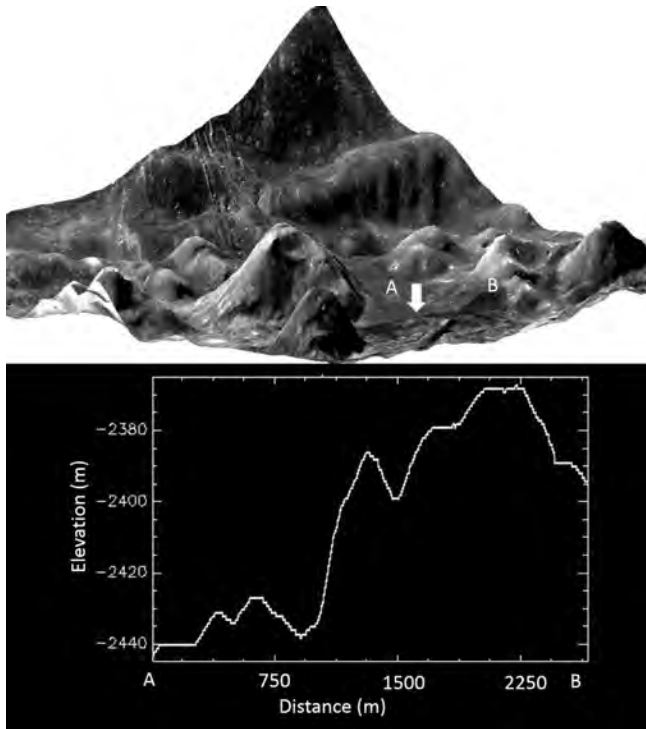


Figure 12: A 3D view and topographic section along AB from Kaguya TC DTM of the Lowell crater formation showing fluids overtopping significant and steep topography subsequent to travelling on almost flat surfaces.

(Neeraj Srivastava)

Debris-flow Gully Landforms on Mars: Implications for Liquid Water

There is growing number of studies using the Mars Reconnaissance Orbiter Context Camera (CTX) and High-Resolution Imaging Science Experiment (HiRISE) which suggests that Martian gullies owe their genesis to seasonal CO_2 frost that persisted infrequently over millions of years. Thus discounted the role of liquid water; hence has implication to the studies that regarded Martian gullies as an evidence for melting and runoff from snow/ground-ice within the past few million years. In the present study, we used the HiRISE images, to investigate the debris-flow landforms that are preserved in the interior of northern mid-high latitude craters. It has been observed that the rim wall slopes of craters contain overlapping terminal lobes and tongue-shaped/lobate deposits, levées, and broad/small depositional deposits. Further, we observed that the source alcoves and the individual debris-flow lobes are dominated by assorted lithoclast assemblages (pebbles and boulders). The textural attributes preserved in the gullies developed on debris-flows suggests that the

features discussed above support a model in which episodic melting of snow accumulated within the sheltered alcoves seems to be the likely source of water. Further, comparison of the Martian gullies with their terrestrial analogue from Ladakh ranges indicate melting of snow accumulated within the sheltered alcoves is a potential mechanism for generating the debris-flow landforms and associated gullies. Thus, from observation of water-bearing debris-flow landforms in the interior of more than ten Martian craters, we tend to suggest that the contribution of debris-flows to the formation of gullies is consequential.

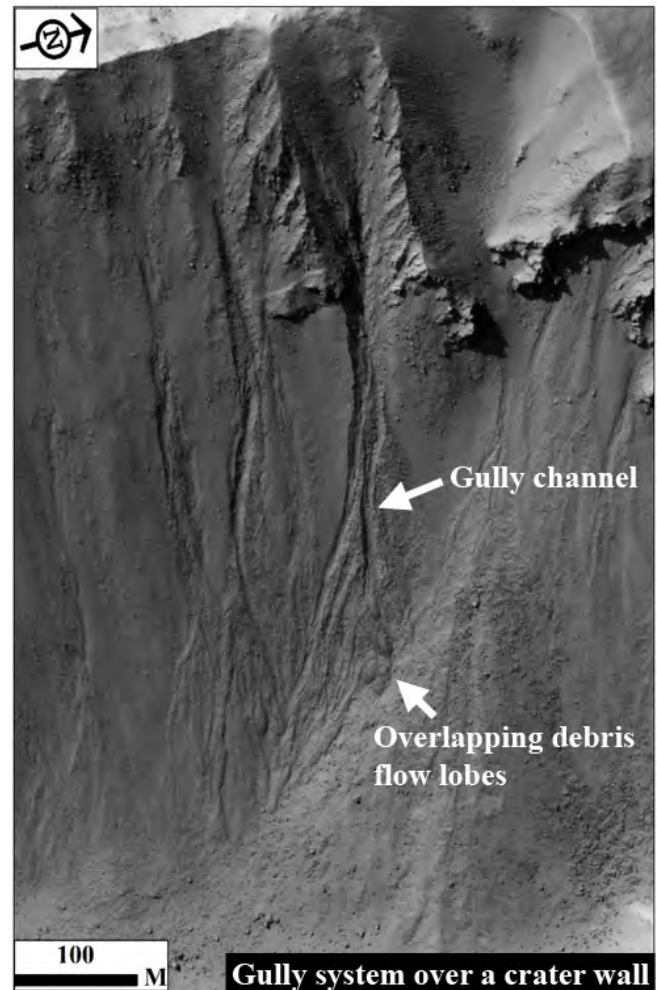


Figure 13: MRO HiRISE based geomorphic evidence of terminal debris-flow lobes at the foot of crater rim wall slopes imply gully formation by water bearing debris flows in the past.

(Rishitosh K. Sinha, Vijayan S., Anil D. Shukla)

Ice-related flow features around Tanaica Montes, Mars: Implications for Late Amazonian debris-covered glaciation

Lobate debris aprons (LDA) and lineated valley fill (LVF) have been broadly recognized in the mid-latitudes of Mars and their subsequent analyses using data from the SHallow RADar (SHARAD) instrument has suggested evidence for contemporary ice preserved beneath

these features. In this study, we conducted detailed characterization of newly identified LDA/LVF units within the Tanaica Montes region (39.55° N, 269.17° E) of Mars to understand the processes that led to their formation. We utilize the Mars Reconnaissance Orbiter (MRO) Context Camera (CTX) images and SHARAD (SHARAD) datasets for geomorphic and subsurface analysis and Mars Global Surveyor (MGS) Mars Orbiter Laser Altimeter point tracks for topographic analysis. Our analysis reveals that: (1) the LDA/LVF units are emplaced with highly integrated pattern of downslope flow, (2) the topographic profile of these flow units exhibit a typical convex-up, steep terminus characteristic, (3) episodic glaciation occurred in the region as suggested by superposed flow features, (4) glacial ice is preserved till today in the subsurface of some of the LDA/LVF units, and (5) the probable period of glaciation within this region is ~ 100 -700 Ma. Together, these observations and the interpretations suggest classical LDA/LVF system preserved within the study region. We infer that the accumulation and compaction of glacial ice in alcoves and along the montes flanks resulted into highly integrated downslope flow patterns that led to emplacement of LDA/LVF units. These results indicate that a widespread accumulation and preservation of ice has occurred on Mars during the Late Amazonian.

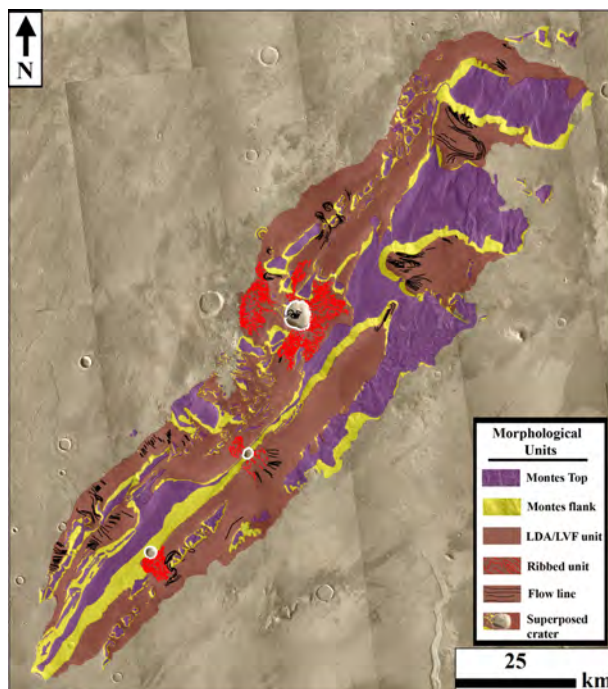


Figure 14: MRO CTX based geomorphologic map of study region. The map illustrates the extent of the different ice-related flow units identified within the study region.

(Rishitosh K. Sinha, Vijayan S., Rajiv R. Bharti)

Fluvial outflow channels in Jovis Tholus region, Mars

Outflow channels are prevalent on the surface of Mars and they are one of the strongest lines of evidence for fluvial activity. They provide the best evidence that great quantities of water once flowed on the surface of Mars. Although channel formation hypothesis is explained

by array of process, but most of the origin consider water as the major source. The purported presence of some of the channel networks on the Amazonian surface provides evidence for recent surficial fluvial activity on the surface of Mars. We describe morphological evidence for fluvial origin channels northwest of Jovis Tholus, within the Tharsis volcanic province. To decipher the fluvial relationships, we examined 1) morphology of catastrophic effusion associated with the graben system superposed over NW portion of an unnamed crater ejecta (19.85° N, 118.03° W), and 2) estimated the tentative period of the fluvial activity.

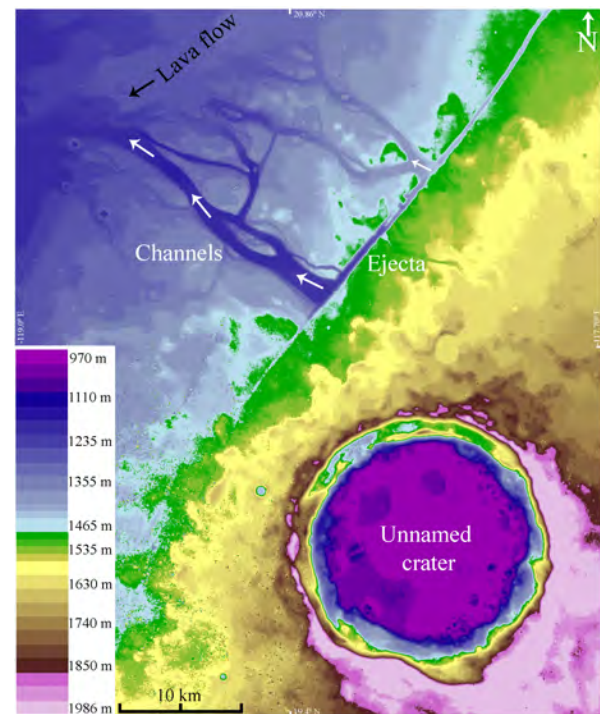


Figure 15: Fluvial outflow channels originate from the graben system and portrays the typical fluvial geomorphic features like streamlined island and braided like channels. The unnamed crater ejecta on the NW side is eroded by the fluvial channels.

Channels, streamlined islands, terraces, divide crossing channels, networks of braided like channels and eroded ejecta are suggestive of fluvial outflow that emanated from the graben. Chronological analysis revealed that the unnamed crater formed at ~ 3.4 Ga. Subsequently, the NW part of crater ejecta was incised by a channel network originating from the graben. The current channel floor has undergone volcanic and aeolian resurfacing to some extent, and the estimated modeled resurfaced channel age is ~ 0.2 -0.5 Ga. This reveals that the fluvial activity possibly occurred after the crater formation, but before channel floor resurfacing, which is during Early-to-Middle Amazonian. However, the potential source for the channel formation likely persisted under this region since the pre-Amazonian epoch. Late Amazonian lava flows occurred outside the channel network has significantly concealed the real extent of the channel networks. The suite of these features within the inferred Jovis Tholus region outflow channel system thus add one another evidence for Early Amazonian fluvial activity and consistent with previous studies that younger Mars supported surficial fluvial activity.

(Vijayan S and Rishitosh K Sinha)

Geomorphological study of a fresh Martian crater "Kotka"

Young impact craters reflect the evolution of the target surface as well as helps document the most recent geological and climatic environment of the Mars. Hence, the study of large, well preserved craters is of utmost importance in establishing better understanding of Martian processes and cratering mechanics. Kotka, a 39.4 km rayed impact crater located at 19.25°N 169.88°E in the Elysium region is one of the youngest example of a fresh impact crater of its size on Mars.

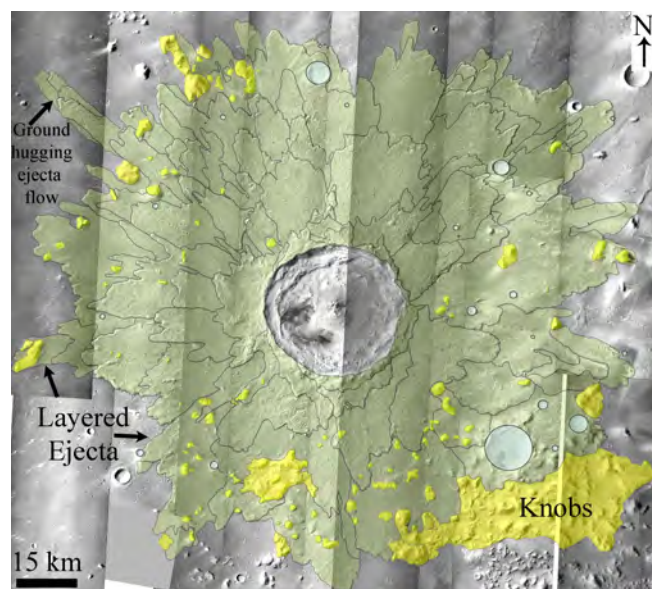


Figure 16: A very fresh Martian craters with pristine multiple layered ejecta, reveals the ejecta emplacement and flow dynamics.

High resolution imagery (25cm/pixel and 6m/pixel) have revealed a plethora of morphologically pristine features such as boulder tracks, clast assemblages, pitted material and banded TAR. The pristine nature of the ejecta morphology in conjunction with formation over the knobby terrain of the Tartarus cones provided a unique opportunity to better understand the ejecta emplacement and flow dynamics. The ejecta mobility obtained for this crater suggested a fluidized mode of emplacement further manifested in the flow of ejecta over and around obstacles suggesting the role of direct emplacement in connotation with ground hugging flow. Mapping at scales of 1:80,000 also revealed the presence of pits within the ejecta blanket and at its periphery interpreted to be secondary craters formed due to the Kotka impact. Emplaced on Late Amazonian volcanic units, Kotka displays a model age of 17Ma (\pm 6Ma) giving rise to the hypothesis of Kotka as a source impact for Martian meteorites. This young age of Kotka given its size is inconsistent with cratering statistics that suggested such an impact takes place only once every few hundred million years, thus demanding a reassessment of the contemporary understanding.

(Ritu Anil Kumar, Vijayan S and Rishitosh K Sinha)

Subaqueous mass-flow deposits at Noachian Terby Crater, Mars

The subaqueous slope and base-of-slope depositional systems are one of the major components of specific sedimentary settings,

where gravity induced mass-flow are the most important transport mechanism and, addition and subtraction of water control the depositional properties. Such underwater flow related deposits are broadly classified into four different categories, i.e. slides, slumps, debris flow and turbidites, and commonly clubbed under subaqueous mass-transport deposits (MTDs).

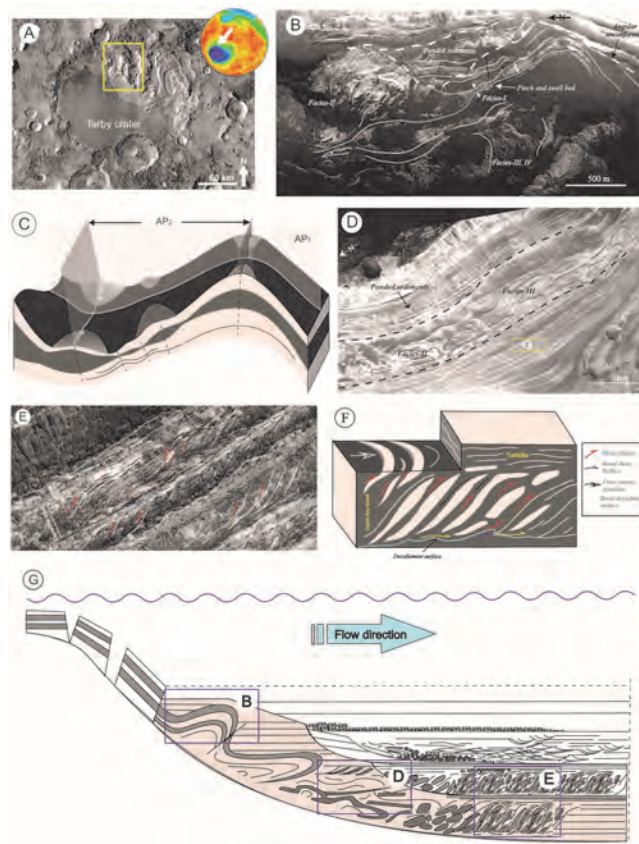


Figure 17: (A) Location of Terby impact crater at the north of Hellas basin, yellow box marked the study area. (B) Folded outcrop of slump deposit located at the basal part of the succession. (C) Conceptual model of the (B) slump unit. (D) Mega-slump unit (marked by dashed line) sandwiched between layered rocks. (E) Successive debris-flow units exhibits imbricated fabric, erosional (sheared) bottom and top bounded by parallel bedded units (high density turbidites). (F) Conceptual model of debris flow unit in (E). (G) Interpreted mass-transport model of Terby.

About 2 km thick Noachian layered succession of Terby crater, located at the northern rim of Hellas basin, is one of the best exposed geological cross sections. The Terby crater has preserved a unique record of subaqueous depositional settings on Mars. Under the present study we have identified a wide range of mass-flow related deposits using high resolution orbital images (Fig. 15). The succession has been subdivided into several litho-facieses and further clubbed under *three* major associations. Multiple episodes of mega slumps, cohesive debris flow, channelized flow, and turbidity flow deposits are the major identified litho-associations in this study. The depositional geometry, internal fabrics, size, shape and mutual associations are been identified. Dominance of compressional deformed sedimentary layers associated with debris flow deposits suggests the basin was initiated under a high energy condition. However, the contradictory occurrence of significant hydrous minerals, previously reported from this area, indicates low energy depositional environment. Based on our observations, we are proposing that the

semi-consolidated materials could be transported from the inter-crater sedimentary terrain of the northern Hellas area and re-deposited, immediately after the Terby impact.

(P. Das, A. Basu Sarbadhikari)

Development of Payloads for Space Missions

Mars Orbit Dust Experiment (MODEX)

To study origin, abundance, flux, distribution and possible seasonal variation of high altitude dust at Mars, a Mars Orbit Dust Experiment (MODEX) is proposed for future Mars orbiter. The additional objective is to measure interplanetary dust particle (IDP) during cruise phase of orbiter for understanding the dynamical evolution.

A prototype design of impact ionization dust detector and its electronics have been initiated at PRL. The preliminary circuit of front end electronics has been designed, implemented and tested successfully. The detector was initially tested using a pulse laser to mimic the dust impact.

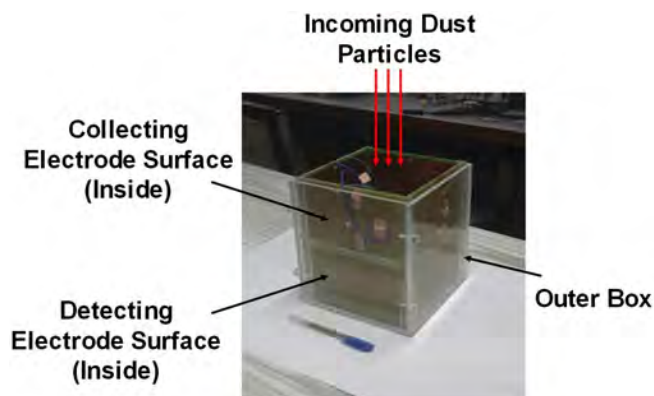


Figure 18: Snapshot of a prototype dust detector.

Figure 18 shows a snapshot of the prototype detector, Figure 19 depicts the ion channel response of the detector, while Figure 20 shows the electron channel response of the detector. Comparing with the calibration of similar detector, the ion channel signal is found equivalent to a dust impact of 239 nm radius particle at 54.5 km/s while the electron channel signal is found equivalent to a dust impact of 398 nm radius particle at 34.5 km/s.

The effect of solar wind particles and GCR on the detector has been computed. It has been found that possible noise can easily be separated from the dust signals by using detector entry screens, high speed data acquisition module and signal coincidence technique for ion and electron channels of the detector along with consideration of neutral channel. Cleanliness requirement for the dust detector has been studied and space qualified material has been identified for further realization of the detector. In parallel, we are exploring PVDF type dust detector for realization of the dust detector. Further work in this direction is underway.

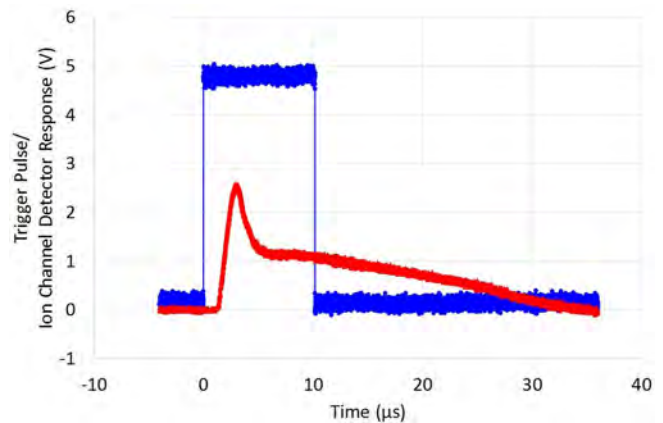


Figure 19: Ion channel response of dust detector after initial testing.

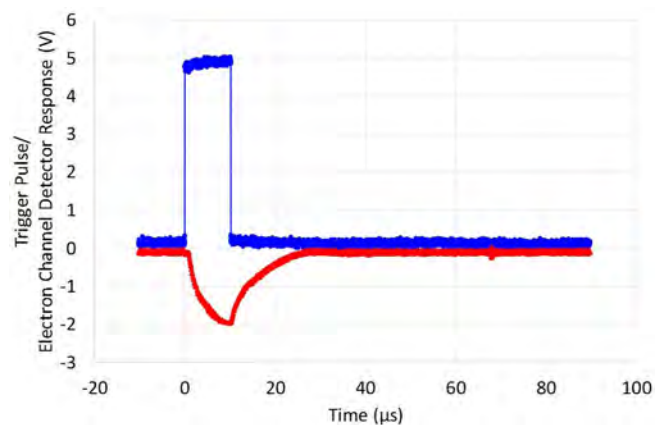


Figure 20: Electron channel response of dust detector after initial testing.

(J. P. Pabari, V. Sheel, K. Acharyya, B. M. Pandya, S. A. Haider, R. Mahajan, A. Kumar, R. Singh, and S. Goyal)

Supra Thermal & Energetic Particle Spectrometer (STEPS) - Subsystem of ASPEX payload

Aditya Solar wind Particle EXperiment (ASPEX) is one of the scientific experiments onboard the Aditya - L1 mission, the first Indian solar mission. The primary scientific objective of the ASPEX experiment is to carry out in-situ, multi-directional measurements of solar wind ions in the energy range of 100 eV/n to 20 MeV/n. ASPEX instrument is configured with two subsystems namely Solar Wind Ion Spectrometer (SWIS) and Supra Thermal & Energetic Particle Spectrometer (STEPS). SWIS will measure the angular and energy distribution of solar wind ions in the energy range of 100 eV to 20 keV and STEPS will measure the energy spectrum of high energetic particles from six directions covering the energy range of 20 keV/n to 20 MeV/n. The scientific objective of the STEPS is to investigate the origin of the supra thermal particles and their relationship with the primary solar wind constituents by measuring the spectrum of protons, alpha and other heavier particles with a narrow conical field of view.



Figure 21: Front end electronics for custom made dual window Si-PIN detector

STEPS subsystem is configured into three packages: STEPS-1, STEPS-2 and processing electronics package. In STEPS, customized dual window Si-PIN detector along with Scintillator detector is used for the species separated spectra. The customized Si-PIN detector is having two detectors on a common substrate. The inner detector (0 mm to 9 mm diameter) has $0.1\ \mu\text{m}$ dead layer of high Z material, while outer detector (9 mm to 18 mm diameter) has $1.0\ \mu\text{m}$ high Z dead layer. The Breadboard model of the developed electronics along with the custom Si-PIN detector is shown in Figure 21. The CSPA is AC coupled amplifier with 2N4416 FET at the input followed by LM6172 operational amplifier. The output of CSPA is further amplified and shaped using shaping amplifier of $3\ \mu\text{s}$ peaking time. The spectrum acquired using ^{241}Am and ^{109}Cd X-ray radioactive sources shows that low energy threshold ($< 20\ \text{keV}$) is achieved using in-house developed electronics, which is essential for the STEPS subsystem.

STEPS uses permanent magnetic assembly (Sm-Co) for the deflection of the electrons. The magnets are shielded using Mu metal to avoid any leakage outside the assembly as well as to create the magnetic path for the field lines. The magnetic leakage test was carried out for the magnet assembly (design1) at LEOS, Bangalore. The magnetic leakage measured at a distance of 40 cm is $< 100\ \text{nT}$. These measurements will be repeated with the latest design (design 2) of the magnetic assembly.



Figure 22: Mechanical model for the STEPS-1 package (without electronics), Size: 290 mm x 155 mm x 124 mm

STEPS-1 package has 4 detector units to measure particles from Sun radial direction, Parker Spiral direction, Intermediate direction

(between Sun radial and Parker Spiral) and Northward direction. The mechanical package for the STEPS-1 is shown in Figure 22. Overall dimensions of the STEPS-1 package are: 290 mm x 155 mm x 124 mm. Similarly STEPS-2 package has 2 detector units to measure particles from Earth direction and Southward direction. The mechanical package is shown in Figure 23. Overall dimensions of the STEPS-2 package are: 157 mm x 160 mm x 136 mm.

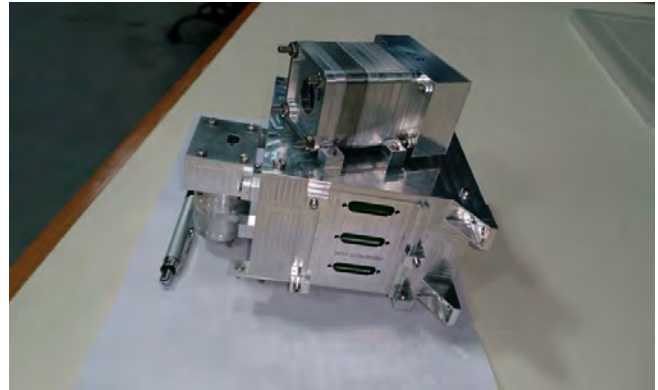


Figure 23: Mechanical model for the STEPS-2 package (without electronics), Size: 157 mm x 160 mm x 136 mm

Preliminary design review (PDR) of the ASPEX was carried out in December 2016. SAC, Ahmedabad is also involved in the development of certain aspects of the payload.

(S. K. Goyal, M. Shanmugam, A. R. Patel, Neeraj K. Tiwari, T. Ladiya, Mithun N. P. S., S. V. Vadawale, P. Janardhan, D. Chakrabarty and A. Sarkar)

Design & development of Hard X - ray imaging detector using Scintillator and Si Photomultiplier

Silicon Photomultiplier (SiPM) is a new development in the field of photon detection and can be described as 2D array of small (hundreds of μm^2) avalanche photodiodes. The Avalanche Photo Diodes (APD) operate in Geiger mode, where the output is independent of the number of incoming photons. The gain of each APD is $\sim 10^5 - 10^6$ electrons. The current flow through the parallel combination of APDs is linearly proportional to the number of incoming photons. SiPM is a linear amplifier device, where the amount of output charge is linearly proportional to the number of incoming photons, as long as these numbers of incoming photons does not exceed the total number of APDs in detection area. We are developing a hard X - ray imaging detector (1D and 2D) using SiPM and new generation Scintillators. This project has been accepted under Technology Development (TDP) program of PRL.

In our experiment, we are evaluating the performance of different types of SiPMs which have different characteristics in terms of dark count rate, biasing voltages etc. We are also using CsI (TI), Plastic scintillators, CeBr_3 and NaI (TI) Scintillators, which are read out using SiPMs. Figure 24 shows the CsI scintillator of size 15 mm x 15 mm x 3 mm which is readout using custom made SiPM array (4 x 4). The results obtained using this combination is shown in Figure 25 which

shows the low energy threshold of ~ 10 keV. The SiPM readout for 4x4 array PCB will also be carried out using ASIC, to have position information of the incident array. The same experiment is planned to be conducted using CeBr₃ scintillator and custom designed SiPM array (6 x 6), which are shown in Figure 24. These 2 different designs will provide the 2D imaging of the incident X-rays.

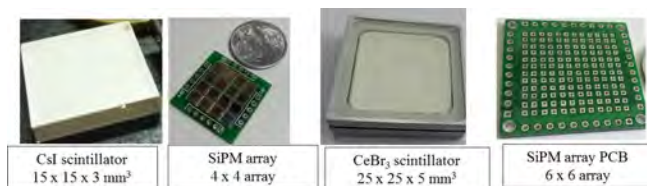


Figure 24: CsI Scintillator, SiPM array PCB (4x4), CeBr₃ Scintillator and SiPM array PCB (6 x 6)

Nal scintillator (100 mm x 20 mm x 5 mm) as shown in Figure 26 (front side) has carbon filter window of ~ 0.2 mm, which has $\sim 70\%$ transmission efficiency at 5 keV. PCB designed for the readout of the SiPM from both the ends of the Nal scintillator is shown in Figure 27. This PCB contains two parallel chains of the CSPA, shaping amplifier (5 poles) and discriminators. The size of the PCB is 105 mm x 25 mm. This design will be used for the 1D imaging of the incident X-rays.

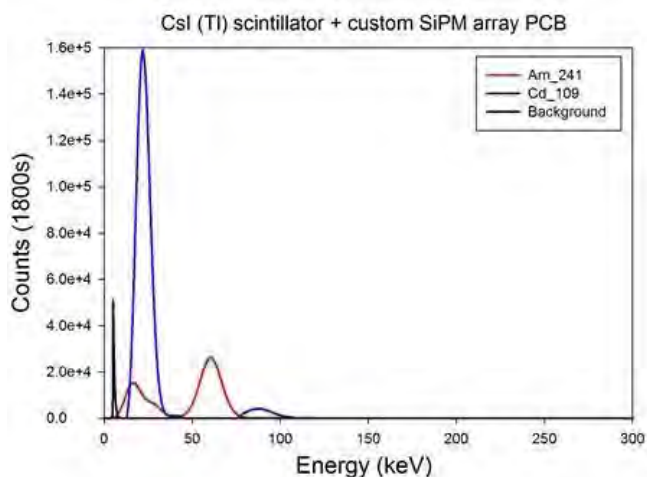


Figure 25: Energy spectrum for the CsI scintillator + custom SiPM array



Figure 26: Nal Scintillator with both sides readout using SiPM (front side)



Figure 27: Nal Scintillator connected with the Front End Electronics (FEE) card (rear view)

(S. K. Goyal, S. Vadawale, Mithun N. P. S., Neeraj K. Tiwari, A. R. Patel, and T. Ladiya)

Alpha Particle X-ray Spectrometer onboard Chandrayaan-2 rover

Alpha Particle X-ray Spectrometer (APXS) is a well proven instrument for quantitative elemental analysis of the planetary surface through in-situ measurements. This technique involves measurement of X-ray fluorescence by irradiating the lunar surface with Alpha particles and X-rays using radioactive alpha source. The objective of APXS instrument is to acquire the spectral response of several soil/rock samples along the rover track in the high latitude south polar region for the major elements giving fluorescent X-rays in the energy region 1 to 25 keV. APXS uses Cm-244 radioactive alpha source which emits both Alphas and X-rays. The energy of alpha particle is ~ 5.8 MeV and the energy of X-rays are 14.3 keV and 18.4 keV. It is well known that the PIXE is dominant for low Z elements while XRF is for high Z elements, allowing the determination of elements from Na to Br, spanning the energy range of 0.9 to 25 keV, for the $K\alpha$ X-rays. We use six alpha sources, each with activity of ~ 5 mCi (total activity of ~ 30 mCi).

APXS instrument is configured as single package and it is mounted in the front side of the Rover with motor based mechanism. APXS is placed in a stowed condition during the launch and also during the rover movement. The motor based mechanism lowers the APXS instrument close to the lunar surface to an height of ~ 50 mm during the measurement. APXS experiment uses Silicon Drift Detector (SDD) to detect the low energy X-rays, which provides very high energy resolution with active area of 30mm^2 with 450m thick. The instrument is designed with stack of two PCBs containing sensitive front-end charge readout electronics followed by analog pulse processing electronics, peak detection, A/D conversion. The design also consists of high voltage bias generation and the peltier controller. The mechanical model of the APXS is as shown in Figure 28. The engineering model of the APXS instrument is completed and tested for the performance requirement. It is shown that the APXS instrument provides the energy resolution of ~ 150 eV @ 5.89 keV when the SDD operated at -35°C . PIXE and XRF measurements were also carried out using Cm-244 alpha source. Several other instrument characterization are in progress. A sample

spectra acquired for titanium target with Cm-244 alpha source inside the vacuum environment is shown in Figure 29. We target to complete the Qualification and Flight Model of APXS payload by July, 2017.

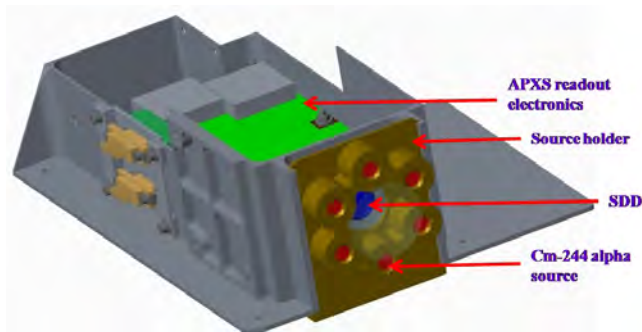


Figure 28: APXS mechanical configuration.

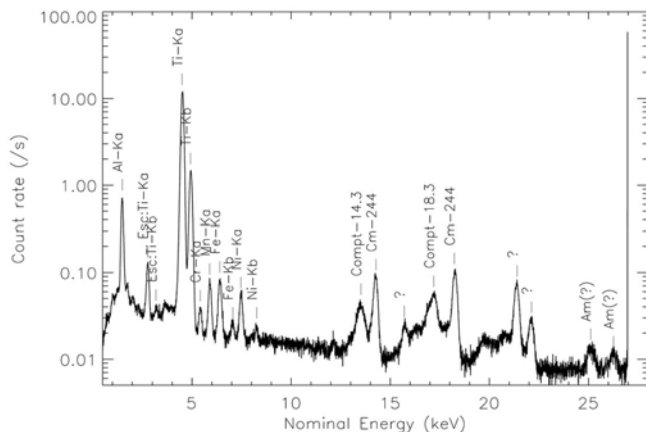


Figure 29: PIXE and XRF measured using Cm-244 alpha source inside the vacuum environment.

(M. Shanmugam, A. Patel, S. K. Goyal, N. P. S. Mithun, Hitesh Kumar, Tinkal Ladiya, Neeraj Kumar Tiwari and S. V. Vadawale)

Investigation of radiation damage due to space radiation on Silicon Drift Detector

Earth is surrounded by extremely intense radiation regions known as Van Allen radiation belts which consists of highly energetic electrons and protons trapped within the Earth's magnetosphere. Such harsh radiation environment is known to adversely affect the performance of X-ray detectors used in the space experiments. Forth coming Chandrayaan-2 mission, the second Indian mission to the Moon will have two X-ray spectrometer experiments using Silicon Drift Detectors (SDD) namely Solar X-ray Monitor (XSM) and Alpha Particle X-ray Spectrometer (APXS). Silicon detectors are sensitive to displacement damage which is due to the Non Ionizing Energy Loss (NEIL) of charged and neutral particles. The displacement damage leads to increase in the detector leakage current and thus degrades the

energy resolution. Hence, it is essential to estimate the performance degradation of the X-ray detector and the spectrometers for its operational period.

The total radiation dose encountered by the SDD is estimated for Earth to the Moon transfer and also for the mission life of one year on the lunar orbit using SPENVIS software suit considering the Chandrayaan-2 launch profile. It is estimated that the SDD will encounter the total radiation dose of ~ 3 krad during its operational period. To quantify the SDD based X-ray spectrometer performance degradation, we carried out proton irradiation experiment at TIFR-BARC Pelletron facility using 10MeV proton beam. Since the direct proton beam is extremely intense, we employed the configuration of the Rutherford scattering experiment, where the incident 10MeV protons were scattered by a gold foil. The SDD module with readout electronics was mounted on a movable platform at a distance of 20 cm with scattering angle of 20 degree. A silicon detector based radiation dose monitor was used to derive the proton fluence and hence the radiation levels received by the SDD. A monitor detector was mounted at an scattering angle of 40 degrees. The experimental setup is shown in Figure 30.

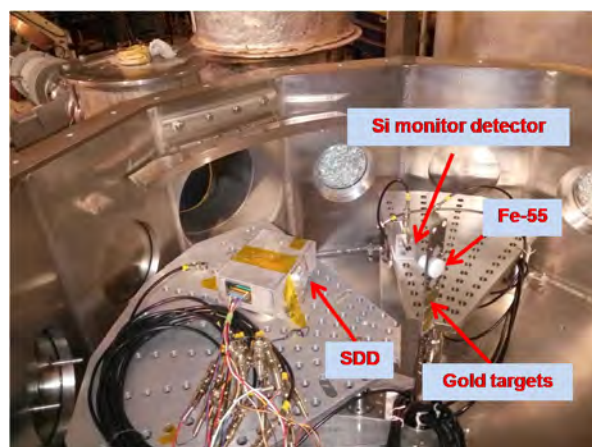


Figure 30: Proton irradiation experimental setup.

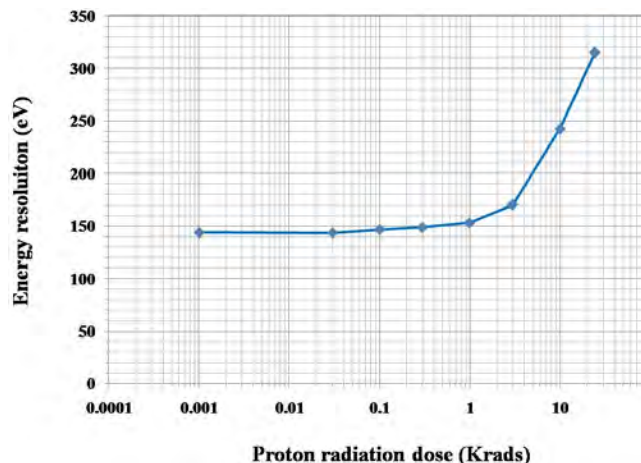


Figure 31: Energy resolution versus proton dose.

The irradiation experiment was carried out in steps of proton doses and at each step, the proton beam was stopped and measured the detector leakage current and the energy resolution. It is shown that there is no significant degradation in the energy resolution for the doses up to 3 krad. The extended irradiation showed the energy resolution degraded from ~ 142 eV at 5.89 keV to ~ 242 eV for the proton dose of ~ 10 krad for the detector operating temperature of $\sim -35^\circ\text{C}$ as shown in Figure 31. The measured leakage current shows systematic correlation with the energy resolution. This proves the concept of using leakage current measured onboard can be used to estimate the X-ray spectrometer performance without using any additional hardware. Use of such technique reduces the mass and power requirement by eliminating the motor based mechanism carrying radio-active source for instrument calibration which is the general practice.

(M. Shanmugam, S. V. Vadawale, A. Patel, S. K. Goyal and Tinkal Ladiya)

Solar X-ray Monitor (XSM) onboard Chandrayaan-2 Orbiter

The primary scientific objective of Solar X-ray Monitor (XSM) onboard Chandrayaan-2 Orbiter is to provide the real time solar X-ray spectrum for quantitative interpretation of lunar X-ray fluorescence spectra measured by a companion instrument Chandra's Large Area Soft X-ray Spectrometer (CLASS). The simultaneous observation of X-ray fluorescence from the lunar surface and the Solar X-rays are essential for quantitative estimation of elemental composition of the Moon. The XSM instrument is being developed at Physical Research Laboratory (PRL), Ahmedabad and the CLASS instrument is being developed at ISRO Satellite Centre (ISAC), Bangalore. XSM will accurately measure the Solar X-ray spectrum in the energy range of 1-15 keV with high energy resolution of ~ 180 eV @ 5.89 keV. This is achieved by using state-of-the-art Silicon Drift Detector (SDD) with precision readout electronics and the combined system having the capability of maintaining high energy resolution at very high incident X-ray rates (up to 10^5 counts per second) expected from the Sun. This instrument also provides high temporal resolution of ~ 1 s.

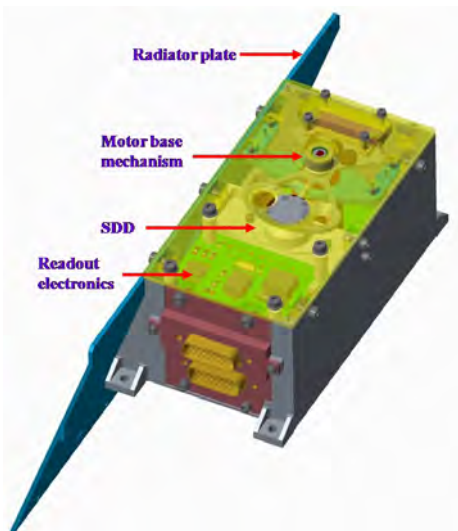


Figure 32: Mechanical model of XSM sensor package.

XSM instrument consists of two packages namely XSM sensor package and XSM processing electronics package. The XSM sensor package houses SDD detector module, analog front-end electronics for charge to voltage conversion, pulse shaping amplified, peltier controller to maintain the stable detector temperature during the payload operation. The mechanical model of XSM sensor head is shown in Figure 32. The solar X-ray intensity is highly variable and can become extremely high. Therefore, the XSM sensor package also has a motor based active energy threshold control mechanism in order to limit the incident count rate at the detector up to 100 kcps during large X-class flares. XSM processing electronics package consists of Field Programmable Gate Array (FPGA) based control & data readout system, DC-DC converters, power switching circuits based on telecommand and driver circuits for the motor based mechanism. The design of engineering model of XSM completed and characterized for the performance requirement, importantly the energy resolution and the peak energy position for higher X-ray incident rates. The energy resolution versus count rate and the peak energy position versus count rate using Fe-55 X-ray source are shown in Figure 33 and Figure 34. The detailed characterization of engineering model of XSM is in progress. We target to complete the Qualification and Flight Model of APXS payload by July, 2017.

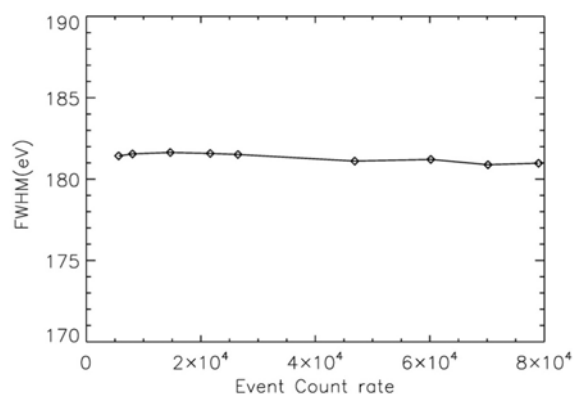


Figure 33: Energy resolution versus incident X-ray rates using Fe-55 X-ray source.

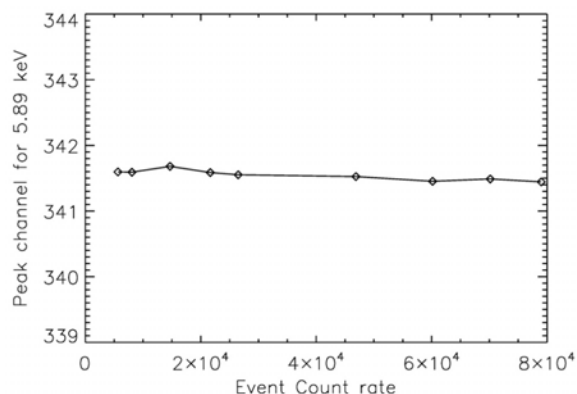


Figure 34: Peak energy position versus incident X-ray rates using Fe-55 X-ray source.

(M. Shanmugam, A. Patel, S. K. Goyal, N. P. S. Mithun, Hitesh Kumar, Tinkal Ladiya and S. V. Vadawale)

Development of Gamma Ray Spectrometer (GRS) using HPGe detector

One of the basic keys to an understanding of the formation and evolution of any planet is the knowledge of the elemental composition of its surface. Gamma spectroscopy for any planet provides a unique opportunity to measure the elemental composition of its surface. We are developing gamma ray spectrometer using High Purity Germanium (HPGe) detector for future planetary missions. The scientific objective of the instrument is to map the naturally occurring radioactive elements (Th, U, and K) and other major elements (Fe, Mg, Cl, Al, Si, S, Mg, Cl) over the entire surface. The GRS will have HPGe as the main detector, surrounded with another HPGe detector working as Anti-Coincidence Shield (ACS) for the background subtraction. The block schematic of the configuration is shown in the Figure 35. This detector is going to be cooled using cryocooler. We have procured the Ricor make cryocooler which is ~ 450 gm in weight and takes ~ 10 minutes to reach to 77 K from room temperature. The photograph of the actual cryo-cooler is shown in Figure 36. This cryocooler will be connected to the off the shelf available HPGe detector, to evaluate its performance.

GEANT4 simulation has been carried out to study the design requirements for a gamma ray spectrometer which includes the selection of the size of HPGe detector, selection of the detector material and thickness for the ACS detector. Figure 37 shows the detector efficiency (absolute efficiency and photo peak efficiency) for 3 different sizes. The photo-peak efficiency for 3 inch (l) x 3 inch (h) is $\sim 45\%$ at 1 MeV and $\sim 12\%$ at 7 MeV.

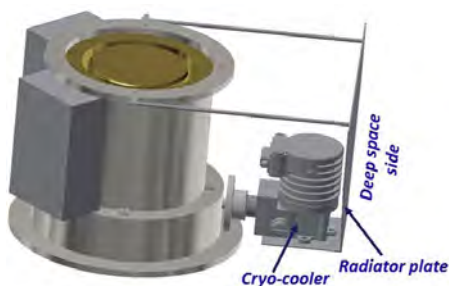


Figure 35: Block schematic of the configuration for Gamma Ray Spectrometer



Figure 36: Ricor make cryocooler

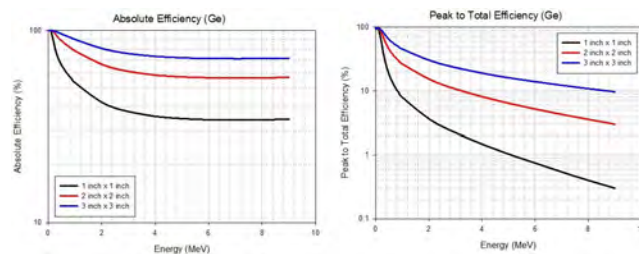


Figure 37: Absolute efficiency and photo peak efficiency of the Ge detector for 3 different sizes.

(S. K. Goyal, D. Banerjee, Dipak K. Panda, Neeraj K. Tiwari, S. Vadawale, Mithun N. P. S., M. Shanmugam, A. R. Patel, T. Ladiya, A. Basu Sarbadhikari and R. Sinha)

Development of a Cerium bromide gamma ray spectrometer for space applications

Elemental composition of a planetary surface can be deduced from in-situ measurements, remote sensing techniques, and by laboratory analysis of returned samples. Gamma ray and neutron spectroscopy comprise some of the basic tools for mapping of planetary surfaces. We are developing a gamma ray spectrometer (GRS) for future planetary orbiter missions for global mapping of U, Th, K, Fe and other major elements on moon and Mars, and the feasibility of using a CeBr₃ detector for measuring individual concentrations of ⁴⁰K, ²³⁸U and ²³²Th in laboratory samples using gamma ray spectra. Since LaBr₃:Ce crystal has a large intrinsic activity which inhibits estimation of the concentrations of Th and K, we next attempted the development of a CeBr₃ gamma ray spectrometer. The energy resolution at 662 and 1274 keV, measured using ¹³⁷Cs and ²²Na radioactive source, are $\sim 4.0\%$ and 2.8% respectively.



Figure 38: Photograph of 1"x1" CeBr₃ gamma ray detector

The linearity curve plotted for the ADC channel against energy fitted with a straight line having a slope (gain) of ~ 0.36 and an intercept (offset) of ~ 4.8 . The intrinsic activity count-rate for the $1'' \times 1''$ CeBr₃ gamma ray spectrometer is ~ 0.03 counts s⁻¹ for the ⁴⁰K energy window (1400-1520 keV), and $\sim 0.003 \sim 0.04$ and ~ 0.001 counts s⁻¹ for the ²³⁸U and ²³²Th (2550-2700 keV) energy window respectively. The intrinsic activity of CeBr₃ shows a much lower activity as compared to the intrinsic activity from LaBr₃:Ce. The U concentration of a sample (3A) from a granite rock was estimated to be ~ 2.1 ppm and agrees with the 2.04 ppm value determined using a HPGe gamma ray spectrometer. The K concentration of sample 3A was estimated to be 3.8% and is consistent with the 3.7%, value determined independently using a HPGe gamma ray spectrometer. The estimation of Th concentration was not possible because of the smaller size of the detector. A CeBr₃ detector having ultra-low background where the intrinsic activity is comparable with that of NaI(Tl), can perhaps be used for precise estimation of concentration of K, U and Th.

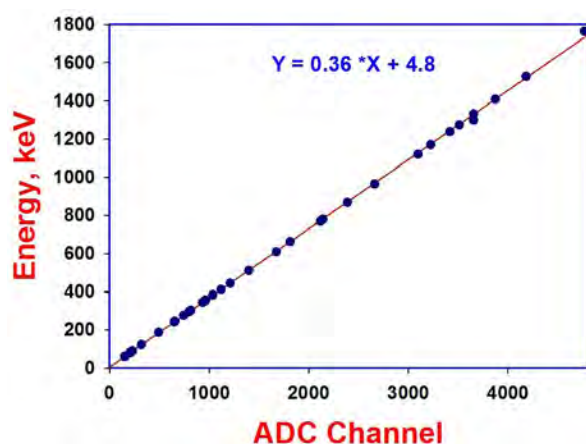


Figure 39: Linearity curve for CeBr₃ gamma ray detector

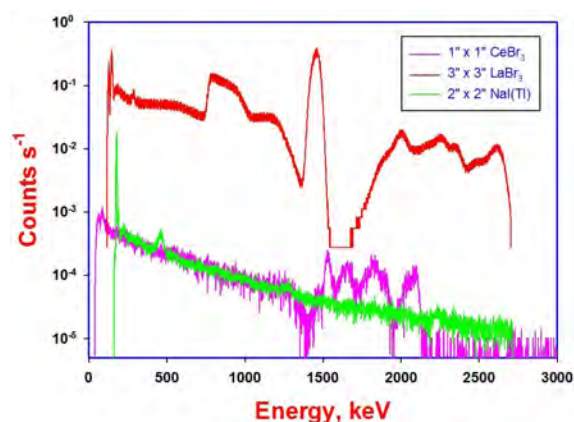


Figure 40: Comparison of gamma ray background spectra from CeBr₃, LaBr₃:Ce and NaI(Tl).

(D. K. Panda, D. Banerjee, S.K. Goyal, A. R. Patel A. D. Shukla and Tinkal Ladia)

Front-End Electronics Development for ChaSTE Payload onboard Chandrayaan-2 Lander

Lunar Subsurface heat flow measurements are often perturbed by external thermal forcing due to solar insolation. Therefore, assessment of present day internal heat flux on the Moon requires precise estimation of equilibrium boundary between external (solar) and internal (due to radioactive decay and accretion) heat fluxes. To address this aspect, PRL Ahmedabad and SPL/VSSC Trivandrum are jointly developing the ChaSTE (Chandra's Surface Thermophysical Experiment) payload that will be flown on Chandrayaan-2 Lander. ChaSTE will measure vertical temperature gradient and thermal conductivity within top 10 cm of the regolith. The experiment will deploy a thermal probe with ten, 4 wire Platinum RTD sensors at the Chandrayaan-2 landing site.

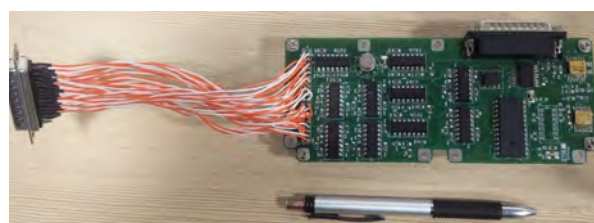


Figure 41: Engineering Model PCB of ChaSTE Front - End electronics



Figure 42: ChaSTE Payload Integrated Testing SPL/VSSC, Trivandrum

The Front-End electronics for the payload is being developed at PRL. The Front -End electronics is responsible for acquiring the sensor data, signal conditioning and digitization of data for further processing by back-end electronics. Based on the landing site constraints, the electronics is designed to measure surface/subsurface temperatures from -175°C to 125°C . The front-end electronics consists of 10 signal conditioning channels, one for each RTD followed by a Multiplexer and ADC for digitization. After undergoing several iterations in the design, the final Engineering model of the electronics has been realized, fabricated and tested. For this purpose, a custom checkout and Processing electronics card was also developed in-house. Figure 41 shows the engineering model of the front end electronics card. After stability and calibration testing at PRL, integrated testing of ChaSTE payload was carried out at SPL/VSSC Trivandrum with Front-End, Processing Electronics, DC-DC convertor and Probe system (Probe,

Heater and Motor). The Figure 42 shows a setup of the Integrated system testing at SPL. The qualification model of ChaSTE electronics is currently under progress.

(K. Durga Prasad, Chandan Kumar, Sanjeev Mishra, Arpit Patel, Tinkal Ladiya, M. Shanmugam, Vinai K. Rai, S.V.S. Murty, C. Suresh Raju and ChaSTE Team, SPL/VSSC)

Development of Calibration and Characterisation Setup for ChaSTE Payload

As part of our ChaSTE payload development for Chandrayaan-2 Lander, a calibration and characterization facility has been setup in our SIMPEX (Simulations for Planetary Exploration) Lab at PRL. This activity will cater to the needs of ChaSTE calibration and characterization aspects right from sensor level upto the overall integrated system. The choice of the sensors while designing ChaSTE was such that its response is expected to be linear in the range of -250°C to 250°C . However, based on the landing site constraints, the expected measurements from ChaSTE on the Moon are expected to be in the range from $\sim -175^{\circ}\text{C}$ to 125°C . The temperature sensor employed in ChaSTE are Pt1000 RTD sensors. In order to calibrate and characterize the full ChaSTE system (Sensor + Probe + Front End Electronics), a dry block calibration facility has been setup that can facilitate calibration from -95°C to 140°C with an accuracy of better than 0.1°C both for sensor as well as the integrated system. To achieve an extreme lower temperature point, a Liquid Nitrogen (-197°C) bath is used. The calibration process is done at three levels: sensor, probe and system. At sensor level, the electronics offset is first corrected by cross-referencing the sensor readings with a standard RTD Calibrator. After this, each individual RTD Sensor is calibrated over the entire range of temperatures. This process provides the coefficients which are then used for online data correction by incorporated them in the code used for the microcontroller. The temperature measurement at random points is then verified using the ChaSTE electronics with reference to a certified, RTD Calibrator. Similar procedure is adopted at probe level. Since the sensors are mounted in the probe in this case, the effect of probe material, design and dimensions are also accounted for. Same procedure is followed for instrument level characterization as well.



Figure 43: Set up for ice point calibration of RTD sensors and FE Electronics

A setup for systematic derivation of thermophysical properties from ChaSTE temperature measurements is also established in this lab. Using these setups, temperatures and thermophysical properties have been estimated for samples of various lunar analogous materials and compared with their known values for reference. The repeatability of measurements was also ascertained. Characterization of samples under simulated lunar environment is currently under progress.

(K. Durga Prasad, Sanjeev Mishra, Chandan Kumar, Vinai K. Rai, S.V.S. Murty)

Thermophysical behaviour of Lunar Analogues under Simulated Lunar Environment

The lunar surface, in particular the upper most porous layer of few cm, exhibiting a complex thermophysical behavior is not well understood so far. The principal reason for this is the inter-dependence of various physical properties and their effect on heat exchange within the medium and the extreme temperature and vacuum conditions of the Moon. Further, when the grain sizes are of the order of few microns and when the environment is hard vacuum as in the case of the top surficial layer (few cm) of the Moon, the soil exhibits an unconventional behavior. Such a behavior has not been systematically studied so far, particularly for lunar soils. Therefore, an effort has been made to systematically investigate this behavior using lunar analogous soils. A chamber that can simulate temperature and vacuum conditions close to that of surface of the Moon has been custom-designed, fabricated and tested. Experiments to understand thermophysical behavior conducted on analogous samples inside this chamber can mimic the experiments as conducted on the lunar surface. For this purpose, the sample with desired material, grain size/stratigraphy under investigation is placed inside a cylindrical sample holder made of Teflon with a copper plate at bottom. Using basalt samples of various grain sizes, experiments were conducted to study the dependence of thermophysical parameters (Thermal diffusivity and Heatflow) on various properties like ambient pressure, grain size, composition, stratigraphy of the sample. The two main compositional rock types present on the Moon are Basalt and Anorthosite. It is important to understand the role of composition on the thermophysical behavior. To this effect, the thermophysical parameters have been measured for Basalt and Anorthosite samples of $250\text{ }\mu\text{m}$ grain size. The temporal evolution of temperatures for basalt and anorthosite samples at four different depths are compared in Figure 44.

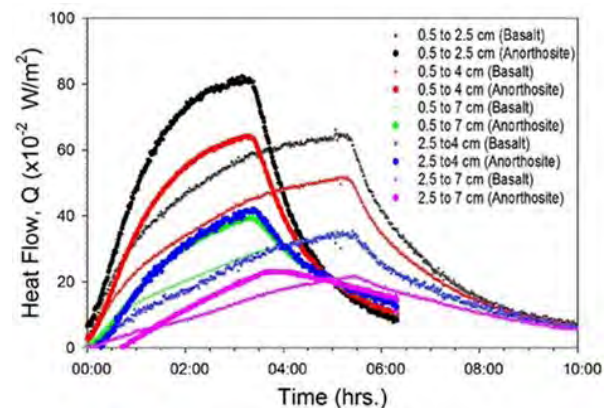


Figure 44: Comparison of heat flow profile for Basalt and Anorthosite samples

It is observed that the temperature rise is faster in the case of anorthosite than that of basalt. Similar trend of higher heat flow within anorthosite sample when compared to that of basalt was also observed. Although the thermal conductivity and specific heat capacities of Basalt and Anorthosites are comparable, the observed trend is puzzling and needs a de-tailed investigation. At this point, it may be assumed that this trend could be due to the arrangement of grains as a result of their shapes (effective contact area). A detailed study is underway.

(K. Durga Prasad, Vinai K. Rai, S.V.S. Murty)

Science

Space and Atmospheric Sciences

Trends in aerosol optical depth over the global oceans

Dust, sea salt and sulfate aerosols produced over the oceans dominate the natural global aerosol abundance, however, dust in the atmosphere could also arise from anthropogenic processes such as construction work, and wear and tear of automobile tires. Similarly, smoke from forest fires is treated as natural component of biomass burning; while the burning of fuel wood, dung cake and agricultural crop waste burning are manmade. Aerosol optical depths over the world oceans during the last 15-years have been analyzed to determine the trends and anthropogenic contribution in different seasons. Percentage change in aerosol optical depths over the Arabian Sea and Indian Ocean during winter is found to be maximum (30%) and the change is significant at 95% confidence level. Percentage change in anthropogenic contribution over the Arabian Sea and Indian Ocean are maximum when compared to the Atlantic and Pacific Oceans.

This work was done in collaboration with Dr. Sumita Kedia, Centre for Development of Advanced Computing, Pune.

(S. Ramachandran)

Spatial and temporal variation in black carbon aerosol over western India region: Role of meteorological dynamics

Black carbon (BC) aerosol loading produces a large radiative impact on climate. Spatial and temporal variability in BC mass concentration are investigated over two distinct locations in western India, namely, Ahmedabad (23.03°N, 72.55°E) (urban industrialized location, 55 m above mean sea level) and Gurushikhar (24.65°N, 72.78°E) (high altitude remote site, 1680 m above mean sea level). The observed BC mass concentrations at Ahmedabad are about a factor of 4-higher than Gurushikhar values. BC mass concentration

exhibits distinct diurnal variability over the study locations (Figure 1).

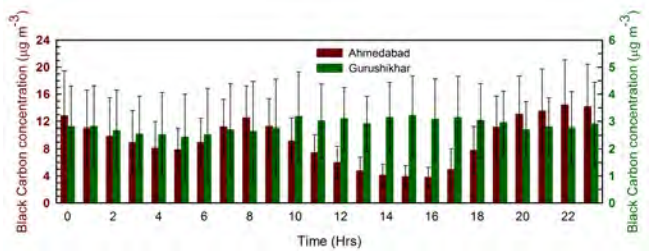


Figure 1: Diurnal variations of black carbon (BC) mass concentration over an Ahmedabad (urban location in western India) and Gurushikhar (a high altitude remote site in western India) during November 2015. Vertical bars indicate $\pm 1\sigma$ variation from the mean.

The BC maximum at Gurushikhar corresponds to the BC minimum observed at Ahmedabad, due to the significant effect of the diurnal evolution of atmospheric boundary layer. During the sunlit time the Earth's surface gets heated which increases the surface temperature resulting in the transport of pollutants from the foothills to the observational location which is in the free troposphere. Gurushikhar BC values can be considered as the representative of the regional background values for the western Indian region. The study highlights the significant role atmospheric dynamics plays in modulating the BC levels in different locations.

(T. A. Rajesh and S. Ramachandran)

Black carbon aerosol concentration from single and double spot aethalometers: Radiative implications

Black carbon (BC) is a primary aerosol emitted directly from the incomplete combustion of fossil fuel and biomass burning. It

strongly absorbs incoming solar radiation and outgoing terrestrial radiation, which have significant implications on aerosol radiative forcing. Aethalometer uses optical technique to measure BC mass concentrations. It collects aerosol particles on the filter continuously and measures the transmission of light through the filter spot. The AE31 aethalometer is a single spot instrument in which significant uncertainty in BC mass concentration arises due to filter loading effect. A double spot AE33 aethalometer is a modified version of AE31 which is used to measure BC mass concentrations along with real time source apportionment. BC mass concentrations measured using a single and double spot aethalometers at an urban location are examined.

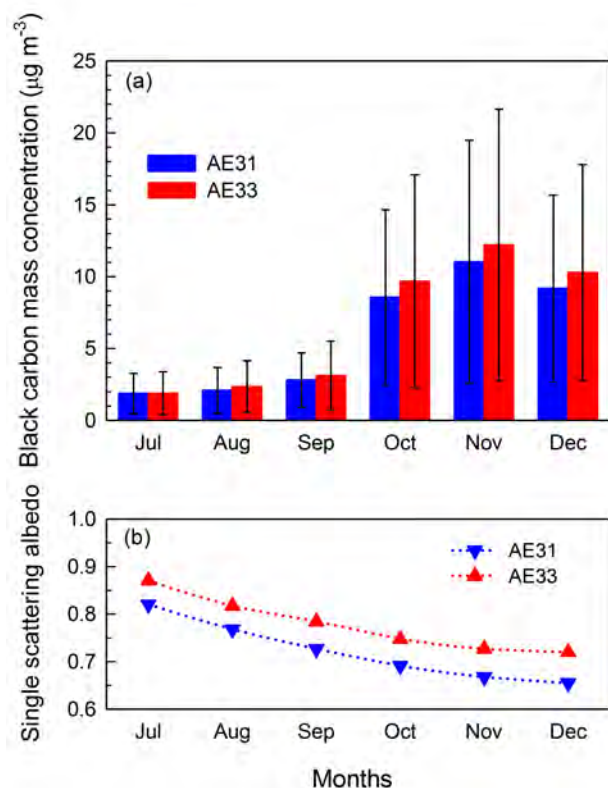


Figure 2: Monthly mean variations of (a) black carbon (BC) mass concentrations and (b) single scattering albedo at 550 nm from single spot (AE31) and dual spot (AE33) aethalometers over Ahmedabad during 2014. Vertical bars represent $\pm 1\sigma$ variation from the mean.

BC mass concentration from aethalometer AE33 are higher than BC measured by AE31 (Figure 2a). BC data from both the aethalometers show a very good linear agreement (correlation coefficient 0.97). Aerosol absorption coefficients are derived from the multi-wavelength BC aerosol absorption data, which along with the simultaneously measured aerosol scattering coefficients using a nephelometer are used to compute the single scattering albedo (SSA). SSA (550 nm) estimated from the double spot aethalometer AE33 is always found to be higher ($\sim 8\%$) than SSA from single spot aethalometer AE31 (Figure 2b). SSA shows a dominant absorption in AE31 as compared to AE33. Estimates of aerosol radiative forcing show that when SSA changes from 0.65 to 0.7 over urban regions the atmospheric warming changes by 10%, while when SSA changes from 0.85 to 0.90 the atmospheric warming changes by 25%. This study emphasizes the

non-linear relation between SSA and aerosol forcing, and that an accurate determination of SSA is important to reduce the uncertainty in radiative forcing estimate.

(T. A. Rajesh and S. Ramachandran)

Aerosol size distribution: Seasonal variability

Size distribution is perhaps the basic aerosol parameter used in determining other properties of aerosols, provided their composition and physical state are known. The seasonal variability in aerosol size distribution measured over Ahmedabad, an urban location using an aerosol particle spectrometer is examined. Aerosols follow a lognormal distribution and show two distinct modes (Figure 3), one each in sub-micron and super-micron radius ranges respectively. The number density and the mode radii of sub-micron and super-micron aerosols are maximum during post-monsoon with values of 243 particles cm^{-3} and 133 particles per cm^{-3} , and 0.42 and 1.7 μm respectively. Aerosol number density is highest during post-monsoon due to lower ventilation coefficient and lower wind speeds. During monsoon aerosol number density is lowest due to the dominant aerosol scavenging by washout. The study illustrates that over an urban region the aerosol size distribution is mainly governed by the relative strengths of different production (emissions) and removal (wet removal) mechanisms.

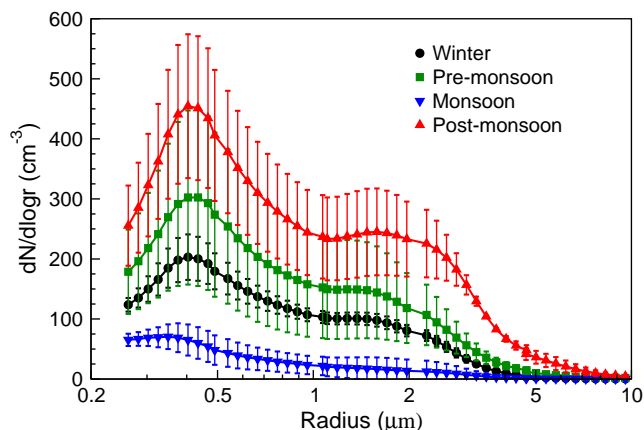


Figure 3: Aerosol size distributions measured using an aerosol particle spectrometer over Ahmedabad. The vertical bars represent $\pm 1\sigma$ variation from the mean.

(S. Ramachandran, A. S. Pipal, and T. A. Rajesh)

Aerosol-cloud interactions over the Indo-Gangetic Basin

Clouds are one of the major factors that influence the Earth's radiation budget and also change the precipitation pattern. Atmospheric aerosols play a crucial role in modifying the cloud droplet number concentration, cloud droplet size and hence cloud albedo. In the present study aerosol-cloud interactions during normal monsoon

years and drought years over entire Indo-Gangetic Basin (IGB), one of the most polluted regions of the world, is investigated. The IGB is divided into six major sub regions based on annual mean aerosol loading. With this objective, fifteen years (2001-2015), daily mean aerosol optical depth and cloud parameters data obtained from Moderate resolution Imaging Spectroradiometer (MODIS) on board Terra satellite are analyzed over each sub region of IGB for monsoon season (June, July, August and September). Results for two regions covering $5^{\circ}\times 5^{\circ}$ latitude-longitude grid of $24-29^{\circ}\text{N}$, $66-71^{\circ}\text{E}$ (R1) and $26-31^{\circ}\text{N}$, $76-81^{\circ}\text{E}$ (R2) which have distinct aerosol emission sources. Figure 4 shows the frequency distribution of aerosol optical depth (AOD) and cloud parameters over both the regions. During drought years a slight increment in higher AOD (>0.6) can reduce the significant contribution of higher cloud fraction (>0.8) over both regions. For liquid and ice phase cloud during drought years, cloud effective radius (CER) decreases over both the regions while liquid water path increases. These results bring out the complexity in attributing the role of aerosols in aerosol-cloud interactions over the Indo-Gangetic Basin.

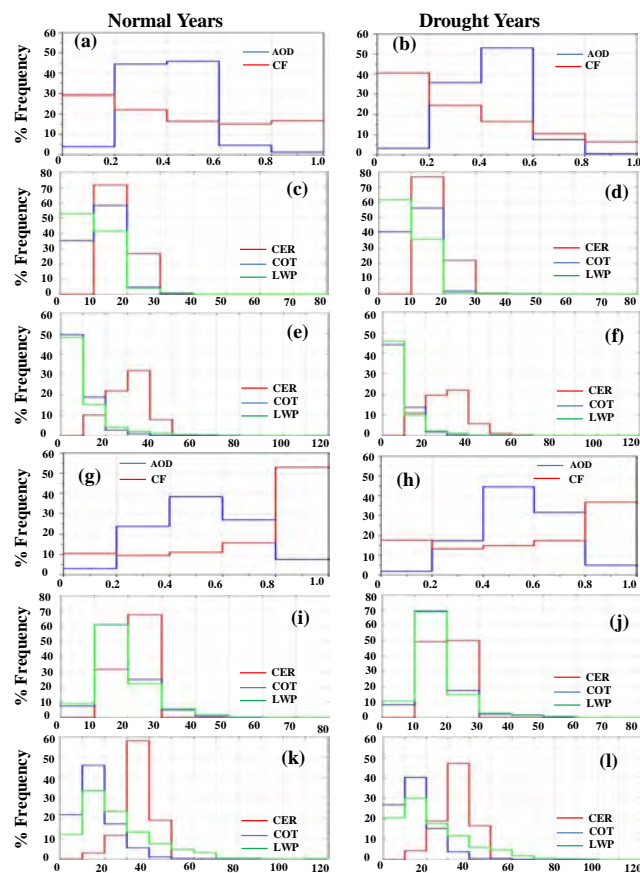


Figure 4: Frequency distribution of aerosol optical depth and cloud parameters during normal and drought years respectively over the Indo-Gangetic Basin for Region 1 (a), (b) aerosol optical depth (AOD) and cloud fraction (CF), (c), (d) cloud effective radius (CER), cloud optical thickness (COT) and liquid water path (LWP) for liquid phase cloud, (e), (f) cloud effective radius (CER), cloud optical thickness (COT) and liquid water path (LWP) for ice phase cloud. Frequency distribution of aerosol optical depth and cloud parameters during normal and drought years respectively for Region 2 (g), (h) AOD and CF, (i), (j) CER, COT and LWP for liquid phase cloud, and (k), (l) CER, COT and LWP for ice phase cloud.

(S. Tiwari and S. Ramachandran)

Impact of biomass burning on trace-gases concentration and aerosol properties

Biomass burning activity is a major source of several of volatile organic compounds, trace-gases and aerosol particles globally. It is a major concern for maintenance of regional air quality and to protect public health. Forest fires, agricultural waste burning and domestic fuel constitute major biomass burning activities over South Asia. In future, one expects changes in all the three sectors of biomass burning. Dryness or wetness future climate will determine whether there will be decrease or increase in forest fires. People may adopt less polluting or more polluting fuels for domestic use depending on changes in their economic status and poverty level. Level of agricultural waste burning will change depending amount of agricultural products needed for industries, to feed the population of world, policy changes and technological advancements that can utilise agricultural wastes.

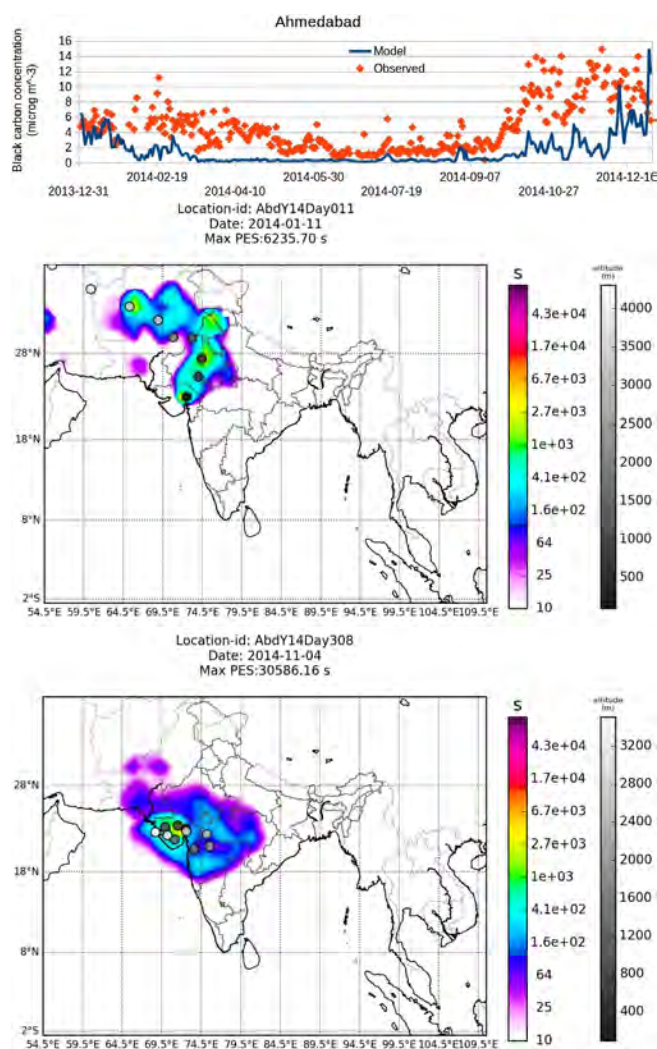


Figure 5: (a) Daily mean values of observed and modelled black carbon concentration over Ahmedabad. (b) Source Receptor relationship with Ahmedabad being the receptor on 11 January 2014. (c) Same as b but for 4 November 2014.

In spite of high importance of biomass burning activities in understanding current air pollution problem and future changes in air quality, very little is known quantitatively due to lack of infrastructure

to monitor biomass burning activities and air quality in remote areas. We have initiated research to address this issue which uses novel technique that combines ground based measurements of black carbon particles, satellite data for detecting fire hot-spots and dispersion model to estimate emissions from biomass burning. The Figure 5(a) shows comparison of black carbon concentration measured at Ahmedabad with the concentration estimated by a dispersion model whereas Fig 5 (b) and (c) show example source-receptor relationship for two days. The difference between model and observation combined with source receptor relationship will be utilised to estimate emission fluxes using optimal estimation method. The estimates will further be constrained with fire hot-spot estimated from satellites.

(H. Gadhavi, S. Ramachandran, and T. A. Rajesh)

Development of remote sensing algorithm to retrieve aerosol properties from Geostationary Satellites

Air pollution is responsible for millions of premature deaths annually world wide. Aerosols constitute major component of air pollution along with tropospheric ozone and oxides of nitrogen. Their monitoring is essential for identifying sources, health risk assessment and designing effective policy for abatement. Wide spread monitoring of pollutants over countries like India is a challenging task and highly expensive. Space based monitoring of air pollution can offer cost effective solution for pollution monitoring. We have initiated research activity to develop remote sensing algorithm that can be used to estimate aerosol optical depth from geostationary satellites. The algorithm will utilise changes in radiation values as function of scattering angle which in turn changes with time of a day. The scattered radiation as a function of scattering angle is described by phase function. Since the phase function of aerosol is significantly different from that of air molecules and surface reflectance, it offers potential means to separate aerosol contribution from that of air molecules and surface reflectance. An advantage of this algorithm will be its ability to estimate aerosol optical depth over bright surfaces which is the case for most regions over land.

(H. Gadhavi and S. Ramachandran)

Contribution of biogenic emissions to ambient VOCs during winter to summer transition period at a semi-arid urban site in India

Measurements of VOCs using a high resolution proton transfer reaction-time of flight-mass spectrometer (PTR-TOF-MS) were made at Ahmedabad city in India during February-March 2014, a winter to summer transition period. Almost all VOCs exhibited strong diurnal, day-to-day and synoptic variations. During the evening rush, levels of VOCs were highest and strongly correlated ($r^2 > 0.70$) with benzene due to predominance of vehicular emissions. Nighttime emission ratios of $\Delta\text{VOCs}/\Delta\text{benzene}$ were used to estimate the relative contributions of vehicle exhaust and other sources. Peaks of acetone and acetaldehyde during forenoon/noon were due to additional contributions from other sources. Daytime fractions of acetone, acetaldehyde and isoprene to the sum of measured VOCs in March were higher than those in February. Similarly, daytime ratios

of OVOCs/benzene and isoprene/benzene increased from February to March due to increasing contribution of photo-oxidation and biogenic sources. Variations of VOCs in the lower temperature regime were mainly controlled by anthropogenic emissions. At high temperatures ($32\text{--}40^\circ\text{C}$), particularly in March, variations of OVOCs and isoprene were determined by biogenic emissions. In addition, levels of VOCs also showed strong sensitivity to change in wind parameters. Contributions of direct vehicle exhaust to OVOCs were small (20-40%) compared to other sources. From February to March, contributions of biogenic/secondary sources to OVOCs and isoprene increased by 10-15% (Figure 6). This study provides clear evidence that the winter to summer transition has an impact on source and composition of VOCs in tropical urban areas.

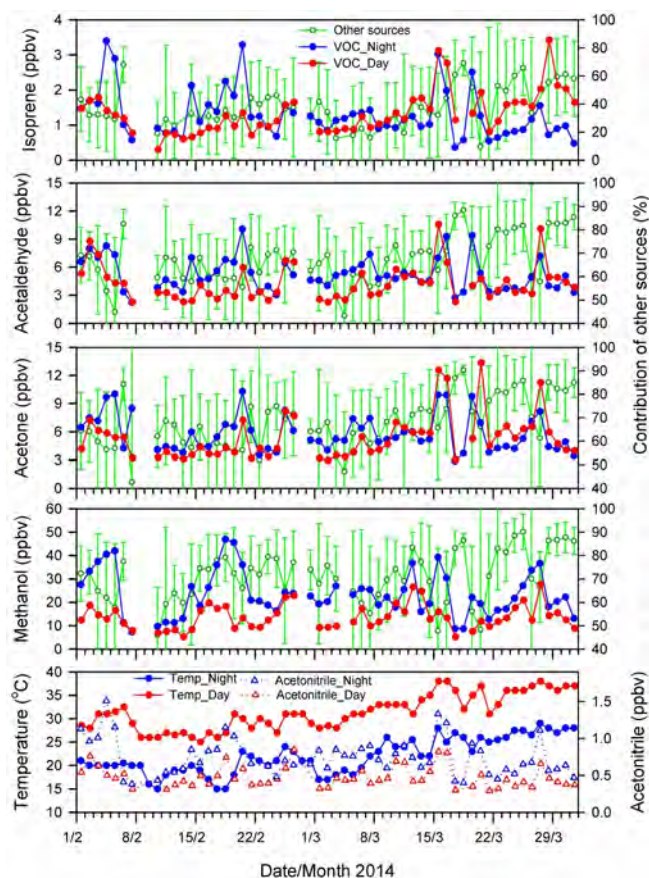


Figure 6: Time series of daytime and nighttime mixing ratios of OVOCs, isoprene and acetonitrile along with contributions from other sources (biogenic, secondary and biomass burning) during 01 February-31 March, 2014.

(L. K. Sahu, N. Tripathi, and R. Yadav)

Seasonal variation of non-methane volatile organic compounds (NMVOCs) at an urban site of Udaipur in western India

Atmospheric non-methane volatile organic compounds (NMVOCs) were measured in Udaipur city of western India during the year 2015. Air samples were collected for analysis of various NMVOCs using a Gas Chromatograph equipped with Flame Ionization Detector

(GC/FID) and Thermal Desorption (TD) system. The main focus is to understand the diurnal and seasonal variations sources of NMVOC and evaluating their role in ozone formation. The mixing ratios of C₂-C₇ NMHCs show peaks during morning and evening rush hours and lowest in afternoon hour. Diurnal dependence of most NMVOC species was influenced by local emission, PBL and photochemical loss with reactions with OH radical. Seasonally, higher mixing ratios of NMVOCs (except isoprene) were observed during winter and lower levels during the monsoon season due to the seasonal change in meteorological, transport path of air parcel and boundary layer conditions. The high levels of propane (C₃H₈) and butanes (C₄H₁₀) show the dominance of liquified petroleum gas (LPG) at the study site. For other NMVOCs, the strong correlations of NMVOCs-benzene suggest that vehicular emission is a predominant source in Udaipur. The PMF analysis suggests that the source factors namely biomass burning/ bio-fuel, automobile exhaust, Industrial/ natural gas/power plant emissions, petrol/diesel, gasoline evaporation, and use of LPG contributes to the loading of NMVOCs. The propylene-equivalent concentration and ozone formation potential of NMVOCs have also been calculated in order to find out their OH reactivity and contribution to the photochemical ozone formation.

(R. Yadav, N. Tripathi, and L. K. Sahu)

Impact of tropical convection and ENSO variability in vertical distributions of CO and O₃ over an urban site of India

The Measurement of Ozone and water vapour by Airbus in-service aircraft (MOZAIC) data of vertical ozone (O₃) and carbon monoxide (CO) over Hyderabad during November 2005-March 2009 were investigated. Measurements in the upper troposphere show highest values of O₃ (53-75 ppbv) and CO (80-110 ppbv) during the pre-monsoon and post-monsoon seasons, respectively. The episodes of strong wind shears (>20 ms⁻¹) were frequent during the monsoon/post-monsoon months, while weak shear conditions (<10 ms⁻¹) were prevalent during the winter season. The profiles of both O₃ and CO measured under southerly winds showed lower values than those measured under northerly winds in each season. The strong and weak wind shears over the study region were associated with the El Niño and La Niña conditions, respectively. The outgoing long-wave radiation (OLR) and wind shear data indicate enhancement in the convective activity from monsoon to post-monsoon period. Higher levels of O₃ were measured under the strong shear conditions, while CO and H₂O show enhancements under weak shear conditions. The near surface observation and simulations show increase of O₃ with increasing OLR, while insignificant relation in the upper region. In case of CO, the MOZAIC and the Chemistry Climate Model (CCM2) show weaker dependence while Model for Ozone And Related Chemical Tracers (MOZART-4) shows rapid increase with OLR indicating large overestimation of convective transport. A modified Tiedtke convective scheme provides better representation compared to the Hack/Zhang-McFarlane schemes for both O₃ and CO during the monsoon season. The difference between observation and simulations were particularly large during transition from El Niño to La Niña phases. The different convection scheme and horizontal resolution in the MOZART-4 and CCM2 seem to be the major causes of disagreement between these models.

(L. K. Sahu and V. Sheel)

An estimation of losses of crops of wheat and rice in India due to surface level ozone

Surface ozone is mainly produced by photochemical reactions involving various anthropogenic pollutants, whose emissions are increasing rapidly in India due to fast growing of anthropogenic activities. Higher levels of surface ozone can damage various crops. Measurements of surface ozone and related species are being made at 15 stations in India under the project Atmospheric Trace gases-Chemistry, Transport and Modelling (ATCTM) of ISRO-GBP. A study has been done to estimate the losses of wheat and rice crop yields using surface ozone observations from this network covering different parts of India. We used the M7 (mean ozone for 7 hrs during the day) and AOT40 (accumulated ozone over a threshold of 40 ppbv) metrics for the calculation of crop losses for the northern, eastern, western and southern regions of India (Fig. 7). Our estimate showed total all India annual loss of 3.2-16.4 million ton (3.4-17.4%) for wheat and 0.3-6.7 million ton (0.3-6.3%) for rice based on 4 months of crops period. The results show lower crop loss for rice than that of wheat mainly due to lower surface ozone levels during the cropping season. These estimates based on a network of observations show much lower loss of crops than those estimated using global models but higher than the estimates from a regional model. Also, the results show large differences in the loss rates of the two crops using these two metrics. This study brings out the need for new metrics for this region for better estimation of crop losses.

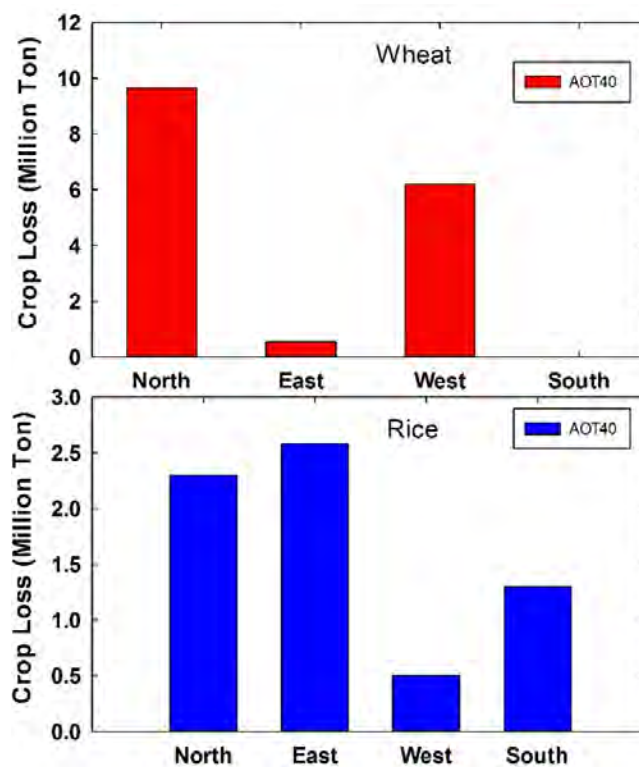


Figure 7: Annual loss of wheat and rice crops due to surface ozone calculated using AOT40 metric for the four regions of India.

(S. Lal)

Ozone in the semi-urban area-Vallabh Vidyanagar, Anand

Surface ozone is being measured at, Sardar Patel University (SPU), Vallabh Vidyanagar (V. V. Nagar), Anand, a semi-urban site. This measurement site is situated at a distance of about around 60 km South-Southeast of Ahmedabad. Anand has a population of about 30,000, and has a number of educational institutions.

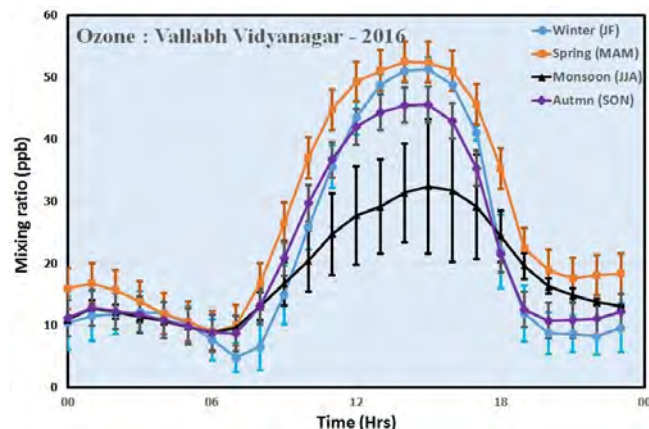


Figure 8: Seasonal variation of diurnal pattern of ozone at Vallabh Vidyanagar. Vertical bars indicate $\pm 1\sigma$ variation from the mean.

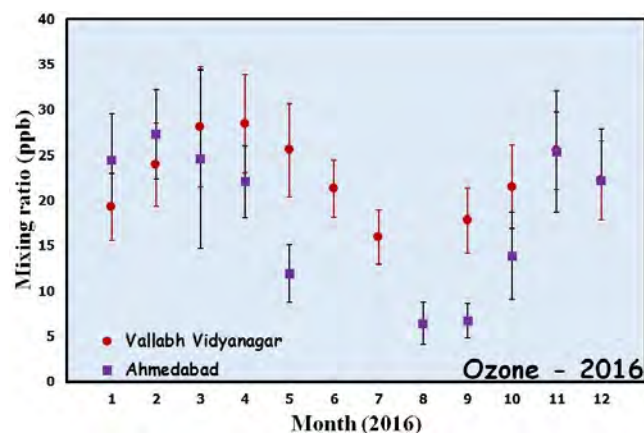


Figure 9: Monthly average ozone at Vallabh Vidyanagar and Ahmedabad during 2016. Vertical bars represent $\pm 1\sigma$ variation from the mean.

Figure 8 below depicts the seasonal variation in the diurnal build-up of ozone during 2016. The maximum diurnal value of ozone is in the range of 40-55 ppb during all months except during Jun-Jul-Aug. The maximum value is encountered during Mar-Apr-May when maximum sunlight is available. This maximum value drops to around 30 ppb during Jun-Jul-Aug when this region experiences rain and fresh air due to the south-west monsoon. The presence of a distinct peak point in the diurnal build-up during noon time is in contrast to the flat peak found at Ahmedabad. Figure 9 gives the monthly averaged value of ozone for V. V. Nagar and Ahmedabad during the year 2016. The ozone values at V. V. Nagar are always higher than the Ahmedabad value except during November and December. Lower NO_x values at V. V. Nagar when compared to Ahmedabad is the probable cause of high ozone value. The maximum ozone value is observed during

spring at V. V. Nagar whereas at Ahmedabad it is observed during winter. This peak-point along with the absence of local emissions, due to lesser number of vehicles, possibly indicate lower values of NO_x when compared to Ahmedabad values and hence the dominance of transport processes.

(S. Venkataramani and S. Lal)

Solar flare effect on Equatorial electrojet in East Brazil

As part of the study of the equatorial electrojet currents in the south Atlantic anomaly region, the effect of Solar flare, sudden commencement of magnetic storm and of the disturbances ring current on the equatorial electrojet in the Eastern Brazil region, where the ground magnetic declination (D) is as large as 20°W is studied based on geomagnetic data with one minute resolution from Bacabal during November-December 1990. It is shown that the mean diurnal vector of the horizontal field was aligned along 2°E of north at Huancayo and 30°W of north at Bacabal during the month of December 1990. Number of solar flares that occurred on 30 December 1990 indicated the direction of solar flare related ΔH vector to be aligned along 5°E of north at Huancayo and 28°W of north at Bacabal. This is expected as the solar flare effects are due to the enhanced conductivity in the ionosphere. The SC at 2230 UT on 26 November 1990 produced a positive impulse in ΔX and negative impulse in ΔY at Bacabal with ΔH vector aligned along 27°W of north. At Huancayo the ΔH vector associated with SC is aligned along 8°E of N. The magnetic storm that followed the SC had a minimum Dst index of -150nT. The corresponding storm time disturbance in ΔX at Huancayo as well as at Bacabal were about -250nT but ΔY at Bacabal was about +70nT and very small at Huancayo, that give the alignment of the H vector due to ring current about 16°W of north at Bacabal and almost along N-S at Huancayo. Thus alignment of the ΔH vector due to ring current at Bacabal is 14°E of the mean direction of ΔH vector during December 1990. This is consistent with the direction of ring current dependent on the dipole declination at the ring current altitude which is about 5°W of north over Bacabal and the deviation of declination due to the ring current during disturbed period given by the angle (Ψ -D), where Ψ is the angle perpendicular to the dipole declination.

This work is done in collaboration with Dr. N B Trivedi of INPE Brazil and Prof. Vidal Erick of Instituto Geofisico del Peru, Huancayo, Peru.

(R. G. Rastogi, P. Janardhan and H. Chandra)

Investigations of the Middle Atmospheric Thermal Structure and Oscillations over Subtropical Regions in the Northern and Southern Hemispheres

The temperature retrieved from the SABER (Sounding of the Atmosphere using Broadband Emission Radiometry) on-board TIMED (Thermosphere Ionosphere Mesosphere Energetics and Dynamics) satellite during January 2002 to September 2015 are used in this study to delineate the differences of middle atmospheric thermal structure in the Northern hemisphere (NH) and Southern hemisphere

(SH). Two stations namely Mt. Abu (24.59°N , 72.70°E) in NH and Reunion Island (21.11°S , 55.53°E) in SH are chosen over sub-tropical regions. Temperature climatology from SABER observations suggests that stratopause is warmer ($\sim 3\text{ K}$), and upper mesosphere is cooler in NH as compared to SH. Three atmospheric models are used to understand the monthly thermal structure differences for different altitudes. Moreover, semi-annual, annual and quasi-biennial oscillations are studied using Lomb Scargle Periodogram and Wavelet transform techniques. Over NH, summer and winter season are warmer ($\sim 4\text{ K}$) and cooler ($\sim 3\text{ K}$), respectively in stratosphere as compared to SH. It is important to note here that Mt. Abu temperature is warmer ($\sim 9\text{ K}$) than Reunion Island in winter but in summer season Mt. Abu temperature is cooler in upper mesosphere and above mesosphere NH shows warming. Results show that annual oscillations are dominant in both hemisphere as compared to semi-annual and quasi-biennial oscillations. In upper mesosphere, strength of annual oscillations are substantial in NH, while semi-annual oscillations are stronger in SH. It is found that the annual oscillations are stronger in NH near mesopause, while semi-annual oscillations are strong in SH. This work has been done in collaboration with LACY, University of Reunion, France.

(Som Sharma and R. Vaishnav)

Statistical Study of Cloud Base Heights over Ahmedabad in Western India using Ceilometer Lidar

A comprehensive statistical analysis of the Cloud Base Height (CBH) measured from ground based Vaisala ceilometer CL31 instrument has been performed to study the different cloud layers over PRL, Ahmedabad (23.03°N , 72.54°E), India during year 2014. An annual cloud occurrence frequency shows $\sim 82\%$ cloud cover based on $\sim 72\%$ of data availability over this region. Seasonal variation of measured CBH and cloud occurrence frequency revealed that the maximum cloud cover is found during peak Indian summer monsoon and the minimum value exists in pre-monsoon period. All three CBH are measured by ceilometer during monsoon months which reduced to two CBH for other months. First CBH is detected mainly in lower troposphere and upper troposphere during SW monsoon and summer period respectively. Second CBH is detected majorly in SW monsoon and summer period at 500-3000 m, and third CBH is available in SW monsoon only. Ceilometer measurements are also used to see the variations of cloud cover during day and night time which shows that during day time CBH is more as compared to night time in pre- and post-monsoon period.

(Som Sharma, R. Vaishnav, S. Venkataramani, S. Lal, and Y. B. Acharya)

A Study of Middle Atmospheric Thermal Structure over Western India: Satellite and Model Perspectives

Long term variations of middle atmospheric thermal structure in the upper stratosphere and lower mesosphere (20 km to 90 km) have been studied over Ahmedabad (23.1°N , 72.3°E , 55 m amsl), India using SABER (Sounding of the Atmosphere using

Broadband Emission Radiometry) onboard TIMED (Thermosphere, Ionosphere, Mesosphere, Energetics and Dynamics) observations during year 2002 to year 2014. For the same period, three different atmospheric models show over-estimation of temperature ($\sim 10\text{ K}$) in stratopause and in upper mesosphere, and a signature of under-estimation is seen above mesopause when compared against SABER measured temperature profile. Estimation of monthly temperature anomalies reveals a downward trend of lower temperature from mesosphere to stratosphere during January to December. Further, a detailed study of the semi-annual, annual and quasi-biennial oscillations has been done to diagnose the wave dynamics in the stratosphere-mesosphere system. Results suggested that semi-annual, annual and quasi-biennial oscillations exist in stratosphere, whereas, semi-annual and annual oscillations are observed in mesosphere. In lower mesosphere, our analyses revealed conspicuous absence of annual oscillations in altitude range of ~ 55 to 65 km, and semi-annual oscillations are not found in the altitude region of 35 to 45 km. Four monthly oscillations are also reported in the altitude range of about 45 to 65 km. The temporal localization of oscillations using wavelet analysis shows strong annual oscillation during year 2004-2006 and 2009-2011.

(Som Sharma, R. Vaishnav, K. K. Shukla and U. Deva)

Characteristics of quasi-16-day wave in the Southern hemisphere middle atmosphere

A comparative study of the quasi-16-day wave (QSDW) in the middle atmosphere using meteor radar observations and reanalysis data from three Southern hemispheric stations, Sao Joao do Cariri (7.4°S , 36.5°W) (CA), Cachoeira Paulista (22.7°S , 45°W) (CP) and Santa Maria (29.7°S , 53.7°W) (SM) has been carried out in the year 2005 to delineate its latitudinal variability characteristics.

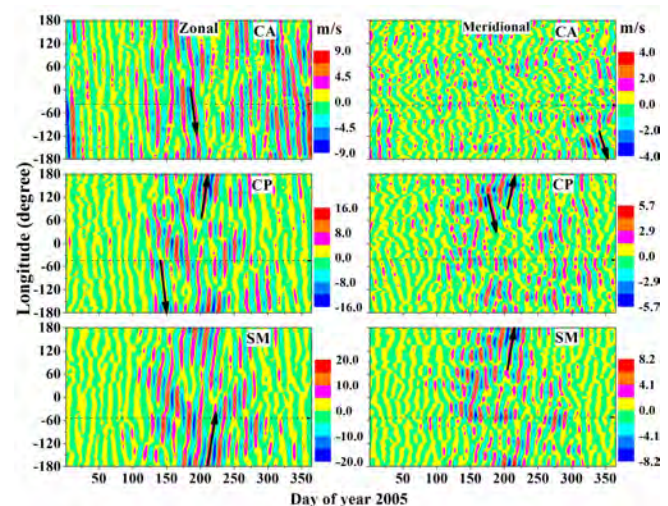


Figure 10: Longitudinal and temporal variation of the filtered zonal and meridional winds in the period band 12-20 days at 10 hPa pressure level for the locations 7.5°S ($\sim \text{CA}$), 22.75°S ($\sim \text{CP}$) and 29.75°S ($\sim \text{SM}$). The arrows in the plots show the direction of the propagation of the waves. The plots clearly show change of preferential direction of propagation from west to eastward with the increase of latitude.

The broad spectral behavior around 16-day periodicity may indicate multiple modes of the concerned wave component. The wave amplitude shows a number of peaks over the year with the largest one in summer and winter in the case of mesosphere-lower-thermosphere (MLT) and stratosphere, respectively. A potential coupling of the concerned wave with other short period planetary waves, especially at CA and CP is evinced. Although zonal propagation exhibits both eastward as well as westward waves there is a general preference of eastward waves at mid-latitude and westward waves at tropical latitudes.

(A. Guharay)

Response of solar flux variation in the mesosphere

A positive response to the variations in solar activity is known to exist in the thermosphere due to its dependence on solar EUV flux. However, this is not the case in the mesosphere, whose dynamics is influenced, by and large, by the atmospheric forcing from altitudes below.

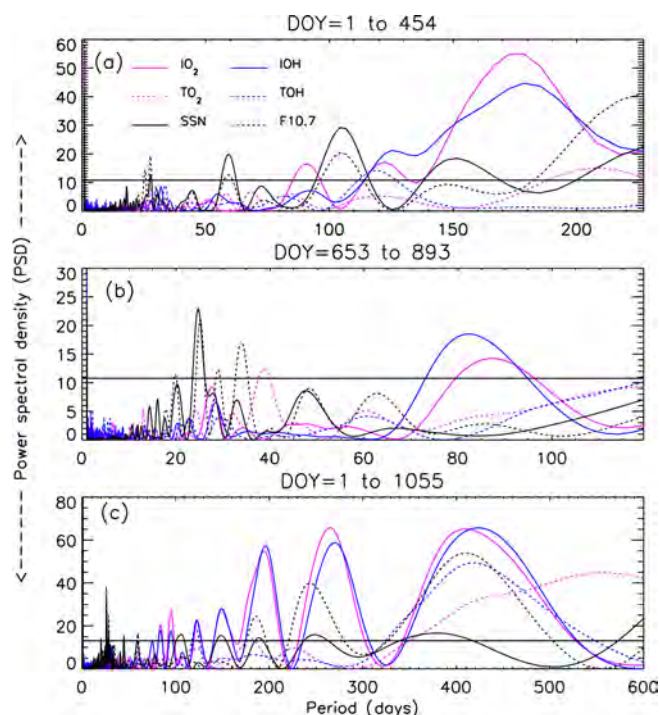


Figure 11: (a) LombScargle periodograms of the O_2 and OH intensities and corresponding temperatures for the first 455 days of observations (DOY 1 to 454). Power spectral density (PSD) along with the 90% false-alarm level (FAL) is shown for different periods of atmospheric nightglow and solar parameters. (b) Significant periodicities obtained using LombScargle periodogram analysis of 241 days of data (DOY 653 to 893). (c) Similar to (a, b) but for 1056 days of optical observations (DOY 1 to 1055). It should be mentioned here that, for solar parameters, continuous data without any gaps are considered. It is striking to note that, in addition to atmospheric periodicities that are present in the mesospheric intensity and temperature variations, several coherent periods are present in the O_2 and OH intensities and temperatures showing commonality with those obtained from SSN and F10.7.

Nevertheless, based on over three years (2013-2015) of mesospheric OH and O_2 optical nightglow emissions (that originate from 87 and 94 km) measurements from Gurushikhar, Mt Abu, it is shown that mesosphere too is affected by the variations in solar flux. This solar

influence (measured both in sun spot numbers and in the F10.7 cm flux) on OH and O_2 emissions emanates from the requirement of O and O_3 concentrations as reactants for their production, which are known to be solar activity dependent. Due to a data gap, the analysis were carried out for two durations DOY 1-454 (DOY1 being 1 Jan 2013), and DOY 653-893. Panels (a) and (b) of Figure 11 correspond to the results obtained from Lomb Scargle analyses of the data for several solar and mesospheric parameters for these two durations, while panel (c) shows the result obtained by considering all the existing data. Both O_2 and OH intensities show variations similar to those of the number of sunspots and F10.7 cm radio flux with coherent periodicities of 150, 195, 270, and 420 days indicating a strong solar influence on mesospheric dynamics. The mesospheric wave dynamics, however, show other periodicities, of 84, 95, and 122 days, which are purely of atmospheric origin.

(R. P. Singh and D. Pallamraju)

Investigations on mesospheric temperature inversions from Gurushikhar

Measurement of $O_2(0-1)$ and OH (6-2) nightglow emission intensities and their corresponding temperatures ($T(O_2)$ and $T(OH)$) which originate from 94 and 87 km altitudes are being carried out using an in-house built Near InfraRed Imaging Spectrograph (NIRIS) from Mount Abu (24.6°N, 72.8°E), in India. In general, it is seen that $T(O_2)$ is lower than $T(OH)$ which is the normal behaviour of the mesospheric temperature structure over low latitudes. However, on several occasions it was observed that $T(O_2)$ is greater than $T(OH)$. These are uncommon and were investigated in the context of mesospheric temperature inversions (MTIs). MTIs are the regions of enhanced temperatures above their normal values and can have a thickness of several kilometres. They can appear in MLT regions over low- and mid-latitudes at any time of the year. MTIs are generally attributed to the energy deposition of upward propagating tides and gravity waves and / or chemical heat released in-situ by several exothermic reactions in the MLT regions. The NIRIS derived temperatures over a long period are used to study the possible cause(s) for the occurrence of MTIs. Vertical propagation of wave is confirmed by investigating downward phase propagation at OH and O_2 emission altitudes. There are observations of existence of MTIs when such vertical propagations are observed. There are also several nights when MTIs are observed but vertical propagation is absent. Detailed analyses have been carried out to ascertain the cause for the observed MTIs. Based on this study it appears that chemical heating in the mesosphere could be a more probable cause in comparison to vertical propagation of waves.

(R. P. Singh and D. Pallamraju)

Imprint of equatorial electrodynamics in the diurnal pattern of oxygen dayglow emissions at off-equatorial latitudes

Daytime airglow emission intensity measurements at three wavelengths OI 777.4 nm, OI 630.0 nm, and OI 557.7 nm are being obtained since 2010 from the optical aeronomy observatory at a low-latitude location, Hyderabad (17.5°N, 78.4°E; 8.9°N MLAT) under PRL-JNTUH collaboration. The diurnal behaviour in the neutral

optical dayglow emissions are expected to show a solar zenith angle dependent behaviour (i.e., symmetric with respect to local noon) considering the photochemical nature of the production mechanisms. However, on several days they do show asymmetric behaviour with respect to local noon wherein the peak in emission intensities is obtained in the afternoon instead of around noon. The extent and magnitude of deviations in time and intensity of the peak with respect to local noon (LN) is quantified as $(T_{Peak} - T_{LN}) \cdot I_{Peak} / I_{LN}$, wherein, T_{Peak} and T_{LN} indicate the times at which the emission intensity at its peak, I_{Peak} , and local noon, I_{LN} , are obtained. This quantity is referred to as the asymmetry in time (AT), and it can be noted that it is independent of the measurement technique used as the ratio in intensities is obtained. In the detailed analysis it was noted that the AT values were greater (>0.4 h) on several days in the years 2014-2016, however, in the three previous years 2010-2013 the values were predominantly smaller than 0.4 h (thereby indicating a symmetric diurnal pattern). This discrepancy was seen in the context of contrast in solar activity between these two periods (lower during the years 2010-2013). To ascertain solar activity dependence, if any, of the AT in dayglow diurnal emission pattern, past data from the published literature on visible dayglow intensities (which exist from 1989) were looked into. AT values were estimated and are plotted along with the sunspot numbers for all these years. From Figure 12 it can be seen that AT values show a clear solar activity dependence. This variation in AT arises through the solar activity dependent variation in equatorial electric field which has been captured clearly in the neutral dayglow emission variations from a low-latitude location.

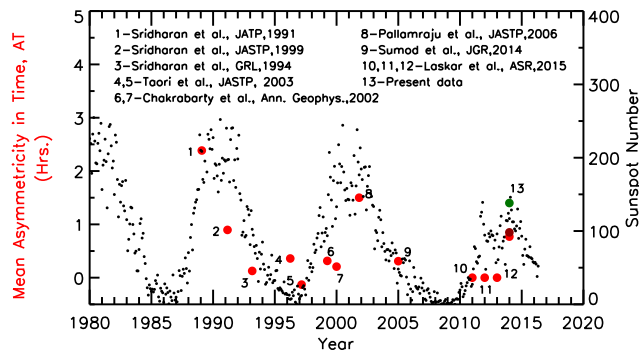


Figure 12: Variation of mean asymmetry in time (AT) at OI 630.0 nm emissions in different years as obtained from the published literature.

(D. K. Karan and D. Pallamraju)

Longitudinal differences in equatorial electrodynamics discovered in small separations (3° - 8°) in longitudes

The equatorial upper atmospheric dynamic processes show both latitudinal and longitudinal variability. While the variability in latitudes can exist over small distances (~ 100 s km), the longitudinal behavior has been shown to be existing mainly over large spatial separations (~ 1000 s km). In the present work we have used variations in thermospheric optical dayglow emissions at OI 557.7, 630.0, and 777.4 nm as tracers of neutral dynamics. These emissions are obtained simultaneously from a high resolution slit spectrograph,

MISE (Multi wavelength Imaging Spectrograph using Echelle grating) from a low-latitude location, Hyderabad (17.5° N, 78.4° E; 8.9° N MLAT), in India, to investigate the longitudinal differences in the upper atmospheric processes over short separations. Spectral analyses of gravity waves carried out on the dayglow emission intensity variations for different independent viewing directions on some days show dissimilar periodicities suggesting the existence of longitudinal differences (Figure 13). Gravity wave scale sizes and the propagation characteristics on these days are different from those in which longitudinal differences are not seen. Further, the zenith diurnal emission intensity patterns are different on the days with and without the observed longitudinal variability. This work shows for the first time that longitudinal differences in upper atmospheric processes can exist at even as small as 3° longitude separations. Such longitudinal differences seen in the neutral dayglow emission intensities are attributed to the zonal variation in the daytime equatorial electrodynamics.

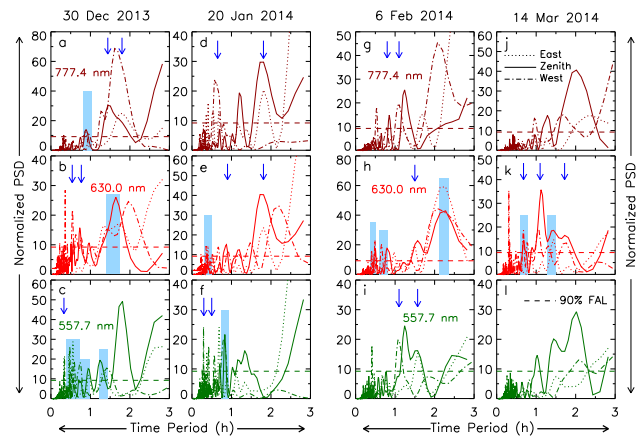


Figure 13: Results of the periodogram analyses carried out for various emission wavelengths obtained over west, zenith, and east directions on four sample days are shown. Periodograms in the upper (a,d,g,j), middle (b,e,h,k), and lower (c,f,i,l) panels represent those that were obtained for 777.4, 630.0, and 557.7 nm wavelengths, respectively. The shaded portion in blue corresponds to the time period in which gravity waves obtained from all the three directions are coherent. The blue arrows on the top indicate the values of time periods in which GWs are coherent in any two directions. It may be noted that coherency in GW periodicities at all wavelengths and in two directions is seen more readily on the two days on the left as compared with the two on the right. The two days on the left/right demonstrate the absence/presence of longitudinal differences in the gravity wave domain within 3° - 8° longitude separations.

(D. K. Karan and D. Pallamraju)

Gravity waves in the ionosphere as derived from digisonde measurements at Ahmedabad, India.

Neutral waves of different spectral and spatial characteristics exist in the ionosphere. The sources of waves are many and range from lower atmosphere, high latitudes during geomagnetic storms, and differential solar forcing. While the neutral optical airglow emission variability is known to respond to the gravity wave variability, we present results on gravity waves derived from a method using digisonde situated at Ahmedabad, (23.0° N, 72.5° E). A special mode of analyses was adopted wherein iso-electron contours are obtained at several fixed frequencies. On several occasions the iso-electron

contours show a clear downward phase propagation indicating an upward movement of gravity waves. From such datasets, gravity wave time periods, and their propagation characteristics are obtained. The spectral analysis indicates that the periodicities in waves exist from a few minutes to less than 4 hours. The vertical propagation speeds and the vertical wavelength of waves are seen to be in the range of $10\text{--}80\text{ ms}^{-1}$ and $50\text{--}800\text{ km}$. These values are compared with those derived from both daytime and nighttime optical airglow methods, the results of which are encouraging.

(D. Pallamraju, S. Mandal, D. K. Karan, and R. P. Singh)

Plasma drifts over Indian sector during daytime and Comparison with model

Using the equatorial electrojet model developed in PRL and the measurements obtained from the Indian magnetic observatories, a methodology is evolved to obtain the ionospheric electric fields and corresponding vertical plasma drifts during daytime which are otherwise difficult to obtain systematically over Indian sector in the absence of incoherent scatter radar. The comparison of this result with the global empirical model of vertical drifts based on the satellite measurements reveals fairly good agreement with the daytime derived vertical drifts and also with other ensemble of observations obtained at other times. More importantly, by comparing the ensemble of observational results and daytime electric fields with the empirical model, important scientific insights like the relationship between the plasma drifts and the occurrence of counter electrojet and generation of streaming waves are brought out.

(K. Pandey, R. Sekar, S. P. Gupta, D. Chakrabarty and B. G. Anandarao)

Contribution of Storm-Time Substorms to the Prompt Electric Field Disturbances in the Equatorial Ionosphere

By using observations of unusual equatorial plasma drift data from JULIA (Jicamarca Unattended Long-term Investigations of the Ionosphere and Atmosphere) during two space weather events, it is shown that substorms can induce both eastward and westward penetration electric fields under steady southward Interplanetary Magnetic Field (IMF Bz) conditions. During one such event (see left panel of Figure 14), the enhancement of the daytime eastward electric field over Jicamarca due to substorm is found to be comparable with the Sq and Interplanetary Electric Field (IEFy) generated electric fields combined. During the second event (see the right panel of Figure 14), the substorm is seen to weaken the daytime eastward field thereby inducing a westward field in spite of absence of northward turning of IMF Bz (overshielding). The westward electric field perturbation in the absence of any overshielding events is observationally sparse and contrary to the earlier results. This investigation shows quantitatively that at times substorm contribution to the disturbed time prompt electric fields can be quite significant and thus should be taken into consideration in evaluating penetration events over low latitudes.

This work is done in collaboration with the scientists from Los Alamos National Laboratory, USA, Department of Earth and Planetary

Sciences, Kyushu University, Japan and Institute for Space-Earth Environmental Research, Nagoya University, Japan.

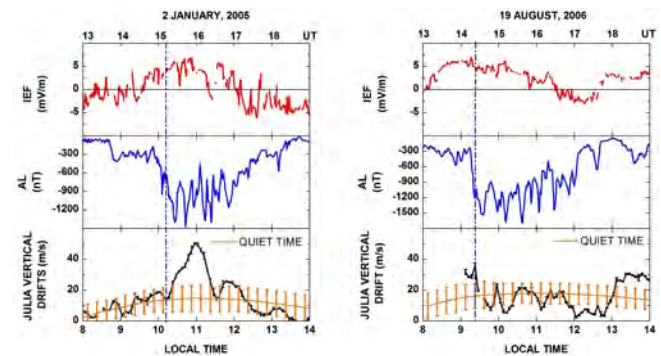


Figure 14: Left panel shows the eastward (enhancement of upward drift) electric field perturbation and the right panel captures the westward (reduction in the upward drift) electric field perturbation due to substorms (vertical dashed lines are the onset times of the substorms) in the equatorial vertical plasma drift as measured (bottom) by the JULIA radar in Jicamarca, Peru.

(D. Hui, D. Chakrabarty and R. Sekar)

Ionospheric responses over Indian and American sectors due to a CME driven sheath region

The responses of the global ionospheric electric fields have been investigated using Incoherent scatter radar measurements of Jicamarca and Arecibo (post-midnight sector) along with the variations of equatorial electrojet strength over India (day sector) during the passage of sheath region of an ICME. DP2-type electric field perturbations with ~ 40 min periodicity were found to affect the ionosphere over both the sectors for about 2.25 hr. In addition, a possible pseudo-breakup event was triggered during this time that caused a weak counter electrojet over the Indian sector. The strength of the equatorial ionization anomaly was also significantly reduced. This result brings out, for the first time, the modification in the low latitude ionosphere on both day and night sectors due to the passage of the sheath region of an ICME.

This work is done in collaboration with the scientists from Indian Institute of Technology, Roorkee, Indian Institute of Geomagnetism, Navi Mumbai, Center for Atmospheric and Space Sciences, Utah State University, USA, Pennsylvania State University, USA, Arecibo Observatory, Puerto Rico, Los Alamos National Laboratory, USA, and Computational Physics Inc., USA.

(D. Rout, D. Chakrabarty and R. Sekar)

Investigation on the efficiency of prompt penetration electric field and the duration of the effect of over-shielding electric field

The quantification of efficiency of prompt penetration (PP) electric field over non-Peruvian sectors (e.g. India) is sparse owing to non-availability of direct measurements of ionospheric electric fields. The efficiency of PP over the Indian sector is computed for two

extreme PP events using electric fields derived with magnetometer records in conjunction with an equatorial electrojet model. The computed efficiency of PP is found to be $\sim 6.5\%$. Further, the decay time constant for the over-shielding electric field is also calculated and found to be ~ 20 min. Importantly, the duration of the effects of over-shielding is found to vary from 60 min to 90 min depending upon the amplitude of over-shielding electric field and local time of the occurrence of the event. This explains the difference between observed effects and theoretical expectation based on decay times.

(K. Pandey, R. Sekar, D. Chakrabarty, B. G. Anandaram and D. Rout)

Direct observational evidence for disturbance dynamo on the daytime low-latitude ionosphere

Direct observational evidence for disturbance dynamo on the daytime low-latitude ionosphere is brought out using total electron content (TEC) observations from a GPS network of stations in the Indian equatorial, low and middle latitude regions. The importance of the study lies in the delineation of the disturbance dynamo effects on the daytime low-latitude ionosphere and the Equatorial Ionization Anomaly (EIA) from the compositional variations during the recovery phase of geomagnetic storm.

This work is done in collaboration with the scientists from the Space Physics Laboratory, VSSC, Airport Authority of India/Space Application Centre, Ahmedabad, and Indian Institute of Geomagnetism, India.

(D. Chakrabarty)

Solar, interplanetary causes and geomagnetic consequences of a long duration southward IMF Bz event

The solar and interplanetary causes for an exceptionally long duration (~ 44 hrs) southward IMF Bz condition during 2-4 May, 1998 and its geomagnetic consequences have been investigated. This long duration southward IMF Bz condition is shown to be associated with the origin of the IMF from the same active region in the sun as well as a favorable draping of the outward directed IMF due to the presence of interplanetary Coronal Mass Ejection structure present in the medium.

This work is done in collaboration with the scientists from the National Astronomical Observatories, Chinese Academy of Sciences, China, Department of Earth and Planetary Sciences, International Centre for Space Weather Science and Education, Kyushu University, Japan, and Institute for Space-Earth Environmental Research, Nagoya University, Japan.

(D. Chakrabarty and P. Janardhan)

Conjugate ionospheric response to the St. Patrick's Day storms of 2013 and 2015

The ionospheric response to the St. Patrick's Day storms of 2013 and 2015 along the 100°E meridian is investigated and compared using multi-instrument data from magnetically near conjugate stations from middle to low and equatorial latitudes. Longitudinal and hemispherical differences in the ionospheric responses during these storms are brought out in this investigation. The hemispherical asymmetry of the negative storm response is contributed mainly by the asymmetric expansion of the disturbed thermospheric composition, whereas the longitudinal asymmetry in ionospheric response is attributed to electrodynamic as well as thermospheric processes. Importantly, this investigation also shows that the storm-induced upward vertical drift at sunrise can be larger than the drift during evening pre-reversal enhancement. This led to sharp height increase and consequently triggered generation of fresh F-region irregularity structures during the 2015 storm.

This work is done in collaboration with the scientists from the Dibrugarh University, Dibrugarh, Indian Institute of Geomagnetism, Navi Mumbai, Space Weather Services, Bureau of Meteorology, Australia, Department of Physics, Kohima Science College, Kohima, National Institute of Information and Communications Technology, Japan, Faculty of Engineering, King Mongkuts Institute of Technology Ladkrabang, Thailand, Department of Electrical Engineering, Chiang Mai University, Thailand, Space Science Center, Indonesian National Institute of Aeronautics and Space, Indonesia, and Institute of Geophysics, Vietnamese Academy of Science and Technology, Vietnam.

(D. Chakrabarty)

Science

Geosciences

Natural isotopic composition of particulate organic nitrogen in the Eastern and Central Arabian Sea

Nitrogen isotopic composition ($\delta^{15}\text{N}$, expressed as deviation in parts per thousand (‰) from atmospheric air standard) of particulate organic nitrogen (PON) provides an insight into various biogeochemical transformations occurring in the marine nitrogen cycle. The $\delta^{15}\text{N}$ of phytoplankton varies as a result of biologically mediated isotopic discrimination and primarily depends on the $\delta^{15}\text{N}$ of the N source and the biological isotopic fractionation during uptake and assimilation of the nutrient source. Under a nitrogen replete environment, phytoplankton preferentially assimilate ^{14}N relative to ^{15}N resulting in the lower $\delta^{15}\text{N}$ of phytoplankton relative to that of the nitrogen source. On the other hand, under nitrogen limiting conditions, phytoplankton utilize available nitrogen completely and $\delta^{15}\text{N}$ of phytoplankton closely reflects that of the nitrogen source.

Cyanobacteria lowers the $\delta^{15}\text{N}$ of PON by converting atmospheric N_2 ($\delta^{15}\text{N} \approx 0\text{‰}$) into organic nitrogen. Further, nitrogen recycling also lowers the $\delta^{15}\text{N}$ of PON, because of isotopic fractionation during heterotrophic processes. The low- $\delta^{15}\text{N}$ ammonium released by zooplankton is assimilated by phytoplankton leading to a lower $\delta^{15}\text{N}$ of surface PON. Further, the $\delta^{15}\text{N}$ of PON also depends on phytoplankton species, physiology and the rate and phase of growth of phytoplankton. Sinking particulate matter likely to propagate these surface generated signals to the sea floor and thus, nitrogen isotopic compositions of sediments are being used to decipher the information on long-term variation in surface nitrogen utilization and critical oceanic N cycle processes. In this context, measurements of the $\delta^{15}\text{N}$ of plankton and dissolved inorganic nitrogen are critical to the interpretation of sedimentary $\delta^{15}\text{N}$ records as well as in quantifying the sources of nitrogen that support production in contemporary oceanic ecosystems.

A variety of geochemical and biological processes are known to be active in the Arabian Sea; e.g., higher primary productivity during

the winter and summer monsoons due to the entrainment of nutrients into the mixed layer by convective overturning and coastal upwelling, respectively. Such episodic events of higher productivity result in oxygen deficiency in middle layers of the water column. Loss of oxidized form of nitrogen to the atmosphere by intense denitrification and anaerobic ammonium oxidation is also observed. The Arabian Sea, with its well-developed oxygen minimum zone (OMZ) is one of the major regions of water column denitrification in the world ocean. However, the basin gains new nitrogen from the atmosphere by the occurrence of N_2 -fixing cyanobacteria, mainly *Trichodesmium* bloom during inter-monsoon every year. All the above processes affect the $\delta^{15}\text{N}$ of the inorganic nitrogen pool and hence the average $\delta^{15}\text{N}$ of PON and sinking particles. Study of $\delta^{15}\text{N}$ of surface PON may elucidate the strength of certain water column processes. We made measurements of isotopic composition of nitrogen ($\delta^{15}\text{N}$) of particulate organic nitrogen (PON) at eighteen sampling locations in the north-eastern and central Arabian Sea during the waning phase of the summer monsoon. This season is ideal to detect signatures of upwelling and denitrification in the Arabian Sea. Our observations indicate significant spatial variability in the $\delta^{15}\text{N}$ as a result of the upper ocean response to the monsoonal forcing that triggers upwelling and thus supplies sub surface nitrate to the surface. An increasing (decreasing) trend has been found in the $\delta^{15}\text{N}$ (PON) from the upwelling zone to the open ocean, which tracks the progressive utilization of advected nitrate from the coast. Monsoon-driven mixing and supply of nitrate and/or PON with lower $\delta^{15}\text{N}$ from the west through advection are mainly confined to the upper 50 m, however, at some locations advection imprints its signature in the deeper layers as well. The results have implications to the interpretation of sedimentary $\delta^{15}\text{N}$ record from this region and deciphering the role of monsoonal forcing over the nitrogen utilization by plankton.

This work was carried out in collaboration with Dr. Naveen Gandhi, IITM, Pune.

(R. Ramesh)

Response of a coastal tropical pelagic microbial community to changed salinity and temperature

Studies on the responses of tropical microbial communities to changing hydrographic conditions are presently poorly represented. Our mesocosm experiments, conducted jointly with Universities of Gothenburg and Kristianstad, Sweden and the College of Fisheries, Karnataka, yielded the following results. A mesocosm study was conducted in southwest (SW) coastal India to investigate how changes in temperature and salinity will affect a tropical microbial community. The onset of algal and bacterial blooms, the maximum production and biomass, and the interrelation between phytoplankton and bacteria were studied in replicated mesocosms. The treatments were set up featuring ambient control (28°C, 35 PSU), decreased salinity (31 PSU), increased temperature (31°C) and a double stressed treatment with increased temperature and decreased salinity (31°C, 31 PSU). The reduced salinity treatment had the most considerable influence manifested as significantly lower primary production, and the most dissimilar phytoplankton species community. The increased temperature acted as a positive catalyst in the double manipulated treatment, and higher primary production was maintained in this treatment. We investigated the dynamics of the microbial community with a structural equation model approach, and found a significant interrelation between phytoplankton and bacterial biomass. Using this methodology it became evident that direct and indirect effects influence the different compartments of the microbial loop. In the face of climate change, we conclude that in relatively nutrient replete environments, such as the tropical coastal zones, nutrient assimilation is dependent on salinity and temperature and will have significant effects on the quantity and the character of microbial biomass and production.

(P.S. Bhavya, S. Kumar, R. Ramesh and A. Singh)

Indian monsoon rainfall variations during the last ~25 ka from planktonic foraminiferal $\delta^{18}\text{O}$ from the Eastern Arabian Sea

Stable oxygen isotopic composition of ($\delta^{18}\text{O}$) of foraminifera from the sediments of the Northern Indian Ocean has been used to decipher past changes in the intensity of the South Asian Monsoon. Duplessy, analysing several sediment cores from the Bay of Bengal, showed that the summer monsoon rain was significantly reduced during the Last Glacial Maximum (LGM): $\delta^{18}\text{O}$ of LGM planktonic foraminifera were relatively higher, resulting from reduced freshwater discharge from the major monsoon fed Indian rivers. Likewise, we had earlier shown that the winter monsoon rains intensified during LGM by analysing four different species of planktonic foraminifera from a sediment core from the Eastern Arabian Sea. These prompted further studies on the high resolution $\delta^{18}\text{O}$ analysis planktonic foraminifera preserved in marine sediment cores from locations of rapid sedimentation, both from the Western and the Eastern Arabian Sea. Except for the early work of Duplessy, inferences from most subsequent studies were based on single cores collected at different locations, and most lacked modern calibration for the interpretation of planktonic foraminiferal $\delta^{18}\text{O}$. For instance, we had earlier used limited data as an approximate calibration to show that the Eastern Arabian Sea responded to the summer monsoon runoff from the Western Ghats of peninsular India. We had inferred that the summer monsoon rains steadily increased during the Holocene. In contrast, Gupta et al. surmised that during the Holocene, monsoon winds had significantly

weakened over the Western Arabian Sea, based on the abundance counts of *G. bulloides*, believed to be an upwelling indicator. There was no modern calibration of this proxy, other than the assumption that upwelling is related to the square of the wind strength. This result, bolstered by subsequent reports of speleothem $\delta^{18}\text{O}$ records from Oman (located in the western limit of the South Asian Monsoon) and China (East Asian Monsoon), led to the general acceptance of the weakening summer monsoon trend during the Holocene, in spite of the evidence to the contrary: Kudrass et al had showed that the monsoon runoff into the Bay of Bengal had steadily increased from 21 ka (LGM) to ~4ka.

Two recent developments nudge us to revisit the reconstructed monsoon variability during the past ~25 ka. First, a new, high resolution spatio-temporal $\delta^{18}\text{O}$ data set of 631 seawater samples has become available for testing the assumptions based on which down-core $\delta^{18}\text{O}$ variations were interpreted viz., the variation in the $\delta^{18}\text{O}$ and salinity of the Eastern Arabian Sea surface is dominantly governed by the summer monsoon runoff from the Western Ghats. Second, increasing number of sediment cores has been analysed during the past decade from the Eastern Arabian Sea alone and high resolution planktonic foraminiferal $\delta^{18}\text{O}$ variations have been reported.

We have demonstrated that the surface seawater $\delta^{18}\text{O}$ variations in the Eastern Arabian Sea are mainly governed by the influx of low salinity water through the Winter Monsoon Current from the relatively fresher Bay of Bengal, and transported northwards by the West India Coastal Current. This is made possible by a careful reanalysis of recently published large body of surface seawater salinity and $\delta^{18}\text{O}$ data. Armed with this “calibration” for the present day, we then revisited the south Asian summer monsoon variability during the past ~25 ka by compiling high resolution fossil planktonic foraminiferal $\delta^{18}\text{O}$ data from a large number of well dated sediment cores from the Eastern Arabian Sea. We have clearly demonstrated that there is no evidence to believe that the south Asian Sumer monsoon steadily declined during the Holocene as reported in a few earlier papers from the Western Arabian Sea and speleothems from Oman. On the contrary, a majority of sediment core data support a steadily increasing monsoon rain during the Holocene. Thus the idea of south Asian monsoons driven by past insolation changes alone is called into question.

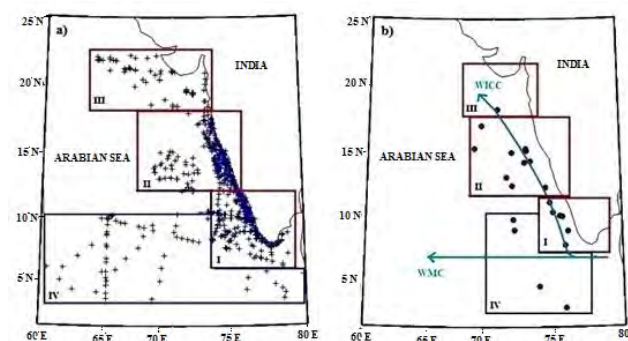


Figure 1(a): Seawater sampling locations in the Eastern Arabian Sea (Deshpande et al., 2013), sub-divided into four regions: I 6°N-12°N, II 12°N-18°N, III 18°N-22°N and IV 4°N-10°N/79°E-60°E. b Locations of sediment cores (see Table 1 for details). Region IV marked here is smaller because high resolution analyses of sediment cores have not been reported west of this box.

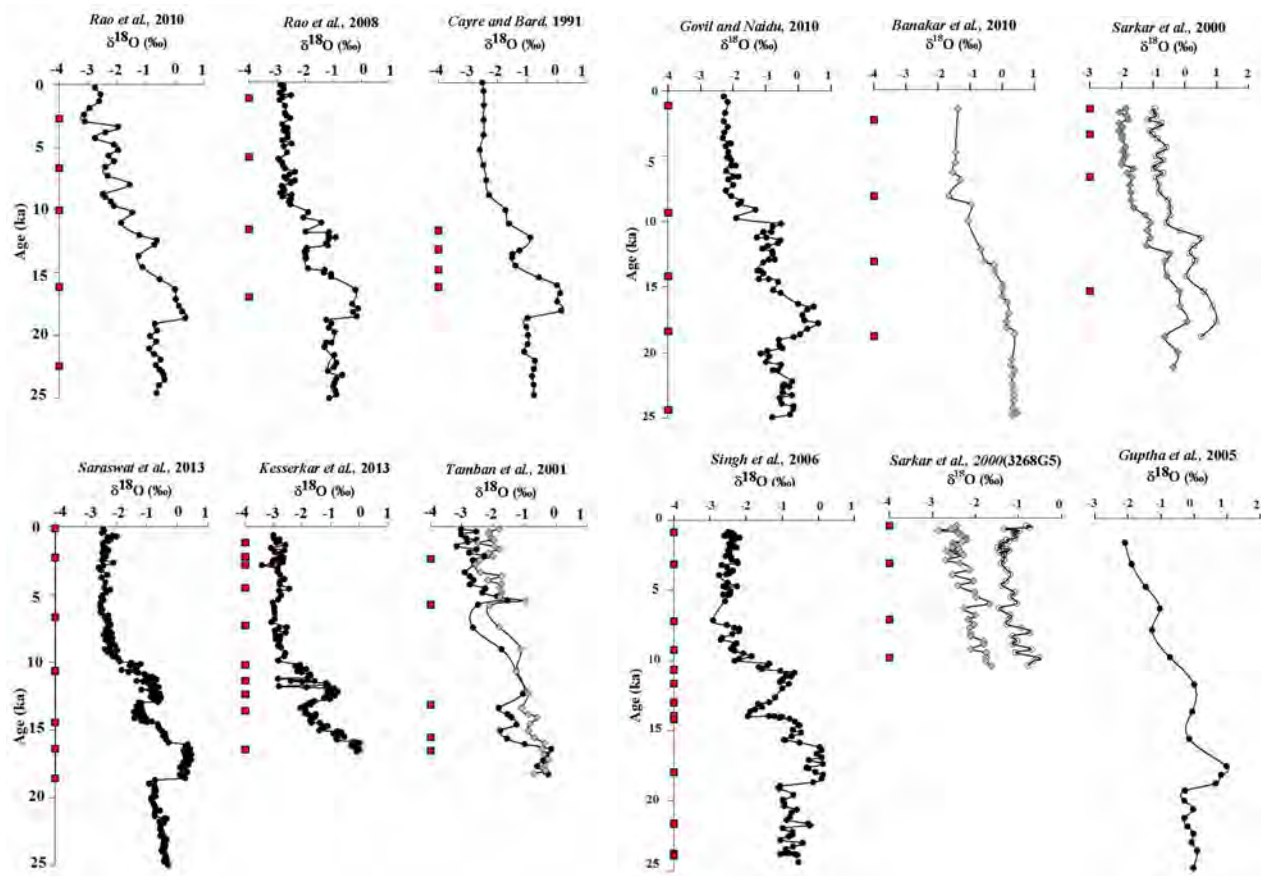


Figure 2: $\delta^{18}\text{O}$ records of *G. ruber* (●) and *G. sacculifer* (◆) and *G. menardii* (○) from various sediment cores from the a) region I (6°N - 12°N); b) region II (12°N - 18°N) and region III (18°N - 20°N)

(P. Kirankumar and R. Ramesh)

and three SWM wind strengths are bridged by decline in the SWM at different intervals, such as SWMD-I (~17 to 16 ka), SWMD-II (~12 to 11 ka) and SWMD-III (9.7 ka to 8.2 ka).

Wind Strength Variability in the Western Arabian Sea since the Last Glacial Maximum: Southwest vs. Northeast Monsoon Modes

Both the southwest monsoon (SWM) and the northeast monsoon (NEM) winds are responsible for the variations in the biological productivity in the western Arabian Sea (WAS), as recorded in the Arabian Sea sedimentary planktic foraminiferal record. While most earlier studies from this region ascribe the total observed variability predominantly to SWM, here we attempt to differentiate between the two monsoons based on the relative abundances of depth stratified planktic foraminifera assemblages. We observe a number of intervals of enhanced SWM. The first intensification (SWMI-I) occurred during ~16 to 12 ka and is possibly an outcome of early deglacial melting and stepwise increase in SWM strength after the end of the last glacial maximum (LGM). The second intensification (SWMI-II) is recorded at around ~10 ka, after the gradual strengthening from the end of the Younger Dryas cold episode. The last interval of intensification (SWMI-III) occurred around (~8.2 to 7.8 ka). In addition, there are two intervals of enhanced NEM: NEMI-I at around 19 to 17 ka and NEMI-II (~8.0 to 5.4 ka). These intervals of two enhanced NEM

This work was done in collaboration with University of Delhi.

(R. Ramesh)

Provenance of sediments in Andaman Islands and onset of Indian Monsoon

The timings of the onset and subsequent intensifications of the South Asian Monsoon system remain largely speculative. With the primary objective of reconstructing the evolutionary history of the monsoon, we investigated the Cenozoic sedimentary record of the Andaman Accretionary Prism, formed as a result of exhumation of trench-forearc deposits at the convergent margin between the Indian and Eurasian plates. We used Sr-isotope stratigraphy and tephrochronology to establish chronology of deposition, and geochemical and isotopic (Sr-Nd) proxies as indicators of sediment provenance. The study reveals that whereas the Burmese Arc had remained a constant source of sediments to the Andaman Basin throughout the Paleogene, the turbidites deposited between ~35 Ma and 20 Ma had recorded a

steady increase in continental input (Fig.3) from the eastern Myanmar sources and possibly the nascent eastern-central Himalayan sources as well, apparently mobilized by enhanced rainfall linked to an

onset/intensification of the Indian Monsoon system in the Oligocene.

(N. Awasthi and J.S. Ray)

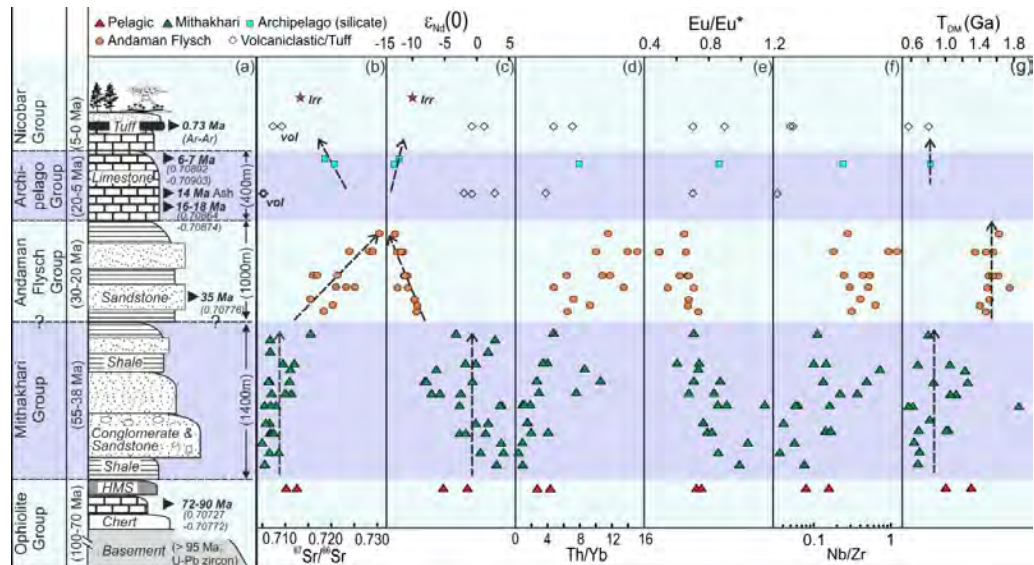


Figure 3: (a) Stratigraphic litholog showing different rock units exposed on the Andaman Islands prepared based on literature [e.g., Curray, 2005; Pal et al., 2003] and inferences from our own field investigations. Dates in brackets, on the left, are approximate depositional age ranges [Allen et al., 2007; Curray, 2005]. U-Pb zircon age for ophiolite basement is from Pedersen et al. [2010]. Ages given on the right of the stratigraphic column are obtained from Sr isotope stratigraphy ($^{87}\text{Sr}/^{86}\text{Sr}$ are in brackets) of carbonate formations (this work), tephrochronology in Archipelago Group using isotope fingerprinting and $^{40}\text{Ar}-^{39}\text{Ar}$ dating of the Mile Tilek Tuff [Awasthi et al., 2015]. Stratigraphic variations of various geochemical and isotopic proxies in siliciclastics and silicate fractions in limestones are presented in (b). Data for volcaniclastic sediments in tuffs and limestones are presented. Isotopic compositions of modern sediment in Irrawaddy River (Irr) are marked [data source: Colin et al., 1999]. Arrows show the secular trends in the data. HMS: hemipelagic mud stone; vol: volcaniclastic. TDM = Nd-model age, represents the age of derivation from a depleted mantle.

Bitter Spring $\delta^{13}\text{C}$ anomaly in the Vindhyan Supergroup, Rajasthan, India

The Balwan Limestone is the topmost carbonate formation of the Vindhyan Supergroup, India and is developed only in the western sector, in Rajasthan. It underlies the youngest horizon of the supergroup, the Dholpur Shale, and belongs to the Bhandar Group, which is known for occurrences of numerous controversial fossils of earliest animal life. The lone available age constraint based on Pb-Pb dating of carbonates, though not very robust, suggests a depositional age of 866 ± 180 Ma [Gopalan et al., 2013], making it one of the few possible Cryogenian carbonate deposits in India. The Formation is exposed along the northwestern slope of an 18 km long and SW-NE trending anticlinal ridge, representing the Maihar (Sikhaoda) Sandstone, near the township of Lakheri. Lying conformably over the sandstone, the formation varies in thickness from ~ 50 to 120 m. The lower part is characterized by molar tooth structures and stromatolites and the upper part is dominated by stromatolites that are different from the older member. An intra-formational conglomerate horizon, 10-20 m, bounded by beds containing chert nodules at the bottom and bedded chert at the top, is present in the middle of the formation. $\delta^{13}\text{C}$ of the least-altered calcite matrix components from five sections, of 15 to 72 m thick, shows no obvious correlation with $\delta^{18}\text{O}$, thus its variations can be considered primary. The $\delta^{13}\text{C}$ hovers around $0 (\pm 1.5)\text{‰}$ in the bottom half of the sections and dips to -5.3‰ in the cherty horizon, and then bounces back to positive values ($4.0 \pm 2.0\text{‰}$) in upper portions - reaching as high as 6.6‰ in one section (Fig. 4). There is a basin wide consistency in the $\delta^{13}\text{C}$

variation and it mimics the ~ 800 Ma Bitter Spring anomaly observed globally. The lowest observed $^{87}\text{Sr}/^{86}\text{Sr}$ of 0.70676, associated with lowest Mn/Sr and high positive $\delta^{13}\text{C}$ (4.5‰), suggests that the Balwan Limestone most likely was deposited during 780 ± 100 Ma. This would mean that the sedimentation in the Vindhyan basin continued well into the Neoproterozoic and the closure of the basin predates the major global glacial events of the Cryogenian.

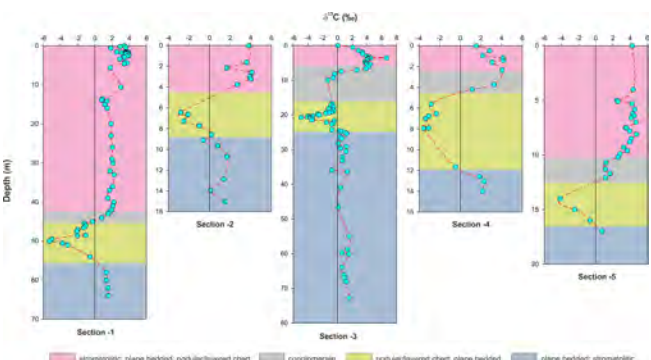


Figure 4: Plot of $\delta^{13}\text{C}$ versus depth in five sections of the Balwan Limestone Formation studied in this work.

(J.S. Ray, A.D. Shukla, B.G. George, A. Chatterjee and I. Gautam)

Dependence of $\mu^{142}\text{Nd}$ anomalies on the choice of terrestrial standard

$^{142}\text{Nd}/^{144}\text{Nd}$ isotope ratio is a tracer of the early differentiation of the silicate Earth. Anomalous $\mu^{142}\text{Nd}$ values, where $\mu = (((^{142}\text{Nd}/^{144}\text{Nd})_{\text{rock}} / (^{142}\text{Nd}/^{144}\text{Nd})_{\text{terrestrial standard}}) - 1) \times 10^6$, have been widely used for deciphering nature and timing of such early differentiation events. The very definition of μ assumes that the $^{142}\text{Nd}/^{144}\text{Nd}$ of the terrestrial standard is equivalent to that of the modern accessible mantle. Unfortunately, however, several recent studies have shown that the $^{142}\text{Nd}/^{144}\text{Nd}$ ratios of commonly used terrestrial standards are not identical. The same is true for other non-radiogenic isotopic ratios of Nd as well. Our analyses of Ames Nd and JNdi-1 reveal that $^{142}\text{Nd}/^{144}\text{Nd}$ of JNdi-1 ($n=11$) is 6 ppm lower than that of the Ames Nd (long-term average). Therefore, it is highly likely that a $\mu^{142}\text{Nd}$ anomaly observed with respect to one standard might disappear with the other. We did observe exactly the same while analyzing alkaline rocks/TTG from India, wherein negative/zero values with respect to Ames Nd became zero/positive when calculated against JNdi-1. Thus it is highly desirable that the terrestrial standard (and its $^{142}\text{Nd}/^{144}\text{Nd}$) be fixed uniformly. JNdi-1 appears to be a good candidate for the purpose.

(I. Gautam and J.S. Ray)

The GEOTRACES-India cruise in the Indian Ocean

The GEOTRACES-India cruise onboard Sagar Kanya (SK 338, GI10) was started on January 28, 2017 from Chennai and ended (Fig. 5) on March 3, 2017 at Goa with about 20 participants (Fig. 5a). During 35 days of cruise time samples for Trace elements and isotopes in

seawater, sediments and aerosol have been collected in the Bay of Bengal, the Andaman Ocean, the Indian Ocean and the Arabian Sea in 25 sampling stations. The cruise was successful and most of the objectives of the cruise were met, as follows:

Accomplishments on cruise SK 338:

1. Sampling has been done on 25 stations during the cruise SK 338.
2. A total of 51 clean CTD casts have been done during the cruise time to study biogeochemical cycles of trace elements and their isotopes.
3. McLANE is operated successfully 12 times (at 5 stations) to collect the particulate matter.
4. Continuous aerosol sampling was done while ship was on move.
5. Sampling was done at Japanese cross-over station in the Bay of Bengal.

Onboard analytical analysis of parameters:

1. Measurement of basic parameters like pH, Salinity, Alkalinity and dissolved oxygen analysis have been done onboard.
2. Ammonia, Nitrate, Nitrite, Silicate and Phosphate have been measured onboard.
3. Dissolved Zinc in the seawater has been analysed onboard using Zn-FIAS system by Fluorometric detection.

(V. Chinni, S.K. Singh and all cruise participants)

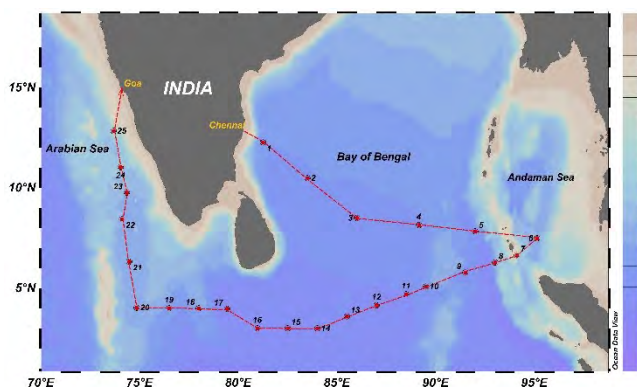


Figure 5(a): SK 338 - Cruise Track, 5(b): SK 338 - Cruise participants

Fluorometric detection of nanomolar level concentrations of dissolved Zinc (DZn) in the seawater

Zinc (Zn) is considered as an essential trace nutrient for microorganisms in the seawater, which limits the primary production. Zn present in nanomolar (nM) levels in the open Ocean seawater. Measuring nM level concentrations of Zn in seawater is highly

challenging due to its ubiquitous nature, which is more prone for contamination. With the establishment of sensitive flow injection system, we can measure DZn concentrations precisely without any contamination problems. The technique couples flow injection system with fluorometric detection. An iminodiacetate resin is used to separate Zn from the seawater matrix at a pH of 5.10 ± 0.05 . Zn-pTAQ fluorescent complex is formed by mixing the pTAQ with the Zn eluted from the AF Chelate- 650 M (Iminodiacetate) resin. The fluorescence

was measured using Shimadzu RF 20A fluorometer at an excited and emission wavelength of 365 nm and 500 nm respectively. Method has been tested by using the available international reference standards. A single sample can be analysed in 9 min. The system was fully operated automatically by using software interface developed in Labview. The schematic diagram below shows the Zinc Flow injection system (Zn-FIS).

Low Zinc seawater is prepared by passing surface sample collected in open ocean region through Nobias resin at a pH of 5.1 ± 0.1 to remove Zn from the seawater. This column passed seawater was used for making the working standards in seawater. A five-point calibration line was run every time during the analysis of seawater samples. Each sample was measured twice. Reference standards, internal standard and blanks were measured during the analysis of seawater samples. All bottles used were made of Teflon which were rigorously cleaned by following the trace metal clean sampling protocols. An interface was prepared using Labview software to measure samples without any user interference. In the following figures, we can see the typical profile for Zn, a five-point calibration line and chromatogram for all the

samples during one analytical cycle.

The accuracy and method establishment was checked by measuring the GEOTRACES reference seawater standards for Zn provided by Prof. Kenneth Bruland, University of California, Santa Cruz using Zn-FIS (Table 1).

Table 1: Reported and consensus values for the GEOTRACES reference standards.

S.NO	Standard	Reference value (nM)	Lab value (nM)
1	D ₁	7.40± 0.35	7.62± 0.12 (n [*] =6)
2	GD	1.71± 0.12	1.81± 0.03 (n [*] =6)

* n = No. of samples

(V. Chinni, M.S. Shah and S.K. Singh)

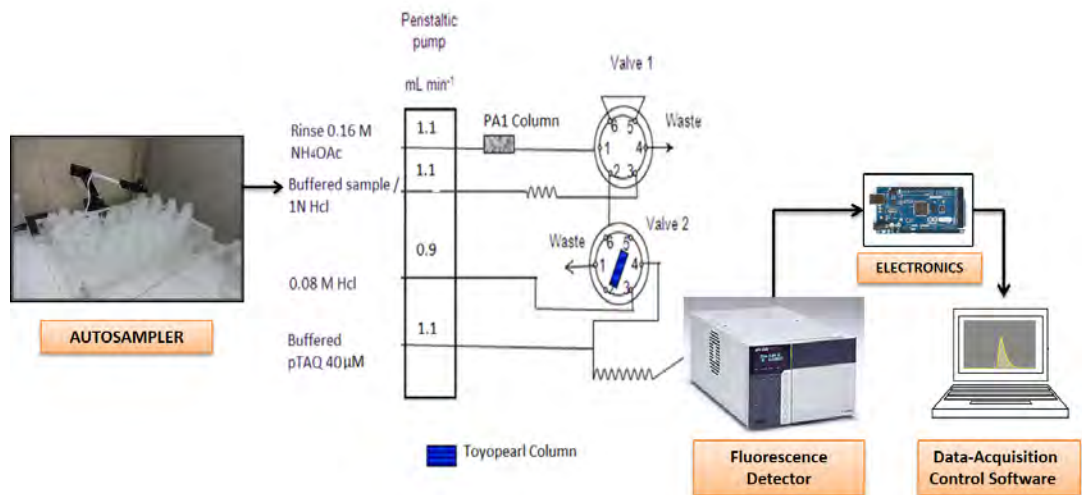


Figure 6: Schematic diagram of Zn-FIS.

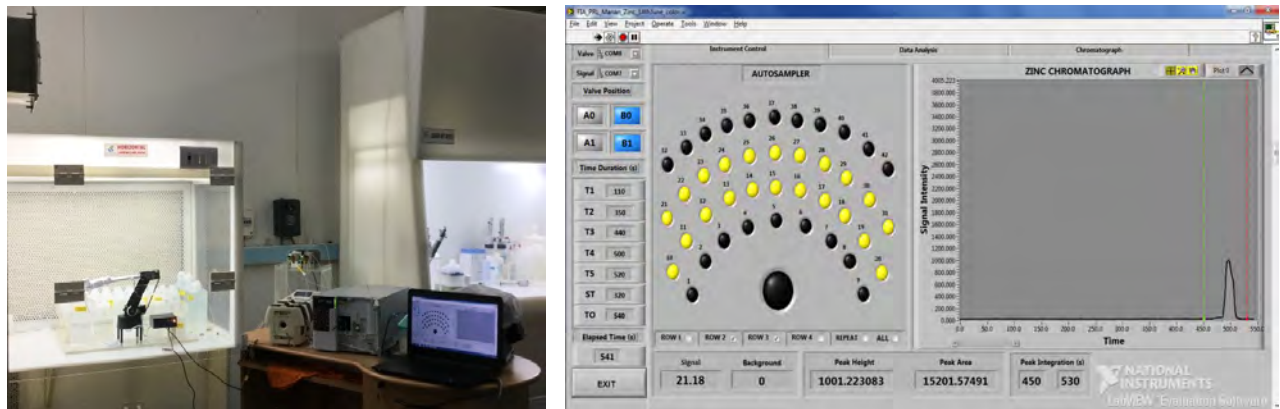


Figure 7(a): Zinc flow injection system (Zn-FIS), Figure 7(b): Instrument control Panel.

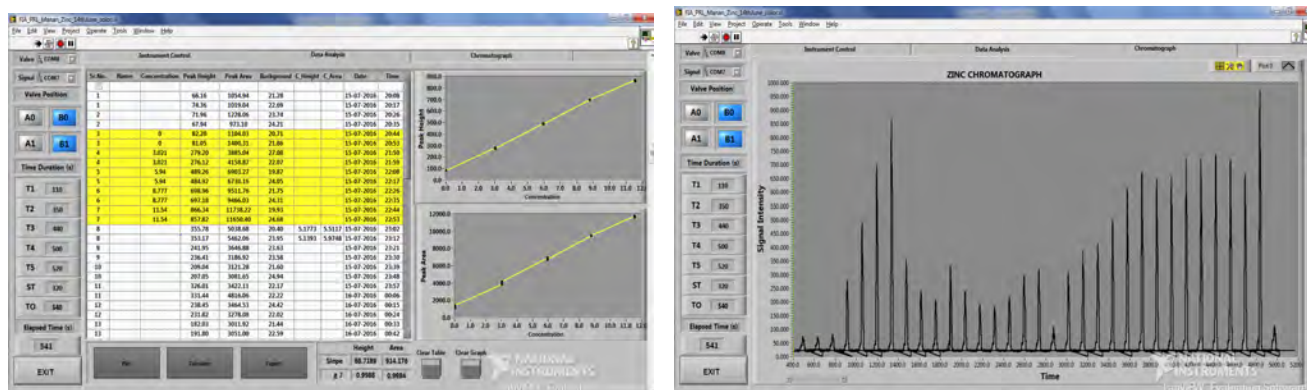


Figure 8(a): Data and Analysis Tab showing an external calibration graph. Figure 8(b): Chromatograms for the samples.

Dissolved Zinc (DZn) distributions from the Northeastern and Indian Oceans

Total dissolved Zinc (DZn) were analyzed in 12 full vertical profiles in the northeastern Indian Ocean including Andaman Sea and Indian Ocean. DZn was measured using flow injection system by fluorometric detection. Overall, the DZn concentrations range from 0.24 nM to 11.53 nM (Fig.9 and 10) with surface low and increased with depth, indicating a typical nutrient type distribution.

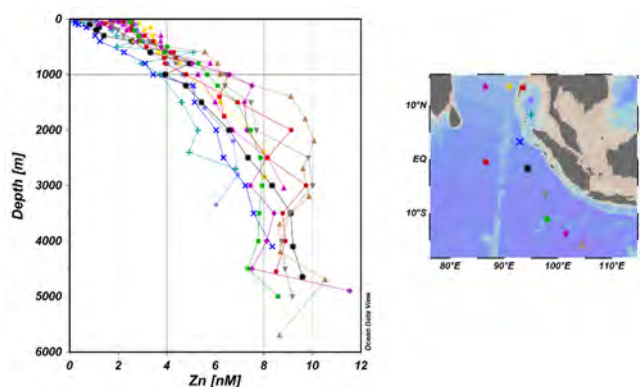


Figure 9: DZn vertical profiles from Northeastern and Indian Oceans. Samples collected during SK-304.

Relatively high surface (≤ 25 m) concentrations were observed in the northern stations closer to the river prone Ganga-Brahmaputra, Irrawaddy and Salween rivers compared to the southern stations. A strong Zn-Si relationship was observed in all the stations sampled in the northeastern Indian Ocean with a slope consistent to a global average value. Decoupling of Zn and Si in some of the stations where dissolved oxygen is less than $50 \mu\text{M}$ has been observed in the transect. Similar observations on decoupling of Zn and Si in the water column were observed in the oxygen minimum zone (OMZ) regions of the Northeast Pacific Ocean. The plausible reason for the observed low slopes between Zn and Si in the OMZ could be due to the formation of Zinc Sulfides. We observe this decoupling

phenomenon between Zn and Si in sampling stations from the Andaman Sea that gives relatively lower slope than those observed for north-eastern Indian Ocean and the average value of global ocean.

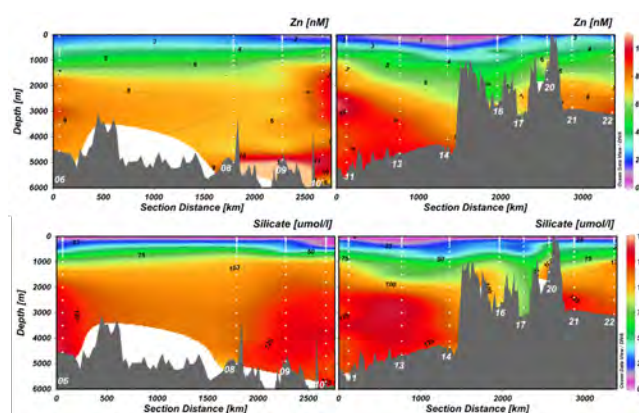


Figure 10: Section plot for DZn during SK-304 cruise.

The concentrations of Zn in deep waters (>1200 m) of the Andaman Sea are continuously replenished with intermediate waters of the Bay of Bengal. This observation suggests a continuous vertical mixing in the water column of the Andaman Sea with the incoming waters of northeastern Indian Ocean. These findings are vital to understand the biogeochemical cycle of Zn to better estimate the link between Zn and the Carbon cycle.

(V. Chinni, S.K. Singh, R. Bhushan and R. Rengarajan)

Dissolved ϵ_{Hf} in the Indian Ocean waters: Implications to the sources trace metals and isotopes

Recent studies suggest that the dynamics of Nd and Hf isotopic compositions (ϵ_{Nd} and ϵ_{Hf}) in ocean waters can be used to track the oceanographic circulations and their sources. Very limited data of ϵ_{Hf} is available in global seawaters, due to analytical complications associated with measuring very small quantities of Hf. As a part of GEOTRACES-India programme, Hf isotopic compositions were

measured, for the first time, in the Arabian Sea and northeast Indian Ocean water columns to distinguish the sources and distribution patterns of trace metals and isotopes and water masses. In the Arabian Sea (AS) water column, ϵ_{Hf} varies from -10.74 to +2.14 (Fig.11). Surface waters in the northern AS are unradiogenic in ϵ_{Hf} compared to southern AS, indicating the continental input from the Himalaya and aeolian inputs regulates the chemical composition of the northern AS surface waters. However, ϵ_{Hf} varies with a narrow range of -2.16 to 2.14 in the intermediate to bottom waters of the Arabian Sea (Fig. 11), signifying that, the north Atlantic deep waters (NADW) and Antarctica bottom waters (AABW) controls of these waters. In the northeast Indian Ocean waters, ϵ_{Hf} varies from -10.35 to +7.78 (Fig.11). Surface waters of the Indian Ocean are quite less radiogenic Hf, which is possibly resulting from the dissolution of unradiogenic Hf from the sediments delivered from the Ganga-Brahmaputra (G-B) system in the north and dust deposition from Australian deserts in the southern Indian Ocean. Deep and bottom waters of Andaman Sea have high radiogenic ϵ_{Hf} , which could be due to local input from volcanos. Deep and bottom waters in the Bay of Bengal (BoB) moderately less radiogenic, could be due to leaching of sediment discharged from the G-B system. The intermediate waters of the BoB are radiogenic in Hf, similar to those of the Andaman Sea, which indicates the supply of the intermediate water from the Andaman to the Eastern BoB. However, the deep and bottom waters from the Indian Ocean display a ranges of ϵ_{Hf} 0.32 to 4.96 and -0.56 to +3.95, (Fig.11) respectively, close to the NADW and AABW ϵ_{Hf} values reported in the Atlantic Ocean, which indicate that, the NADW and AABW regulate the deep and bottom waters in the Indian Ocean.

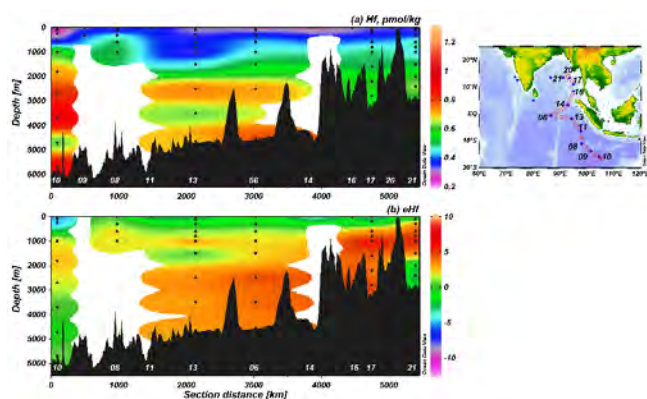


Figure 11: The distribution patterns of (a) concentration of Hf and (b) ϵ_{Hf} in the Indian Ocean water column along with the sampling locations.

(K. Damodharao, S.K. Singh, R. Bhushan and R. Rengarajan)

Insights into hydro-meteorological processes revealed from long term Isotope data of precipitation at Ahmedabad

A long term (12 years) oxygen and hydrogen isotopic dataset ($\delta^{18}O$ and δD) of daily precipitation samples collected at Physical Research Laboratory, Ahmedabad during 2005 to 2016 has been examined in conjunction with ground based and remotely sensed meteorological parameters to understand both systematic and erratic hydrometeorological processes operating in this semi-arid region, and its inter-annual variability.

A compilation of daily rainfall on each rainy day, ground level temperature, $\delta^{18}O$ and d-excess ($= \delta D - 8 \times \delta^{18}O$) and Rh is shown in Fig.12.

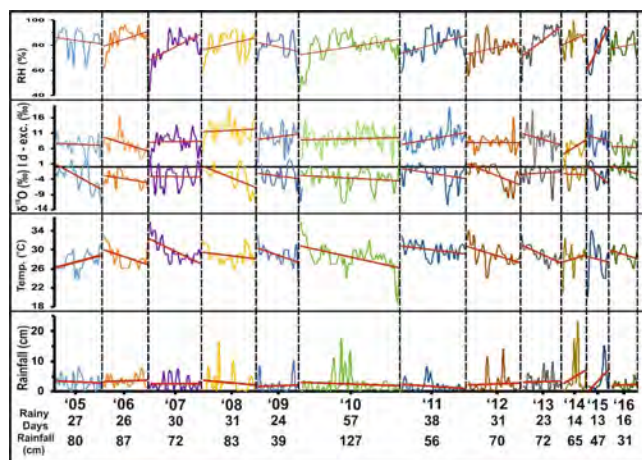


Figure 12: A compilation of daily rainfall on each rainy day, ground level temperature, $\delta^{18}O$ and d-excess ($= \delta D - 8 \times \delta^{18}O$) and Rh

A conspicuous isotopic depletion in precipitation is observed in the later half of monsoon (August-September) in 10 out of 12 years suggesting a systematic hydro-meteorological process which occurs during most of the monsoon seasons. As such there are several processes which can cause isotopic depletion in rain, but since there is a seasonal pattern of isotopic depletion in the later part of the monsoon, there must be some systematic seasonal transition in the processes / factors causing isotopic depletion, which has been enquired in this study.

A $\delta^{18}O$ - δD plot of month wise isotopic composition of daily rain events with d-excess values in the common range of 10 ± 10 ‰ (d-excesses: 20 to 0 ‰) is shown in Fig.13, with inset showing bar diagram of amount weighted average monthly $\delta^{18}O$ values for June to September. Isotope depletion in later half of monsoon is obvious from the fact that out of 146 rain events in the months of June-July, only 33 events (i.e. 23%) had $\delta^{18}O$ values lower than the amount weighted seasonal average of -4.1‰. Correspondingly, of the 97 rain events with $\delta^{18}O$ values lower than the amount weighted seasonal average (-4.1‰), 65 events (i.e. 67%) occurred in the month of August-September.

In order to discern the factors / processes responsible for late monsoon isotopic depletion the corresponding variation in d-excess, temperature, Rh and wind trajectories have been evaluated which suggests that temperature and Rh are not the principal controlling factors; instead, contribution of terrestrial vapour source increases in the latter half of monsoon season. This is possibly because of the increased availability of water in the terrestrial environment (lakes, rivers, fields, soil, forests etc.)

Isotopically erratic rain events (i.e. having d-excess > 20 ‰ or < 0 ‰) have been examined in light of the four important parameters ($\delta^{18}O$, δD , d-excess and rain amount) as a subset of entire dataset in the form of a $\delta^{18}O$ - δD regression plot. The $\delta^{18}O$ - δD regression line for samples with normal range (10 ± 10 ‰) of d-excess values (20 to 0 ‰) has regression line slope (7.8) and intercept (8) values similar

to the global meteoric water line (GMWL: slope = 8; Intercept=10). However, if erratic rain events are included, the regression line slope (7) and intercept (5) differs considerably from GMWL.

The erratic rain events can be broadly grouped in to four categories: 1. low d-excess, low rainfall; 2. Low d-excess, high rainfall; 3. High d-excess, low rainfall; 4. High d-excess, high rainfall. These events of four categories seem to be associated with unusual weather situation such as, strong convection, localised winds, cyclonic disturbances and heat wave. These unusual weather situations effectively results in admixture of variable proportion of continentally derived moisture with marine vapour. However, interpretation of individual erratic rain events is complicated because other meteorological parameters such as cloud height, cloud top temperature, degree of supersaturation, cloud liquid content can affect isotopic composition of rainfall.

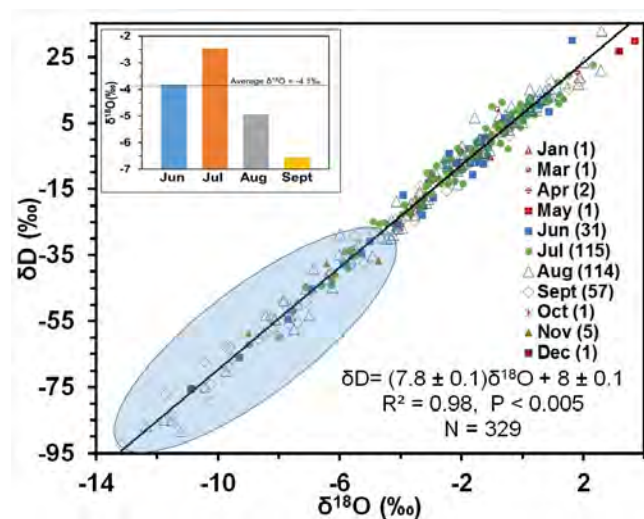


Figure 13: A $\delta^{18}\text{O}$ - δD plot of month wise isotopic composition of daily rain events with d-excess values in the common range of $10 \pm 10\text{‰}$ (d-excesses: 20 to 0 ‰). Numbers in parenthesis represents no. of rain events.

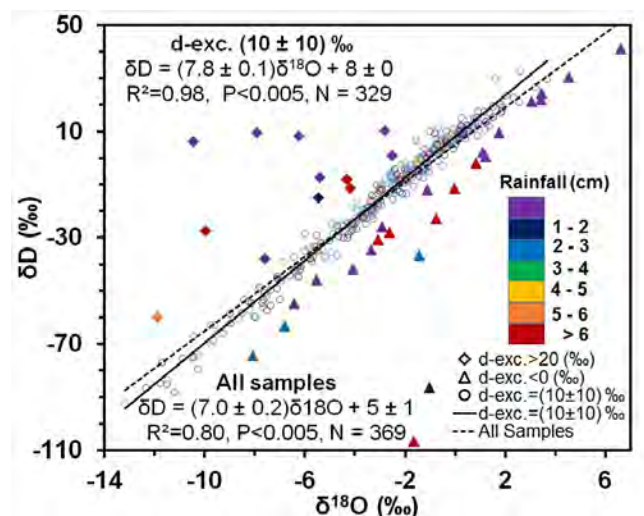


Figure 14: A $\delta^{18}\text{O}$ - δD regression plot for daily rain events at Ahmedabad during 2005 to 2016.

The detailed study of processes and factors responsible for the observed systematic patterns and the erratic events in daily rainfall is continuing. This knowledge is important for obtaining early insights about the ongoing subtle changes in contemporary hydrological processes.

(H. Oza, V.R. Padhya and R.D. Deshpande)

Isotope characterisation of shallow groundwater across India

Isotope characterization of shallow groundwater across the country was initiated under the IWIN National Programme. The Central Ground Water Board (CGWB) was the principal collaborator which provided the groundwater samples (nearly 6000 samples) during several annual campaigns organized by regional directorates of CGWB. Analyses of all these samples have been completed recently by the IWIN Mass Spectrometer Laboratory at PRL. Compilation and interpretation of the entire isotope data has been initiated in collaboration with a team from CGWB which provides geohydrological inputs.

As a first major outcome of this programme, pre-monsoon and post-monsoon isotope maps of shallow ground water of India are available for $\delta^{18}\text{O}$ (Fig.15) and d-excess (Fig.16). It is noteworthy from the sampling location map, that barring States in northeast and north with logistic issues and the state of Rajasthan with paucity of shallow groundwater wells, entire country is well represented in the isotope maps.

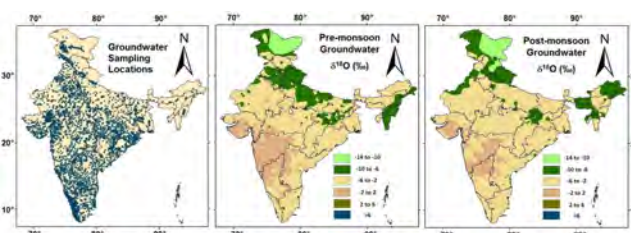


Figure 15: Pre-monsoon and post-monsoon $\delta^{18}\text{O}$ maps of shallow groundwater in India

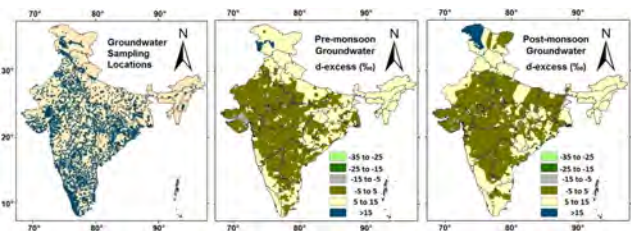


Figure 16: Pre-monsoon and post-monsoon d-excess maps of shallow groundwater in India.

Seasonal variation in $\delta^{18}\text{O}$ (Fig.15) and d-excess (Fig.16) can be interpreted in terms of recharge characteristics in different parts of the country. The shallow groundwater in most part of the country is found have higher $\delta^{18}\text{O}$ values during the pre-monsoon season compared to the post-monsoon season. However, there are some regions where $\delta^{18}\text{O}$ values are higher in post-monsoon compared to pre-monsoon

season. Corresponding seasonal changes are also observed in case of d-excess values of shallow ground waters.

These observations can be broadly explained in terms of: 1. Influx of isotopically lighter rainwater during post-monsoon season or its absence depending on the geohydrology and rainfall; 2. Influx of isotopically lighter water transported by canal or rivers from higher altitude regions during pre-monsoon season and influx of isotopically heavier rainwater (compared to water transported from higher altitude regions) during post-monsoon season; 3. Presence or absence of recharge through preferential migratory pathways; 4. Recharge from surface reservoirs or surface water bodies; 5. Pumping effect due to withdrawal of water from shallow aquifers. Regions specific recharge characteristics and the principally responsible factor (among the above possibilities) is being identified for which isotope data are being interpreted in conjunction with detailed hydrogeological information. This programme of national and societal interest is being pursued and is progressing depending on availability of geohydrological inputs from the CGWB.

This work was carried out in collaboration with S.N. Dwivedi and Dipankar Saha from CGWB.

(V.R. Padhya and R.D. Deshpande)

Mid-Late Holocene paleomonsoon reconstruction from Diu mudflats, Western India

Unlike glacial-interglacial periods, mid-late Holocene remained deprived of drastic climate perturbations.

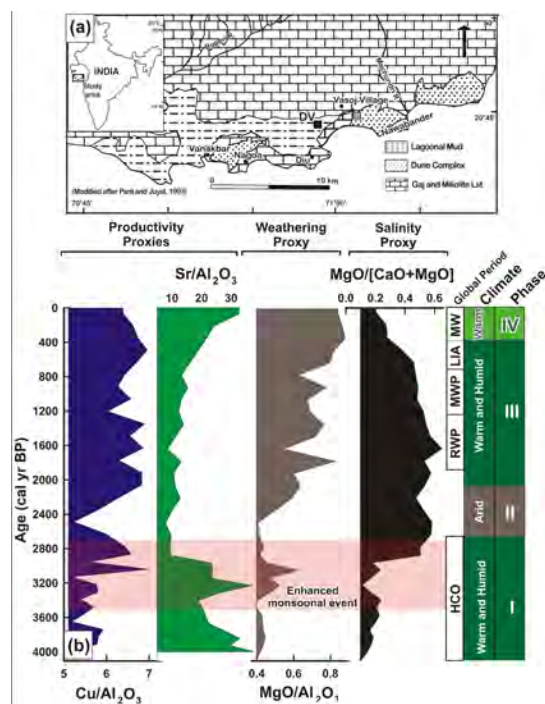


Figure 17: [a] Geological map of southern Saurashtra coast. The core location DV is marked by filled square. [b] Reconstruction of the paleoclimate based on geochemical proxies suggesting ISM fluctuation during last 4000 yr BP for the western India.

The Indian subcontinent witnessed fluctuations in Indian summer monsoon (ISM) causing extreme droughts and flood events in last few decades. The mudflats of Diu Island, western India which mainly receive detrital contribution primarily due to activation of ephemeral rivers during ISM rainfall, is an ideal analogue for deciphering Holocene ISM variability. Multi-proxy approach on a sediment core supported by radiocarbon dates from active mudflat of Diu Island provides climatic records for the last 4000 yr BP. Based on geochemical proxies (productivity, weathering and detrital), warm and humid conditions between 4105–2880 cal yr BP and 1930–355 cal yr BP due to ISM intensification interspersed with arid conditions between 2880–1930 cal yr BP can be observed (Fig.17). The mudflat has responded in accordance with the global climatic perturbations during last 4000 yrs. Signatures of Roman Warm Period (RWP) and Medieval Warm Period (MWP) followed by cool and humid Little Ice Age (LIA) with persistence of recent warming since last 300 yr has been evidenced.

This study was carried out in collaboration with Prof. A.J.T. Jull from NSF Arizona AMS Laboratory, University of Arizona, Tucson, AZ 85721, USA

(U.S. Banerji and R. Bhushan)

Evidence of anoxic bottom water during LGM near equatorial Indian Ocean

Redox sensitive elements have been extensively used to decipher past redox conditions at sediment-water interface which in turn helps in identifying the bottom water anoxic conditions in oceanic basins.

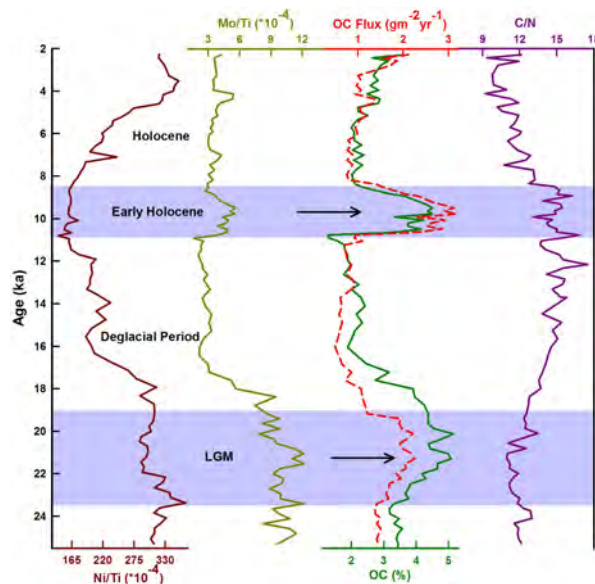


Figure 18: Downcore variation of redox proxies sensitive proxies and organic carbon (OC) suggesting preservation of OC during LGM and early Holocene Period.

Multi-proxy approach on a radiocarbon dated sediment core was employed to ascertain the late Quaternary changes in the redox conditions at sediment-water interface near equatorial Indian Ocean. Enrichment in redox sensitive elements such as Mo and Ni along

with organic carbon in the sediment core during Last Glacial Maxima (LGM) suggests prevalence of anoxic condition due to poorly ventilated bottom waters (Fig.18). Whereas, high organic carbon with depleted redox sensitive element during early Holocene indicates better preservation of organic carbon as a result of high sedimentation rate. The study underlines the process of organic carbon preservation resulted due to poor bottom water ventilation and high sedimentation rate during LGM and early Holocene respectively.

This work has been carried out in collaboration with Prof.A.J.T.Jull, NSF Arizona AMS Laboratory, University of Arizona, Tucson, AZ 85721, USA

(K.R. Chandana and R. Bhushan)

Coastal Eutrophication along the western continental margins of India

Reconstruction of climate change for last two centuries has been the prime focus to delineate the impacts of natural and anthropogenically induced perturbations. To address decadal scale climate changes, a sediment core (SM-29/13-03; Water depth: 30 m) from the continental shelf of the Arabian Sea, off Goa was investigated for various geochemical proxies.

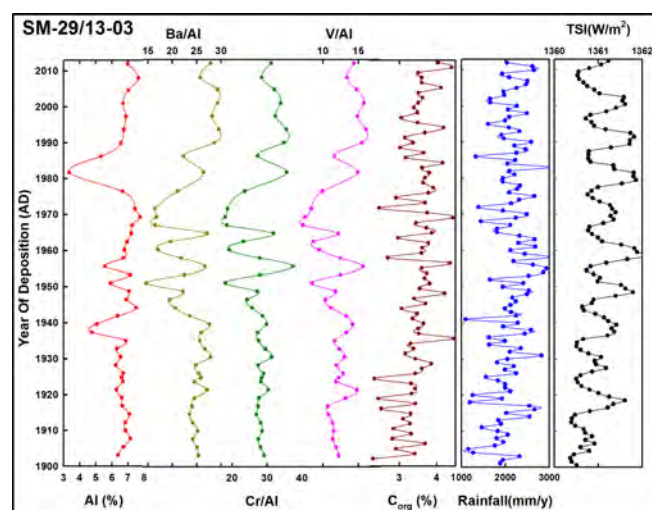


Figure 19: Comparison of depth-profiles of productivity proxies with rainfall and TSI in the Arabian Sea core SM-29/13-03.

The chronology of the core was ascertained by ^{210}Pb dating technique supported by ^{137}Cs which provided a depositional history of last ~ 115 yr. Based on instrumental rainfall record, Total Solar Irradiance (TSI) and downcore variation of geochemical proxies, it has been observed that there existed rather low productivity with simultaneously low monsoonal conditions till 1940 AD, followed by a marginal increase in the productivity and rainfall till 1970 AD. Interestingly post-1970 AD, enhanced productivity was observed along with gradual decline in the rainfall (Fig.19). Such contrasting signatures post-1970 AD imply that both natural and anthropogenic perturbations were responsible for causing enhanced terrestrial nutrient supply resulting in high productivity between 1970-2013 AD.

Increased anthropogenic activities in the form of mining, coastal recreation, marine transportation along the Goa coast post-1970 AD has been reported which might have resulted in high nutrient supply leading to enhanced productivity (eutrophication) along Goa coastal shelf post-1970 AD.

(R. Bhushan, C. Shah and U. S. Banerji)

Coral growth rates from Amini Island, Lakshadweep

Corals are marine organisms mostly found in tropical shallow marine regions living in symbiotic relationship with zooxanthellae algae and secrete carbonaceous skeleton forming wall like structure known as reefs. They form alternate dense and light bands annually that provide geochemical changes occurring in sea water during their growth.

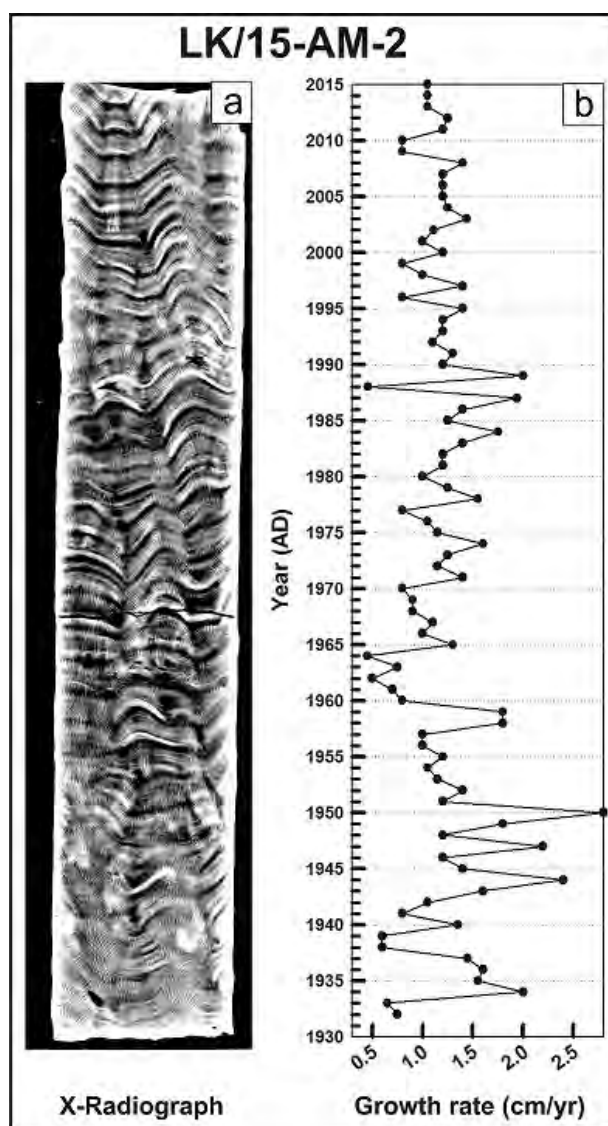


Figure 20: (a) X-radiograph of the coral core slice showing alternate dark and light bands; (b) Bandwidth (cm) V/s Year plot showing a decreasing trend in band thickness.

The identification of dense and light band couplet can provide chronology and growth rate for corals. The annual bands of corals provide high-resolution paleoclimatic and paleoenvironmental conditions prevailed during their growth. Nearly ~1m long coral drill core was retrieved from the Amini Island of Lakshadweep Islands for paleoclimatic study from the tropical Indian ocean. X-Radiograph of the coral slice was analysed to ascertain the chronology and growth rate (Fig.20). The X-radiograph of the coral core showed typical alternate dark and light bandings, suggestive of oscillating warm and cold sea surface temperature in the region (Fig. 20a). Based on the band couplet counting, age of the coral core extends up to 1930. The growth rate of the Amini coral ranges between 0.4 to 2.4 cm/year with an average growth rate of 1.2 cm/year. Slowest and rapid growth of ~0.4 and ~2.4 cm/yr is evidenced during 1965 and 1950 respectively (Fig.20b). High-resolution sampling of the Amini Coral is being carried out for further analysis of $\Delta^{14}\text{C}$, $\delta^{13}\text{C}$, $\delta^{18}\text{O}$ and trace elements to decipher the past variation in SST, ocean acidification, rainfall, salinity and monsoonal winds.

(H. Raj, U.S. Banerji, C. Shah and R. Bhushan)

Installation of 1 MeV Accelerator Mass Spectrometer (AMS) PRL-AURiS: Accelerator Unit for Radioisotope Studies

A 1 MeV Accelerator Mass Spectrometer (AMS) procured under the XIIth five-year plan was successfully installed in PRL Thaltej campus (Figure 21).



Figure 21: View of PRL Accelerator Mass Spectrometer (AURiS)

AMS consists of an accelerator combined with a mass spectrometer meant for the measurement of isotope ratios in a very small amount of samples quantity (mg level). PRL AMS has been specifically tuned for the measurement of the cosmogenic radioisotopes, ^{14}C , ^{26}Al and ^{10}Be with half-life of the order of thousand to millions of years. The present AMS comprises following units:

1. Ion Source,
2. Bouncer Injector Magnet Assembly,
3. 1 MV Accelerator with Argon as stripper gas,
4. High Energy Magnet,

5. Electrostatic Analyser,
6. Low Background Magnet and,
7. Gas Ionisation Detector.

The machine has been tested for the detection of ^{14}C , ^{26}Al and ^{10}Be isotopes; ^{14}C at 1.0 MV terminal voltage (charge state +2), ^{10}Be at 1.0 MV (+1) and ^{26}Al at 700 kV (+1) with precision and background as per the specifications (Table 1). The AMS acronymed as PRL-AURiS (Accelerator Unit for Radioisotope Studies) would provide a major thrust to PRL research in the field of earth and planetary sciences.

Table 1: Precision and background levels achieved during the performance test of ^{14}C , ^{26}Al and ^{10}Be isotopes.

Isotopes			Expected value	Measured value
1	$^{14}\text{C}/^{12}\text{C}$	Isotope ratio	5×10^{-16}	3.9×10^{-16}
		Precision	0.2%	0.2%
2	$^{10}\text{Be}/^9\text{Be}$	Isotope ratio	1×10^{-15}	5.8×10^{-16}
		Precision	1%	0.5%
3	$^{26}\text{Al}/^{27}\text{Al}$	Isotope ratio	5×10^{-15}	1.6×10^{-14}
		Precision	1%	0.5%

(R. Bhushan, M.G. Yadava, M. S. Shah, A. Dabhi and H. Raj)

Influence of western Arabian Sea upwelling on southwest monsoon rainfall

The strength of Indian summer monsoon has major impact on socio-economic conditions of the Indian sub-continent. Understanding the factors responsible for the past variation in southwest monsoon rainfall has been one of the main focus areas of palaeoclimate and climate modelling. To understand the relation between western Arabian Sea upwelling and southwest monsoon rainfall, history of the Somali upwelling during the last 18.5 ka has been reconstructed using biogenic silica fluxes, estimated from western Arabian sea sediment core. The reconstructed record demonstrates periodic weakening and strengthening of the Somali upwelling during the past 18.5 ka. Variations in biogenic silica fluxes suggest weak upwelling during the last glacial period (18.5-15 ka BP). Strengthened upwelling during the Bolling-Allerød period (15-13 ka BP) points to post-glacial onset of the ISM. The Younger Dryas (13-11 ka BP) is again marked by reduced upwelling strength. Intensification of the Somali upwelling in early Holocene and decline at 8 ka BP are observed (Fig.22). Increase in upwelling strength recorded since 8 ka BP suggests strengthening of the ISM during the later part of the Holocene. Based on upwelling variations and ISM precipitations, a major shift in the relationship between the strength of the Somali upwelling and southwest monsoon rainfall from positive to negative can be observed during pre-Holocene to the Holocene. The observed shift is attributed to the variation in the ISM strength due to the latitudinal change of the Intertropical Convergence Zone (ITCZ) associated with changes in moisture sources.

This work is being carried out in collaboration with Prof. L.S. Chamyal and Mr. D. Balaji from M.S. University of Baroda, Vadodara.

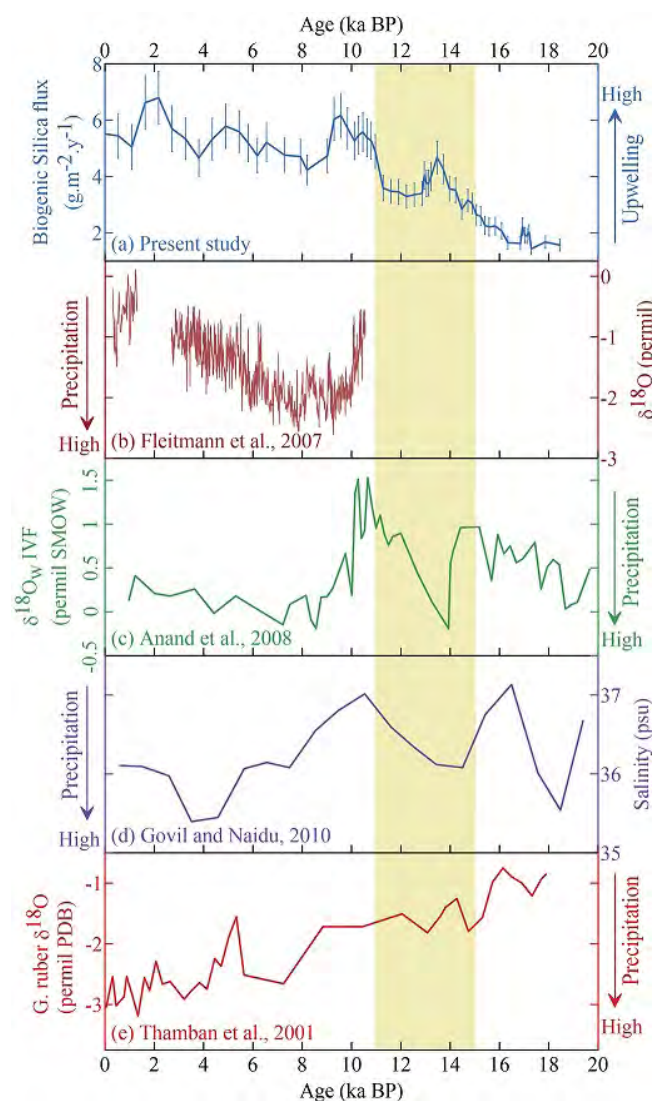


Figure 22: Comparison of Somali upwelling with southwest monsoon rainfall records. (a) Biogenic silica flux (present study), (b) Oman speleothem record, (c) $\delta^{18}\text{O}_w$ data from sediment core SK-17, (d) Salinity record of sediment core AAS9/21, (e) $\delta^{18}\text{O}$ record of sediment core GC-5. Shaded region marks the deglacial period.

(R. Bhushan)

Isotopic composition of rain and cave seepage water

Stalagmites (cave deposits) have a great potential for providing monsoon reconstruction for hundreds of thousands of years. It is necessary to understand how the rainwater isotopic composition is modified when it percolates down in the soil and bedrocks before it becomes drip water through which stalagmites are formed. Effect of evaporation can be seen from the observed data in a typical study carried out in Belum cave, Kurnool district of Andhra Pradesh. It suggests that the rainwater is evaporated to some extent before becoming part of the cave hydrology (Fig. 23).

The present work was carried out with collaboration from University Of Hyderabad.

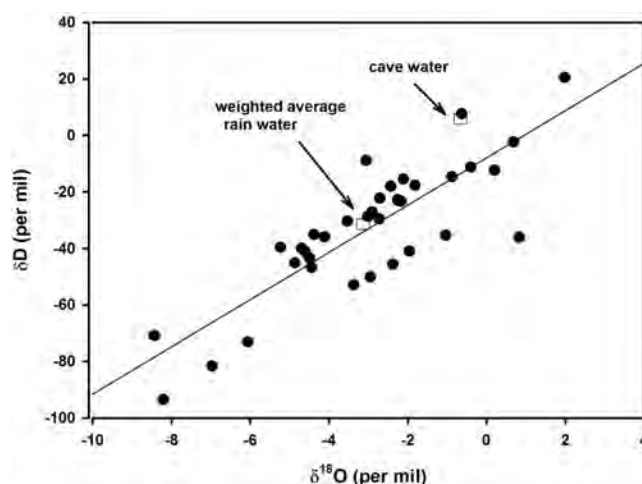


Figure 23: δD vs. $\delta^{18}\text{O}$ plot for all the rainwater samples collected above the Belum cave. Boxes show the weighted average isotopic compositions of the rain water ($\delta^{18}\text{O} = -3.1$ ‰ and $\delta\text{D} = -31.5$ ‰) and average isotopic composition of drip water ($\delta^{18}\text{O} = -0.7$ ‰ and $\delta\text{D} = -5.6$ ‰).

(M.G. Yadava, R. Ramesh and R. A. Jani)

Nitrogen and Carbon Cycling in the Indian Ocean: International Indian Ocean Expedition 2 (IIOE-2)

Detailed exploration of physico-chemical and biological properties of the Indian Ocean began with the first International Indian Ocean Expedition (IIOE-1) from 1959–1965. Major parameters measured during that time were primary productivity using ^{14}C -method, phytoplankton, zooplankton and fish abundances, nutrient concentrations, and physical properties. These investigations played a significant role in characterizing biogeochemical properties of the Indian Ocean and were stepping stone for the present Indian Ocean research. While completing 50 years of the first Indian Ocean expedition series, numerous direct and indirect methods have been developed to trace the biogeochemical behaviour of the ocean. To retrace the IIOE-1 series expeditions, a similar set of expeditions known as IIOE-2 series have begun with more advanced methods. We participated in the inaugural cruise from Goa to Mauritius to study the nitrogen (N) and carbon (C) transformation rates in the open Indian Ocean. Experiments to measure N and C uptake rates throughout the euphotic depth were performed at five locations using ^{15}N tracer technique. Samples were collected to measure the N and C isotopic composition in the particulate matter along with particulate N and C concentrations. Top 40 m of the euphotic depth at all locations was devoid of nitrate, which increased to $20\text{ }\mu\text{M}$ at 120 m. Ammonium concentrations varied from 0.03 to $1.2\text{ }\mu\text{M}$ in the upper 120 m. Nitrate and ammonium uptake rates in the euphotic depth varied from 0.001 – $0.051\text{ }\mu\text{mol N l}^{-1}\text{ h}^{-1}$ and 0.004 – $0.064\text{ }\mu\text{mol N l}^{-1}\text{ h}^{-1}$, respectively; with higher ammonium uptake compared to nitrate uptake at majority of depths. Isotopic composition of N and C in particulate matter varied from 5.39 to 9.54 and -25.8 to -23 per mil, respectively; indicating role of different biogeochemical processes in their origin and transformations.

(P.S. Bhavya and S. Kumar)

Carbon biogeochemistry of Indian estuaries

An extensive field campaign was carried out during April-May, 2016 to understand the carbon (C) biogeochemistry of anthropogenically impacted Hooghly estuary along with mangrove dominated estuaries of the Indian Sundarbans. The estuaries of Sundarbans showed signatures of marine dominance, whereas sharp salinity gradient was noticed for Hooghly estuary. Percentage dissolved oxygen indicated estuaries of Sundarbans to be well oxygenated compared to that of Hooghly. Significant correlation between $\delta^{13}\text{C}_{\text{DIC}}$ and salinity, and departure from conservative mixing line at Hooghly indicates control of fresh and seawater mixing along with organic matter degradation/respiration and CO_2 out-gassing on DIC pool. In contrast, at the estuaries of Sundarbans, DIC appears to be mainly regulated by *in situ* biogeochemical processes. Mean dissolved organic carbon (DOC) level at the major estuaries of Indian Sundarbans was $\sim 47\%$ lower compared to that of Hooghly. Both estuarine systems were supersaturated with respect to CO_2 and CH_4 . $p\text{CO}_2$ at Hooghly estuary was regulated by fresh and saline water mixing as well as *in situ* organic matter respiration while the same was principally exogenous for the estuaries of Indian Sundarbans. But, dissolved CH_4 was entirely exogenous for both estuarine systems. Calculation of air-water exchange flux indicates both estuarine systems to be source of CO_2 and CH_4 to the regional atmosphere.

(M. K. Dutta, R. Mukherjee and S. Kumar)

Study of sources and fate of organic matter in India's largest lagoon and nearby mangrove ecosystem

The organic matter in lake sediments participates in variety of biochemical and geochemical processes. Benthic animals and microbes depend on these organic matter for their survival. The detritus of plants that grow in water and on the nearby land comprises the primary source of organic matter to the bottom sediments. The main aim of this study is to understand the dynamics and cycling of sedimentary organic matter in two different kinds of ecosystems in the east coast of India, i.e., Asia's largest brackish water lagoon (Chilika) and nearby mangrove system (Bhitarkanika; India's second largest mangrove ecosystem). For this study, sediment cores were collected by using a gravity corer up to 30 cm (Chilika) and 60 cm (Bhitarkanika) at eight and three locations, respectively. The samples at different depths were analysed for organic carbon ($\delta^{13}\text{C}$) and nitrogen ($\delta^{15}\text{N}$) isotopic composition and content. Both organic C and N content in the lagoon were higher in northern part where it receives high terrestrial inputs from the distributaries of Mahanadi. $\delta^{13}\text{C}$ in the Chilika lagoon surface sediments varied from -19.91‰ to -21.90‰ and $\delta^{15}\text{N}$ ranged from 3.34‰ to 4.63‰ . Surface C/N ratio of the lagoon ranged between 3.21 to 9.35. In Bhitarkanika mangroves, surface $\delta^{13}\text{C}$ and $\delta^{15}\text{N}$ varied from -24.29‰ to -25.31‰ and 3.91‰ to 4.69‰ , respectively. For all depths, $\delta^{15}\text{N}$ of the organic matter showed overlapping signature in both ecosystems, whereas $\delta^{13}\text{C}$ was clearly different (Fig.24). Similar kind of distinction was observed in C:N where Chilika sediments showed lower values compared to that of mangrove sediments. The study clearly points towards different sources of organic matter and responsible biogeochemical processes in these two ecosystems.

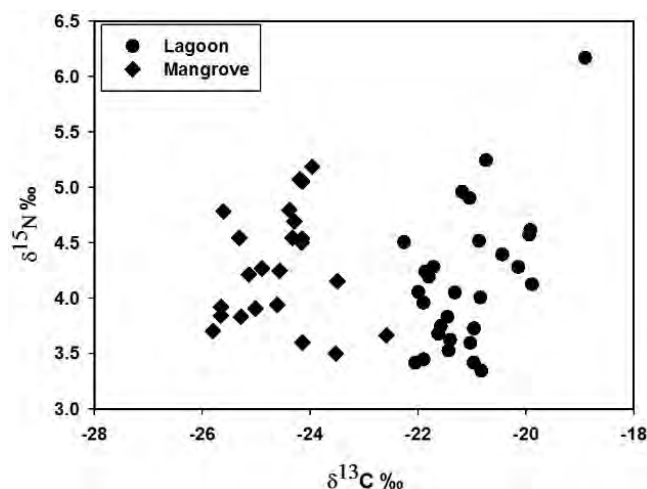


Figure 24: $\delta^{15}\text{N}$ and $\delta^{13}\text{C}$ in sediment organic matter of the Chilika and mangrove ecosystems (Bhitarkanika). Data include all depths.

(R. Mukherjee and S. Kumar)

Nitrogen cycling in soils from different ecosystems of India

Nitrogen (N) plays an important role in controlling the ability of plants to fix atmospheric CO_2 , making them one of the dominant sinks for this potent greenhouse gas. Reactive N, which is usually required by the plants during photosynthesis, is limited in soils due to tough competition for nutrients between plants and soil microbes along with losses by leaching or volatilization. The availability and type of N species (nitrate, ammonium or dissolved organic N) vary with climate and ecosystems, which in turn depends on the rates of cycling of N from one pool to the other. In order to fully understand the cycling of N in tropical setting like India and its effect on the CO_2 sequestration potential by biota, the rates of N transformations must be known. A research program focussed on measuring gross mineralization rates was initiated during 2015 which involved tedious experiments involving isotope dilution techniques. A pilot study carried out in the forests of Kerala, reported in last annual report, indicated effect of land use change on N cycling. Given the varied climatic zones and ecosystems in India, this study has been extended to cover the wet and arid climate for which soil samples from the Western Ghats and Rann of Kutch have been collected and experiments are being carried out.

(N. Sharma and S. Kumar)

Diurnal Characteristics of Atmospheric Brown Carbon over the Indo-Gangetic Plain

Atmospheric carbonaceous aerosols consist of black carbon and organic carbon, and influence Earth's radiative balance by interacting with solar radiation. A significant part of organic aerosols absorbs light (known as brown carbon) is poorly characterized in terms of physicochemical and optical properties. To assess the role of BrC

on regional/global level, it is inevitable to understand their sources and characteristics on temporal and spatial scale. However, such studies are limited in literature. Semi-continuous measurements of water-soluble organic carbon (WSOC) and BrC were performed using particle-into-liquid sampler coupled to liquid waveguide capillary cell and total carbon analyser (PILS-LWCC-TOC) over Kanpur (26.5°N, 80.3°E), a site located in the middle of the Indo-Gangetic Plain (IGP). The IGP spread over northern India perennially receives large amount of primary particles and precursors of secondary particles from vehicles, industries, large-scale post-harvest biomass burning, and bio-fuel burning. Diurnal variability in the absorption coefficient of BrC at 365 nm (b_{abs365}) showed higher values ($35 \pm 21 \text{ Mm}^{-1}$) during late evening through early morning, and attributed to primary emissions from biomass burning and fossil fuel burning. The b_{abs365} reduces by more than $\sim 80\%$ as day progresses, which is ascribed to photo bleaching/volatilization of BrC. Further, diurnal variability in ratios of b_{abs405}/b_{abs365} and b_{abs420}/b_{abs365} suggests that BrC composition was not uniform throughout the day. WSOC exhibited a strong correlation with b_{abs365} , suggesting the presence of significant but variable fraction of chromophores. It is concluded that absorption property of BrC reduces during daytime due to photo-bleaching of BrC and/or due to its volatility.

This study was carried out in collaboration with Prof. S.N. Tripathi (IIT, Kanpur).

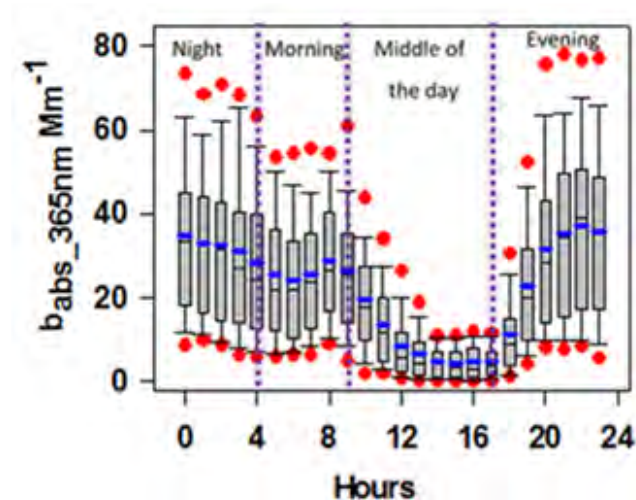


Figure 25: Box-whisker plot showing diurnal trends of b_{abs365} . The boundary of the box closest to zero indicates the 25th percentile, black and blue lines within the box represent median and mean, respectively, and the boundary of the box farthest from zero indicates the 75th percentile. Error bars above and below the box indicate the 90th and 10th percentiles. Red circles are indicative of outliers.

(R.V. Satish and N. Rastogi)

Brown, Black, and Organic Carbon in Ambient Aerosols over the Indo-Gangetic Plain: Role of Emissions from Crop-Residue Burning

Carbonaceous aerosols are mainly composed of organic carbon (OC) and black carbon (BC). Until recently, BC was the major known light absorbing species in the atmospheric aerosols. Recent studies have shown that a certain type of OC also absorb light at

near UV and visible region, and termed as "Brown Carbon" (BrC), which can also affect Earth's radiative forcing as well as cloud evaporation. Further, secondary organic aerosols (SOA) are highly variable fraction of ambient organic aerosols but poorly characterized in literature. Emissions from both biomass and fossil fuel burning are significant sources of carbonaceous species in the atmosphere; however, knowledge on their characteristics on temporal and spatial scale is limited over Indian sub-continent. The main focus of this study is to understand the characteristics of carbonaceous species (especially BrC and SOA) before, during, and after biomass burning episodes over the Indo-Gangetic Plain (IGP). Seventy hi-vol PM_{2.5} filter samples (day/night pairs) were collected before (T1), during (T2) and after (T3) a large scale paddy-residue burning over Patiala (30.2°N, 76.3°E), located in the northwestern IGP.

Temporal variability of OC, elemental carbon (EC), water-soluble OC (WSOC, a measure of SOA), and BrC during the study period is depicted in Fig. 26. Strong diurnal variability was observed with significantly higher nighttime concentrations during T2, which is attributed to source activity (burning usually occurred during evening hours) and shallower boundary layer in the night. OC/EC ratios varied from 2.7 to 19 during the study period with almost double OC/EC ratio (average: 7.3) during T2 in comparison to that during T1 and T3. BrC increased significantly during T2 and remained similar during T3, unlike other carbonaceous species. It was observed that emissions from crop-residue burning almost doubles the fine particles abundances in the atmosphere. Abundances of all carbonaceous species increased significantly during burning period, however, BrC remained similar during post-burning period too, unlike other carbonaceous species. Such studies are necessary but limited over Indian sub-continent.

Logistic support for the sample collection was provided by Mr. Atinderpal Singh and Prof. Darshan Singh (Punjab University, Patiala).

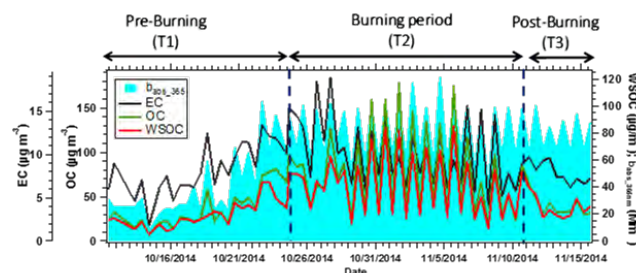


Figure 26: Temporal variability of OC, EC, WSOC, BrC during the study period.

(R.V. Satish and N. Rastogi)

DTT activity of ambient fine aerosols over the Indo-Gangetic Plain

Several studies have depicted direct relationship between high concentrations of ambient aerosols and morbidity and mortality. One of the widely proposed mechanism related to how aerosols affect human health is that several chemical species in aerosols, when inhaled through breathing, produce reactive oxygen species (ROS)

in-situ in human respiratory system. Capability of aerosols to produce ROS is also termed as their oxidative potential (OP). Production of ROS causes imbalance between oxidants and anti-oxidants in the body and may lead to several cardiopulmonary diseases. ROS not only affect the health of human and plants but also atmospheric oxidizing capacity and secondary aerosol formation. The OP of ambient fine aerosols have been measured using most widely used dithiothreitol (DTT) assay over Patiala, Punjab which is located in the Indo-Gangetic Plain (IGP). Subsequently, the chemical species responsible for higher OP were investigated. Elemental carbon (EC) was found to be positively correlated with OP, suggesting the sources emitting EC also produces toxic species and/or their precursors. EC can be emitted from fossil fuel burning (FFB) and/or biomass burning (BB) events. To investigate whether any difference in the toxicity level of species derived from FFB vis-à-vis BB, a ratio BC_{370}/BC_{880} was used with the understanding that $BC_{370}/BC_{880} \leq 1$ represent the dominance of FFB whereas ≥ 1 indicate the dominance of BB. Results suggest that carbonaceous aerosols coming from the BB are more toxic than those coming from FFB (Fig 27). Such studies have more importance in designing the mitigation strategies in terms of air quality.

Logistic support for the sample collection was provided by Mr. Atinderpal Singh and Prof. Darshan Singh (Punjabi University, Patiala).

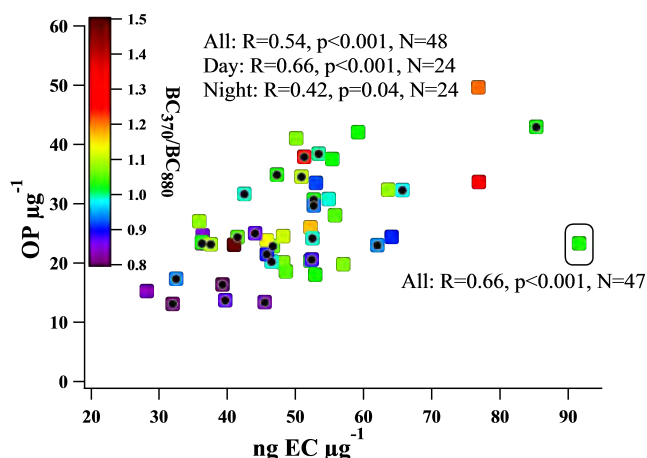


Figure 27: Scatter plot between $OP \mu g^{-1}$ and $EC \text{ mass fraction } (ng \mu g^{-1})$. Color scale shows BC_{370}/BC_{880} ratio in corresponding sample. Black dots in the square represent day time samples. Squarred datum was excluded from linear regression analysis.

(A. Patel and N. Rastogi)

The Holocene floods and their affinity to climatic variability in the western Himalaya, India

The past flood records in the Satluj river valley are investigated to understand the role of regional and global climatic processes in generating the extreme hydrological events. Based on the textural characteristics, ~25 flood events have been identified. The geochemical analyses of the flood sediments suggests that these floods were originated in the higher and trans-Himalaya possibly due to the breaching of the lakes created by the landslides viz.

the landslide lake outburst floods (LLOFs) with some contribution from the glacial lake outburst, viz. the glacial lake outburst floods (GLOFs). Optical chronology indicates that the floods can be clustered in to four major phases dated between 13.4-10.4 ka, 8.3-3.6 ka, 2.2-1.4 ka, and <1.4 ka respectively. Climatically these phases correspond to the cooler and less wet conditions which broadly correlate with the phases of negative Arctic Oscillation (-AO) and negative North Atlantic Oscillation (-NAO). The study thus suggests that the extreme hydrological events in the Satluj valley were coupled between the moisture-laden monsoon circulation and southward penetrating mid-latitude westerly troughs for extreme precipitation events and consequent LLOFs. Importantly, a broad synchronicity in Holocene floods between the western Himalaya and across the mid-latitudinal region ($30^{\circ}N-40^{\circ}N$) suggests a synoptic scale Arctic and Atlantic climate variability.

(S. Sharma, A.D. Shukla and N. Juyal)

Exploring the Paleocene-Eocene Thermal Maxima (PETM) events in the Jaisalmer basin, Rajasthan, Western India.

Paleocene-Eocene Thermal Maximum (PETM) has become a focal point of considerable geoscience research because of the fact that it provides one of the most comprehensive analogues towards understanding the possible impact of increase carbon input to the ocean and atmosphere. So far the reconstruction of early Eocene hyperthermals (EEHS) are based on the sedimentary sequences located in the high-latitude deep ocean sites, with few sections reported from terrestrial environment. There is virtually, very little information exists from the shallow marine PETM sections. In the present study we investigated a shallow marine limestone dominated Paleocene-Eocene sequence (Khuijala Formation) exposed in Jaisalmer basin, western India. This sequence compares well with the reported shallow marine limestone in various part of the globe corresponding to PETM. The preliminary results suggest that the sequence has preserved the signature of PETM events as evident by the negative excursion in $\delta^{13}C$ in carbonates of ~4‰ and co-variation of $\delta^{13}C$ and $\delta^{18}O$. Detailed geochemical and isotopic study is under progress.

(A. Patra, S. Kumar and A.D. Shukla)

Geochemical Study of the Granitoids around Chhota Shigri Area, Himachal Pradesh, India

Alpine-Himalayan belt, lies in an important geodynamic position between the Eurasia and Gondwana. During the Himalayan collision tectonics, brought remobilized continental crust of the Indian Plate. Granitoid plutons associated with the constituents of collision belts are characterized by a large compositional diversity arising from different source compositions. Relationships among the stages of collision, the nature of the produced melts and their chemical composition are controversially discussed in magmatic provinces such as the Alpine-Himalayan orogenic belt. Pre-Himalayan granitoids are exposed in the Chhota Shigri area. Our preliminary geochemical study of the granitoids suggests that they are medium to high-potassic with calcalkaline affinity (peraluminous) with high content of SiO_2 , K_2O/Na_2O ratio, normative corundum, shows the studied granites are

of S-type granite. The granites have more fractionated nature of REE and minor negative Eu anomalies. The various types of granite and gneiss rocks present in the basement indicate the similar magmatic nature.

This work was carried out in collaboration with Dr. M. Bidyananda, Manipur Central University, Imphal

(A. D. Shukla)

Atmospheric input of inorganic nitrogen: Contribution from gaseous ammonia

A significant component of nitrogen cycle is represented by atmospheric deposition and is susceptible to undergo changes due to anthropogenic activities. Information on dry deposition fluxes of particulate inorganic nitrogen is available, but estimates on the contribution from gaseous ammonia (NH_3) is rather limited for Indian region. Real-time measurement of aerosol ionic composition and NH_3 over an urban location, Kochi, in west coast of southern India reveal that NH_3 can contribute significantly to the total atmospheric deposition of nitrogen. The average NH_3 concentration is $0.55 \mu\text{mol m}^{-3}$ during pre-monsoon period, and particulate NH_4^+ and NO_3^- are 0.26 and $0.071 \mu\text{mol m}^{-3}$ respectively. Low values of $\text{NH}_4^+ / (\text{NH}_4^+ + \text{NH}_3)$ ratios indicates the local sources of ammonia. Assuming the dry deposition velocity of particulate matter is $\sim 0.5 \text{ cm s}^{-1}$, the particulate inorganic nitrogen deposition is $\sim 140 \mu\text{mol m}^{-2} \text{ d}^{-1}$ which is comparable to that of gaseous ammonia. The results indicate that gaseous NH_3 can be a major component of atmospheric input of inorganic nitrogen to the oceanic region adjacent to Indian subcontinent during continental outflow period.

(A.K. Sudheer, R. Bhushan, S. K. Singh and R. Rengarajan)

Carbon export flux along the Indian GEOTRACES G102 section in the Arabian Sea and the Indian Ocean

^{234}Th ($t_{1/2} = 24.1 \text{ d}$), present in seawater, is a naturally occurring particle reactive radionuclide formed through the radioactive decay of its parent, ^{238}U ($t_{1/2} = 4.47 \times 10^9 \text{ y}$). The disequilibrium between ^{234}Th and ^{238}U is exploited to quantify fluxes of elements moving out of the euphotic zone by attaching on to sinking particles. As a part of the Indian GEOTRACES programme, high-resolution sampling was carried out on board Sagar Kanya (SK-312) at 11 stations in the Arabian Sea and the Indian Ocean during April - May 2014 from 17°N to 16°S along 65°E transect to estimate the particulate organic carbon export flux from the upper ocean. There is a sub-surface salinity maxima along 50 m depth in the Arabian Sea (Fig 28). In the Arabian Sea, there is hypoxic to anoxic conditions were observed below the euphotic zone. Average ^{234}Th fluxes integrated up to 100 m were 2612 and $1968 \text{ dpm m}^{-2} \text{ d}^{-1}$ for the Arabian Sea and rest of the Indian Ocean, respectively. These values are ~ 5 times higher than those observed on a similar transect along 87°E in the Bay of Bengal ($594 \text{ dpm m}^{-2} \text{ d}^{-1}$) and rest of the Indian Ocean ($539 \text{ dpm m}^{-2} \text{ d}^{-1}$). For the same season, the Arabian Sea and the Bay of Bengal showed highly contrasting carbon export trends (mean: 4.0 and $0.8 \text{ mmol C m}^{-2} \text{ d}^{-1}$, respectively).

As a dual tracer approach, carbon export was concurrently determined by using ^{210}Po - ^{210}Pb disequilibrium along the above transect. ^{226}Ra ($t_{1/2} = 1600 \text{ y}$) in seawater decays to ^{210}Pb ($t_{1/2} = 22.3 \text{ y}$) which further decays to ^{210}Po ($t_{1/2} = 138 \text{ d}$). The ^{210}Pb adheres to particle surface while ^{210}Po is removed both by surface adsorption and biological uptake. ^{210}Po export fluxes integrated up to 100 m varied from 3.5 to $38.4 \text{ dpm m}^{-2} \text{ d}^{-1}$ with high export flux near the north and south of equator. The ^{210}Po deficit flux and the $\text{POC}/^{210}\text{Po}$ ratio in sinking particulate matter are used to calculate the carbon export flux. High ^{210}Po based carbon export fluxes were found near equator, $14.0 \text{ mmol C m}^{-2} \text{ d}^{-1}$ and $11.3 \text{ mmol C m}^{-2} \text{ d}^{-1}$ at 5.5°S and 4°N , respectively. These trends are unique from that observed by ^{234}Th technique indicating that there exist a strong seasonal variation in phytoplankton production and carbon export in the equatorial Indian Ocean.

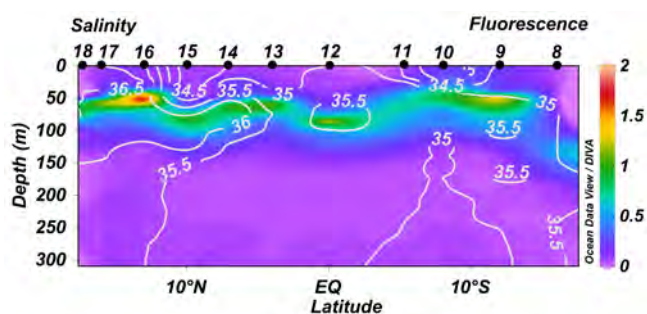


Figure 28: (a) Fluorescence is shown overlain with salinity (white contour lines with labels)

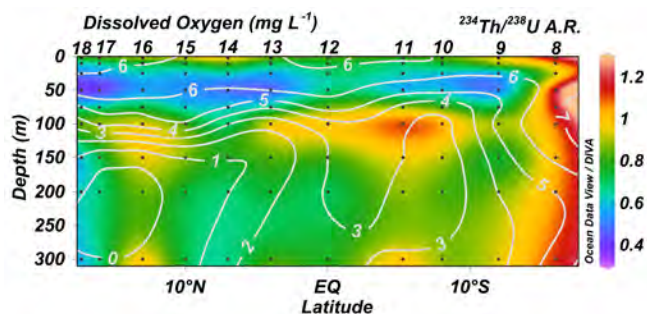


Figure 28: (b) $^{234}\text{Th}/^{238}\text{U}$ (A.R.) is overlain with dissolved oxygen (white contour lines with labels) along the GEOTRACES transect G102 section in the Arabian Sea and the Indian Ocean. The stations are denoted at the top and the black dots represent the ^{234}Th sampling depths.

(R. Rengarajan and S. Subha Anand)

Spatial distribution of POC export flux along the GEOTRACES G103 section

To estimate the spatial variability of upper ocean POC export flux in the south eastern Arabian Sea, Andaman Sea, Bay of Bengal and the Indian Ocean, 14 water column profiles of total ^{234}Th were measured as a part of the Indian GEOTRACES programme during March-May 2013 on board ORV Sagar Kanya (SK-304). The disequilibrium between ^{234}Th ($t_{1/2} = 24.1 \text{ d}$) and its parent ^{238}U and the $\text{POC}/^{234}\text{Th}$

ratio in sinking particles is used to calculate the export flux of carbon settling from the euphotic zone.

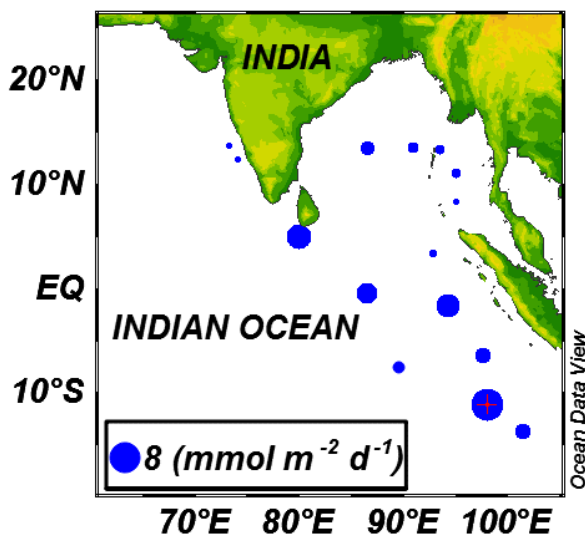


Figure 29: ^{234}Th derived POC export fluxes for the stations on the Indian GEOTRACES G103 section in the Arabian Sea, Bay of Bengal and the Indian Ocean. The area of the circles represents estimated POC export fluxes in $\text{mmol C m}^{-2} \text{d}^{-1}$.

^{234}Th export fluxes in the entire study region varied from negligible to $2025 \text{ dpm m}^{-2} \text{d}^{-1}$. These fluxes were high in the Indian Ocean (mean: $1373 \text{ dpm m}^{-2} \text{d}^{-1}$) followed by that in the Bay of Bengal (mean: $752 \text{ dpm m}^{-2} \text{d}^{-1}$) and the Andaman Sea ($148 \text{ dpm m}^{-2} \text{d}^{-1}$). High ^{234}Th export was recorded in the stations sampled near the equatorial Indian Ocean (5°N to 11°S). The reduced ^{234}Th export in the Bay of Bengal may be attributed to the prominent occurrence of mesoscale anticyclonic eddies. Very low ^{234}Th export in the Andaman Sea is perhaps due to low biological production, currents and proximity of the stations to the shelf region. The $\text{POC}/^{234}\text{Th}$ ratio varied from 0.976 to $5.11 \mu\text{mol dpm}^{-1}$. The high values were found in the Bay of Bengal ($13.5^\circ\text{N } 91^\circ\text{E}$) as well as near the equatorial Indian Ocean (3.63 and $4.87 \mu\text{mol dpm}^{-1}$ at 5°N and 11°S , respectively). The computed POC export fluxes varied from negligible to $7.3 \text{ mmol C m}^{-2} \text{d}^{-1}$, highest value being observed at 11°S near the equatorial Indian Ocean. Weak upwelling along the equatorial region could have enhanced the POC export flux. The average POC export flux in the Indian Ocean was $3.5 \text{ mmol C m}^{-2} \text{d}^{-1}$, whereas, the Arabian Sea, Bay of Bengal and the Andaman Sea recorded very low carbon export (negligible to $1 \text{ mmol C m}^{-2} \text{d}^{-1}$) during the premonsoon season (March-May) (Fig 29).

(R. Rengarajan, S. Subha Anand, R. Bhushan and S.K. Singh)

Science

Theoretical Physics

Z(3) metastable states in Polyakov Quark Meson model

We study the existence of Z(3) metastable states in the presence of the dynamical quarks within the ambit of Polyakov quark meson (PQM) model. Within the parameters of the model, it is seen that for temperatures T_m greater than the chiral transition temperature T_c , Z(3) metastable states exist ($T_m \sim 310$ MeV at zero chemical potential). At finite chemical potential T_m is larger than the same at vanishing chemical potential. We also observe a shift of ($\sim 5^\circ$) in the phase of the metastable vacua at zero chemical potential. The energy density difference between true and Z(3) metastable vacua is very large in this model. This indicates a strong explicit symmetry breaking effect due to quarks in PQM model. We compare this explicit symmetry breaking in PQM model with small explicit symmetry breaking as a linear term in Polyakov loop added to the Polyakov loop potential. We also study about the possibility of domain growth in a quenched transition to QGP in relativistic heavy ion collisions.

(H. Mishra and R. Mohapatra)

Heavy quarkonium moving in a hot and dense deconfined nuclear matter

We study the behavior of the complex potential between a heavy quark and its anti-quark, which are in relative motion with respect to a hot and dense medium. The heavy quark-antiquark complex potential is obtained by correcting both the Coulombic and the linear terms in the Cornell potential through a dielectric function estimated within real-time formalism using the hard thermal loop (HTL) approximation. We show the variation of both the real and the imaginary parts of the potential for different values of velocities when the bound state ($Q\bar{Q}$ pair) is aligned in the direction parallel as well as perpendicular to the relative velocity of the $Q\bar{Q}$ pair with the thermal medium. With increase of the relative velocity the screening of the real part of potential becomes weaker at short distances and stronger at large distances for the parallel case. However, for the perpendicular case, the potential

decreases with increase in velocity at all the distances which results in the larger screening of the potential. In addition, the inclusion of the string term makes the screening of the potential weaker as compared to the Coulombic term alone for both the cases. Therefore, combining all these effects we expect a stronger binding of a $Q\bar{Q}$ pair in moving medium in the presence of the string term as compared to the Coulombic term alone. The imaginary part decreases (in magnitude) with increase in the relative velocity leading to a decrease in the width of the quarkonium state at higher velocities. Inclusion of the string term increases the magnitude of imaginary part which results to increase the width of the quarkonium states. All of these effects lead to the modification in the dissolution of quarkonium states

(H. Mishra, L. Thakur and N. Haque)

Inverse magnetic catalysis and QCD running coupling in weak magnetic field

We study QCD running coupling using one loop hard thermal loop perturbation theory when thermal scale is the most dominant scale with respect to the thermal mass and magnetic field. In this study we show that QCD running coupling (α_s) decreases with increase in magnetic field (B) which is the clear indication of inverse magnetic catalysis (IMC). We follow same procedure as at zero temperature for calculating running coupling at finite temperature and non-zero magnetic field. We also study Debye screening in weakly magnetized quark-gluon plasma and found that in weak field Debye mass almost remain the same as unmagnetized quark-gluon plasma.

(B. Singh and H. Mishra)

Shear viscosity η to electrical conductivity σ_{el} ratio for an anisotropic QGP

We study the transport properties of strongly interacting matter in the context of ultra-relativistic heavy ion collision experiments. We

calculate the transport coefficients viz. shear viscosity (η) and electrical conductivity (σ_{el}) of the quark gluon plasma (QGP) phase in the presence of momentum anisotropy arising from different expansion rates of the medium in longitudinal and transverse direction. We solve the relativistic Boltzmann kinetic equation in relaxation time approximation (RTA) to calculate the shear viscosity and electrical conductivity. The calculation are performed within the quasiparticle model to estimate these transport coefficients and discuss the connection between them. We also compare the electrical conductivity results calculated from the quasiparticle model with the bag model. We compare our results with the corresponding results obtained in different lattice as well as model calculations.

(L. Thakur, P. Srivastav, G. Kadam, M. George and H. Mishra)

Calculations of Shear, Bulk viscosities and Electrical conductivity in Polyakov-Quark-Meson model

We have evaluated the transport coefficients of quark and hadronic matter in the frame work of Polyakov-Quark-Meson model. The thermal widths of quark and mesons, which inversely control the strength of these transport coefficients, are obtained from the imaginary part of their respective self-energies at finite temperature. Due to the threshold conditions of their self energies, some limited temperature regions of quark and hadronic phase become relevant for our numerical predictions on transport coefficients, which are grossly in agreement with earlier results.

(P.Singh, A. Abhisek, S. Ghosh, G. Kadam and H. Mishra)

Geometry-induced modification of fluctuation spectrum in quasi-two-dimensional condensates

We report the structural transformation of the low-lying spectral modes, especially the Kohn mode, from radial to circular topology as harmonic confining potential is modified to a toroidal one, and this corresponds to a transition from simply to multiply connected geometry. For this we employ the Hartree-Fock-Bogoliubov theory to examine the evolution of low energy quasiparticles. We, then, use the Hartree-Fock-Bogoliubov theory with the Popov approximation to demonstrate the two striking features of quantum and thermal fluctuations. At $T = 0$, the non-condensate density due to interaction induced quantum fluctuations increases with the transformation from pancake to toroidal geometry. The other feature is, there is a marked change in the density profile of the non-condensate density at finite temperatures with the modification of trapping potential. In particular, the condensate and non-condensate density distributions have overlapping maxima in the toroidal condensate, which is in stark contrast to the case of pancake geometry. The genesis of this difference lies in the nature of the thermal fluctuations.

(A. Roy and D. Angom)

Optical lattice influenced geometry of quasi-2D binary condensates and quasiparticle spectra

We explore the collective excitations of two-species Bose-Einstein condensates (TBECs) confined in quasi-two-dimensional (quasi-2D)

optical lattices. For this we use a set of coupled discrete nonlinear Schrödinger equations to describe the system, and employ Hartree-Fock-Bogoliubov (HFB) theory with the Popov approximation to analyze the quasiparticle spectra at zero temperature. The ground state geometry, evolution of quasiparticle energies, structure of quasiparticle amplitudes, and dispersion relations are examined in detail. We observe that the TBEC acquires a *side-by-side* density profile when it is tuned from miscible to immiscible phase. In addition, the quasiparticle energies are softened as the system is tuned towards phase separation, but harden after phase separation and mode degeneracies are lifted. In terms of structure, in the miscible phase the quasiparticles have well defined azimuthal quantum numbers, but that is not the case for the immiscible phase.

(K. Suthar and D. Angom)

RCCPAC: A parallel relativistic coupled-cluster program for closed-shell and one-valence atoms and ions in FORTRAN

We report the development of a parallel FORTRAN code, RCCPAC, to solve the relativistic coupled-cluster equations for closed-shell and one-valence atoms and ions. The parallelization is implemented through the use of message passing interface, which is suitable for distributed memory computers. The coupled-cluster equations are defined in terms of the reduced matrix elements, and solved iteratively using Jacobi method. The ground and excited states coupled-cluster wave functions obtained from the code could be used to compute different properties of closed-shell and one-valence atom or ion. As an example we compute the ground state correlation energy, attachment energies, E1 reduced matrix elements and hyperfine structure constants.

Work carried out in collaboration with B. K. Mani from IIT Delhi.

(B. K. Mani, S. Chattopadhyay and D. Angom)

Characteristic temperature for the immiscible-miscible transition of binary condensates in optical lattices

We study a two-species Bose-Einstein condensates confined in quasi-two-dimensional (quasi-2D) optical lattices at finite temperatures, employing the Hartree-Fock-Bogoliubov theory with the Popov approximation. We examine the role of thermal fluctuations on the ground-state density distributions, and the quasiparticle mode evolution. At zero temperature, the geometry of the ground-state in the immiscible domain is side-by-side. Our results show that the thermal fluctuations enhance the miscibility of the condensates, and at a characteristic temperature the system becomes miscible with rotationally symmetric overlapping density profiles. This immiscible-miscible transition is accompanied by a discontinuity in the excitation spectrum, and the low-lying quasiparticle modes such as slosh mode becomes degenerate at the characteristic temperature.

(K. Suthar and D. Angom)

Gravitino production in a thermal Universe revisited

We study the production of spin 1/2 gravitinos in a thermal Universe. Taking into account supersymmetry breaking due to the finite thermal energy density of the Universe, there is a large enhancement in the cross section of production of these gravitino states. We consider gravitinos with zero temperature masses of 0.1 eV, 1 keV, 100 GeV and 30 TeV as representative of gauge mediated, gravity mediated and anomaly mediated supersymmetry breaking scenarios. We find that the abundance of gravitinos produced in the early Universe is very high for gravitinos of mass 1 keV and 100 GeV. The gravitino abundances can be sufficiently suppressed if the reheat temperature is less than 100 GeV and 4×10^4 GeV respectively. However such low reheat temperatures will rule out many models of baryogenesis including those via leptogenesis.

(R. Arya, N. Mahajan and R. Rangarajan)

Asymmetries and observables for $\Lambda_b \rightarrow \Lambda \ell^+ \ell^-$

The semi-leptonic $b \rightarrow s$ decays provide a unique opportunity to test physics beyond the standard model. Experiments have provided some hints of discrepancies between the theoretical predictions and observations. The baryonic decay, $\Lambda_b \rightarrow \Lambda \ell^+ \ell^-$, has been studied in detail and new angular observables have been proposed which can test the standard model and also help discriminate different new physics models.

(G. Kumar and N. Mahajan)

$B^- \rightarrow D^{(*)} \tau \bar{\nu}_\tau$ excesses in ALRSM constrained from B, D decays and $D^0 - \bar{D}^0$ mixing

Many experiments in the flavour sector are hinting at some new physics beyond the standard model. Within the context of a specific left-right symmetric model, various anomalies have been shown to have a consistent explanation after imposing stringent constraints from many different flavour observables.

(C. Hati, G. Kumar and N. Mahajan)

Light neutrino contribution: is it all there is to neutrinoless double beta decay?

Perturbative one loop QCD corrections to the light neutrino contribution to neutrinoless double beta decay are considered for the first time and large enhancement to the rate are found. QCD corrections also generate structures which mimic new physics contributions that usually in many extensions of the standard model. Within some approximations, the net effect seem to almost saturate the experimental limits, and therefore seems to imply that there may not be much room for new physics beyond the standard model in explaining neutrinoless double beta decay.

(N. Mahajan)

Constraints on Scalar Leptoquark from Kaon Sector

The flavour anomalies, as observed by various experiments, could possibly be addressed by a scalar leptoquark. The constraints on such a leptoquark couplings to the standard model particles from the kaon decays and mixing have been considered for the first time. It is found that the model can be tightly constrained, and at the same time the different set of couplings involved yield similar or tighter constraints than those from bottom meson decays.

(G. Kumar)

Dynamical Conductivity of Dirac Materials

For graphene (a Dirac material) it has been theoretically predicted and experimentally observed that DC resistivity is proportional to T^4 when the temperature is much less than Bloch-Grüneisen temperature and T linear in opposite case. Going beyond the DC case, we investigate the dynamical conductivity in graphene using the powerful method of memory function formalism. Several new results are obtained. With the experimental advancement of this field, these results should be experimentally tested.

(L. Rani and N. Singh)

Probing Nonstandard interactions in Future Neutrino Oscillation Experiments

We studied the effect of non-standard interactions (NSI) on the propagation of neutrinos through matter and how it affects the hierarchy sensitivity of the DUNE experiment. We emphasize on the special case when the diagonal NSI parameter $\epsilon_{ee} = 1$ and nullifies the standard matter effect. We show that, if in addition, there is maximal CP violation then this gives rise to an exact intrinsic hierarchy degeneracy, in the appearance channel, irrespective of the baseline and energy. Introduction of off-diagonal NSI parameter, ϵ , shifts the position of intrinsic degeneracy to a different ϵ_{ee} . Moreover the unknown magnitude and phases of the off-diagonal NSI parameters can give additional degeneracies. Overall, given the current model independent limit on NSI parameters, no hierarchy sensitivity can be observed in the DUNE experiment if NSIs exist in nature. A signal of neutrino mass hierarchy at DUNE will therefore be able to rule out certain ranges of the NSI parameters. We also studied the effect of NSI on CP sensitivity.

(S. Goswami, K. N. Deepthi and N. Nath)

Phenomenological study of extended seesaw model for light sterile neutrino

We study the zero textures of the Yukawa matrices in the minimal extended type-I seesaw (MES) model which can give rise to eV scale

sterile neutrinos. In this model, three right handed neutrinos and one extra singlet S are added to generate a light sterile neutrino. The light neutrino mass matrix for the active neutrinos, m , depends on the Dirac neutrino mass matrix (MD), Majorana neutrino mass matrix (MR) and the mass matrix (MS) coupling the right handed neutrinos and the singlet. The model predicts one of the light neutrino masses to vanish. We systematically investigate the zero textures in MD and observe that maximum five zeros in MD can lead to viable zero textures in m . For this study we consider four different forms for MR (one diagonal and three off diagonal) and two different forms of (MS) containing one zero. Remarkably we obtain only two allowed forms of m ($m_{ee} = 0$ and $m_{e\mu} = 0$) having inverted hierarchical mass spectrum. We re-analyze the phenomenological implications of these two allowed textures of m in the light of recent neutrino oscillation data. In the context of the MES model, we also express the low energy mass matrix, the mass of the sterile neutrino and the active-sterile mixing in terms of the parameters of the allowed Yukawa matrices. The MES model leads to some extra correlations which disallow some of the Yukawa textures obtained earlier, even though they give allowed one-zero forms of m . We show that the allowed textures in our study can be realized in a simple way in a model based on MES mechanism with a discrete Abelian flavor symmetry group $Z_8 \times Z_2$.

This work was done in collaboration with Monojit Ghosh from TMU, Tokyo, Japan and Shivani Gupta from University of Adelaide Australia.

(S. Goswami and N. Nath)

Naturalness, Vacuum Stability and Leptogenesis in the Minimal Seesaw Model

The right-handed neutrinos within the type-I seesaw mechanism can induce large radiative corrections to the Higgs mass, and naturalness arguments can then be used to set limits on their mass scale and Yukawa couplings. Driven by minimality, we consider the presence of two degenerate right-handed neutrinos. We compare the limits from naturalness with the ones from the stability of the electroweak vacuum and from lepton number violation. Implications from neutrinoless double beta decay are also discussed and renormalization effects for the light neutrino parameters are presented. Adding small perturbations to the degenerate heavy neutrino spectrum allows for successful leptogenesis.

This work was done in collaboration with Werner Rodejohann from Max Planck Institute, Heidelberg, Germany and P.S.B. Bhupal Dev from Washington University, USA.

(S. Goswami and G. Bambhanya)

Singlet extended standard Model for Neutrino Mass, Dark matter and Vacuum Stability

We considered Standard Model extended by fermion and scalar singlets. The fermion singlet extension can give rise to TeV scale seesaw models which can give rise to small neutrino masses. The singlet scalar is a candidate for the dark matter. We study the

effect of this model on the stability of the electroweak vacuum and find the parameter spaces for which vacuum is stable, unstable and metastable.

(S. Goswami, N. Khan and K.N. Vishnudath)

Decaying atmospheric neutrinos at INO

Neutrino oscillation solution to atmospheric neutrino problem is well established now and the focus has shifted to probe if subdominant solution to oscillations can be constrained from future data.

We explore the situation where one of the neutrino states decay so that one can have both decay and oscillations. At the analytical level the problem is interesting because the Hamiltonian in presence of decay is non-hermitian. We have worked on finding the methodology of diagonalizing such Hamiltonians. We have also studied the constraints that can be obtained on the neutrino decay parameter from atmospheric neutrinos at the ICAL detector of India-Based Neutrino Observatory (INO). We have also obtained the precision of atmospheric parameters in presence of decay. Further we have explored how the hierarchy sensitivity of INO is affected if the neutrinos are decaying.

This work is done in collaboration with Sandhya Choubey from Harish-Chandra Research Institute and Tarak Thakore from Louisiana State University, USA.

(S. Goswami, C. Gupta and L. S. Mohan)

Semi-invisible Tau pair production at LHC reconstruction

We study the possibility of utilizing the constrained mass variable, M_{2Cons} , in reconstructing the semi-invisible events originated from a resonant production at the LHC.

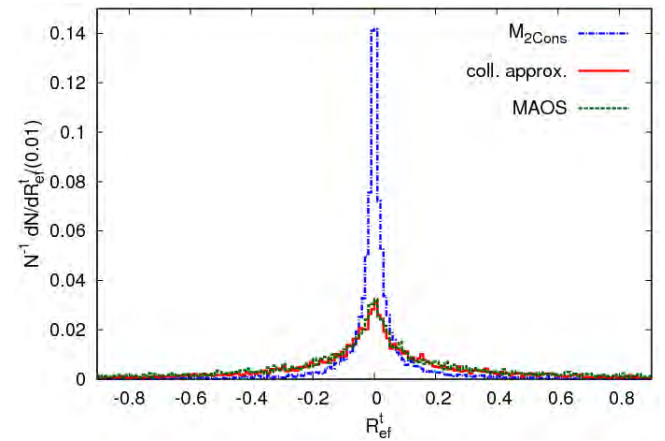


Figure 1: Efficiency of different methods for reconstructing the events coming from semi-invisible Higgs boson decay through τ pair production, after considering hadronic decays of τ , consists of both 1-prong and 3-prong decays. The event reconstruction capability of the collinear approximation and MAOS method are of same order, while M_{2Cons} , with the help of additional mass constraint, is showing significant improvement.

While this proposal is effective for any similar antler type production mechanism, here we demonstrate with a potentially interesting scenario, when the Higgs boson decays into a pair of the third generation τ leptons. Buoyed with a relatively large Yukawa coupling, the LHC has already started exploring this pair production to investigate the properties of Higgs in the leptonic sector. Dominant signatures through hadronic decay of tau, associated with invisible neutrinos compound the difficulty in the reconstruction of such events. Exploiting the already existing Higgs mass bound, this new method provides a unique event reconstruction, together with a significant enhancement in terms of efficiency over the existing methods.

(P. Konar and A.K. Swain)

Heavy neutrino production at the LHC Next to leading order

Majorana and pseudo-Dirac heavy neutrinos are introduced into the type-I and inverse seesaw models, respectively, in explaining the naturally small neutrino mass. TeV scale heavy neutrinos can also be accommodated to have a sizable mixing with the Standard Model light neutrinos, through which they can be produced and detected at the high energy colliders.

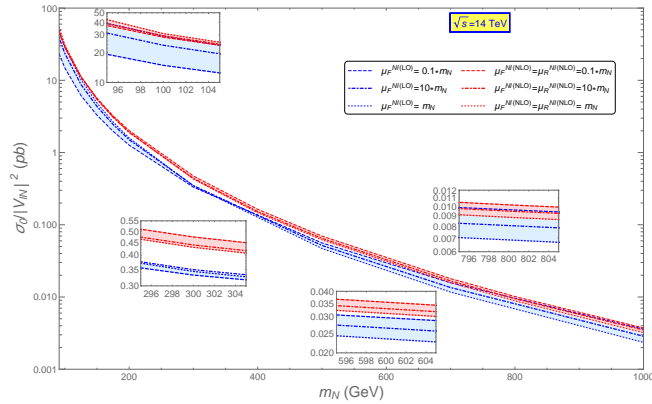


Figure 2: Heavy neutrino production cross-section from $pp \rightarrow \tilde{a} \tilde{D} S N$ at the 14 TeV LHC as a function of m_N . Both LO and NLO predictions are shown with the scale variation effect as a band. The cross-sections are normalized by the square of the mixing angles. Inset plots showing zoomed bands at different masses.

In this paper we consider the Next-to-Leading Order QCD corrections to the heavy neutrino production, and study the scale variation in cross-sections as well as the kinematic distributions with different final states at 14 TeV LHC and also in the context of 100 TeV hadron collider. The repertoire of the Majorana neutrino is realized through the characteristic signature of the same-sign dilepton pair, whereas, due to a small lepton number violation, the pseudo-Dirac heavy neutrino can manifest the trileptons associated with missing energy in the final state. Using the CM energy 8 TeV, 20.3 $fb^{\tilde{a}\tilde{L}\tilde{S}1}$ and 19.7 $fb^{\tilde{a}\tilde{L}\tilde{S}1}$ data at the ATLAS and CMS respectively, we obtain prospective scale dependent upper bounds of the light-heavy neutrino mixing angles for the Majorana heavy neutrinos at the 14 TeV LHC and 100 TeV collider. Further exploiting a recent study on the anomalous multi-lepton search by CMS at 8 TeV with 19.5 $fb^{\tilde{a}\tilde{L}\tilde{S}1}$ data, we also obtain the prospective scale dependent upper bounds on the

mixing angles for the pseudo-Dirac neutrinos. We thus project a scale dependent prospective reach using the NLO processes at the 14 TeV LHC.

This work was done in collaboration with Das, A. from Alabama Univ. and Majhi, S. from Achhruram Memorial College, WB.

(P. Konar)

Non-commutative geometry at Large Hadron collider

We study the Drell-Yan process at the Large Hadron Collider in the presence of the non-commutative (NC) extension of the standard model. Using the Seiberg-Witten map, we calculate the production cross section to first order in the noncommutative parameter $\Theta_{\mu\nu}$. The idea of field theories on the NC space-time is rather old, introducing a fundamental length scale in the model consistent with the symmetry. This outlook is further revived after realization of their possible connection with quantum gravity, where NC is perceived as an outcome of certain string theory embedded into a background magnetic field. Theoretically NC scale is unknown, but one can try to extract the lower bounds directly from the collider experiments by looking at the characteristic signals this framework can provide.

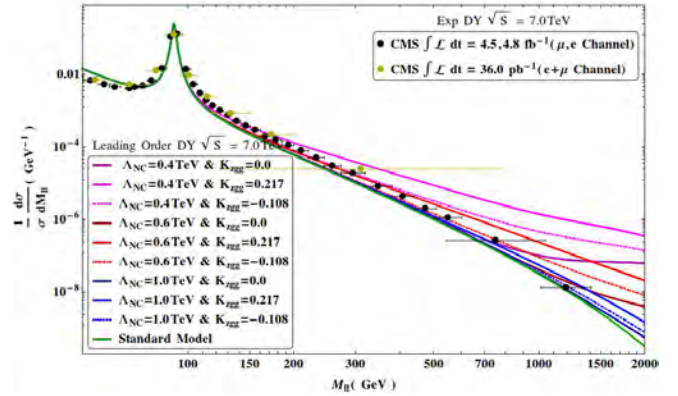


Figure 3: Normalized invariant mass distribution as a function of the invariant mass M_{ll} (GeV) is shown corresponding to the machine energy 7 TeV and

This is one of the initial LHC study in this direction, since only a limited amount of phenomenological analysis has been completed, and this was mostly in the context of the linear collider. An outstanding feature from this nonminimal non-commutative standard model not only modifies the couplings over the SM production channel but also allows additional nonstandard vertices which can play a significant role. Hence, in the Drell-Yan process, as studied in the present analysis, one also needs to account for the gluon fusion process at the tree level. Some of the characteristic signatures, such as oscillatory azimuthal distributions, are an outcome of the momentum-dependent effective couplings. We explore the NC scale $\tilde{I}Z_{NC} \geq 0.4\text{TeV}$, considering different machine energy ranging from 7 to 13 TeV.

(P. Konar)

Contact fermion-Higgs interactions at an electron-positron collider with polarized beams

The possibility was investigated of new physics represented by contact interactions giving rise to interaction vertices of the form $e^+e^-Hf\bar{f}$, where f represents a charged lepton or a (light) quark, and H the recently discovered Higgs boson. Such vertices would give contributions beyond the standard model to the Higgs production processes in association with a fermion pair at a future electron-positron collider. The most general form for these vertices allowed by Lorentz symmetry were written down. Assuming that such contact interactions contribute in addition to the standard model production processes, where the final-state fermion pair comes from the decay of Z boson, the differential cross section for the process allowing for the possibility of polarized beams was calculated. Several observables with differing CP and T properties were proposed, which, if measured, can be used to constrain the couplings occurring in contact interaction vertices. The corresponding sensitivity at a high-energy collider was also obtained.

This work was carried out in collaboration with K. Huitu of Helsinki University, K. Rao of IIT Bombay and P. Sharma of Adelaide University.

(S. Rindani)

Why the angular distribution of the top decay lepton is 'independent' of the anomalous tbW coupling

A simple physical picture is given to understand the observation that the angular distribution of the top decay lepton depends only on the polarisation of the top and is independent of any anomalous tbW coupling to linear order. We find that this can be traced to the fact that the b quark and the neutrino produced in the leptonic decay of the top, via the Standard Model interactions, appear only in spin-0 combination, thus leading to the transfer of the entire information on the top-quark spin to the decay lepton. It is shown how that the occurrence of the b -quark neutrino state in just the $J = 0$ combination, crucial for the above mentioned independence, follows from some simple spinor identities.

This work is done in collaboration with R.M. Godbole of CHEP, IISc Bengaluru and R.K. Singh of IISER Kolkata.

(S. Rindani)

Science

Atomic, Molecular and Optical Physics

Exhumation studies in the Lower Himalayas using Luminescence Thermochronology

A coordinated program to systematically estimate the exhumation rates in different regions Himalaya on varied time scales has been initiated to understand various aspect of geodynamics, the evolution of its landscape, the role of climate and long term changes in sediment fluxes. In respect of luminescence studies, the aim is to explore the luminescence signals that have different thermal stability and hence closure temperature. As a pilot study, samples from the lower, higher and Tethys Himalaya in central Himalayas, were targeted and these includes sites such as North Almora Thrust (lower Himalaya) near Srinagar, Main Central Thrust in Helang (higher Himalayas) and Malari in Tethyan Himalaya. These samples covered elevations ranging from 600 m to 3200 m. The rock types comprised quartzite, gneiss and leucogranite. The OSL and TL measurements were done on quartz and feldspar grains extracted from these rocks. Isothermal annealing and initial rise measurement gave trap depths of 1.69 eV for quartz. Measurements for feldspar are still going on. Measurement of De using BLSL of quartz 600 m and 1000 m respectively gave paleodose of 69 Gy -56 Gy with corresponding ages of 67 ka and 125 ka. These translate to net local exhumation rate of 5.9 mm/y and after subtracting an erosion rate of 0.8 mm/ka gives an uplift rate of 5.1 mm/y. This implies an uplift of 350 m during the 58 ka. This region of Himalaya is considered to be in a state of quiescence, and the units on the south and north of North Almora Thrust fault are considered to be locked. On the other hand, studies by Juyal et al., 2010 provided OSL ages on strath terraces in Srinagar suggest a regional uplift and an average incision rate of about 4.7 mm/a during the past 17 ka. The present data is consistent with this. Further measurements using other OSL signals are underway.

This work is done in collaboration with N. Rana of National Center for Seismology, New Delhi.

Development of rotational and lift mechanism for automation of luminescence detection system

Development of a manual spatially resolved luminescence (SRL) system using electron multiplying charge coupled device (EMCCCD) camera was successfully demonstrated in one of our earlier works. The system is capable of recording the faint luminescence emitted by samples in form of images which can be used to estimate region specific or pixel specific doses/ages. The sample was successfully tested for laboratory dosed and natural samples. However, the routine application of the system is limited due to low success rate of measurement and laborious work involved in each sample measurement. For routine application to geological samples automation of system is necessary. The automation of the system will further enable us to develop our own TL/OSL readers and the technology thus developed can be used for development of dosimetry systems for space dosimetry programs.

As a first step towards the automation of present system, a rotational mechanism for the sample movement between irradiation and detection/stimulation unit and a lift mechanism for lifting the sample at desired position for luminescence recording is developed. A GUI (Graphical User Interface) controllable automatic sample placing technique is developed using LabVIEW (Laboratory Virtual Instrument Engineering Workbench) based interfacing software. User selected parameters are processed in LabVIEW and communicated to the Arduino Mega 2560 microcontroller via serial communication cable. Coding for Arduino is done in Arduino IDE (Integrated Development Environment). Two-way serial communication between LabVIEW and Arduino is done using Virtual Instrument Serial Architecture (VISA) which allows communication with most of the instrument buses like Serial, GPIB (General Purpose Interface Bus), USB, Ethernet etc. VISA APIs (Application Programming Interface) offer portability of programs from one platform to other platforms. A rotational mechanical setup is fabricated in which sample disks are positioned on a rotating circular platter and are arranged in a circle. The circular

platter is attached to the DC (Direct Current) motor which is connected to the Arduino board through the motor driver circuit. The firmware loaded in controller accepts serial commands from board to rotate and stop the motor at user defined positions provided by user through GUI interface.

Arduino processes the data received from LabVIEW and commands the DC motor to rotate the platter. Each position of rotating platter has a hole which is used for sample position detection. To identify the sample position IR (Infrared) sensors (consisting IR LED, photodiode, LM358 comparator IC (Integrated Circuit) and potentiometer) are used, in which receiver and transmitter are placed on the either side of the platter having holes. Number of holes are counted by IR position sensors and platter is stopped at desired position. The stimulation and detection units can then be triggered after achieving desired position.

In addition to that lifting of the sample is employed to lift the sample to the detection unit with the help of servo motor. Rotation of the servo can be controlled accurately as per the degree of rotation specified in Arduino code, which in turns generates PWM signals of variable duty cycle. Then lifting mechanism utilize this rotation to lift the sample up and put it down.

This work is a part of M. Tech. project of Hardik Vaghela of GTU PG School, Ahmedabad.

(Hardik Vaghela and N. Chauhan)

Fluorescence and Phosphorescence in CVD grown diamonds and role of SiV⁻ Centre on these properties: Photoluminescence(PL) and Thermoluminescence (TL) Studies

Phosphorescence of II_b diamonds is strongly correlated with their photoconductivity and also room temperature thermoluminescence peak. This property can be effectively used for the detection of II_b- synthetics in melee star sizes in diamond packets containing large number of diamonds. In addition to II_b- HPHT synthetic diamonds, we have also investigated large number of CVD grown synthetic diamonds for their phosphorescence, fluorescence and thermoluminescence(TL) properties. The visual phosphorescence and fluorescence under deep UV excitation (225 nm) were studied using a home built unit, fluorescence of point defects using Renishaw Raman and TL/OSL using a commercial RIS TL/OSL reader. CVD diamonds examined have fallen into three categories (i) those exhibiting phosphorescence and fluorescence (ii) those exhibiting only fluorescence and (iii) those exhibiting none of the above i.e. those containing some centers responsible for quenching of luminescence (both fluorescence and phosphorescence), and TL have shown interesting correlation with the above mentioned behavior and the intensity of SiV⁻ signal and room temperature TL emission. In the CVD diamonds showing phosphorescence, a room temperature TL peak and another around 100°C were observed; in these crystals SiV⁻ signal was weak or moderate (smaller than the intensity of Raman signal). In these crystals which did not exhibit phosphorescence and fluorescence, the SiV⁻ signal was found to be very strong suggesting that this could be quenching the 450-500 nm emission from CVD diamonds under the few seconds exposure of 225 nm(D2) UV radiation. However, these diamonds under intense UV illumination using diamond view with higher integration time had shown relatively weak blue emission under diamond view. However,

they were found to be inert under relatively weaker UV excitation (D2 lamp) in our home built unit. The large concentration of SiV-centres suppressed the 100°C TL peak significantly and exhibited an intense 220°C peak. The suppression/quenching of blue band luminescence was also observed in electron beam treated synthetic II_b diamonds, presumably due to the presence of GR1. Lakoubovskii et. al. (2000), (2001) have reported the striking similarity of oscillations in PLE spectra of blue band, and SiV⁻ (1.68 eV) centre and also of GR1, albeit with different energies. These lead us to suggest a highly effective energy transfer between blue band and SiV⁻ center.

This work is done in collaboration with M. P. Gaonkar and Prof. M.D. Sastry from GII, Mumbai.

(N. Chauhan and Vinayak Kumar)

TL/OSL properties Al₂O₃ nanophosphor synthesized by microwave combustion method

The luminescence is property of defects. In normal phosphors the defects present in the volume are responsible for luminescence however in nanophosphors, as the surface to volume ratio is significantly higher, so the surface defects also become important. Interesting luminescence properties are observed in the phosphors. Aluminium Oxide (Al₂O₃) is one of the phosphor which is being used in luminescence dosimetry related studies. Doping of Al₂O₃ with different impurities result in significant improvement in its properties and several highly sensitive phosphors were developed using Al₂O₃. The phosphor can be stimulated both thermally and optically. Stable α-phase of Al₂O₃ was synthesized by combustion method using controlled microwave oven. Formation of α-Al₂O₃ compound is confirmed by x-ray diffraction pattern and XRD pattern well matches with the JCPDS file No. 5-712. The average crystallite size of Al₂O₃ is found to be 45 nm calculated using W-H relation. Thermoluminescence (TL) properties of beta irradiated Al₂O₃ samples have been studied in UV, blue and open (UV & visible) windows. It is observed that TL of Al₂O₃ in open window is more sensitive than UV and blue window. TL glow curve of Al₂O₃ shows prominent peak at 472 K along with two shoulders at 416 and 513 K. TL glow peak (472 K) intensity increases linearly with increasing irradiation time up to 12.32 Gy. Optically stimulated luminescence (OSL) properties of beta irradiated Al₂O₃ samples have been studied in UV and blue window. Sensitive OSL emission is observed for UV window but TL blue window emission is more sensitive than UV window. OSL of beta irradiated Al₂O₃ shows linear response up to 6.16 Gy. TL kinetic parameters of Al₂O₃ are examined using deconvoluted glow curves with computerized glow curve deconvolution (CGCD) method.

This work is done in collaboration with Dr. K. R. Nagabhushana from Physics R & D Center, PES Institute of Technology, Bangalore.

(N. Chauhan)

Thermo and optically stimulated luminescence of monoclinic zirconia

This is a collaborative work in which thermoluminescence (TL) and optically stimulated luminescence (OSL) properties of ZrO₂ and

$ZrO_2 : Dy$ (1 mol%) phosphor synthesized by combustion technique are investigated. ZrO_2 doped with different impurities is a material of research owing to its luminescence properties and can be easily doped with a rare earth element. Materials are an ideal host material for various phosphors, because of its wide bandgap and presents low phonon energy. X-ray diffraction of the samples reveal monoclinic phase with space group P12/c1 symmetry. Morphology and chemical composition of materials are analyzed by field emission scanning electron microscopy and Energy dispersive spectroscopy. TL glow curve exhibit peaks at 422 and 465 K for ZrO_2 and 460 K for $ZrO_2 : Dy$ (1 mol%) samples. OSL decay curves recorded on the same samples by stimulating with blue light at 40°C. TL and OSL signal intensities increases linearly with increase of beta radiation time up to 200 second. Time dependent fading behavior of the ZrO_2 and $ZrO_2 : Dy$ (1 mol%) are tested for 10 hour and found to be 20% and 5% for TL and 1–2% for OSL respectively. In addition, the samples show good repeatability for both TL and OSL measurement. OSL decay of light intensity showed a dependence on illumination time. TL kinetic parameters are calculated by computerized curve deconvolution analysis. TL and OSL result suggest that, $ZrO_2 : Dy$ (1 mol%) is suitable for TL dosimeter.

This work is being carried in collaboration with Dr. K. R. Nagabhushana, PES Institute of Technology, Bangalore.

(N. Chauhan)

Estimation of limits of luminescence dating using samples of known ages -ancient and modern

The blue light stimulated, infrared stimulated and post infrared-infrared stimulated luminescence (BLSL, IRSL₅₀ (stimulated at 50°C) and pIR-IRSL₂₉₀ (stimulated at 290°C)) signals of quartz and feldspars grains from samples of, i) diverse depositional environments, ii) antiquity far beyond the luminescence dating range and iii) recently deposited sediments, were analyzed to understand the extremum limits of ages that can be obtained using these signals. The environmental dose rate in these samples ranged from 1.5 Gy/ka to 3 Gy/ka. The depositional environments varied from palaeofan/fluvial settings of Siwaliks in the foothills of Himalaya, to sediments deposited by recent tsunami and aeolian sands from the Thar Desert. The Siwalik samples had age controls based on paleomagnetic data and the ages ranged from 1.7–5.24 Ma.

Important observation from this study indicated equilibrium paleodoses for quartz to be upto 150 ka indicating 100 ka being the limiting age in favorable radiation dose environment. For Feldspars, infrared (IR)- and post infrared- inferred (pIRIR) stimulated luminescence equilibrium doses ranged upto 2.2 Ma with correction for athermal fading. The minim ages on modern samples return doses of 1-3 ka indicating that a finite zero error could accrue to do measurement limitations at the same time suggesting pIR-IRSL being the preferred method for dating samples in the range 1ka and above. Further a plot of IRSL and pIR-IRSL ages could be fitted to a single saturating exponential and this correlation could provide a first order way to correct existing IRSL ages.

This work was carried out in collaboration with Rohatas Kumar, WHIG, Dehradun and P.N. Gajjar, Gujarat University, Ahmedabad.

(H. M. Rajapara, R.H. Biswas, N. Chauhan, A. K. Singhvi)

Distribution of Channel Sands in Brahmaputra Fan Delta; Assessment of tectonic and discharge on sedimentation pattern

We participated in a collaborative program to understand the relative role of tectonics and discharge on sedimentation patterns and were responsible to providing the chronometric data on these samples. Three related studies are listed below.

The Brahmaputra River bends sharply around the Himalayan syntaxis and again around the edge of the Shillong Plateau (SP), resulting in a tectonically-controlled anfractuous flow path. Understanding the role of allogenic forcings, like changes in slope induced by tectonics, in modulating the river course and construction of fluvial stratigraphy is essential for modeling stratigraphic architecture. Extensive drilling and dating of the Brahmaputra system has enabled document the river location before and after uplift of the SP. Prior to Plio - Pleistocene uplift, the Brahmaputra occupied the region east of the incipient plateau. Presently the river was routed along the western margin of the SP. Based on the interpretation of numerous exposures along the Shillong margin and hundreds of well bores in the adjacent delta, the distribution of channel sands was divided into 3 distinct fan lobes. Depositional ages of each of these lobes were measured by luminescence dating, chronicling the history of river and its movement in response to uplift of the plateau margin over the past few hundred ka. The easternmost sediment lobe records the location of the river during incipient uplift; the western lobe documents deflection of the river to its westernmost position as recently as 100 ka; and the central lobe tracks the river course as it eroded eastward into the plateau margin toward its present course. This stratigraphy indicates that uplift of the plateau provides the first order control on channel sand distribution in the fan delta at this temporal resolution (10^5 years). Despite ongoing uplift of the SP, the river has been able to erode eastward into the plateau margin, the timing of which is coincident with a period of paleoflood events. Paleohydrological reconstructions suggest that some of these were megafloods with discharge $>10^6$ m³/s.

Because these events coincide with eastward erosion of the river into the plateau margin, we propose that repeated increased discharge events contributed to the rivers ability to overcome the uplift-induced deflection. Occurring over a period of 10^4 years, these high discharge events were a second order control on the channel sand distribution in the fan delta. Results document fan-scale changes induced by allogenic forcing and will be used to inform analog models for this and other tectonically-influenced river systems and for improved understanding of sedimentation patterns in the linked Bengal fan system.

This work was done in collaboration with J. L. Pickering of Shell Projects Technology and S.L. Goodbred, Vanderbilt University USA.

(H. M. Rajapara and A. K. Singhvi)

Terrace formation in the upper Bengal basin since the Middle Pleistocene: Brahmaputra fan delta construction during multiple highstands

Floodplains, paleosols and antecedent landforms near the apex of the Brahmaputra fan delta in north-central Bangladesh comprise cycles of

fluvial sediment deposition, erosion and weathering. Together these landforms and associated deposits comprise morphostratigraphic units that define the river's history, its channel position and avulsion behavior through the Late Quaternary.

Floodplains, paleosols and antecedent landforms near the apex of the Brahmaputra fan delta in north-central Bangladesh comprise cycles of fluvial sediment deposition, erosion and weathering. Together these landforms and associated deposits comprise morphostratigraphic units that define the river's history, its channel position and avulsion behavior through the Late Quaternary.

Previously, temporal differentiation within these units was insufficient to decipher their sequence of deposition, an important step in understanding the spatial pattern of migration of the Brahmaputra River. Holocene units in this region are fairly well established by radiocarbon dating of in situ organic material, but pre-Holocene units are considered Pleistocene aged based on organic material radiocarbon dated >48 ka BP (the limit of radiocarbon dating) and the fact that the sediments are beneath a prominent paleosol, interpreted as a buried soil horizon that developed during a previous sea level lowstand.

Here we use detailed sediment analysis to better differentiate morphostratigraphic units at the Brahmaputra's avulsion node, establishing the sequence of deposition and subsequent weathering of these bodies. We then tested this relative chronology by luminescence dating of the sands beneath these landform surfaces. This work provides the first absolute depositional age constraints of terrace sediments for the Middle to Late Pleistocene Brahmaputra River and upper Bengal basin. The luminescence ages were complemented by detailed compositional trends in the terrace deposits, including clay mineralogy and the degree of weathering. Together, these newly dated and carefully described morphostratigraphic units reflect eustasy-driven cycles of terrace development by way of highstand floodplain deposition and subsequent lowstand exposure and weathering, along with active tectonic deformation. Defining this Late Quaternary history of terrace development and position of the Brahmaputra River is a first step toward an integrated understanding of basin and delta evolution over multiple glacioeustatic cycles and tectonically relevant timescales.

This work was done with Prof. S. L. Goodbred Jr, and his associate at the Vanderbilt University, USA.

(H. M. Rajapara and A.K. Singhvi)

Effect of Tectonic and Co-Seismic Uplift on Complex Channel Avulsion in the Meghna River Floodplain since Mid Holocene:

Channel migrations and river avulsions in deltaic river systems are driven by differential changes of surface topography, such as the super-elevation of channels due to sedimentation. In addition to such autocyclic processes, tectonic events, such as earthquakes, may also lead to avulsions from sudden uplift. The eastern part of the Ganges-Brahmaputra-Meghna Delta (GBMD) is underlain by the blind mega thrust of the Indo-Burma subduction zone. In this region a 100 km long sinuous abandoned channel of the Meghna River was examined. It has been previously shown that immediately south of the channel the topography is higher than on the rest of the Delta and

an oxidized Holocene exposure surface was seen. Part of the Titas River flows northward from this area into the abandoned channel belt, opposite of the southward flowing rivers of the delta.

Detailed investigations of this abandoned channel of the Meghna River using stratigraphic logs of hand-drilled wells, resistivity profiles, sediment analyses and OSL and radiocarbon dating. The OSL ages constrained the possible date of the abandonment event. Numerical modeling was used to evaluate the hypothesis that the co-seismic uplift associated to an earthquake can trigger the channel migration. Our modeling approach aimed to estimate the co-seismic uplift associated with potential seismic events using an elastic Coulombs dislocation model. The geometry of fault in this model was estimated using geologic and GPS constraints with standard elastic parameters (Young's modulus = 80 GPa; Poisson's ratio = 0.3). Different potential earthquakes geometries that involve the megathrust, a splay fault, or the megathrust terminating in the splay were then explored. The magnitude and distribution of co-seismic slip are also varied between a rupture length of 112.5km and 180km along a 225km long fault. This study suggested that any class of models can produce an uplift (1-2 m) necessary to initiate the river avulsion. Thus the avulsion could be due to a $> M8$ megathrust earthquake or a $M7$ splay fault rupture. In either case, the rupture cannot extend west of the abandoned channel to the current Meghna River, and thus did not rupture to the deformation front, where the megacity of Dhaka now lies.

This work was done in collaboration with A. Dunham of Pennsylvania State University, C. Gral and M. B. Philosobian, S. Steckler, of Columbia University of New York; D.R. Mondal CUNY Queens College, B. Kumar and S. H. Akhter University of Dhaka.

(H. M. Rajapara and A.K. Singhvi)

Plasma-screening effects in the electronic structure of multiply charged Al, Mg and Fe ions

Atomic structures of plasma embedded multiply charged Al, Mg and Fe ions in the weakly and strongly coupling regimes by accounting for the plasma screening effects using the Debye and ion sphere (IS) models have been investigated. In the Debye model approximation, special attention is given to demonstrate the roles of the spherical and non-spherical plasma-screening effects through the electron-electron interaction potential in calculating the spectral properties. The relativistic coupled-cluster (RCC) method has been employed to describe the relativistic and electronic correlation effects in these atomic systems. The variation in the ionization potentials (IPs) and excitation energies (EEs) with the screening parameters are shown explicitly.

This work was done in collaboration with M. Das, National Institute of Technology, Rourkela, Odisha - 469008, India and S. Pal, Indian Institute of Technology Bombay, Powai, Mumbai - 400076, India.

(B. K. Sahoo)

Plasma-screening effects in the electronic structure of multiply charged Al, Mg and Fe ions

Atomic structures of plasma embedded multiply charged Al, Mg and Fe ions in the weakly and strongly coupling regimes by accounting

for the plasma screening effects using the Debye and ion sphere (IS) models have been investigated. In the Debye model approximation, special attention is given to demonstrate the roles of the spherical and non-spherical plasma-screening effects through the electron-electron interaction potential in calculating the spectral properties. The relativistic coupled-cluster (RCC) method has been employed to describe the relativistic and electronic correlation effects in these atomic systems. The variation in the ionization potentials (IPs) and excitation energies (EEs) with the screening parameters are shown explicitly.

This work was done in collaboration with M. Das, National Institute of Technology, Rourkela, Odisha - 469008, India and S. Pal, Indian Institute of Technology Bombay, Powai, Mumbai - 400076, India.

(B. K. Sahoo)

Proposed trapping geometry for atoms with magnetic sublevel independent magic wavelengths

A generic scheme to trap atoms at the magic wavelengths that are independent of vector and tensor components of the interactions of the atoms with the external electric field is presented. The magic wavelengths for the laser cooling D2 lines in the Rb and Cs atoms are demonstrated and their corresponding polarizability values without vector and tensor contributions are given. Consequently, these magic wavelengths are independent of magnetic sublevels and hyperfine levels of the atomic states involved in the transition, thus, can offer unique approaches to carry out many high precision measurements with minimal systematics. Inevitably, the proposed technique can also be used for electronic or hyperfine transitions in other atomic systems.

This work was carried out in collaboration with S. Singh and B. Arora of Department of Physics, Guru Nanak Dev University, Punjab, India.

(B. K. Sahoo)

Unexpectedly large difference of the electron density at the nucleus in the $4p^2P_{1/2,3/2}$ fine-structure doublet of Ca^+

The isotope shift in the (D2) transition in singly-ionized calcium ions has been measured using photon recoil spectroscopy. The high accuracy of the technique enables us to resolve the difference between the isotope shifts of this transition to the previously measured isotopic shifts of the (D1) line. This splitting isotope shift is extracted and exhibits a clear signature of field shift contributions. From the data we were able to extract the small difference of the field shift coefficient and mass shifts between the two transitions with high accuracy. This J-dependence is of relativistic origin and can be used to benchmark atomic structure calculations. As a first step, we use several ab initio atomic structure calculation methods to provide more accurate values for the field shift constants and their ratio. Remarkably, the high-accuracy value for the ratio of the field shift constants extracted from the experimental data is larger than all available theoretical predictions.

This work was carried out in collaboration with C. Shi, F. Gebert, A. Surzhykov, V.A. Yerokhin, F. Wolf, J. C. Heip, and P. O. Schmidt

of Physikalisch-Technische Bundesanstalt, Germany and C. Gorges, S. Kaufmann, and W. Noertershaeuser of Institut fuer Kernphysik, Technische Universitaet Darmstadt, Germany and J. C. Berengut of School of Physics, University of New South Wales, Sydney, Australia.

(B. K. Sahoo)

Highly charged ions as promising optical clock candidates

Transitions among the first three low-lying states in the highly charged W^{13+} , Ir^{16+} and Pt^{17+} ions and the $3p^2P_{1/2} - 3p^2P_{3/2}$ transitions of many Al-like ions are found to be suitable for ultra-high precision clock frequencies. By determining their energy levels, lifetimes and other spectroscopic properties that are decisive quantities for estimating dominant systematics due to stray electromagnetic interactions in an experiment, we scrutinize that it can be possible to measure frequencies of the lowest forbidden transitions below 10^{-19} precision level in the above ions and hence, they seem to be suitable for frequency standards. Furthermore, clocks based on these ions are found to be apt for corroborating the hypothesis of temporal and spatial variation of the fine structure constant.

This work was carried out in collaboration with Yan-mei Yu, Beijing National Laboratory for Condensed Matter Physics, Institute of Physics, Chinese Academy of Sciences, Beijing 100190, China and D. K. Nandy, Theoretical Chemistry Division, University of Waterloo, Ontario, Canada.

(B. K. Sahoo)

Improved limits on the hadronic and semi-hadronic CP violating parameters and role of a dark force carrier in the electric dipole moment of ^{199}Hg

Combining the recently reported electric dipole moment (EDM) of ^{199}Hg atom due to breaking of parity and time-reversal symmetries with the improved relativistic atomic calculations, precise limits on the tensor-pseudotensor (T-PT) electron-nucleus (e-N) coupling coefficient and the nuclear Schiff moment (NSM) interactions are determined. Using these limits with the nuclear calculations, we infer limits on the EDMs of neutron and proton as $d_n < 2.2 \times 10^{-26}$ e-cm and $d_p < 2.1 \times 10^{-25}$ e-cm, respectively. and on the quantum chromodynamics (QCD) parameter and the combined up- and down-quark chromo-EDMs as $\Theta_{\text{QCD}} < 1.1 \times 10^{-10}$ and $|\vec{d}_u - \vec{d}_d| < 5.5 \times 10^{-27}$ e-cm, respectively. These are the best limits till date to probe new sources of CP violation beyond the standard model (SM) from a diamagnetic atom. Role of considering a capable many-body method to account the electron correlation effects to all orders for inferring the above limits has been highlighted. From this analysis, constraints on the T-PT e-N coupling coefficient with a large range of mass of a possible dark matter carrier between the atomic electrons and nucleus are given.

(B. K. Sahoo)

Parity-nonconserving interaction induced light shifts in the ultracold ^{210}Fr atoms to probe new physics beyond

We have demonstrated an experimental technique to measure light shifts due to nuclear spin independent (NSI) parity-nonconserving (PNC) interaction in the $7S_{1/2} - 6D_{3/2}$ transition of ultracold ^{210}Fr atoms. The major advantage in our approach is more than 10^4 number of ultracold ^{210}Fr atoms can be considered in a trap to enhance the shot noise limit. A relativistic coupled-cluster method has been employed to calculate parity nonconserving electric dipole transition matrix elements. Based on these calculations, we have analyzed different transitions among hyperfine levels of the $7S_{1/2}$ and $6D_{3/2}$ states and appropriate transitions are established for their aptness for carrying out PNC measurement. It is possible to probe new physics beyond the standard model with mass scale up to 5.5 TeV using our proposed scheme upon the fruition of the experiment.

This work was done in collaboration with T. Aoki and Y. Torii, University of Tokyo, Japan, B. P. Das of Tokyo Institute of Technology, Japan, K. Harada, T. Hayamizu, K. Sakamoto, H. Kawamura, T. Inoue, A. Uchiyama, S. Ito, R. Yoshioka, K. S. Tanaka, and M. Itoh of Tohoku University, Sendai, Japan, A. Hatakeyama and of Department of Applied Physics, Tokyo University of Agriculture and Technology, Japan and Y. Sakemi of Center for Nuclear Study, The University of Tokyo, Japan.

(B. K. Sahoo)

Pancharatnam phase in non-separable states of light

We generate the non-separable state of polarization and orbital angular momentum using a laser beam. The generated state undergoes a cyclic polarization evolution which introduces a Pancharatnam geometric phase to the polarization state and, in turn, a relative phase in the non-separable state. We experimentally study the violation of the Bell-like inequality for different Pancharatnam phases introduced by various cyclic polarization evolutions with linear and circular states as measurement bases. While measuring in linear bases, the Bell-CHSH parameter oscillates with a Pancharatnam phase. One can overcome this dependence by introducing a relative phase in one of the projecting states. However, for measurements in circular bases, the Pancharatnam phase does not affect the Bell-like inequality violation.

(P. Chithrabhanu, S. G. Reddy, Nijil Lal, Ali Anwar, A. Aadhi and R. P. Singh)

Generating arbitrary cebits on the orbital angular momentum Poincaré sphere

Using classical laser beams, we generate a general complex superposition state, cebit, of orbital angular momentum (OAM) of light. We use a nonseparable beam of polarization and OAM generated by a modified Sagnac interferometer for the generation of OAM cebits which can be represented as points on the OAM Poincaré sphere. The general cebit state is represented as a function of the rotation angle of the wave plates so that one can easily generate the required state.

(P. Chithrabhanu, A. Aadhi, S. G. Reddy, Shashi Prabhakar and R. P. Singh)

Topological structures in vector speckle fields

We here demonstrate on both theoretical and experimental bases a method to recover the topological structure of a monochromatic optical field that has suffered diffuse transmission. This method consists of two steps: first, a linearly polarized sample beam is mixed with a coaxial Gaussian beam in orthogonal polarization states resulting in a Poincaré beam; second, a polarization-related spatial correlation function is considered and measured for the overall speckle field arising by optical diffusion. The singularities of the sample beam turn out to be imaged into the correlation function of the vector speckle field.

This work was done in collaboration with B. Piccirillo of Dipartimento di Fisica Ettore Pancini, Universi di Napoli Federico II, Complesso Universitario di Monte Sant'Angelo, 80126 Napoli, Italy.

(Vijay Kumar, B. Piccirillo, S. G. Reddy and R. P. Singh)

Generating a perfect quantum optical vortex

In this work we have introduced an interesting quantum state, the perfect quantum optical vortex state which exhibits a highly localized distribution along a ring in the quadrature space. We have examined its nonclassical properties using the Wigner function and the negativity volume. Such a quantum state can be a useful resource for quantum information processing and communication.

This work was done in collaboration with Anindya Banerji and Abir Bandyopadhyay of Hooghly Engineering and Technology College, Hooghly along with D. Banerjee of Department of Physics, Jadavpur University, Kolkata.

(Anindya Banerji, R. P. Singh, D. Banerjee and Abir Bandyopadhyay)

Entanglement propagation of a quantum optical vortex state

We study the entanglement evolution of a quantum optical vortex state propagating through coupled lossless waveguides. We consider states generated by coupling two squeezed modes using a sequence of beam splitters and also by subtracting photons from one of the output modes in spontaneous parametric down conversion. We use the Wigner function to study the variation in the structure of the vortex state with distance and quantify the entanglement after propagation using logarithmic negativity.

This work was done in collaboration with Anindya Banerji and Abir Bandyopadhyay of Hooghly Engineering and Technology College, Hooghly along with D. Banerjee of Department of Physics, Jadavpur University, Kolkata.

(Anindya Banerji, R. P. Singh, D. Banerjee and Abir Bandyopadhyay)

Elemental Composition using LIBS

The laser produced plasma (LPP) experimental setup in the laboratory was augmented to undertake laser induced breakdown spectroscopy (LIBS). In addition to the existing KrF excimer laser, a Nd:YAG laser with fundamental and 3 higher harmonic frequencies also is being used to ablate the sample. The ambient pressure in the plume expansion region can be controlled from $\sim 10^{-5}$ mbar to ~ 10 mbar. The plasma spectrum is collected by a fiber and is being fed to an ICCD echelle spectrograph. Both intensity and wavelength calibration of the setup have been completed. A few data sets on pure metal samples have also been collected.

(Prashant Kumar, R K Kushawaha, S B Banerjee and K P Subramanian)

Lab qualification of SWIS instrument of ASPEX payload on Aditya L1 satellite

The solar wind ion spectrometer (SWIS) instrument of ASPEX payload consists of two top-hat electrostatic energy analyzer (THA) to measure the solar ion energy spectrum in 100 eV to 20 keV energy range. The performance of the THA and its subsystems are studied in the lab by housing them in a test station established at Thaltej campus of PRL. Hydrogen, helium and noble gas ion beams having energy in the range 500 keV to 5 keV are produced using an ion gun and were directed along the analyzing plane of the THA. The bias voltages on the THA electrodes were tuned and the transmitted ions were detected by the MCP and resistive anodes. For measuring performance for various angular sectors of the anode, provisions were made to turn the THA along its axis. The Preliminary Design Review (PDR) of the ASPEX payload was completed in Dec 2016, and many actions suggested there were closed out recently. The hardware and electronics parts of the SWIS instrument have attained maturity. Most of the critical parameters for SWIS instrument hardware and electronics are analyzed and frozen and it is expected that the engineering model (EM) will be ready to be delivered by the end of 2017.

(S B Banerjee, Prashant Kumar, Pranav R Adhyaru, K P Subramanian)

Pattern of Holocene glaciation in the monsoon-dominated Kosa Valley

In continuation of our endeavor towards understanding the Holocene valley glacier response to climate variability, monsoon dominated Kosa valley located in the upper Dhaul Ganga river is investigated. Based on the geomorphology, lateral moraine stratigraphy, and limited optical chronology suggests that the valley experienced four glacial advances during the late glacial to late Holocene. The oldest and most extensive glaciation, termed as Raj Bank Stage-1 (RBS-1), is represented by the degraded moraine ridge. This glaciation remains undated; however, the chronology of outwash terrace gravel dated to 12.7 ± 1.3 ka indicates that the RBS-1 probably represents the Last Glacial Maximum (LGM). The second glacial advance (RBS-2) is preserved as a curvilinear lateral moraine and is dated to 6.1 ± 0.4 ka. The third glacial advance viz. RBS-3 is bracketed between 5.0 \pm

0.5 and 4.0 ± 0.4 ka. Following this, the glacier receded in pulses that are represented by two distinct recessional moraines (RBS-3a and b).

The fourth glacial stage (RBS-4), which is dated between 2.2 ± 0.2 and 1.6 ± 0.2 ka, shows a pulsating recession and is represented by a prominent recessional moraine (RBS-4a). Whereas, presence of unconsolidated, poorly defined moraine mounds proximal to the glacier snout are ascribed as neoglacial advance corresponding to the Little Ice Age (LIA). With the limited chronometric data, we speculated that the glaciation was driven during the weak to moderate Indian Summer Monsoon (ISM) aided by lowered temperature. Presence of recessional moraines associated with mid-Holocene glacial phase indicates that the monsoon-dominated glaciers respond sensitively to minor (sub-millennial scale) changes in temperature and precipitation conditions. The observations are broadly in accordance with the studies carried out in other monsoon-dominated valleys in the central Himalaya, implying that in ISM dominated regions, lowered temperature seems to be the major driver of glaciations during the late glacial to late Holocene.

This work was carried out in collaboration with the Department of Geology, HNB Garhwal University and BSIP, Lucknow, central Himalaya, Uttarakhand, India.

(N. Juyal)

Multi-gigahertz, femtosecond Airy beam optical parametric oscillator pumped at 78 MHz

We report a high power ultrafast Airy beam source producing femtosecond pulses at multi-gigahertz (GHz) repetition rate (RR). Based on intra-cavity cubic phase modulation of an optical parametric oscillator (OPO) designed in high harmonic cavity configuration synchronous to a femtosecond Yb-fiber laser operating at 78 MHz, we have produced ultrafast 2D Airy beam at multi-GHz repetition rate through the fractional increment in the cavity length. While small (<1 mm) crystals are used in femtosecond OPOs to take the advantage of broad phase-matching bandwidth, here, we have exploited the extended phase-matching bandwidth of a 50-mm long Magnesium-oxide doped periodically poled LiNbO₃ (MgO:PPLN) crystal for efficient generation of ultrafast Airy beam and broadband mid-IR radiation. Pumping the MgO:PPLN crystal of grating period, $\Lambda = 30 \mu\text{m}$ and crystal temperature, $T = 100^\circ\text{C}$ using a 5-W femtosecond laser centred at 1064 nm, we have produced Airy beam radiation of 684 mW in ~ 639 fs (transform limited) pulses at 1525 nm at a RR of ~ 2.5 GHz. Additionally, the source produces broadband idler radiation with maximum power of 510 mW and 94 nm bandwidth at 3548 nm in Gaussian beam profile. Using an indirect method (change in cavity length) we estimate maximum RR of the Airy beam source to be ~ 100 GHz.

(A. Aadhi, Varun Sharma, Apurv Chaitanya N. and G. K. Samanta)

Controlled switching of orbital angular momentum in an optical parametric oscillator

Controlled switching of orbital angular momentum (OAM) of light at practical powers over arbitrary wavelength regions can have important

implications for future quantum and classical systems. Here we report on a single source of OAM beams based on an optical parametric oscillator (OPO) that can provide all such capabilities. We demonstrate active transfer of OAM mode of any order, l_p , of pump to the signal and idler in an OPO, to produce l_{p+1} number of different OAM states, by controlling the relative cavity losses of the resonated beams. As a proof-of-principle, we show that when pumping with OAM states, $l_{p=1}$ and $l_{p=2}$, for different relative losses of signal and idler, the OPO has two ((1,0), (0,1)) and three ((2,0), (1,1) and (0,2)) output states, respectively. Our findings show that using a suitable loss modulator, one can achieve rapid switching of the OAM mode in OPO output beams in time.

This work was done in collaboration with Prof. Majid Ebrahim-Zadeh and Dr. S. Chaintanya Kumar, ICFO-the Institute of Photonic Sciences, Barcelona, Spain.

(A. Aadhi and G. K. Samanta)

Hollow Gaussian beam generation through nonlinear interaction of photons with orbital angular momentum

Hollow Gaussian beams (HGB) are a special class of doughnut shaped beams that do not carry orbital angular momentum (OAM). Such beams have a wide range of applications in many fields including atomic optics, bio-photonics, atmospheric science, and plasma physics. Till date, these beams have been generated using linear optical elements. Here, we show a new way of generating HGBs by three-wave mixing in a nonlinear crystal. Based on nonlinear interaction of photons having OAM and conservation of OAM in nonlinear processes, we experimentally generated ultrafast HGBs of order as high as 6 and power >180 mW at 355 nm. This generic concept can be extended to any wavelength, timescales (continuous-wave and ultrafast) and any orders. We show that the removal of azimuthal phase of vortices does not produce Gaussian beam. We also propose a new and only method to characterize the order of the HGBs.

(Apurv Chaitanya N., M. V. Jabir, J. Banerji and G. K. Samanta)

Ultrafast Airy beam optical parametric oscillator

We report on the first realization of an ultrafast Airy beam optical parametric oscillator (OPO). By introducing intracavity cubic phase modulation to the resonant Gaussian signal in a synchronously pumped singly-resonant OPO cavity and its subsequent Fourier transformation, we have generated 2-dimensional Airy beam in the output signal across a 250 nm tuning range in the near-infrared. The generated Airy beam can be tuned continuously from 1477 to 1727 nm, providing an average power of as much as 306 mW at 1632 nm in pulses of ~ 23 ps duration with a spectral bandwidth of 1.7 nm.

This work was done in collaboration with Prof. Majid Ebrahim-Zadeh and Dr. S. Chaintanya Kumar, ICFO-the Institute of Photonic Sciences, Barcelona, Spain.

(Apurv Chaitanya N., A. Aadhi and G. K. Samanta)

Ultrafast optical vortex beam generation in the ultraviolet

We report on the generation of ultrafast vortex beams in the deep ultraviolet (DUV) wavelength range at 266 nm, for the first time to our knowledge. Using a Yb-fiber-based green source in combination with two spiral phase plates of orders 1 and 2, we were able to generate picosecond Laguerre Gaussian (LG) beams at 532 nm. Subsequently, these LG beams were frequency doubled by single-pass, second harmonic generation in a 10 mm-long β -BaB₂O₄ crystal to generate ultrafast vortex beams at 266 nm with a vortex order as high as 12, providing up to 383 mW of DUV power at a single-pass, green-to-DUV conversion efficiency of 5.2%. The generated picosecond UV vortex beam has a spectral width of 1.02 nm with a passive power stability better than 1.2% rms over >1.5 h.

This work was done in collaboration with Prof. Majid Ebrahim-Zadeh and Dr. S. Chaintanya Kumar, ICFO-the Institute of Photonic Sciences, Barcelona, Spain.

(Apurv Chaitanya N. and G. K. Samanta)

Airy beam optical parametric oscillator

Airy beam, a non-diffracting waveform, has peculiar properties of self-healing and self-acceleration. Due to such unique properties, the Airy beam finds many applications including curved plasma wave-guiding, micro-particle manipulation, optically mediated particle clearing, long distance communication, and nonlinear frequency conversion. However, many of these applications including laser machining of curved structures, generation of curved plasma channels, guiding of electric discharges in a curved path, study of nonlinear propagation dynamics, and nonlinear interaction demand Airy beam with high power, energy, and wavelength tunability. Till date, none of the Airy beam sources have all these features in a single device. Here, we report a new class of coherent sources based on cubic phase modulation of a singly-resonant optical parametric oscillator (OPO), producing high-power, continuous-wave (cw), tunable radiation in 2-D Airy intensity profile existing over a length >2 m. Based on a MgO-doped periodically poled LiNbO₃ crystal pumped at 1064 nm, the Airy beam OPO produces output power more than 8 W, and wavelength tunability across 1.511.97 μ m. This demonstration gives new direction for the development of sources of arbitrary structured beams at any wavelength, power, and energy in all time scales (cw to femtosecond).

(A. Aadhi, Apurv Chaitanya N., M. V. Jabir, P. Vaity, R. P. Singh, and G. K. Samanta)

Deuterated Formaldehyde in the low mass protostar HH212

HH212 is a nearby (450 pc) source in Orion, which might be a Class 0 protostellar system with a Keplerian disk and collimated bipolar SiO jets. No deuterated complex molecule has been reported in this source except the recent report of deuterated water, HDO (Codella et

al. 2016). Here, we report the HDCO (deuterated formaldehyde) line observation from ALMA data to probe the inner region of HH212. We compare HDCO line with other molecular lines to explain the possible chemistry and physics of the source. HDCO emission is elongated along the SiO jet and possibly associated with the outflow at the base. The emission also shows a rotation but it is not associated with the keplerian rotation of disk or the rotating infalling envelope, rather it is associated with the outflow.

This work was carried out in collaboration with Y.C Minh, Ankan Das, Indian Center for Space Physics.

(D Sahu and B Sivaraman)

Chemical Diagnostics of the Massive Star Clusters-Forming Cloud G33.92+0.11 II. DCN, HDCS and $\text{H}_2\text{C}^{34}\text{S}$

Sub-clumps in a massive star clusters-forming region, G33.92+0.11, have been investigated for the emission from deuterated species, DCN and HDCS, with sub-arcsecond angular resolution observations using ALMA. The strong and extended DCN emission was found towards the A1 and A2 clumps which suggests that this species traces the warm and dense gas influenced by the post-stage star formation activities, since this species is formed efficiently in the lukewarm gas-phase. The emission peak of HDCS in A5 suggests the existence of a large abundance of cold gas in the present star-forming site, which may imply that the massive star formation is taking place fast. In a region between A2 and A5, a high value of the HDCS/H₂CS ratio was probably resulted from the cold gas associated with the “arm-c3” of this source, as traced by the 13CS absorption feature. HDCS and $\text{H}_2\text{C}^{34}\text{S}$ observed in the A9 clump may result from the cold dense gas contained in the inflowing gas from the ambient, previously identified as the “arm-c4”.

This work was carried in collaboration with Young Chol Minh and Tatsuhiko Hasegawa. Young Chol Minh, Haoyu Baobab Liu, Roberto Galva-Madrid, Jinhua He, and Tatsuhiko Hasegawa.

(D Sahu)

Adsorption energies of H and H₂ : a quantum-chemical study

The chemical composition of interstellar grain mantle is mostly dependent on adsorption energies of the surface species. Since hydrogen is widespread either in atomic or in molecular form, our aim in this work is to review (by quantum chemical calculations) the variation of the adsorption energies of H and H₂ depending on the nature of the adsorbents. Choice of adsorbents was based on relative abundances of interstellar materials. Since carbonaceous and silicate grains are very abundant, we used them as our adsorbents. To save computational time, benzene (smallest structure sample of PAHs) is employed as carbonaceous material and for silicate grain, simple cluster of silicon dioxide (silica) (SiO_2)₃ is used. Around dense cloud regions, water is the major constituent of a grain mantle, therefore, usage of binding energies with bare grains is immaterial.

To mimic the water as the adsorbents, we use a water-cluster ($(\text{H}_2\text{O})_6$). We found that, for all types of adsorbents considered here, binding energies of H are always lower than those of H₂, whereas, some of the experimental values are just the other way around. Assuming a steady state solution to the rate equation method, we also present the H₂ formation efficiency window in various cases.

This work was carried out in collaboration with Ankan Das, Indian Center for Space Physics.

(D Sahu)

Developing electrons and ions imaging methods for understanding chemical dynamics

The 3D velocity map imaging (VMI) of electrons and ions emerged as very powerful techniques to study the molecular fragmentation and ultrafast processes in photoexcitation/ionization of molecules. An experiment is being planned to probe the ultrafast processes using femtosecond laser. These processes are occurred in atomic and molecular systems in time domain of picosecond to attosecond. The pump-probe setup will be developed for time-resolved study. The development of this spectrometer can be categorized in two parts prior to testing phase. In Part-I, work related to the simulation of electrons and ions trajectories in given electrostatic field. In part-II, the designing and development of the vacuum chamber, spectrometer plates, etc. will be undertaken. The vacuum chamber, electrostatic plates and other required items are already being designed. All subsystems and required components and the experimental chamber are under procurement. The simulation of electron trajectories is performed using SIMION 8 software. The preliminary simulation result is shown in Figure 1. In this simulation, the trajectories of electrons ejected from sphere having diameter 2mm are projected on detector by electric lens. The standard VMI setup, proposed by Eppink and Parker (1997) is based on three-plate electrodes which is suitable for low energy electrons up to 100eV. The PRL VMI spectrometer is designed to analyze electron energies up to 1keV. A modified VMI with 11 plates is being proposed to undertake this task.

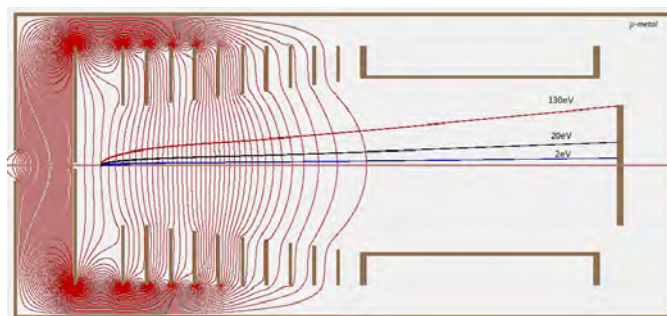


Figure 1: Multi-plates velocity map imaging spectrometer

(R K Kushawaha and Ekta Patel)

Establishing femtosecond laser lab in PRL

We are establishing new femtosecond laser lab in AMOPH PRL to study the ultrafast processes in atomic and molecular systems. The nuclear dynamics is ranging from picosecond to femtosecond time domain whereas the electron dynamics is in attosecond time scale. The processes occurring in this time domain are named as ultrafast processes. Understanding the time-resolved ultrafast processes has opened a new direction in atomic and molecular physics, where the evolution dynamics and subsequent changes in molecular structure are probed during the reactions. This has led to the possibility of controlling chemical reaction for molecular engineering. With aim to probe the ultrafast processes in molecules, generate and use of attosecond pulses and probing the THz vibration of molecules we are establishing this new femtosecond laser lab which is under development.

(R. K. Kushawaha, Prashant Kumar, S. B. Banerjee and K. P. Subramanian)

Study of isomer-dependent fragmentation dynamics in photo-induced molecular fragmentation

Photo-induced fragmentation dynamics of 2,6- and 3,5 - difluoriodobenzene are studied using coincident electron and ion momentum imaging. By analyzing the ion momentum correlation between iodine and fluorine cations in three-fold ion coincidence events, we can distinguish the two isomers experimentally. In analysis, we found that the three-body fragmentation channels show clear evidence for sequential fragmentations. Our results demonstrate that the coincident electron-ion momentum imaging technique is a powerful method to study even such rather complex molecules consisting of twelve atoms.

This work is done in research collaboration with Prof. Daniel Rolles and team of KSU, USA.

(R. K. Kushawaha)

Probing the THz vibrations of singly ionized CO₂ molecules

Temporal evolution of electronic and nuclear wave packets created in strong-field excitation of the carbon dioxide molecule is studied using Velocity map imaging and pump-probe scheme. The femtolaser (Kansas Light Source: 35fs, 4mJ and 2KHz) of KSU was used in this experiment. The 8fs pulses were generated using a noble-gas filled hollow fibers and compressor based on an ultra-broadband dispersive mirrors. The pump beam was used to generate singly ionized CO₂ which has vibration in 4-45 THz range predicted in calculations. These vibrations were probed in the experiment.

This work is done in research collaboration with Prof. V. Kumarappan and team of KSU, USA.

(R. K. Kushawaha)

Far ultraviolet spectroscopy of saturn's moon RHEA

The focus of this research project is an analysis of far ultraviolet reflectance spectra of the icy surface of Saturn's second largest satellite, Rhea. Spectral studies carried out using the Cassini Visual Infrared Mapping Spectrometer (VIMS) have shown that Rhea, like the other icy satellites of the Saturnian system, is dominated by water-ice, with small amounts of carbon dioxide and other minor contaminants. Further chemical information may be derived from far-UV reflectance spectra that have been collected using the Cassini Ultraviolet Imaging Spectrometer (UVIS) during three different flybys of Rhea. However, to date there no detailed analysis of the far-UV region of Rheas Surface has been performed. Therefore, we have undertaken a detailed analysis of spatially resolved far-UV reflectance spectra of Rheas upper surface layer. The far-UV spectra sample Rheas leading and trailing hemispheres allowing us to look for spectral trends across the satellites surface. To carry out the geochemical survey of Rheas surface these UVIS observations are compared with vacuum-UV spectra measured in laboratory experiments. Thin film laboratory spectra of water-ice and other molecular compounds in the solid phase were collected at near-vacuum conditions and temperatures identical to those at the surface of Rhea. Some of the laboratory ice spectra were also irradiated to simulate bombardment of the surface ice by electrons originating from Saturn's magnetosphere. Our results comparing UVIS spectra with laboratory spectra show that, while Rheas surface is dominated by water-ice (as evident by the 165-nm absorption edge seen in the data), other chemical species are present as evidenced by a weak absorption feature centred near 184 nm.

This work was done in collaboration with Amanda Hendrix, Planetary Science Institute, USA and B M Cheng, National Synchrotron Radiation Research Center, Taiwan and Mark Elowitz / N J Mason, The Open University, UK.

(B Sivaraman)

ACID- AstroChemical Ices Database

The AstroChemical Ices Database (ACID) is a unique data repository that contains Vacuum UltraViolet (VUV) and InfraRed (IR) spectra collected from experiments that mimic the icy mantles of the interstellar dust analogs.

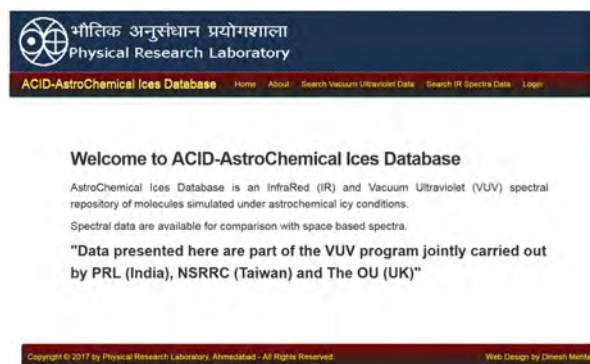


Figure 2 : Screenshot of ACID- AstroChemical Ices Database

Spectra presented in the database are from molecules that are already identified in the interstellar medium and also potential candidates that await identification. There is a dire need for such spectral studies in order to understand the physico-chemical nature of the molecular ices. In particular, the VUV spectra presented are also of use to compare data from UltraViolet Imaging Spectrograph (UVIS) on board Cassini spacecraft that scans the moons of Saturn.

This database is expected to evolve into a larger database where we aim at creating and unifying the atomic / molecular database for Indian researchers.

(D Mehta, B Vaishnav and B Sivaraman)

Reversible Phase Change Observed in Astrochemical Ethanethiol Ices

Thiol molecules are known to be present in the InterStellar Medium (ISM) since 1970's. Recent finding of ethanethiol ($\text{CH}_3\text{CH}_2\text{SH}$) in the ISM suggest that even larger thiols might be a part of the complex chemical processes at such extreme conditions. Chemical reaction networks leading to the formation of even a larger thiol molecule, propanethiol, suggest that such larger thiols are even synthesized in the ISM.

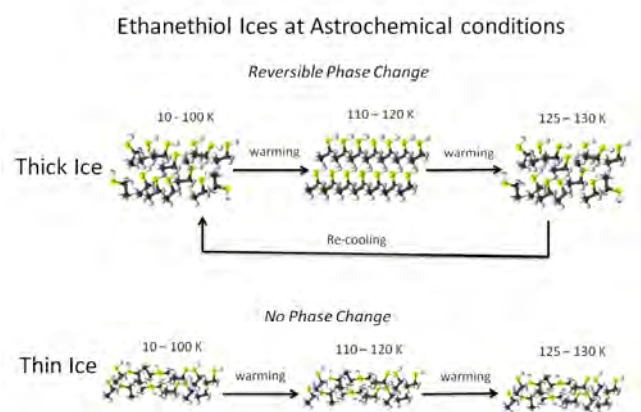


Figure 3: Ethanethiol Ices at Astrochemical Conditions

Therefore we investigated the morphology of thiols, such as methanethiol (CH_3SH), ethanethiol and propanethiol ($\text{CH}_3\text{CH}_2\text{CH}_2\text{SH}$) at astrochemical conditions. Experiments were carried out at Physical Research Laboratory (PRL) in India and at the National Synchrotron Radiation Research Center (NSRRC) in Taiwan. Experimental conditions employed in both the laboratories are similar where an ultrahigh vacuum chamber is used to cool down ZnSe/KBr substrates to 10 K/4 K. After achieving low temperature, thiol molecules were let into the chamber to freeze on to the windows. Temperature cycling was carried out from 10 K until phase change and then cooled back to lower temperatures with subsequent recording of infrared spectra at specific temperatures.

For methanethiol, spectra obtained at lower (10 K) and higher

temperatures (110 K) revealed phase change to have occurred in the ice which is consistent to those reported by Hudson (2016). In the case of propanethiol, a shoulder band in the S-H stretching region is an indication of phase change to have set in the ice before sublimation. However, for a thin ethanethiol ice there was no phase change until sublimation whereas a thick ice was found to change phase from amorphous to crystalline around 115 K and then another phase change from crystalline to amorphous at 125 K. This reversible phase change was found to repeat by subjecting the sample to temperature cycle until the sample turns thin by losing molecules during every phase change.

This work was done in collaboration with B M Cheng, National Synchrotron Radiation Research Center, Taiwan and N J Mason, The Open University, UK.

(B Sivaraman)

Identification of A Unique VUV Photoabsorption Band of Carbonic Acid for its Identification in Radiation and Thermally Processed Water-Carbon Dioxide Ices

Carbonic acid was synthesized within an ice containing water and carbon dioxide by irradiation of ~ 9 eV photons.

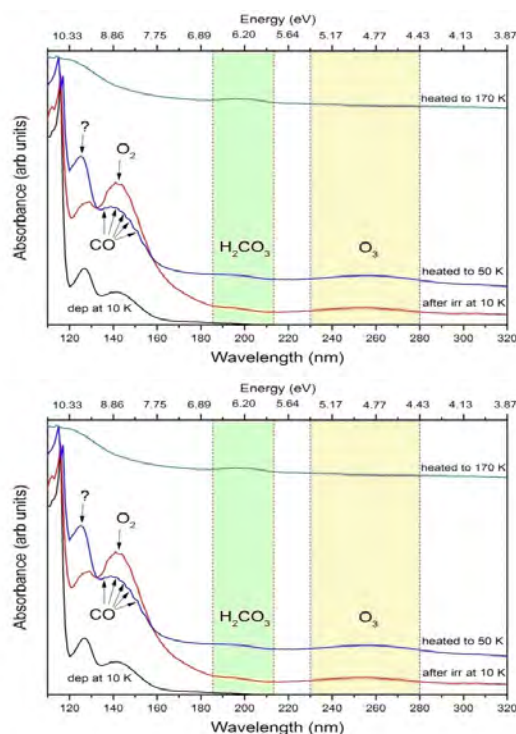


Figure 4: Vacuum Ultraviolet photoabsorption spectra of $\text{H}_2\text{O} - \text{CO}_2$ (1:2) ice layered (H_2O over CO_2) deposited on the LiF substrate at 10 K, irradiated with VUV photons and subsequently warmed to higher temperatures.

Vacuum UltraViolet (VUV) / UltraViolet (UV) photoabsorption spectra of the irradiated ice revealed absorption features from carbon dioxide, ozone, water, carbon monoxide and oxygen in addition to a band peaking at ~ 200 nm which is identified to be characteristic of

carbonic acid. After thermal processing of the irradiated ice leading to desorption of the lower volatile ices, a pure carbonic acid spectrum is identified starting from 170 K until sublimation above 230 K. Therefore the ~ 200 nm band in the VUV region corresponding to carbonic acid is proposed to be a unique identifier in mixed ices, rich in water and carbon dioxide typically encountered on planetary and satellite surfaces.

This work was done in collaboration with B M Cheng, National Synchrotron Radiation Research Center, Taiwan and N J Mason, The Open University, UK.

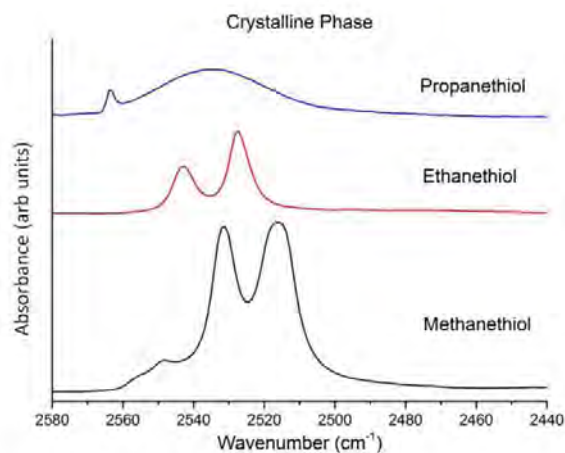
(B Sivaraman)

SH Stretching Vibration of Propanethiol Ice - A Signature for its Identification in the Interstellar Icy Mantles

Among the most commonly existing thiol molecules, methanethiol and ethanethiol were discovered in the interstellar medium and identification of the next larger thiol molecule, propanethiol, is long awaited. By simulating icy astrochemical conditions and probing propanethiol ices under infrared spectroscopy we propose the use of SH stretching vibrations observed in the propanethiol molecular ice as a probe towards its identification in the interstellar medium. Though there are conformational changes within the ice (as observed in both VUV and IR spectra), the SH stretching vibration of propanethiol is observed to be unique among the set of thiol molecules, methanethiol and ethanethiol, which enables the detection of propanethiol ice in

interstellar dust mantles using the James Webb Space Telescope.

This work was done in collaboration with B M Cheng, National Synchrotron Radiation Research Center, Taiwan and N J Mason, The Open University, UK.



SH stretching vibrational band of the crystalline ices of propanethiol, ethanethiol and methanethiol.

(D Sahu and B Sivaraman)

Publications

Publications in Journals

Astronomy and Astrophysics

1. Baliyan, K. S., Kaur, N., Chandra, S., Sameer and Shashikiran, G., 2016, "Multi-wavelength Study of Blazars Using Variability as a Tool", *Ap&SS*, v. 33, p. 177-183.
2. Baug, T., Dewangan, L. K., Ojha, D. K. and Ninan, J. P., 2016, "Star formation around mid-infrared bubble N37: Evidence of cloud-cloud collision", *ApJ*, v. 833, p. 85-102.
3. Bayo, A., Barrado, D., Allard, F., Henning, T., Comeron, F., Morales-Calderon, M., Rajpurohit, A. S., Pena Ramirez, K. and Beamin, J. C., 2017, "Physical parameters of late M-type members of Chamaeleon I and TW Hydrae Association: dust settling, age dispersion and activity", *MNRAS*, v. 465, p. 760-783.
4. Bisht, D., Yadav, R. K. S. and Durgapal, A. K., 2017, "2MASS analytical study of four open cluster candidates", *New Astronomy*, v. 52, p. 55-64.
5. Blinov, D., Pitraavlidou, V., Papadakis, I., Kiehlmann, S., Liodakis, I., Panopoulou, G. V., Pearson, T. J., Angelakis, E., Balokovic, M., Hovatta, T., Joshi, V., King, O. G., Kus, A., Kylafis, N., Mahabal, A., Marecki, A., Myserlis, I., Paleologou, E., Papamastorakis, I., Pazderski, E., Prabhudesai, S., Ramaprakash, A., Readhead, A. C. S., Reig, P., Tassis, K. and Zensus, J. A., 2017, "RoboPol: do optical polarization rotations occur in all blazars?", *MNRAS*, v. 462, p. 1775-1785.
6. Dewangan, L. K. 2017, "Star Formation Activity in the molecular cloud G35.20-0.74: onset of cloud-cloud collision", *ApJ*, v. 837, p. 44-55.
7. Dewangan, L. K., Ojha, D. K., Zinchenko, I., Janardhan, P. and Luna, A., 2017, "Multi-wavelength study of the star-formation in the S237 Hii region", *ApJ*, v. 834, p. 22-39.
8. Dewangan, L. K., Ojha, D. K., Zinchenko, I., Janardhan, P., et al., 2016, "The physical environment around IRAS 17599-2148 : IRDC and bipolar nebula", *ApJ*, v. 833, p. 246-260.
9. Dewangan, L. K., Baug, T., Ojha, D. K., Janardhan, P., Ninan, J. P., Luna, A. and Zinchenko, I., 2016, "Star formation activity in the neighbourhood of WR 1503-160L star in the mid-infrared bubble N46", *ApJ*, v. 826, p. 27-55.
10. Evans, A., Banerjee, D. P. K., Gehrz, R. D., Joshi, V., Ashok, N. M. et al...and 14 co authors, 2017, "Rise and fall of the dust shell of the classical nova V339 Delphini", *MNRAS*, v. 466, p. 4221-4238.
11. Jaisawal, G. K. and Naik, S., 2016, "Detection of Cyclotron Resonance Scattering Feature in High Mass X-ray Binary Pulsar SMC X-2", *MNRAS Letters*, v. 461, p. 97-101.
12. Johansson, J., Goobar, A., ... Banerjee, D. P. K., Joshi V.... and 12 co authors, 2017, "Spitzer observations of SN 2014J and properties of mid-IR emission in Type Ia supernovae", *MNRAS*, v. 466, p. 3442-3449.
13. Kharb P., Lal D. V., Singh V., Bagchi J., Chandra, I. C. H., Hota A., Konar C., Wadadekar Y., Shastri P., Das M., Baliyan K. S., Nath B. B. and Pandey-Pommier, M., 2016, "From Nearby Low-Luminosity AGN to High-Redshift Radio Galaxies : Science Interests with Square Kilometre Array", *J. Astrophys. Astr.*, v. 37, p. 27-34.
14. Kharb P., Srivastava S., Singh V., Gallimore J. F., Chandra, I. C. H. and Hota A., 2016, "A GMRT study of Seyfert galaxies NGC 4235 and NGC 4594 : evidence of episodic activity?", *MNRAS*, v. 459, p. 1310-1326.
15. Kushwaha, P., Chandra, S., Misra, R., Sahayanathan, S., Singh, K. P. and Baliyan, K. S., 2016, "Evidence for Two Lognormal States in Multi-wavelength Flux Variation of FSRQ PKS 1510-089", *ApJ Letters*, v. 822, pp. 1-6.

16. Lillo-Box, J., Demangeon, O., Santerne, A., Barros, S. C. C., Barrado, D., Hbrard, G., Osborn, H. P., Armstrong, D. J., Almenara, J. M., Boisse, I., Bouchy, F., Brown, D. J. A., Courcol, B., Deleuil, M., Delgado Mena, E., Daz, R. F., Kirk, J., Lam, K. W. F., McCormac, J., Pollacco, D., Rajpurohit, A., Rey, J., Santos, N. C., Sousa, S. G., Tsantaki, M. and Wilson, P. A., 2016, "*K2-30 b and K2-34 b : Two inflated hot Jupiters around solar-type stars*", A&A, v. 594A, p. 50-56.
 17. Rajpurohit, A. S., Reyle, C., Allard, F., Homeier, D., Bayo, A., Mousis, O., Rajpurohit, S., and Fernandez-Trincado, J. G., 2016, "*Spectral energy distribution of M-subdwarfs: A study of their atmospheric properties*", A&A, v. 596A, p. 33-42.
 18. Rao, A. R. et al. including Chattopadhyay, T., Mithun N. P. S., Vadawale, S. V., 2016, "*AstroSat CZT Imager Observations of GRB 151006A : Timing, Spectroscopy, and Polarization Study*", ApJ, v. 833, pp. 1-10.
 19. Sand, D. J., Hsiao, E.Y., Banerjee, D. P. K., Marion, G.H., Diamond, T.R., Joshi, V., Parrent, J.T., Phillips, M.M., Stritzinger, M.D. and Venkataraman, V., 2016, "*Post-maximum Near-infrared Spectra of SN 2014J : A Search for Interaction Signatures*", ApJ Letters, v. 822, pp. 1-7.
 20. Santerne, A., Hbrard, G., Lillo-Box, J., Armstrong, D. J., ..., Rajpurohit, A., ... and 72 co-authors 2016, "*K2-29 b/WASP-152 b: An Aligned and Inflated Hot Jupiter in a Young Visual Binary*", ApJ, v. 824, p. 55-64.
 21. Sasikumar R. K., Ingale, M., Ramesh, R., Subramanian, P., Manoharan, P. K. and Janardhan, P., 2016, "*Amplitude of solar wind density turbulence from 10 – 45 Rs*", J. Geophys. Res., v. 121, p. 11605-11619.
 22. Singal, A. K. 2016, "*Compatibility of Larmor's formula with radiation reaction for an accelerated charge*", Foundations of Physics, v. 46, p. 554-574.
 23. Singal, A. K. 2016, "*Do the standard expressions for the electromagnetic field momentum need any modifications?*", Am. J. Phys., v. 84, p. 780-785.
 24. Singal, A. K., 2016, "*Poynting flux in the neighbourhood of a point charge in arbitrary motion and raditive power losses*", Eur. J. Phys., v. 37, p. 1-13.
 25. Singal, A. K., 2016, "*Radiation reaction and pitch angle changes for a charge undergoing synchrotron losses*", MNRAS, v. 458, p. 2303-2306.
 26. Singal, A. K., 2016, "*Radio VLBI and the quantum interference paradox*", Europhysics Letters, v. 116, pp. 1-3.
 27. Singal, A. K., 2016, "*Relativistic Doppler beaming and misalignments in AGN jets*", ApJ, v. 827, pp. 1-6.
 28. Singal, A. K., 2016, "*The genesis of the internal resistance of a battery - a physical perspective*", Phys. Education, v. 33, p. 1-7.
 29. Singal, A. K., 2017, "*Radiation reaction from electromagnetic fields in the neighbourhood of a point charge*", Am. J. Phys., v. 85, p. 202-206.
 30. Singal, A. K., 2017, "*The paradox of power loss in a lossless infinite transmission line*", Phys. Education, v. 33, p. 1-16.
 31. Singh V., Ishwara-Chandra C. H., Kharb P., Srivastava S. and Janardhan P., 2016, "*J1216+0709 : A Radio Galaxy with Three Episodes of AGN-Jet Activity*", ApJ, v. 826, p. 132-138.
 32. Srivastava, M. K., Banerjee, D. P. K., Ashok, N. M., Venkataraman, V., Sand, D. and Diamond T., 2016, "*Near Infrared studies of V2944 Ophiuchi (Nova Ophiuchi 2015)*", MNRAS, v. 462, p. 2074-2084.
 33. Vagshette, N. D., Naik, S. and Patil, M. K., 2017, "*Detection of a pair of prominent X-ray cavities in Abell 3847*", MNRAS, v. 466, p. 2054-2066.
 34. Vagshette, N. D., Sonkamble, S. S., Naik, S. and Patil, M. K., 2016, "*AGN-driven perturbations in the intracluster medium of the cool-core cluster ZwCl 2701*", MNRAS, v. 461, p. 1885-1897.
 35. Venkataramani, K., Ghetiya, S., Shashikiran G., Joshi, U. C., Agnihotri, V. K. and Baliyan, K. S., 2016, "*Optical spectroscopy of comet C/2014 Q2 (Lovejoy) from the Mount Abu Infrared Observatory*", MNRAS, v. 463, p. 2137-2144.
 36. Yoshida, Y., Kitamoto, S., Suzuki, H., Hoshino, A., Naik, S. and Jaisawal, G. K., 2017, "*A Suzaku view of accretion powered X-ray pulsar GX 1+4*", ApJ, v. 838, p. 30-44.
- ### Solar Physics
37. Chandra, R., Mandrini, C. H., Schmieder, B., Joshi, B., Cristiani, G. D., Cremades, H., Pariat, E., Nuevo, F. A., Srivastava, A. K., Uddin, W., 2017, "*Blowout jets and impulsive eruptive flares in a bald-patch topology*", A & A, v. 598, pp. 1-15.
 38. Joshi, B., Kushwaha, U., Veronig, A. M., Dhara, S. K., Shanmugaraju, A., Moon, Y. J. 2017, "*Formation and Eruption of a Flux Rope from the Sigmoid Active Region NOAA 11719 and Associated M6.5 Flare: A Multi-wavelength Study*", ApJ, v. 834, pp. 1-16.
 39. Joshi, B., Kushwaha, U., Veronig, A. M., Cho, K. S., 2016, "*Pre-flare Coronal Jet and Evolutionary Phases of a Solar Eruptive Prominence Associated with the M1.8 Flare: SDO and RHESSI Observations*", ApJ, v. 832, pp. 1-15.
 40. Kumar, S., Bhattacharyya, R., Joshi, B., Smolarkiewicz, P. K., 2016, "*On the Role of Repetitive Magnetic Reconnections in Evolution of Magnetic Flux Ropes in Solar Corona*", ApJ, v. 830, pp. 1-12.
 41. Kumar, B., Raja Bayanna, A., Venkatakrishnan, P., Kuchandy Mathew, S., 2016, "*Analysis of sudden variations in photospheric magnetic fields during a large flare and their influences in the solar atmosphere*", Res. Astron. and Astrophys., v. 16, pp. 1-18.
 42. Mishra, W., Wang, Y., Srivastava, N., 2016, "*On Understanding the Nature of Collisions of Coronal Mass Ejections Observed by STEREO*", ApJ, v. 831, pp. 1-13.
 43. Prasad, A., Bhattacharyya, R., 2016, "*A viable non-axisymmetric non-force-free field to represent solar active regions*", Phys. Plasmas, v. 23, pp. 1-5.
 44. Tomczyk, S., Mathew, S. K., Gallagher, D., 2016, "*Development of a tunable filter for coronal polarimetry*", J. Geophys. Res. Space Physics, v. 121, p. 6184-6195.
- ### Planetary Sciences and PLANEX Program
45. Basu Sarbadhikari, A. , Babu, E.V.S.S.K., Vijaya Kumar, T 2017, "*Chemical layering in the upper mantle of Mars:*

- Evidence from olivine-hosted melt-inclusions in Tissint*, Meteoritics and Planetary Science, v. 2, 251-267.
46. Basu Sarbadhikari, A., Babu, E.V.S.S.K., Vijaya Kumar, T. and Chennaoui Aoudjehane, H. 2016, "Martian meteorite Tissint records unique petrogenesis among the depleted shergottites", Meteoritics and Planetary Science, v. 51, p. 1588-1610
 47. Das, A., Singh, T., Lokabharathi, P.A., Dhakephalkar, P.K., Mallik, S., Kshirsagar, P.R., Khadge, N.H., Nagender Nath, B., Bhattacharya, S., Dagar, A.K., Kaur, P., Ray, D., Shukla, A.D., Fernandes, C.E.G., Fernandes, S.O., Thomas, T.R.A., Mamatha S.S., Mourya, B.S., Meena R.M. 2017, "Astrobiological implications of dim light phototrophy in deep-sea red clays", Life Sciences in Space Research, v. 12, pp. 39-50.
 48. Ghosh, S., Ray, D. and Murty, S.V.S., 2016, "Raghunathpura: An early crystallized IAB iron with sulphide micro nodules", Advances in Space Research, v. 58, pp.1879-1892
 49. Haider, S. A., Batista, I. S., Abdu, M.A., Santos, A. M., Siddhi, Y. Shah, and Thirupathaiah, P. 2016, "Flare X-ray Photochemistry of the E region ionosphere of Mars", J. Geophys. Res. Space Physics, v. 121, p. 6870-6888.
 50. He, J., Acharyya, K. and Vidali, G. 2016, "Binding Energy of Molecules on Water Ice: Laboratory Measurements and Modeling", ApJ, v. 825, pp. 1- 10.
 51. He, J., Acharyya, K. and Vidali, G. 2016, "Sticking of molecules on non-porous amorphous water ice ", ApJ, v. 823, pp. 1-10.
 52. Acharyya, K. and Herbst, E. 2016, "Simulations of the Chemistry in the Small Magellanic Cloud ", ApJ, v. 822, pp. 1-22.
 53. Shanmugam, M., Acharya, Y.B. Vadawale, S.V and Mazumdar, H. S. 2016, "Experimental characterization of Silicon Drift Detector for X-ray spectrometry: Comparison with theoretical estimation", Measurements, v. 91, p. 66-72.
 54. Mahajan R. R 2017, "Noble gases, nitrogen and cosmic ray exposure age of the Sulagiri chondrite", Geoscience Frontiers, v. 8, p. 205-210.
 55. Murty, S.V.S., Ranjith Kumar, P.M., Ray, D., Ghosh, S., Chattopadhyay, B. and Shrivastava, K.L. 2016, "Microstructures, mineral chemistry, noble gases and nitrogen in the recent fall Bhuka iron (IAB) meteorite", Planetary and Space Science, v. 131, p. 119-127.
 56. Pabari J. P. 2016, "Dependence of lunar mare microwave brightness temperature on FeO and TiO₂", Planetary and Space Science, v. 132, pp. 1-12.
 57. Panda, D.K., Banerjee, D. Goyal, S. K., Patel, A. R., Shukla, A.D., 2016, "Development of a cerium-doped lanthanum bromide gamma-ray spectrometer for planetary missions and feasibility studies for determination of elemental abundances of radioactive elements", Current Science, v. 110, p. 1-11.
 58. Ray, D., Ghosh, S. and Murty, S.V.S. 2017, "On possible origin of troilite metal nodules in the Katol chondrite", Meteoritics and Planetary Science, v. 52, p. 72-88.
 59. Ray, D., Ghosh, S., Goswami, T., Jobin, M.J 2017, "More insights into chondrule formation processes and shock-thermal history of Dergaon chondrite (H4-5 fall)", Geosciences Frontier, v. 8, p. 413-423.
 60. Sheel, V., and Haider, S. A. 2016, "Long term variability of dust optical depths on Mars during MY24-MY32 and their impact on subtropical lower ionosphere: Climatology, modeling, and observations", J. Geophys. Res., Space Phys., v. 121, p. 8038-8054.
 61. Sheel, V., Bisht, J., Sahu, L. and Thouret, V. 2016, "Spatio-temporal variability of CO and O₃ in Hyderabad (17N, 78E), central India, based on MOZAIK and TES observations and WRF-Chem and MOZART-4 models ", Tellus B, v. 68, pp. 1-20.
 62. Singh, M., Singhal, J., Arun Prasad, K., Rajesh, V.J., Ray, D. and Sahoo, P 2016, "Spectral Characteristics of Banded Iron formations in Singhbhum craton, eastern India: Implications to hematite deposition in Mars. ", Geosciences Frontier, v. 7, p. 927-936.
- ### Space and Atmospheric Sciences
63. Alvarado, M. J., Lonsdale, C. R., Macintyre, H. L., Bian, H., Chin, M., Ridley, D. A., Heald, C. L., Thornhill, K. L., Anderson, B. E., Cubison, M. J., Jimenez, J. L., Kondo, Y., Sahu, L. K., Dibb, J. E., and Wang, C., 2016, "Evaluating model parameterizations of submicron aerosol scattering and absorption with in-situ data from ARCTAS 2008", Atmos. Chem. Phys. Discuss., v. 16, p. 9435-9455.
 64. Bisoi, S. K., Chakrabarty, D., Janardhan, P., Rastogi, R. G., Yoshikawa, A., Fujiki, K., Tokumaru, M., and Yan, Y., 2016, "A prolonged southward IMF-B_z event of May 02-04, 1998: Solar, interplanetary causes and geomagnetic consequences", J. Geophys. Res. Space Phys., v. 121, p. 3882-3904.
 65. Chakrabarty, D., Hui, D., Rout, D., Sekar, R., Bhattacharyya, A., Reeves, G. D., and Ruohoniemi, J. M., 2017, "Role of IMF B_y in the prompt electric field disturbances over equatorial ionosphere during a space weather event", J. Geophys. Res. Space Phys., v. 122, p. 2574-2588.
 66. Chandra, H., Rastogi, R. G., Choudhury, R. K., and Sharma, S., 2016, "Equatorial Electrojet in the Indian region during the geomagnetic storm of 13-14 November 1998", J. Earth Syst. Sci., v. 125, p. 669-675.
 67. Chandra, N., Lal, S., Venkataramani, S., Patra, P. K., and Sheel, V., 2016, "Temporal variations of CO₂ and CO at Ahmedabad in western India", Atmos. Chem. Phys., v. 16, p. 6153-6173.
 68. Chandra, N., Venkataramani, S., Lal, S., Sheel, V., and Pozzer A., 2016, "Effects of convection and long-range transport on the distribution of carbon monoxide in the troposphere over India", Atmos. Poll. Res., v. 7, p. 775-785.
 69. Das, T. P., Thampi, S., Bhardwaj, A., Ahmed, S. M., and Sridharan, R., 2017, "Corrigendum to Observation of Neon at mid and high latitudes in the sunlit Lunar Exosphere: results from CHACE aboard MIP/chandrayaan-1", ICARUS, v. 284, p. 489-490.
 70. Guharay, A., Batista, P. P., Clemesha, B. R., Buriti, R. A., and Schuch, N. J., 2016, "Latitudinal variability of the quasi-16-day wave in the middle atmosphere over Brazilian stations", Ann. Geophys., v. 34, p. 411-419.
 71. Gunthe, S. S., Beig, G., and Sahu, L. K., 2016, "Study of relationship between daily maxima in ozone and temperature in an urban site of India", Curr. Sci., v. 110, p. 1994-1999.

72. Jindal, P., Shukla, M. V., Sharma, S., and Thapliyal, P. K., 2016, "Retrieval of ozone profiles from geostationary infrared sounder observations using principal component analysis", *Quart. J. Royal Meteorol. Soc.*, v. 142, p. 3015-3025.
73. Kalita, B. R., Hazarika, R., Kakoti, G., Bhuyan, P. K., Chakrabarty, D., Seemala, G. K., Wang, K., Sharma, S., Yokoyama, T., Supnithi, P., Komolmis, T., Yatini, C. Y., and Huy, L. M., 2016, "Conjugate hemisphere ionospheric response to the St. Patrick's Day storms of 2013 and 2015 in the 100°E longitude sector", *J. Geophys. Res. Space Phys.*, v. 121, p.364-390.
74. Karan, D. K., Pallamraju, D., Phadke, K., Vijayalakshmi, T., Pant, T. K., and Mukherjee, S., 2016, "Electrodynamical influence on the diurnal behaviour of neutral daytime airglow emissions", *Ann. Geophys.*, v. 34, p. 1019-1030.
75. Mallik, C., Chandra, N., Venkataramani, S., and Lal, S., 2016, "Variability of atmospheric carbonyl sulfide at a semi-arid urban site in western India", *Sci. Total Environ.*, v. 551-552, p. 725-737.
76. Manke, A. A., and Chakrabarty, D., 2016, "An integrated software platform for GPS/GNSS ionospheric data analysis", *Int. J. Sci. Eng. Tech.*, v. 4, p. 796-804.
77. Pallamraju, D., Karan, D. K., and Phadke, K. A., 2016, "First three dimensional wave characteristics in the daytime upper atmosphere derived from ground-based multiwavelength oxygen dayglow emission measurements", *Geophys. Res. Lett.*, v. 43, p. 5545-5553.
78. Pandey, K., Sekar, R., Anandaram, B. G., Gupta, S. P., and Chakrabarty, D., 2016, "Estimation of nighttime dip-equatorial E-region current density using measurements and models", *J. Atmos. Sol. Terr. Phys.*, v. 146, p. 160-170.
79. Priyamvada, H., Akila, M., Singh, R. K., Ravikrishna, R., Verma, R. S., Philip, L., Marathe, R. R., Sahu, L. K., Sudheer, K. P., and Gunthe, S. S., 2017, "Terrestrial macrofungal diversity from the tropical dry evergreen biome of Southern India and its potential role in aerobiology", *PLoS ONE*, v. 12, pp. 1-21.
80. Ramachandran, S., and Srivastava, R., 2016, "Mixing states of aerosols over four environmentally distinct atmospheric regimes in Asia: Coastal, urban, and industrial locations influenced by dust", *Environ. Sci. Poll. Res.*, v. 23, p. 11109-11128.
81. Rastogi, R. G., and Chandra, H., 2016, "Response of equatorial ionosphere during the super geomagnetic storm of April 2000", *Ind. J. Radio Space Phys.*, v. 45, p. 67-78.
82. Rout, D., Chakrabarty, D., Sekar, R., Reeves, G. D., Ruohoniemi, J. M., Pant, T. K., Veenadhari, B., and Shiokawa, K., 2016, "An evidence for prompt penetration electric field driven by changes in the solar wind density under northward IMF B_z condition", *J. Geophys. Res. Space Phys.*, v. 121, p. 4800-4810.
83. Sahu, L. K., Pal, D., Yadav, R., and Jaalnyam, M., 2016, "Aromatic VOCs at major road junctions of a metropolis in India: Measurements using TD-GC-FID and PTR-TOF-MS instruments", *Aerosol Air Quality Res.*, v. 16, p. 2405-2420.
84. Sharma, S., Chandra, H., and Vaishnav, R., 2015, "Study of sporadic-E layer over Ahmedabad during low and high sunspot years", *Asian J. Phys.*, v. 24, p. 875-882.
85. Sharma, S., Kumar, P., Vaishnav, R., and Lal, S., 2016, "Evaluation of clouds simulated by a weather model over western India", *Remote Sensing Lett.*, v. 7, p. 905-913.
86. Singh, R. P., and Pallamraju, D., 2016, "Effect of cyclone Nilofar on mesospheric wave dynamics as inferred from optical nightglow observations from Mt. Abu, India", *J. Geophys. Res. Space Phys.*, v. 121, p. 5856-5867.
87. Singh, R. P., and Pallamraju, D., 2017, "Large- and small-scale periodicities in the mesosphere as obtained from variations in O_2 and OH nightglow emissions", *Ann. Geophys.*, v. 35, p. 227-237.
88. Sinha, P. R., Sahu, L. K., Manchanda, R. K., Sheel, V., Deushi, M., Kajino, M., Schultz, M. G., Nagendra, N., Kumar, P., Trivedi, D. B., Koli, S. K., Peshin, S. K., Swamy, Y. V., Tzanis, C. G., and Greenivasan, S., 2016, "Transport of tropospheric and stratospheric ozone over India: Balloon-borne observations and modeling analysis", *Atmos. Environ.*, v. 131, p. 228-242.
89. Srivastava, R., Ramachandran, S., and Rajesh, T. A., 2016, "Aerosol mixing over urban region: Radiative effects", *Quart. J. Royal Meteorol. Soc.*, v. 142, p. 1732-1744.
90. Thampi, S. V., Shreedevi, P. R., Choudhary, R. K., Pant, T. K., Chakrabarty, D., Sunda, S., Mukherjee, S., and Bhardwaj, A., 2016, "Direct observational evidence for disturbance dynamo over the daytime low latitude ionosphere: A case study based on the June 28, 2013 Space Weather Event", *J. Geophys. Res. Space Phys.*, v. 121, p. 10064-10074.
91. Yadav, R., Sahu, L. K., Beig, G., and Jaaffrey, S. N. A., 2016, "Role of long-range transport and local meteorology in seasonal variation of surface ozone and its precursors at an urban site of India", *Atmos. Res.*, v. 176-177, p. 96-107.
92. Yadav, S., Sunda, S., and Sridharan, R., 2016, "The impact of the St. Patrick's day storm on the evolutionary pattern of equatorial ionization anomaly over the Indian longitudes using high-resolution spatiotemporal TEC maps: New insights", *Space Weather*, v. 14, p. 786-801.

Geosciences Division

93. Banerji, U.S., Bhushan, R., and Maurya, D.M., 2016, "Sedimentary records of paleoredox conditions at relict mudflat of Vaso, Southern Saurashtra coast, Gujarat", *Earth Sci.* v. 9, p. 114-125.
94. Banerji, U.S., Bhushan, R., Jull, A.J.T., 2016, "Mid-Late Holocene monsoonal records from an active mudflat of Diu Island, Southern Saurashtra, Gujarat, Western India", *Quat. Int.*, v. 10, p. 1-12.
95. Bhavya P.S., Kumar, S., Gupta, G. V. M., and Sudheesh, V., 2017, "Carbon uptake rates in the Cochin estuary and adjoining coastal Arabian Sea", *Estuaries and Coasts*, v. 40, p. 447-456.
96. Bhavya P.S., Kumar, S., Gupta, G. V. M., Sudheesh, V., Sudharma, K. V., Varrier, D. S., Dhanya, K. R., and Saravanane, N., 2016, "Nitrogen uptake dynamics in a tropical eutrophic estuary (Cochin, India) and adjacent coastal waters", *Estuaries and Coasts*, v. 39, p. 54-67.
97. Bikkina, S., Andersson, A., Sarin, M. M., Sheesley, R. J., Kirillova, E., Rengarajan, R., Sudheer, A. K., Ram, K. and Gustafsson, ö., 2016, "Dual carbon isotope characterization of total organic carbon in wintertime carbonaceous aerosols from northern India", *J. Geophys. Res. Atmos.*, v. 121, p. 4797-4809.

98. Damodararao, K., Singh, S.K., Rai, V.K., Ramaswamy, V. and Rao, P.S., 2016, "Lithology Monsoon and Sea-Surface Current Control on Provenance, Dispersal and Deposition of Sediments over the Andaman Continental Shelf", *Front. Mar. Sci.*, v. 3, pp. 1-15.
99. Das, A., Singh, T., LokaBharathi, P. A., Dhakephalkar, P. K., Mallik, S., Kshirsagar, P. R., Khadge, N.H., Nath, B. N., Bhattacharya, S., Dagar, A. K., Kaur, P., Ray, D., Shukla, A. D., Fernandes, C. E.G., Fernandes, S., Thomas, T. R.A., M.S.S., Mourya, B. S. and Meena, R. M., 2017, "Astrobiological implications of dim light phototrophy in deep-sea red clays", *Life Sci. Space Res.*, v. 12, p. 39-50.
100. Jeelani, G. H., Deshpande, R. D., Shah, R. A. and Hassan, W., 2017, "Influence of southwest monsoons in the Kashmir Valley, western Himalayas", *Isotopes Environ. Health Stud.*, v. 53, p. 400-412.
101. Jeelani, G. H., Shah, R. A., Jacob, Noble., and Deshpande, R. D., 2016, "Estimation of snow and glacier melt contribution to Liddar stream in a mountainous catchment, western Himalaya: an isotopic approach", *Isotopes Environ. Health Stud.*, v. 53, p. 18-35.
102. Jickells, T., Altieri, K., Buitenhuis, E., Baker, A., Capone, D., Duce, R., Dentener, F., Fennel, K., Kanakidou, M., LaRoche, J., Lee, K., Liss, P., Middelburg, J., Moore, K., Okin, G., Oschlies, A., Sarin, M. M., Seitzinger, S., Sharples, J., Singh, A., Suntharalingam, P., Uematsu, M. and Zamora, L., 2017, "A reevaluation of the magnitude and impacts of anthropogenic atmospheric nitrogen inputs on the ocean", *Global Biogeochem Cy.*, v. 31, p. 289-305.
103. Kaur-Kahlon, G., Kumar, S., Rehnstam-Holm, A. S., Rai, A., Bhavya, P. S., Edler, L., Singh, A., Andersson, B., Karunasagar, I., Ramesh, R. and Godhe, A., 2017, "Response of a coastal tropical pelagic microbial community to changed salinity and temperature", *Aquat Microb Ecol.*, v. 77, p. 37-50.
104. Kumar, P. K., Singh, A., Ramesh, R. and Nallathambi, T., 2017, " N_2 fixation in the Eastern Arabian Sea: Probable Role of Heterotrophic Diazotrophs", *Front Mar Sci.*, v. 4, pp. 1-10.
105. Lagad, R. A., Singh, S. K., and Rai, V. K., 2016, "Rare Earth Elements and $^{87}Sr/^{86}Sr$ Isotopic Characterisation of Indian Basmati Rice for its Geographical Authenticity", *Food Chem.*, v. 217, p. 254-265.
106. Laskar, A. H., Yadava, M. G., and Ramesh, R., 2016, "Stable and radioactive carbon in forest soils of Chhattisgarh, Central India: implications for tropical soil carbon dynamics and stable carbon isotope evolution", *J. Applied Geochem.*, v. 123, pp. 47-57.
107. Maibam, B., Singh, R. Y., Shukla, A. D. and Ramnathan, A. L., 2016, "Geochemical Study of The Granitoids Around Chhota Shigri Area, Himachal Pradesh, India", *J. Applied Geochem.*, v. 18, p. 408-416.
108. Meena, N.K., Prakasam, M., Bhushan, R., Sarkar, S., Diwate, P., Banerji, U.S., 2017, "Last-five-decade heavy metal pollution records from the Rewalsar Lake, Himachal Pradesh, India", *Environ Earth Sci.*, v. 12, p. 76-39.
109. Nawaz, M., Wasson, R. J., Bhushan, R., Juyal, N., and Sattar, F., 2016, "Topsoil Delivery to Himalayan Rivers : the importance of sampling time", *Hydrol. Process.*, v. 30, p. 4609-4616.
110. Ngangom, M., Bhandari, S., Thakkar, M. G., Shukla, A. D., Juyal, N., 2017, "Mid-Holocene extreme hydrological events in the eastern Great Rann of Kachchh, western India", *Quat. Int.*, ISSN 1040-6182, available online : v. 443, p. 188-199.
111. Olofsson, M., Egardt, J., Singh, A., and Ploug, H., 2016, "Inorganic phosphorus enrichments in Baltic Sea water have large effects on growth, carbon fixation, and N_2 fixation by *Nodularia spumigena*", *Aquat Microb Ecol.*, v. 77, p.111-123.
112. Panda, D. K., Banerjee, D., Goyal, S. K., Patel, A. R., and Shukla, A. D., 2016, "Development of a Cerium-doped Lanthanum bromide gamma ray spectrometer for planetary missions and feasibility studies for determination of elemental abundances of radioactive elements (Th, K and U)", *Curr. Sci.*, v. 110, p. 2135-2138.
113. Rastogi, N. and Patel, A., 2017, "Oxidative Potential of Ambient Aerosols : an Indian Perspective", *Curr. Sci.*, v.112, p. 35-39.
114. Samanta, S., Amrutha, K., Dalai, T.K., and Kumar, S., 2017, "Heavy metals in the Ganga River estuary sediment column: evaluation of association, geochemical cycling and anthropogenic enrichment", *Environ Earth Sci.*, v. 76, p. 140.
115. Sandeep, K., Shankar, R., Warrier, A.K., Yadava, M.G., Ramesh, R., Jani, R.A., Weijian, Z., and Zuefeng, L., 2017, "A multiproxy record of Indian summer monsoon variability during the Holocene in Southern India", *Paleogeog., Palaeoclimatol., Palaeoecol.*, v. 476, p. 1-14.
116. Sarkar, A., Deshpande M., Bera, M.K., Das, B., Juyal, N., Mortheikai, P., Deshpande, R.D., Shinde, V.S. and Rao, L.S., 2016, "Oxygen isotope in archaeological bioapatites from India: Implications to climate change and decline of Bronze Age Harappan civilization", *Sci. Rep. (Nature)*, v. 6, pp. 1-9.
117. Shahul Hameed, A., Resmi, T.R., Praveenbabu, M., Sudheesh, M., and Deshpande, R.D., 2016, "Synoptic variation of stable isotopes in precipitation and ground level vapour in a humid tropical region, Kerala, India", *Environ Earth Sci.*, v.75, p. 1412.
118. Sharma, K., Bhatt, N., Shukla, A. D. Cheong, D., Singhvi, A. K., 2017, "Optical dating of late Quaternary carbonate sequences of Saurashtra, western India", *Quaternary Research*, v. 87, p.133-150.
119. Sharma, S., Chand, P., Bisht, P., Shukla, A. D., Bartarya, S. K., Sundriyal, Y. P., and Juyal, N., 2016, "Factors responsible for driving the glaciation in the Sarchu Plain, eastern Zaskar Himalaya, during the late Quaternary", *J. Quat. Sci.*, v.31, p. 495-511.
120. Singh, A. K., Tiwari, M., Srivastava, A., Sinha, D.K., and Ramesh, R., 2017, "Wind strength variability in the Western Arabian Sea since the last Glacial Maximum : Southwest vs northeast monsoon modes", *J. Climate Change*, v. 2, p. 57-70.
121. Singh, A., Kürten, B., Cedras, R., Fernandes, M., Kumar, N., and 41 authors, 2016, "Perspectives on future Indian Ocean research from early career scientists", *Curr. Sci.*, v. 111, p. 1741-1742.
122. Singh, A., Rastogi, N., Patel, A., and Singh, D., 2016, "Seasonality in size-segregated ionic composition of ambient particulate pollutants over the Indo-Gangetic Plain : Source apportionment using PMF", *Environ. Pollut.*, v. 219, p. 906-915.
123. Singh, A., Rastogi, N., Patel, A., Satish, R.V., and Singh, D., 2016, "Size-segregated characteristics of carbonaceous

aerosols over the northwestern Indo-Gangetic Plain : Year round temporal behavior", Aerosol Air Qual. Res., v. 16, p. 1615-1624.

124. Sridhar, A., Bhushan, R., Balaji, D., Band, S., and Chamyal, L.S., 2016, "Geochemical and Sr-Nd isotopic variations in palaeoflood deposits at mainstem-tributary junction, western India: Implications on late Holocene flood events", CATENA, v. 139, p. 32-43.
125. Srinivas, B., Kawamura, K., and Sarin, M. M., 2016, "Stable carbon and nitrogen isotopic composition of fine mode aerosols ($PM_{2.5}$) over the Bay of Bengal: impact of continental sources", Tellus-B, v. 68, p. 31518.
126. Srinivas, B., Kawamura, K., and Sarin, M. M., 2017, "Secondary organic aerosol formation over coastal ocean : Inferences from atmospheric water-soluble low molecular weight organic compounds ", Environ. Sci. Technology , v. 51, p 4347-4357.
127. Sudheer, A. K., Aslam, M. Y. , Upadhyay, M., Rengarajan, R., Bhushan, R., Rathore, J. S., Singh, S. K. and Kumar, S., 2016, "Carbonaceous aerosol over semi-arid region of western India: Heterogeneity in sources and characteristics", Atmos. Res. , v. 178-179, p. 268-278.
128. Thajudeen, J., Yousuf, J., Veetil, V. P., Varghese, S., Singh, A. and Abdulla, M. H., 2017, "Nitrogen fixing bacterial diversity in a tropical estuarine sediments", World J Microbiol Biotechnol., v. 33, p. 41.
129. Verma, K., Tiwari, M., Yadava, M. G., Sudhakar, M. and Ramesh, R., 2016, "Late Quaternary Paleo-Monsoon History From the Western Continental Margin of India : Consistency of results from $\delta^{18}O$ and Clay Mineral Analysis", J. of Applied Geochem., v.18, p. 447-456.

Theoretical Physics

130. Basak, T., Mohanty, S., and, Tomar, G., 2016, " Explaining AMS-02 positron excess and muon anomalous magnetic moment in dark left-right gauge model", JHEP , v.1603, pp. 1-17.
131. Bhalla P., Kumar, P., Das., N., Singh, N., 2016, "Theory of the dynamical thermal conductivity of metals", Phys. Rev. B., v.94, pp. 1-12.
132. Bhatt, J. R. and Pandey, A. K., 2016, "Primordial magnetic field and kinetic theory with Berry curvature", Phys. Rev. D, v.94, pp. 1-11.
133. Chakravarty, G. K., Gupta, G., Lambiase, G. and Mohanty, S., 2016, "Plateau Inflation in SUGRA-MSSM", Phys.Lett. B, v.760, p.263-266.
134. Chakravarty, G. K., Lambiase, G. and Mohanty, S., 2016, "Dilaton assisted two-field inflation from no-scale supergravity", Phys.Rev. D, v.94, pp. 1-7.
135. Chauhan, B. and Mohanty, S., 2016, "Constraints on leptophilic light dark matter from internal heat flux of Earth", Phys.Rev. D, v.94, pp. 1-6.
136. Das, A., Konar, P. and Majhi, S., 2016, "Production of Heavy neutrino in next-to-leading order QCD at the LHC and beyond", JHEP, v.1606, pp. 0-27
137. Das, D., Hati, C., Kumar, G. and Mahajan, N., 2016, "Towards a unified explanation of $R_D(\text{and } \bar{L}\bar{U})$, R_K and $(g\hat{L}\hat{S}2)_\mu$ anomalies in a left-right model with leptiquarks", Phys. Rev. D, v.94, pp. 1-6.

138. Das, N., Bhalla, P., and Singh, N., 2016, "Memory Function Approach to Correlated Electron Transport: A Comprehensive Review", Int. J. Mod. Phys. B , v.30, pp. 1-23.
139. Dey, U. K. and Mohanty, S. 2016, "Constraints on Leptoquark Models from IceCube Data", JHEP, v.1604, pp. 1-11
140. Dey, U. K., Mohanty, S. and Tomar, G., 2016, "750 GeV resonance in the dark leftright model", Phys.Lett. B, v.756, p.384-389.
141. Ghosh, M., Goswami, S. and Raut, S. K., 2017, "Implications of $CP = 90^\circ$ towards determining hierarchy and octant at T2K and T2K-II", Mod.Phys.Lett. A, v.32, pp. 1-14.
142. Kadam, G. P., Mishra, H. and Deb, P., 2016, "Estimating transport coefficients in hot and dense quark matter", Phys.Rev.D, D94, pp. 1-19.
143. Konar, P. and Swain, A. K., 2016, "Reconstructing semi-invisible events in resonant tau pair production from Higgs", Phys.Lett. B, v.757, p. 211-215.
144. Kumar, A., Bhatt, J. R., Predhiman, K. Kaw, 2016, "On the Chiral imbalance and Weibel Instabilities", Physics Letters B, v.757, p.317-323.
145. Mani, B. K., Chattopadhyay, S. and Angom, D., 2017, "RCCPAC: A parallel relativistic coupled-cluster program for closed-shell and one-valence atoms and ions in FORTRAN", Comp. Phys. Comm., v.213, p.136-154.
146. Roy, A., and Angom, D., 2016, "Geometry-induced modification of fluctuation spectrum in quasitwo-dimensional condensates", New J. Phys., v.18, pp. 1-9.
147. Selvaganapathy, J., Das, P.K., and Konar, P., 2016, "Drell-Yan as an avenue to test noncommutative Standard Model at the Large Hadron Collider", Phys.Rev. D, v.93, pp.1-9
148. Suthar, K. and Angom, D., 2016, "Optical-lattice-influenced geometry of quasi-two-dimensional binary condensates and quasiparticle spectra", Phys. Rev. A, v.93, pp. 1-9
149. Suthar, K. and Angom, D., 2017, "Characteristic temperature for the immiscible-miscible transition of binary condensates in optical lattices", Phys. Rev. A, v.95, pp. 1-9.
150. Thakur, L., Haque, N. and Mishra, H., 2017, "Heavy quarkonium moving in hot and dense deconfined nuclear matter", Phys.Rev.D, v. 95, pp. 1-20.

Atomic, Molecular and Optical Physics

151. Aadhi, A., Kumar, S. C., Samanta, G. K. and Zadeh, M. E., 2017, "Controlled-switching of orbital angular momentum mode in an optical parametric oscillator", Optica, v. 4, p. 349-355.
152. Aadhi, A., Chaitanya, N. A., Jabir, M. V., Vaity, P., Singh, R. P. and Samanta G. K., 2016, "Airy beam optical parametric oscillator", Scientific Reports, v. 6, pP. 1-7.
153. Aadhi, A., Sharma, V., Chaitanya, N.A. and Samanta, G. K., 2017, "High power, multi-gigahertz, femtosecond Airy beam optical parametric oscillator pumped at 78 MHz", Scientific Reports, v. 7, pP.1-8.
154. Anwar, A., Chithrabhanu P., Reddy, S. G., Lal, N. and Singh, R. P., 2017, "Selecting the pre-detection characteristics for fiber coupling of parametric downconverted biphoton modes", Optics Communications, v. 382, p. 219-224

155. Aoki, A., Torii, Y., Sahoo, B.K., Das, B.P., Harada, K., Hayamizu, T., Sakamoto, K., Kawamura, H., Inoue, T., Uchiyama, A., Ito, S., Yoshioka, R., Tanaka, K.S., Itoh, M., Hatakeyama, A. and Sakemi, Y., 2016, "Light shifts induced by nuclear spin-dependent parity-nonconserving interactions", *Asian J. Phys.*, v. 25, p. 1247-1258
156. Aoki, A., Torii, Y., Sahoo, B.K., Das, B.P., Harada, K., Hayamizu, T., Sakamoto, K., Kawamura, H., Inoue, T., Uchiyama, A., Ito, S., Yoshioka, R., Tanaka, K.S., Itoh, M., Hatakeyama, A. and Sakemi, Y., 2017, "Parity-nonconserving interaction induced light shifts in the $7S_{1/2} - 6D_{3/2}$ transition of the ^{210}Fr atoms to probe new physics beyond the standard model", *Applied Phys. B*, v. 123, pp.1-11.
157. Banerji, A., Singh, R. P., Banerji, D. and Badyopadhyay, A., 2016, "Entanglement propagation of a quantum optical vortex state", *Optics Communications*, v. 380, p. 492- 498
158. Banerji, A., Singh, R. P., Banerji, D. and Badyopadhyay, A., 2016, "Generating a perfect quantum optical vortex", *Physical Review A*, v. 94, p. 053838-1-6
159. Batra, N., Sahoo, B.K. and De, S., 2016, "An Optimized Ion Trap Geometry to Measure Quadrupole Shifts of $^{171}\text{Yb}^+$ Clocks", *Chin. Phys. B*, v. 25, pp. 1-8.
160. Bhatt, N., Murari, M.K., Ukey, V., Prizomwala, S. P. and Singhvi, A. K., 2016, "Geological evidences of extreme wave along the Gujarat Coast of western India" *Natural Hazards*, v. 84, p. 1685-1704.
161. Bisht, P., Ali, S.N., Rana, N., Singh, S., Poonam, Sundriyal, Y.P., Bargri, D.S. and Juyal, N., 2017, "Pattern of Holocene glaciation in the monsoon-dominated Kosa Valley", *Geomorphology*, v. 284, p. 130141
162. Chaitanya N. Apurv, Aadhi A. , Jabir M. V. , Kumar S. Chaitanya , Samanta G. K. and M. Ebrahim-Zadeh, 2016, "Frequency-doubling of femtosecond pulses in thick nonlinear crystals with different temporal and spatial walk-off parameters", *IEEE Photonics Journal*, v. 8, p. 1-13
163. Chaitanya N. Apurv, Jabir M. V. and Samanta, G. K., 2016, "Efficient nonlinear generation of high power, higher order, ultrafast "perfect" vortices at 530 nm", *Optics Letters*, v. 41, p. 1348-1351.
164. Chaitanya N. Apurv, Jabir M. V., Banerji, J. and Samanta, G. K., 2016, "Hollow Gaussian beam generation through nonlinear interaction of photons with orbital angular momentum", *Scientific Reports*, v. 6, p. 32464.
165. Chaitanya N. Apurv, Kumar S. Chaitanya, Aadhi, A., Samanta, G. K. and M. Ebrahim-Zadeh, 2016, "Ultrafast Airy beam optical parametric oscillator", *Scientific Reports*, v. 6, p. 30701.
166. Chaitanya N. Apurv, Kumar S. Chaitanya, Devi, K., Samanta, G. K. and M. Ebrahim-Zadeh, 2016, "Ultrafast optical vortex beam generation in the ultraviolet", *Optics Letters*, v. 41, p. 2715-2718.
167. Chithrabhanu P., Aadhi, A., Reddy, S. G., Prabhakar, S. and Singh, R. P., 2016, "Generating arbitrary cebits on the orbital angular momentum Poincar sphere", *International Journal of Quantum Information*, v. 14, pp. 1-7.
168. Chithrabhanu P., Reddy, S. G., Lal, N., Anwar, A., Aadhi, A. and Singh, R. P., 2016, "Pancharatnam phase in non-separable states of light", *Journal of Optical Society of America B*, v. 33, p. 2093-2098.
169. D Bhattacharjee, V Jain, R H Biswas and A. K. Singhvi, 2016, "Geomorphic evidences and chronology of multiple neotectonic events in a cratonic area: Results from the Gavilgarh Fault Zone", *Central India Tectonophysics*, v. 677-678, p. 199-217
170. Das, M., Sahoo, B.K. and Pal, S., 2016, "Plasma screening effects on the electronic structure of multiply charged Al ions using Debye and ionsphere models", *Phys. Rev. A*, v. 93, pp.1-9.
171. Gorai, P., Das, A., Das, A., Sivaraman, B., Etim, E. E. and Chakrabarti, S. K., 2017, "A Search for Interstellar Monohydric Thiols", *The Astrophysical Journal*, v. 836, pp. 1-12.
172. Gorai, P., Das, A., Majumdar, L., Chakrabarti S. K., Sivaraman, B. and Herbst, E., 2017, "The Possibility of Forming Propargyl Alcohol in the Interstellar Medium", *Molecular Astrophysic*, v. 6, p. 36-46.
173. Sharma, K., Bhatt, N., Shukla, A. D., Cheong, D. K., and Singhvi, A. K., 2017, "Optical dating of late Quaternary carbonate sequences of Saurashtra, western India", *Quaternary Research*, v. 87, p. 133-150.
174. Kaur, K., Kaur, J., Sahoo, B.K. and Arora, B., 2016, "Dispersion coefficients for the interaction of Cs atom with different material media", *Phys. Lett. A*, v. 380, p. 3366 (1-7)
175. Kaur, K., Sahoo, B.K. and Arora, B., 2016, "Oscillation Frequencies for Simultaneous Trapping of Heteronuclear Alkali Atoms", *Asian J. Phys.*, v. 25, p. 1061-1068
176. Kumar, V., Piccirillo, B., Reddy, S. G. and Singh, R. P., 2017, "Topological structures in vector speckle fields", *Optics Letters*, v. 42, p. 466-469
177. Methikkalam, R.R.J., Bhuin, R.G., Ghosh, J., Sivaraman, B. and Pradeep, T., 2017, "Interaction of Acetonitrile with Alcohols at Cryogenic Temperatures", *J. Phys. Chem.*, v. 121, p. 2822-2835.
178. Nandy, D.K. and Sahoo, B. K., 2016, "Highly charged W^{13+} , Ir^{16+} and Pt^{17+} ions as promising optical clock candidates for probing variations of the fine structure constant", *Phys. Rev. A*, v. 94, pp. 1-7
179. Pavithraa, S., Methikkalam, R.R.J., Gorai, P. Lo, J.I., Das, A., Raja Sekhar, B.N., Pradeep, T., Cheng, B.M., Mason, N.J. and Sivaraman, B., 2017, "Qualitative observation of reversible phase change in astrochemical ethanethiol ices using infrared spectroscopy", *Spectrochimica Acta A*, v. 178, p. 166-170.
180. Pickering, J.L., Goodbred, S.L., Ayers, B. J. C., Covey, A. K., Rajapara, H. M. and Singhvi, A. K., 2017, "Terrace formation in the upper Bengal basin since the Middle Pleistocene: Brahmaputra fan delta construction during multiple highstands", *Basin Res*, doi: 10.1111/bre.12236, pp. 1-18.
181. Sahoo, B. K., 2017, "Improved limits on the hadronic and semi-hadronic CP violating parameters and role of a dark force carrier in the electric dipole moment of ^{199}Hg ", *Phys. Rev. D*, v. 95, pp. 1-9.
182. Sahoo, B.K. and Das, M. 2016, "Plasma-screening effects in the atrophysically interesting He-like and Li-like Mg and Fe ions", *Eur. Phys. J. D*, v. 70, pp. 1-10.
183. Shi, C., Gebert, F., Gorges, C., Kaufmann, S., Noertershaeuser, W., Sahoo, B. K., Surzhykov, A., Yerokhin, V., Berengut, J., Wolf, F., Heip, J.C. and Schmidt, P.O. 2017,

- "Unexpectedly large difference of the electron density at the nucleus in the $4p^2P_{1/2,1/3}$ fine-structure doublet of Ca^+ ", Applied Phys. B, v. 123, pp. 1-10*
184. Sil, M., Gorai, P., Das, A., Sahu, D. and Chakrabarti, S. K., 2017, "Adsorption energies of H and H_2 : a quantum-chemical study", Eur. Phys. J. D, v. 71, pp. 1-6.
 185. Singh, S., Kaur, K., Sahoo, B.K. and Arora, B., 2016, "Magic wavelengths for the State-insensitive Optical Trapping of Cs Atoms: case studies using the linearly and circularly polarized lights", J. Phys. B, v. 49, pp. (1-9
 186. Singh, S., Kaur, K., Sahoo, B.K. and Arora, B., 2016, "Dispersion coefficients for the interaction of inert gas atoms with alkali and alkaline earth ions and alkali atoms with their singly ionized ions", Asian J. Phys., v. 25, p. 655-666.
 187. Singh, S., Sahoo, B.K. and Arora, B., 2016, "Determination of magic wavelengths for the $7s^2S_{1/2} - 7p^2P_{3/2,1/2}$ transitions in Fr", Phys. Rev. A, v. 94, pp. 1-10.
 188. Singh, S., Sahoo, B.K. and Arora, B., 2016, "Magnetic-sublevel-independent magic wavelengths: Application to Rb and Cs atoms", Phys. Rev. A, v. 93, pp. 1-5
 189. Sivaraman, B., Pavithra, S., Lo, J.I., Raja Sekhar, B.N., Hill, H., Cheng, B.M. and Mason, N. J., 2016, "Vacuum ultraviolet photoabsorption spectra of nitrile ices for their identification on Pluto", The Astrophysical Journal, v. 825, p. 2.
 190. Srivastava, P., Kumar, A., Chaudhary, S., Meena, N., Sundriyal, Y. P., Rawat, S., Rana, N., Perumal, R.J., Bisht, P., Sharma, D., Agnihotri, R., Bagri, D.S., Juyal, N., Wasson, R.J. and Ziegler, A.D., 2017, "Paleofloods records in Himalaya", Geomorphology, v. 284, p. 1730
 191. Srivastava, P., Sangode, S. J., Parmar, N., Meshram, D. C., Jadhav, P. and Singhvi, A. K., 2016, "Mineral magnetic characteristics of the late Quaternary Coastal red sands of Bheemuni, East Coast (India)" J. Appl. Geophys, v. 134, p. 77-88
 192. X. Wei, C. Kong, G. K. Samanta, K. K. Tsia and K. Y. Wong, 2016, "Self-healing highly-chirped fiber laser at $1.0\ \mu m$ ", Optics Express, v. 24, p. 27577-27586
 193. Yamanaka, N., Sahoo, B. K., Yoshinaga, N., Sato, T., Asahi, K. and Das, B.P. 2017, "Probing exotic phenomena at the interface of nuclear and particle physics with the electric dipole moments of diamagnetic atoms: A unique window to hadronic and semi-leptonic CP violations", Eur. Phys. J. A, v. 53, pp. 1-49.
 194. Yu, Y. and Sahoo, B. K., 2016, "Scrutinizing Al-like $^{51}V^{10+}$, $^{53}Cr^{11+}$, $^{55}Mn^{12+}$, $^{57}Fe^{13+}$, $^{59}Co^{14+}$, $^{61}Ni^{15+}$, and $^{63}Cu^{16+}$ ions for atomic clocks with uncertainty below 10^{-19} level", Phys. Rev. A, v. 94, pp. 1-13.

Computer Centre

195. Raval J., 2016, "A Survey on Malware Detection Schemes Using Machine Learning Techniques", International Journal of Research and Scientific Innovation, vol. IV, p. 258-262.

Library & Information Services

196. Alam, M. N., 2016, "Ionosphere, Magnetosphere and Geomagnetism(IMG) : A Quantitative and Qualitative Study", IRA-International Journal of Applied Sciences, v. 3, p. 27-49.
197. Alam, M. N. and Sarkhel, J. K., 2016, "Evaluating Cosmology research in India using Bibliometric and Citation Indicators since 1960s", Research Journal of Library Sciences, v. 4, p. 1-13.
198. Alam, M. N. and Shukla, A., 2016, "Growth of Solar Physics Research in India since 1960 : A Scientometric Analysis", Journal of Indian Library Association, v. 52, p. 63-71.
199. Alam, M.N. and Shukla, A., 2016, "Stellar Research in India : A Scientometric Study", INFOLIB, v. 9, p. 9-20.
200. Alam, M. N. and Shukla, A. and Sarkhel, J. K., 2016, "Research on Astronomical Instrumentation, Methods and Techniques (AIMT) : A Scientometric Analysis", LIS Communication, v. 2, p. 2-12.
201. Alam, M.N. and Shukla, A., 2016, "Progress of Meteorology and Atmospheric Research Publications in India : A Scientometric Analysis", Indian Journal of Library Science and Information Technology, v. 1, p. 66-74.

Publications

Publications in Proceedings of Conference/ Symposia/ Workshops

Astronomy and Astrophysics

1. Janardhan, P., Bisoi, SK, Ananthakrishnan, S., 2016, "A 20 year decline in solar magnetic fields and solar wind micro-turbulence levels: Are we heading towards a Maunder-like minimum?", Proc. URSI Asia-Pacific Radio Science Conference, pp. 1079-1082.
2. Vadawale, S.V., Rao, A. R., Bhattacharya, D., Bhalerao, V. B., Dewangan, G. C., Vibhute, A. M., Mithun, N. P. S., Chattopadhyay, T., and Sreekumar, S., 2016, "In-orbit performance astrosat czti", SPIE Astronomical Telescopes+ Instrumentation, International Society for Optics and Photonics, p. 99051F-99051F.
3. Chattopadhyay, T., Vadawale, S. V., Rao, A. R., Bhattacharya, D., Mithun, N. P. S., and Bhalerao, V. 2016, "Line profile modelling for multi-pixel czr detectors", SPIE Astronomical Telescopes+ Instrumentation, International Society for Optics and Photonics, p. 99054D-9054D.
4. Goyal, S. K., Amisha P Naik, N. P. S. Mithun, SV Vadawale, YB Acharya, AR Patel, T Ladiya, and Niranjana M Devashrayee, 2016, "Design and development of hard x-ray imaging detector using scintillator and Si photomultiplier", SPIE Astronomical Telescopes+ Instrumentation, International Society for Optics and Photonics, p. 99152J-99152J.
5. Kumar, A., Sengupta, A. and Ganesh, S. 2016, "Autonomous Dome for a Robotic Telescope ", in IV Workshop on Robotic Autonomous Observatories (Eds. Mara Dolores Caballero-Garcia, Shashi B. Pandey, David Hiriart & Alberto J. Castro-Tirado) Revista Mexicana de Astronomia y Astrofisica (Serie de Conferencias), v. 48, p. 29-30.
6. Zola, S., Valtonen, M., Bhatta, et al, including Baliyan KS, Kaur N and Sameer, 2016, "A Search for QPOs in the Blazar OJ287: Preliminary Results from the 2015/2016 Observing Campaign", Galaxies, v. 4, p. 41.

Planetary Sciences and PLANEX Program

7. Srivastava, N., 2017, "Future scientific exploration of the Moon: Sample return from the Lowell crater, Orientale basin", Planetary Science Vision 2050 Workshop, LPI Contrib. No. 1989, pp. 1-2.
8. Mahajan R. R. 2017, "Meteorites from Indian subcontinent, a brief", Meteorites from Indian subcontinent, a brief, LPS XLVIII, abstract # 1762, pp. 1-2.
9. Basu Sarbadhikari, A., Mahajan, R. R., Misquita, J., Sisodia, M. S., Shyam Prasad, M., and Bhandari, N. 2016, "Lohawat Howardite: Carbonaceous Chondrite Impactors and Re-Equilibrated Components of Various Exposure Ages on Vesta", 79th Annual Meeting of the Meteoritical Society, Berlin Germany, Abstract # 6145.
10. Ray D., Mahajan R. R., Shukla A.D. and Goswami T. K. 2016, "Fall, petrology, classification, noble gas and cosmogenic records of komar gaon meteorite, the latest fall in India", 79th Annual Meeting of the Meteoritical Society, abstract # 6071, pp. 1.
11. Mahajan R. R., Basu Sarbadhikari A., Sisodia M. S., and Bhandari N. 2016, "Noble gases in Lohawat howardite", The Seventh symposium on polar science, National Institute of Polar Research, Tokyo Japan, abstract # NIPR-2016-OA-Mahajan.00071.01, pp. 1.
12. Goyal, S.K., Shanmugam, M., Patel, A. R., Ladiya, T., Tiwari, N. K., Banerjee, S. B., Vadawale, S. V., Janardhan, P., Chakrabarty, D., Srinivas, A. R., Shukla, P., Kumar, P., Subramanian, K. P., Bapat, B. and Adhyaru, P. R., 2016, "Multi-directional measurements of high energy particles from the Sun Earth L1 point with STEPS", Proc. SPIE 9905, Space Telescopes and Instrumentation 2016: Ultraviolet to Gamma Ray. pp. 1-9.

13. Goyal, S.K., Naik, Amisha P., Mithun N.P.S., Vadawale, S. V., Acharya, Y. B., Patel, A. R., Ladiya, T., Devashrayee, N. M., 2016, "Design & development of Hard X ray imaging detector using Scintillator and Si Photomultiplier", Proc. SPIE 9915, Space Telescopes and Instrumentation 2016: High Energy, Optical and Infrared Detectors for Astronomy VII, 99152J.
14. Goyal, S.K., Banerjee, D., Vadawale, S.V., Panda, D. K., Patel, A. R., Patinge, A., Ladiya, T., and Sarbadhikari, A. B., 2016, "Gamma Ray Spectrometer for future Mars mission: Design concept and Simulation study", Proc. SPIE 9905, Space Telescopes and Instrumentation 2016: Ultraviolet to Gamma Ray, 99056G.
15. Goyal, S.K., Shanmugam, M., Patel, A. R., Ladiya, T., Tiwari, Neeraj K., Banerjee, S. B., Vadawale, S. V., Janardhan, P., Chakrabarty, D., Srinivas, R., Shuklab, P., Kumara, P., P. Subramanian, K., Bapat, B. and Adhyaru, P. R., 2016, "Multi-directional measurements of high energy particles from the Sun-Earth L1 point with STEPS", SPIE, v. 9905N, p. 1-9.
16. Acharyya, K., 2016, "Water in Magellanic Clouds", Water in the Universe: From Clouds to Oceans conference, 12th - 15th April, Leiden, ESA.
17. Jethwa, Masoom P., Haider, S.A., 2016, "Study of dust storm by modeling and analysis of thermal emission spectra of Mars", 19th National Space Science Symposium held at Space Physical Laboratory, Vikram Sarabhai Space Centre, Thiruvananthapuram, Vol: 19, p. 50.
18. Shah, S., Y. and Haider, S. A. 2016, "Model calculation of production rate of H₂O and O₃ on lower atmosphere of Mars: Seasonal variability", 19th National Space Science Symposium held at Space Physical Laboratory, Vikram Sarabhai Space Centre, Thiruvananthapuram, Vol: 19, p. 52.
19. Sinha, Rishitosh K., Vijayan, S. and Bharti, R.R., 2016, "Terrestrial rock glaciers: a potential analog for Martian lobate flow features (LFF)", SPIE Asia-Pacific Remote Sensing, p. 98770K-98770K.
20. Prasad, K. D., Rai, V. K. and Murty, S.V.S., 2016 "A comprehensive 3D Model for an insight into diurnal and latitudinal variability of lunar subsurface temperatures", 76th Lunar and Planetary Science Conference, 1290, pp. 1-2.
25. Rajesh, T. A., Ramachandran, S., and Vinod Kumar, P. C., 2016, "Aerosol optical depth and its component trends over Vallabh Vidyanagar, Anand", IASTA-Bulletin (ISSN 09714510), v. 22, p. 402-405.
26. Singh, V., Kesarkar, A. P., Bhate, J. N., Gadhavi, H. S., and Jayaraman, A., 2016, "Comparative analysis of performance of coupled chemistry-meteorology model WRF-Chem to simulate aerosol and trace gases concentration over India", IASTA-Bulletin (ISSN 09714510), v. 22, p. 305-308.
27. Ravi Kiran, V., Gadhavi, H., and Jayaraman, A., 2016, "Long term observations of black carbon concentration at a rural site Gadanki in Southern India", IASTA-Bulletin (ISSN 09714510), v. 22, p. 635-636.
28. Gadhavi, H., Sai Suman, M. N., Ravi Kiran, V., Wankhede, T., and Jayaraman, A., 2016, "Experimental investigation of aerosol forcing efficiency over south India", IASTA-Bulletin (ISSN 09714510), v. 22, p. 729-730.
29. Sharma, S., Vaishnav, R., Kumar, P., and Shukla, K. K., 2016, "Aerosol optical thickness, water vapor and total column ozone assessment over Ahmedabad", IASTA-Bulletin (ISSN 09714510), v. 22, p. 438-440.

Geosciences Division

Space and Atmospheric Sciences

21. Rajesh, T. A., Manke, A. A., and Ramachandran, S., 2016, "Interactive Visualization Package for Aerosol Physical and Optical Properties", IASTA-Bulletin (ISSN 09714510), v. 22, p. 1-5.
22. Rajesh, T. A., and Ramachandran, S., 2016, "Multiwavelength Sun Photometer (MSP): Instrument for Aerosol Columnar Properties", IASTA-Bulletin (ISSN 09714510), v. 22, p. 14-17.
23. Rajesh, T. A., and Ramachandran, S., 2016, "Aerosol Sampling System: Tool to Study the Effect of Relative Humidity on Surface Aerosol Properties", IASTA-Bulletin (ISSN 09714510), v. 22, p. 18-21.
24. Rajesh, T. A., Ramachandran, S., and Takemura, T., 2016, "Contribution of aerosol components to aerosol optical depth over a semiarid location in Western India", IASTA-Bulletin (ISSN 09714510), v. 22, p. 398-401.
30. Baker, A., Altieri, K., Okin, G., Dentener, F., Uematsu, M., Kanakidou, M., Daskalakis, K., Myriokefalitakis, S., Sarin, M., Duce, R., Galloway, J., Keene, B., Singh, A., and Zamora, L., 2016, "Atmospheric Nitrogen Deposition to the Oceans: Observation- and Model-Based Estimates", EGU General Assembly Conference Abstracts (EGU2016), v. 18, pp. 16328.
31. Chatterjee, A., and Ray, J. S., 2016, "Evidence for a Mid-Holocene Buried Himalayan River beneath the Ghaggar Plains, NW India: A Geochemical Provenance Study", Goldschmidt Conference, v. 414., pp. 1.
32. Chinni, V., Singh, S. K., Bhushan, R., and Rengarajan, R., 2016, "Dissolved Iron in the North-Eastern Indian Ocean", Goldschmidt Conference., v. 481.
33. Gandhi, N. and Ramesh, R., 2016, "Natural isotopic composition of particulate organic nitrogen in the Eastern and Central Arabian Sea", Proc. of the Indian National Science Academy, v. 82, p. 1283-1291.
34. Gautam, I., and Ray, J. S., 2016, "A Comparative Study of Two-Versus Three-Sequence Multi Dynamic Modes for ¹⁴²Nd Analyses by TIMS", Goldschmidt Conference, v. 909.
35. George, B. G., and Ray, J. S., 2016, "Provenance of sediments in the Neoproterozoic Marwar Basin, western India", 35th International Geological Congress, pp. 1.
36. Karri, D., Singh, S. K., and Rai, V. K., 2016, "REEs and ϵ Nd in the Ganga (Hooghly) and other East Indian Estuaries: Massive desorption of particulate REEs to the Ocean", Goldschmidt Conference, p. 593.
37. Loescher, C. R., Fischer, M. A., Neulinger, S. C., Fiedler, B., Philippi, M., Schütte, F., Singh, A., Hauss, H., Karstensen, J., Körtzinger, A. and Künzel, S., 2016, "Hidden biosphere in an oxygen-deficient Atlantic open ocean eddy: future implications of ocean deoxygenation on primary production in the eastern tropical North Atlantic", EGU General Assembly Conference Abstracts, v. 18, pp. 8068.

38. Patel, A., Rastogi, N., Singh, A., and Singh, D., 2016, "Oxidative potential of ambient fine aerosols over the Indo-Gangetic Plain during winter", IASTA-Bulletin (ISSN 0971 4510), v. 22, p. 88-90.
39. Ray, J. S., 2016, "Bitter Spring $\delta^{13}\text{C}$ anomaly in the Vindhyan Supergroup, Rajasthan, India", 35th International Geological Congress, pp. 1.
40. Satish, R. V., Rastogi, N., Singh, A., and Singh, D., 2016, "Brown carbon characteristics during paddy residue burning over the Indo-Gangetic Plain", IASTA-Bulletin (ISSN 0971 4510), v. 22, p. 611-613.
41. Singh, A., and Kumar, N., 2016, "Second International Indian Ocean Expedition (IIOE-2)", nano newsletter, pp. 23.
42. Singh, A., Bansal, O., Singh, D., Babu, S. S., and Rastogi, N., 2016, "Trends in aerosol optical depth and black carbon aerosols over the North Western Indo-Gangetic Plain", IASTA-Bulletin (ISSN 0971 4510), v. 22, pp. 571-574.
43. Singh, A., Kürten, B., Su, D., Raes, E., Todinanihary, G., Fernandes, M., Kumar, N., and Cedras, R., 2016, "Early Career Scientists Network for Indian Ocean Research", The Indian Ocean Bubble, p. 3.
44. Singh, A., Rastogi, N., Patel, A., and Singh, D., 2016, "Use of potassium as a tracer of emissions from biomass burning: assessment based on size-segregated ionic composition of aerosols", IASTA-Bulletin (ISSN 0971 4510), v. 22, p. 46-48.
45. Singh, S. K., Sawant, S., Bhushan, R., Rengarajan, R., and Rai, V. K., 2016, "REEs and ϵNd in the north-eastern Indian Ocean", Goldschmidt Conference, pp. 1.
46. Subha Anand S. and Rengarajan, R., 2016, "Particulate organic carbon export flux in the Bay of Bengal and the Indian Ocean using ^{234}Th - ^{238}U and ^{210}Po - ^{210}Pb disequilibria", Goldschmidt Conference, pp. 1.
47. Zayas, Y., and Singh, A., 2016, "Meeting of NANO Alumni with the POGO members and Nippon Foundation", NF-POGO Alumni E-Newsletter, v.10, pp.2.
52. Lal, N., Shajilal, B., Anwar, A., Perumangatt, C., and Singh, R.P., 2016, "Observing Sub-Poissonian Statistics of Heralded Single Photons Using an Oscilloscope", 13th International Conference on Fiber Optics and Photonics, OSA Technical Digest (online), Optical Society of America, paper Th3A.72.
53. Perumangatt, C., Lal, N., Anwar, A., Reddy, S. G. and Singh, R. P., 2016, "A Stabilized Polarization Controlled Orbital Angular Momentum Sorter", 13th International Conference on Fiber Optics and Photonics, OSA Technical Digest (online), Optical Society of America, paper Tu4A. 46.
54. Anwar, A., Lal, N., Chithrabhanu, P., Kumar, V. and Singh, R. P., 2016, "Tunable Quantum Entangled states", 13th International Conference on Fiber Optics and Photonics, OSA Technical Digest (online), Optical Society of America, paper W2C. 2.
55. Kumar, A., Reddy, S. G. and Singh, R.P., 2016, "Correlation Studies of Work Function and Optical Nonlinearity", 13th International Conference on Fiber Optics and Photonics, OSA Technical Digest (online), Optical Society of America, paper Tu4A. 37.
56. Goyal, S. K., Shanmugam, M., Patel, A. R., Ladiya, T., Tiwari, Neeraj K., Banerjee, S. B., Vadawale, S. V., Janardhan, P., Chakrabarty, D., Srinivas, A. R., Shukla, P., Kumar, P., Subramanian, K. P., Bapat, B. and Adhyaru, P. R., 2016, "Multi-directional measurements of high energy particles from the Sun-Earth L1 point with STEPS", Proc. SPIE 9905, Space Telescopes and Instrumentation 2016: Ultraviolet to Gamma Ray, 99054N.
57. Aadhi, A., Sharma, V., Chaitanya, A. N. and Samanta G.K., 2016, "Multi GHz repetition rate Airy beam radiation in higher-harmonic fractional cavity OPO", 13th International Conference on Fiber Optics and Photonics, OSA Technical Digest (online), Optical Society of America, paper Tu2D, p. 4.
58. Jabir, M.V., Chaitanya, A. N., Mathew, and Samanta, G.K., 2016, "Generation of hybrid entangled two photon state by transferring classical non separable state", 13th International Conference on Fiber Optics and Photonics, OSA Technical Digest (online), Optical Society of America, paper Tu3C, p. 3.
59. Chaitanya, A. N., Jabir, M.V., Banerji, J. and Samanta G.K., 2016, "Nonlinear generation of hollow Gaussian beam", 13th International Conference on Fiber Optics and Photonics, OSA Technical Digest (online), Optical Society of America, paper Tu4A, p. 25.
60. Aadhi, A., Kumar, S. C., Samanta G.K. and M. Ebrahim-Zadeh, 2016, "Controlled generation of tunable vortex beams in an optical parametric oscillator", 13th International Conference on Fiber Optics and Photonics, OSA Technical Digest (online), Optical Society of America, paper Tu5D, p. 4.
61. Chaitanya, A. N., Jabir, M.V., and Samanta G.K., 2016, "Nonlinear generation of perfect vortex beam", 13th International Conference on Fiber Optics and Photonics, OSA Technical Digest (online), Optical Society of America, paper W3A, p. 5.
62. Chaitanya, A. N., Jabir, M.V., Banerji, J. and Samanta G.K., 2016, "Nonlinear generation of high power and higher order hollow Gaussian beam", Frontiers in Optics, paper FTh5B, p. 5.
63. Jabir, M.V., Chaitanya, A. N. and Samanta, G.K., 2016, "Control of spatial distribution of entangled photons by the spatial structure of classical pump beam", Frontiers in Optics, paper JTh2A, p. 18.

Theoretical Physics

48. Kumar, A. K. and Bhatt, J. R. 2016, "Primordial Generation of Magnetic Fields", Springer Proc. Phys., v.1507, p.01795.

Atomic, Molecular and Optical Physics

49. Singhvi, A.K., Banerjee, D.M. Dasgupta, S.N., Mohan, R., Chandrashekhara, P., Ahmad, T., Bajpai, S., Raju, S. and Srinagesh, S. (eds) 2016, "Proceedings of Indian National Science Academy, Special issue on Glimpses of Geosciences Research in India", This Indian Report to IUGS 2012-2016, v. 82, p. 403-1145.
50. Kumar, V., Reddy, S. G. and Singh, R. P., 2016, "Realization of Coherence Vortex Using Poincaré Beams" 13th International Conference on Fiber Optics and Photonics, OSA Technical Digest (online), Optical Society of America, paper Th3A.7.
51. Reddy, S. G., Kumar, V., Singh, R. P. and Miyamoto, Y., 2016, "Scattering of vector vortex beams: polarization speckles", Asia Communications and Photonics Conference 2016, November 2-5, Wuhan, China, AS1K. 4.

64. Jabir, M.V, Chaitanya, A. N., Aadhi, A. and Samanta, G.K., 2016, "*Generation of variable sized perfect vortex and its effect in parametric down conversion process*", Frontiers in Optics, paper JW4A, p. 8.
65. Wei, X., Kong, C., Samanta, G. K. Ko, H., Tsia, K.K. and Wong, K.K., 2016, "*Compact Airy-beam optical swept-source at 1.0 μm* ", CLEO: Science and Innovations, paper STh3G, p. 1.
66. Aadhi,A., Samanta, G.K., Ebrahim-Zadeh, M. and Kumar, S.C., 2016, "*Tunable, continuous-wave, doubly-resonant vortex beam optical parametric oscillator*", CLEO: Science and Innovations, paper SW1Q, p. 2.
67. Chaitanya, A. N., Kumar,S.C., Samanta, G.K. and Ebrahim-Zadeh, M., 2016, "*Optical vortex beam generation in the deep-ultraviolet*", CLEO: Applications and Technology, paper JW2A, p. 71.

Computer Centre

68. Raval, J., 2017, "*Web Framework For Malware Detection using Machine Learning Technique*", 4th International Conference on Innovations In Information, Embedded and Communication Systems (ICIIECS17), (Paper ID:IEEES786), 17-18th March, 2017 held at Coimbatore, Tamilnadu, v. 3, p. 870.

Publications

Books Edited / Review Articles / Other Publications

Books Edited

1. Sahoo, B.K. 2017, "*Relativistic Calculations of Atomic Clocks*", Springer Publication An invited chapter for Handbook on Relativistic Quantum Chemistry, Ed. by Wenjian Liu
2. Singh, N. 2016, "*Electronic Transport Theories from weakly to strongly correlated systems*", CRC Press 2016
3. Band, S.T., Yadava., M.G, and Ramesh. R., 2016, "*Stalagmites reveal past drought records*", Geography and You v. 16(96), p. 36-39.
4. Kiran Kumar, P., and Ramesh, R., 2017, "*Indian Monsoon rainfall variations during the last ~ 25 ka*", The Indian Ocean Bubble 2v. 6, p. 13-14.
5. Ramesh, R. and Singh, A., 2017, "*Applications of nitrogen and carbon isotopes in Oceanography*", IANCAS Bulletin v. 17, p. 51-51.
6. Ramesh, R., Borgaonkar, H., Band, S., and Yadava, M.G., 2017, "*Proxy climatic records of past monsoon, in: (M.N. Rajeevan and S. Nayak, eds.) Observed climate variability and Change over the Indian region*", Springer, Singapore pp. 271-284.

7. Vijayan S., 2017, "*Regolith thickness, Estimation from FeO+TiO₂ variation model*", Encyclopedia of Lunar Science, Springer, pp. 1-7.

Review Articles

1. Ambastha, A. 2016, "*Solar activity and explosive transient eruptions*", Asian journal of Physics, v.v. 25, p. 267-294.

Technical Report

1. Pallamraju, D., and Solomon, S., 2016, "*Role of the Sun and the Middle Atmosphere/Thermosphere/Ionosphere In Climate (ROSMIC)*", VarSITI Newsletter v. 4, p. 3-4, November 2016.

PRL Technical Notes

1. Rajesh, T. A., and Ramachandran, S., 2016, "*Aerosol optical depth computational package for hand-held Sun photometer*", PRL Technical Note PRL-TN-2016-109.

Promotion of Basic Sciences, Official Language and Outreach Activities

Foundation Day Celebration at PRL 11 November 2016

The foundation day of Physical Research Laboratory, Ahmedabad was celebrated on 11 November 2016, Friday with a tree plantation ceremony in the morning followed by the presentation of Shri Hari Om Ashram Prerit Dr. Vikram Sarabhai Research Awards and PRL Award for the year 2015 to four scientists. Following the award ceremony, the Awardees made a presentation highlighting their significant research contributions.

In the field of Space Sciences, the Hari Om Ashram Prerit Dr. Vikram Sarabhai research award was conferred jointly to Dr. Nishim Kanekar from the NCRA-TIFR, Pune for his important contribution in studies of galaxy evolution and multi-phase structure of the interstellar medium and to Dr. Dibyendu Chakrabarty from PRL, Ahmedabad for his significant contribution and to the development of instrumentation to bring out space weather signatures in airglow emission at low latitudes.

Dr. Neelesh B. Mehta, IISC, Bangalore received the Hari Om Ashram Prerit Dr. Vikram Sarabhai research award in the field of ELECTRONICS, INFORMATICS, TELEMATICS & AUTOMATION for his fundamental contributions in modeling, design, and analysis of modern wireless communication systems. These find many applications in green wireless sensor networks and 4G/5G cellular system.

The recipients of the PRL Award was Dr. Geeta Vichare from the Indian Institute of Geomagnetism, Navi Mumbai for her work on detection of daytime sub storm signatures in the topside ionosphere, which is very vital for the space weather studies.

Each award carried a Medal and a Cash Prize of Rs.50,000/-.

The Vikram Sarabhai Research Awards were instituted from funds provided by Pujya Shri Mota of Hari Om Ashram, Nadiad, and the PRL Award is supported by the Aruna Lal Endowment Fund established by late Prof. Devendra Lal, former Director of PRL.



The recipients of the Hari Om Ashram Prerit Dr. Vikram Sarabhai research awards and PRL Award, in a photo from left to right: Shri Tapan Misra, Shri Jitendra Amin, Dr. Geeta Vichare, Dr. D. Chakrabarty, Dr. Nilesh Mehta, Shri A. S. Kiran Kumar, Prof. P. Janardhan, Shri Sanat Patel and Dr. Kartikey V. Sarabhai.

ISRO Story of the Week:

The paper "Observation of Suprathermal Argon in the exosphere of Mars" by Anil Bhardwaj et al. published in Geophysical Research Letters (2017) made the Story of week at ISRO website on 27 March 2017.

Activities on the promotion of Basic Sciences

PRL has been organizing popular lectures by eminent scientists open to the public. In this series the following popular lectures were organized during the this year.

- “A Brief History of Light”, Prof. Majid Ebrahim-Zadeh, The Institute of Photonic Sciences (ICFO), Spain.
- “The Mysterious Magnetic Personality of our Sun”, popular lecture under aegis of 21st National Conference on Atomic, Molecular and Optical Physics, hosted by PRL, Ahmedabad, Prof. Arnab Rai Choudhuri, IISc, Bangalore.

Science Day Celebration and PRL Scholarship

As has been the practice for several years, a day-long celebration was held on 25 February 2017 at the Physical Research Laboratory, Ahmedabad to mark the National Science Day. The celebrations aim

to attract young minds and motivate them to take up science as one of their career options.

National Science Day is also observed to spread the message of the importance of science and its application among the people and to accelerate the pace of development among them. PRL Scholarships from the Aruna Lal Endowment Fund, established by late Prof. Devendra Lal, former Director, were awarded to five students on this occasion. The selection was done on the basis of their performances in the state level screening test, poster competition and oral interview. All the five students are to receive Rs. 10,000/- per year for two consecutive years and for the third year provided the students continue to study in the science stream with the high academic record.

A multilingual (English, Hindi and Gujarati) dedicated web page for National Science Day activities was created, that contributed towards significant impact in the participation of students from remote centers of Gujarat, especially due to information and application forms made available in Gujarati language. This was the unique initiative of its kind.



Glances of NSD and Open house science exhibition.

In addition to the Aruna Lal scholarship, other prizes were awarded like centre wise top students (14) in the state level screening test held in January 2017 and poster/model competitions (12). Also, to give an impetus to young students about the various scientific research

being done at PRL, a small science exhibition was organised. All the students and teacher participants visited the exhibits and interacted with PRL scientists.

Also, to give an impetus to young students about the various scientific research being done at PRL, a small science exhibition was organized. All the students and teacher participants visited the exhibits and interacted with PRL scientists.

A unique panel discussion for teachers and parents on "Women In Science" was also organized on this day.

Open house Science Exhibition

PRL organised an 'Open house Science Exhibition' during 27-28 February 2017 at PRL that coincided with National Science Day celebrations. In this exhibition live experiments, live laboratory measurements, dynamic models, pathbreaking in-house built equipment, rare specimens of terrestrial and extra-terrestrial material, together with infographics on current research trends were exhibited. The objective of this exhibition was to reach out to students, teachers, researchers and a common man with interesting and exciting exhibits. Around 6500 people including kids and young school/college/university students visited PRL during this event.

Outreach Activities by Udaipur Solar Observatory, Udaipur



Glimpses of Outreach Activities by Udaipur Solar Observatory.

Two school outreaches were conducted by USO members on 3rd September 2016 and 7th January 2017 at the 'Government Boys High School, Dewali' and 'The Study, Badi' for students of classes 8-10.

Each of these events had around 10 volunteers participating from USO, and were attended by approximately 100 students along with their teachers. The duration of the programs was around 2 hours, which included talks on the solar system, basics of astronomy, optics, and also involved a hands-on session with simple astronomy kits. The outreach helped the students to get a general overview of the scientific activities taking place at the solar observatory and comprehend the role of astronomy towards the betterment of the society. The students were motivated to take up science as a future career option and also encouraged to contact the observatory members for guidance.

PRL Student chapter

PRL student chapter was formed in June 2015 with a group of PhD students working in the fields of optics and photonics by Dr. Goutam Samanta as faculty adviser. The major focus of the PRL student chapter is to popularize optics and photonics under the outreach program called Experiments with light among the school and college students through hands on experiments.



Glimpses of Open house science exhibition.

However, with the joining of PhD students from other divisions of PRL, the chapter has expanded its scientific portfolio by incorporating hands on experiments from other branches of science. So far the PRL student chapter have devised more than 50 hands on basic experiments to explain many phenomenon in our daily life including "what is the need of two eyes", "why sky is blue and red at sunrise and sunset?", "principle of fiber optics communication" and advanced experiments including optical tweezer, and effect of polarization in double slit interference pattern, super-conductivity, Lenz's law, and principle of roller coaster. The student chapter also distributes optics kit comprising with polarizers, 2D grating and liquid crystal sheet to the students. So far the student chapter members have demonstrated their experiments to more than 10000 students in Gujarat, India. In addition, the PRL student chapter also organizes an annual conference named as Students' Conference in Optics and Photonics (SCOP), for the professional development of the PhD students. This is two days conference, organized by the students and participated by the students from different parts of India. To enhance the quality of the conference they also invites few young faculties of different Institutes of India and a plenary talk by an eminent scientist from abroad. Due to such initiative, the M.Sc., PhD and postdoctoral students from

different parts of India get the opportunity to PRL with full funding and share their research and build networking among themselves. In its inception, SCOP-2016 has been widely acknowledged as a great success with a participation of 30 students from 25 different Indian Institutes/ Universities and 15 in-house participants. The details of SCOP-2016 can be found using the webpage, (<https://www.prl.res.in/~prlosachap/SCOP2016/index.php>). In its second year, the conference has already started getting appreciation from different parts of the research community.



Glimpses of Open house science exhibition.

Activities on the Promotion of Official Language

- A Hindi Technical Seminar was organized in PRL on 29.04.2016 whose title was Recent breakthroughs in Science and technology: New initiatives and findings at PRL. Around 22 papers were presented by different scientific Divisions of PRL.
- According to the Directives of DOS different days were celebrated which were marked with two Hindi Extempore Competition organized on Anti-Terrorism Day on May 21, 2016 and another under Swachh Bharat Abhiyan respectively.
- The task of preparing a bilingual medical directory in the mobile app "Sampark" is completed.
- The newly updated PRL website is also fully updated in Hindi.
- A Parliamentary Committee visited two premises of PRL located in Mount Abu and Udaipur in the month of June and a bilingual report of meetings of Scientific Parliamentary Committee was prepared.
- An Orientation program for Hindi Officials and staff was organized by Department of Space in Bangalore on 14-15 July 2016 which was attended by Hindi Officer-II & O.S.D., PRL. This program is regarding the propagation of Hindi and its progress. PRL Hindi section staff members also participated in the Inter Center Hindi Technical Seminar held in Space Applications Center on July 21, 2016.
- In every quarter OLIC meetings are organized to review the progress of Hindi and to fulfill the targets of correspondence. Throughout the year OLIC quarterly meetings were organized on 25.07.2016, 30.09.2016, 30.12.2016 and 25.03.2017 in different campuses of PRL in Ahmedabad, Udaipur and Mount Abu. In this, data related to correspondence and official language activities from all sections are sought and compiled. In particular, the emphasis is on the achievement of target in correspondence.
- Hindi Workshops are also organized alongside OLIC meetings, in which the staff members of different sections deliver talk related to their work.
- PRL representative attended the first half-yearly TOLIC meeting organized in Space Applications Center on July 26, 2016. First prize was awarded to PRL staff member in poetry competition. PRL also organizes the TOLIC meeting in which the Heads of all the central government offices of Ahmedabad were present. PRL also contributed to the content for the magazine that was released by TOLIC. PRL has received prize for the excellent implementation of the Official Language. PRL participated in the second half-yearly TOLIC meeting held in ONGC. First prize was awarded to PRL staff member in poetry competition organized by TOLIC.
- Hindi Pakhwada was celebrated in P.R.L. during September 14-28, 2016. The highlights of the celebration included debates, extempore, word quiz, typing, Hindi essay and self-written poetry competition.
- Translation of P.R.L. Annual Report was done in October 2016.
- Departmental Inspection of Official Language of Regional Remote Sensing Center, Kolkata and APEP Aluva was done by Hindi Officer. In-house inspection of all sections of PRL was completed by December.
- PRL participated in Space Glossary meeting in V.S.S.C. Trivandrum.
- A Hindi Nibandh competition was organized in PRL on 10th January, 2017 on the occasion of Vishwa Hindi Diwas.
- National Science Day question paper was prepared in bilingual, also support was given to faculty members in Hindi talk.
- Outreach booklet was published in bilingual.
- PRL Organized 3-Day meeting on inclusion of Hindi in COINS.
- Important contribution was made by PRL Hindi section in the publication of the Purchase Manual Department of Space and Space Glossary.
- Shri R.S. Gupta, Hindi Officer-II & O.S.D. delivered lectures in Hindi at workshops held by various Departments like BSNL, IIM, Doordarshan, NID, ONGC, Food Corporation of India, CONCOR and others on different topics regarding its progressive use and various applications of computers in Hindi.

Facilities and Services

Computer Centre

Computational Services Group

The Computational Services Group (CSG) is responsible for providing services/facilities like Networking (Internet, Local Area Network, Wifi, SPACENET), High performance Computing, E-mail, Web, DNS, Proxy, Centralized Printing, DHCP, Video Conference, software development and maintenance. Following services/facilities are added/upgraded during the year 2016-2017.

1. Newly Developed PRL Website Computer Centre has designed a new website of Physical Research Laboratory both in English and Hindi. The site was inaugurated by Director, PRL on 26th January 2017. Following are the new features of website:

- The website is designed using latest Content Management System (CMS) Drupal
- The website has Responsive Design i.e. easy to navigate on devices like smartphones
- There is no impact on the division web pages managed by respective divisions. Still they all are covered under responsive design
- Easy navigation
- Ease in the management of the website.
- RSS (Rich Site Summary, often called Really Simple Syndication) uses a family of standard web feed formats to publish frequently updated information like new updates (Job Vacancies, Tenders), audio, video etc.

The site has also following New Captions:

- Outreach - to show our science popularization activities

- Accolades - to show several recognitions received by our scientists/engineers.

- PRL in News - to show PRL activities covered in various newspapers / media

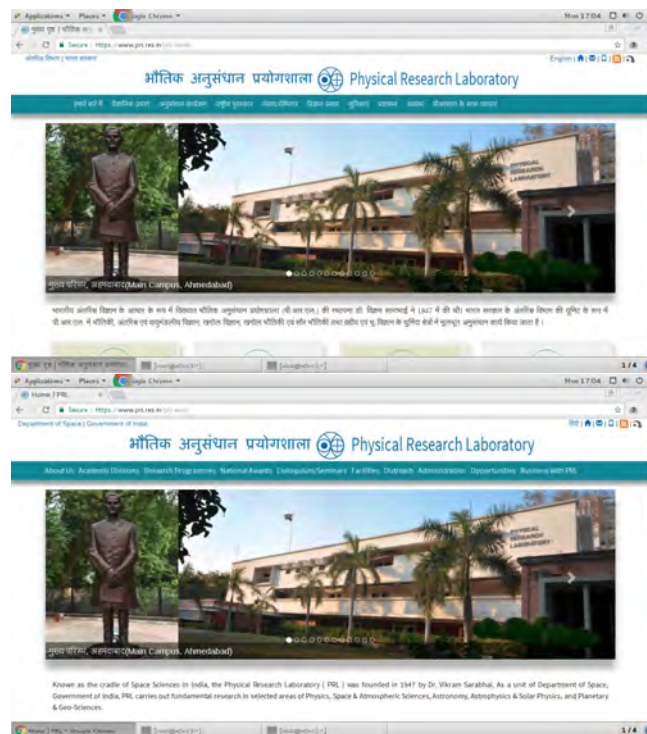


Figure 1: Screen-shots of New PRL Website.

2. Campus wide Wifi Network- 'Tarang'

Wireless network is established to allow access of PRL network and computing facilities using Laptops, PC with wireless card, and Smart Phones. Total 130 wifi access points are installed all over the PRL campuses (Main Campus, Thaltej Campus, Udaipur Campus, and Mt. Abu Campus). The wifi network is managed controlled using central wifi controller. User need to register the Physical/Hardware/MAC address of their devices. Only authorized/registered devices can get access to PRL wireless network. To automate users device registration and management, in-housed software is also developed. We have also established a backup/secondary controller at Thaltej campus to provide Smart Redundancy and un-interrupted services to all WLAN users of PRL.

3. Scientific Network Licenses software

Computational Services Group (CSG) manages centralized network licenses of various scientific software like Mathematica, Matlab, IDL, Maple, Sigmaplot and many others. CSG has procured latest version of Matlab R2016a with 20 concurrent network user licenses along with 2 concurrent network users for different toolkits of Matlab. CSG has also upgraded the Sigmpplot software version 11 to version 13. All the details are available on Intranet site of Computer Centre.

4. Connectivity between Mt. Abu and Main Campus

The point-to-point network connectivity between Infrared Observatory, Mt. Abu and Main Campus was operational over managed 02Mbps copper line provided by Bharat Sanchar Nigam Limited (BSNL). The line is upgraded over Optical Fiber Cable and bandwidth is also upgraded to 50Mbps.

5. Internet Connectivity from National Knowledge Network (NKN) at Udaipur Solar Observatory (USO), Udaipur Campus, Udaipur, Rajasthan

USO, Udaipur Campus became part of National Knowledge Network over 100Mbps Optical Fiber Cable (OFC) Internet connectivity from Bharat Sanchar Nigam Limited (BSNL). A separate secure proxy/gateway server is configured and running at USO campus which allows USO users to browse Internet over 100Mbps link. A server configured with automatic switch over to proxy server running at Main Campus. This enables seamless Internet browsing facility to users at USO, Udaipur campus. USO is also connected to Main Campus, PRL over point-to-point 50Mbps Optical Fiber Link through BSNL.

6. Established following Computational services at Thaltej Campus

SPACENET Data Access: To access ISRO Closed User Group (CUG) network a dedicated PC has been setup at Thaltej computer centre for easy and immediate access to Thaltej Scientific community and Payload project groups. Video Conferencing facility over Internet/NKN: To conduct various ISRO mission projects and other scientific meetings through Video Conference mode facility has been established and started at Thaltej campus too over NKN/Internet for the convenience and as a redundancy facility to PRL users. Network

expansion: Gigabit Network expansion was carried out through Optical Fiber Cable (OFC) for EPMS lab and Transit building-2 to upgrade their LAN and provide Wireless LAN network to users. Near Disaster Recovery Site of PRL: Protecting Organizational data and performing recovering from any undesired event is always a major goal for any organization to achieve this and minimize the downtime for PRL IT services we has set up PRLs near Disaster Recovery Site at Thaltej campus and almost 20 Virtual machines of PRL It services are being replicated their at certain defined intervals.

7. National Science Day Website in Gujarati

PRL celebrates National Science Day on 28th February every year. PRL webmaster had already prepared the website in English for online participation registration. This year, to encourage and motivate more participation from Gujarati medium school, the entire website was translated and developed in Gujarati language. The effort was well appreciated by many participating schools and students.

8. Security Awareness campaign during Open House Event:

Team Members of CSG had participated in the Open House Event organized at Main Campus, PRL during 27th- 28th February 2017 and spread the Awareness about Cyber Security to the visitors.

Library & Information Services

During 2016-17, two hundred and thirty eight (238) scientific, 29 general books, 53 hindi books and 53 CDs/DVDs were added in the Main, Thaltej and USO libraries. Subscription of twelve journals has been added to the existing library collection of 171 journals. During this period, number of visitors, visiting the library was 4293 and number of documents issued and returned were 1562 and 1584 respectively. Twenty one (21) book grant requests were processed to assist the students this year. Number of photocopies made, in house were 39452 and by outside agency were 92239.

PRL Library continues to have access to full-text databases like AGU Digital Library, GSA Archive, Nature archive (access from 1987), PROLA, Science Archive, SPIE and IEEE Digital Library. During 2016-17, AIAA Journals were made accessible as a part of ISRO Consortium. As no library can be completely self-sufficient, the Library also provides document delivery service through ILL. The number of document delivery requests for articles fulfilled by PRL Library was 245 and that of requests of PRL staff fulfilled by other libraries was 55. The Library homepage acts like a window through which it is possible to access the digital content subscribed by PRL as well as open access content. Primarily, it gives links to 176 online journals out of the 185 journals subscribed by the library. The PRL library also subscribes to EBSCO Discovery Tool which searches a topic through all the journals simultaneously with filters like full-text and available in the Library. In 2016-17, Library has started carrying out similarity check for students using the ithenticate tool as it is becoming mandatory for students to carry out the similarity / originality check before submitting the thesis and most of the journals carry out the originality check during peer review.

The PRL Library maintains an institutional repository which consists of journal articles published by the PRL authors from 1994 to present

and is also linked through the Library homepage. More than 4000 articles by PRL authors are now part of the repository. All the PRL theses from 1952 onwards (395) are now available full text for PRL users. All the Technical Notes since 1977, published by PRL have been digitized (109) and are available full text for PRL users. Two hundred and seventy e-books can be accessed through the library homepage. E-books page has been redesigned so as to give access to the collection by subject, alphabetical and publisher wise lists. These collections can be accessed from library homepage (<http://www.prl.res.in/~library>). The Library has taken up the digitization of the photographs archive. Scanning of the photographs of about 250 albums is completed. Giving the captions and metadata for each photograph for easy retrieval has started.



Figure 1: Book exhibition organized in November 2016, Awareness session on iThenticate - plagiarism check tool organised in March 2017.

Workshop

Design and Fabrication of coral cutting fixture on existing Vertical Band Saw Machine

Corals are important marine creatures that archive ambient sea water chemistry during their growth. Hence coral cores act as potential paleoclimatic proxies. The coral samples were 4 inch diameter cylindrical drills comprising various pieces of varying lengths for single location. In order to derive the past climatic signatures, all the coral cores were supposed to be cut in to two equal halves with the help of Vertical Band Saw machine. From one of the half piece of the coral, a slice of nearly 5-7mm thick coral piece was cut for further analysis. As cutting such thin slab from the core was not feasible with the help of same machine, modification and fabrication of fixture

along with x-y slide movement was designed, fabricated and installed on existing band saw machine done wherein X-Y movement of the sample core was possible which helped us in providing thin slices of coral core with an nearly uniform thickness of 5-7 mm. The entire fabrication and modification of the instrument was carried out in Workshop. Nearly 12 cores of 1 m length were cut and sliced for further analysis. They would be examined by measurement of various geochemical and isotopic signatures for retrieving high resolution past climatic information.



Figure 1: Coral cutting fixture & Sample of Corals

Mechanical support during the installation of Accelerator Mass Spectrometer (AMS)

Workshop technician helped and supported at various stages during AMS installation ,alignment, balancing ,accelerator tank handling etc.The following jobs were also made for AMS.

1. Making SS chiller plumbing assembly.
2. Do Chiller frame modification.
3. Developing exhaust system for AMS.
4. Developing prototype for AMS Target Holder of Cu and AL on bulk basis.
5. Fabricate new AMS Sample Carousel.
6. Glove Box Modification.

7. Protection chamber (perspex) for water chiller dispenser in AMS Lab.
8. Develop air circulation system for UPS room in AMS Console Room.

Fabrication of Glove Box for Handling Cs for Ion Source of Accelerator Mass Spectrometer (AMS)

One of the critical requirement of Accelerator Mass Spectrometer (AMS) is handling of Cs for the ion source. Since Cs is highly reactive in atmosphere it needs to be handled in an inert gas atmosphere. As part of this requirement, a glove box capable of handling materials without getting in touch with atmosphere.



Figure 2: Glow box

This Glove Box has been fabricated using perspex material with special butyl gloves. This glove box has inlet for an inert gas (Argon, Nitrogen) and an outlet through which the whole glove box chamber can be flushed for any atmospheric contamination. The sample to be handled can be placed from the side opening and then the chamber can be flushed with inert gas. Through the two gloves, necessary procedure of handling can be done inside this chamber. This glove box would be used for handling Cs ampoules for filling in the Ion Source of AMS, which require inert atmosphere. Additionally, it would be highly useful for handling any hazardous chemicals or material where safety needs to be taken while handling.

Aerosol sampling system

An aerosol sampling system (AeroSS) is being developed to sample the ambient atmospheric aerosols, sequentially at an ambient relative humidity and dry air condition, in order to study and quantify the effect of relative humidity on the aerosol optical and physical properties. The schematic view of the aerosol sampling system is illustrated in Figure 3. The ambient atmospheric aerosols are sampled into the system through an inlet manifold and is processed and further fed into the aerosol sampling instruments through outlet manifold. The manifolds have sensors for monitoring the air temperature and humidity at the inlet and outlet of the aerosol sampling system.

Ambient air is fed to one of the two parallel stainless steel cylinder C1 & C2 through straight 0.75 inch bore electrical actuated ball valves V1 & V2 respectively. The sampling cylinder C1 (length 1500 mm and inner diameter 150 mm) is filled with approximately 11 kg of Silica gel (orange beads) and houses 9 aerosol ducts (length 1500 mm and inner diameter 10 mm) made up from stainless steel (SS 316) wire mesh (wire diameter 0.25 mm and mesh open area 0.4 sq mm). The Silica gel is used to remove the moisture content in the ambient air sample. The ambient sampling cylinder C2 with a length 880 mm and an inner diameter of 40 mm is used to sample the ambient aerosol without any conditioning. The valves are electronically controlled and has been programmed to sample the ambient air in a predefined sequence. The complete assemblies made of aluminum (Al 6061 T6) using vertical machining center VMC-850 and has been silver hard anodized for moisture resistant. The system is been working successfully at Aerosol Monitoring Laboratory, PRL.

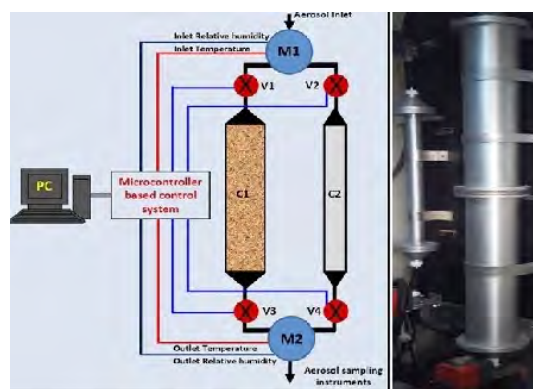


Figure 3: Aerosol sampling system

Prcised machining components for pay load work

1. **APXS mechanical box - 2 parts** Mechanical part for APXS detector package along with source holder.
2. **XSM XY position scanning setup with manual XYZ stage** Copper 'L' bracket with Al base plate for illuminating source at different positions of XSM Silicon Drift Detector. Present setup is made using manual XY translation stage
3. **APXS mounting, manual and motorized target movement setup** Aluminum plate for mounting APXS detector box inside vacuum chamber. Perspex target holder to keep metallic targets at different distances with respect to APXS detector. This setup has provision for mounting targets at every 5 mm distance from the detector and hence changing the distance is manual.
Modification of previous setup to move the target using two linear motors mounted on APXS base plate. Additional mounting provisions for motors, harness and shaft to target plate were made
4. **APXS experiment vacuum chamber assembly for horizontal mounting** Stand with wheels for mounting 2 vacuum chambers together for APXS experiment setup. A rail rod mechanism is attached with the stand which helps in removing/assembling the flange where APXS is base plate is mounted.

5. **Stand for adjustable height source holder** Adjustable height radioactive source holder
6. **Dummy sources and SS cups for APXS** Dummy sources like the APXS Cm-244 radioactive sources and SS cups to be used for shielding the sources
7. **Source storage box - 1 piece** Storage box made of 5mm SS and 3 mm lead walls. It has removable top cover and handles. This is to be used for storage and transport of radioactive source assembly of APXS.
8. **APXS rover motor assembly test setup** Al plate and mounting brackets for APXS motor mechanism.
9. **ASPEX Payload work** Four detector units were fabricated in PRL workshop. These detector units are the part of STEPS-1 package Subsystem of ASPEX payload). Each detector units consist of few collimator plate and magnet assembly. Where collimator plates were fabricated with aluminum material and magnet assembly consist of MS shielding and base holder. Where mild steel is used for shielding and aluminum is used to fabricate base holder. One aluminum box was fabricated for the testing of front-end electronics related to ASPEX project.

One black delrin box was fabricated for the testing of Si-pin detector. Black delrin material was used because testing requires light tight environment.



Figure 4: APXS experiment vacuum chamber assembly for horizontal mounting



Figure 5A: Aspx payload work



Figure 5B Aspx payload work

Installation of Dome (Astro Heaven) at Gurushikher at Mount Abu

Photometry is the technique by which probable planet candidates around a star can be found. For ground based photometry survey a dedicated telescope is required. A dome structure is needed for the protection of telescope. A 12 ft. Dome from Astro heaven is made up of fibre glass material. (Light weight and strong material). A dome for this telescope is installed. The dome is installed in a sequence and procedure given by manufacturer. The following are major steps in installing the dome

1. Uncarting the dome components
2. Assembly of base quadrants
3. Attaching the dome base to concrete floor
4. Assembly of shutter over base quadrants
5. Electrical connections
6. Testing and operation of dome

Attaching of dome to the base quadrants to the concrete floor was one of the critical part when installing the dome. This work is done by using a special technique called grouting with Hilti epoxy adhesive



Figure 6A: Dismantling of Dome



Figure 6B Installed Dome at Mt.Abu Gurushikher

A Preliminary Design of Temperature Cryostat for testing small detector

A small temperature cryostat has been designed to study the characteristics of very size small detector. The cryostat has been completely of copper and the top cover is made of SS material. The cryostat is designed such that the detector tested in cold and hot condition. For this a liquid nitrogen chamber also has been made in the cryostat. To test the detector in the hot condition, a small heater is incorporated in the PCB near to the detector. To maintain the vacuum at present is it kept inside a vacuum shield thermo-flask. At present proto type design has been done for small detector testing. In future the plan will be made to test bigger size (upto 3x 3) size. And also to test the detector under high vacuum the modification will be done.



Figure 7: Preliminary Design of Temperature Cryostat for testing small detector

Opto-Mechanical Design and Development of MFOSC-P

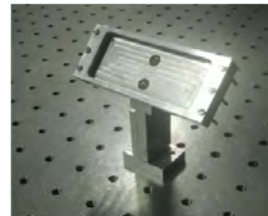
A Faint Object Spectrograph and Camera (FOSC) Named Mt. Abu FOSC Pathfinder(MFOSC-P) is being developed for PRL 1.2m Optical-Near Infrared(NIR) telescope at Gurushikhar site, Mt.Abu. The conceptual and final design is finalised with scientist. Some of the prised machining components for testing, alignment and assembly is fabricated in workshop. The other components are also under machining.

Fabrication of the various Opto- mechanical components

Following are the some major opto-mechanical components fabricated in PRL workshop. Some of these components had been already fabricated, some of under process. While fabrication number of factors like material selection, tolerance(0.1mm along the optical axis and 0.05 mm in the perpendicular to the optical axis),weight etc. should be considered. Aluminum alloyis the most common material due to its low cost and ease of machining. Stainless steel (SS 304) is also popular because it has a low CTE and high stiffness.

c.1) Telescope Glass window: It is basically a 70 mm diameter and 5 mm thick glass plate through which telescope beam enter in to the instrument. It is mounted on the top plate of the instrument. Designing concept of the slits is under process O ring is to be put on both sides of glass window

c.2) Calibration unit fold mirror It is a 31mm x 77 mm rectangular mirror of thickness 3.2 mm. It is mounted on a BGS Linear Translator stage guiding system that can be moved as per requirement. It is used to feed the beam from the calibration unit in to the instrument. Fabrication of this part is completed and ready for testing.



Calibration unit fold mirror

Figure 8

c.3) collimator and camera cage rod system with barrels and mounts. This is the most critical part of the instrument. Main optics of the instrument is to be mounted in this cage system. Assembling a system in a barrel provides protection from the environment and simplifies the system alignment. The lens mounts is often given a 50/100-m larger diameter than the lens outer diameter to provide room for loading the optics without jamming. The retaining rings and spacers should contact the lenses at the same diameter that the seats do; this avoids imparting a moment in the lens, causing distortion stepped lens mounts are design can accommodate lenses of varying sizes and uses machined seats to hold the lenses at the proper separation. These lens mount then slide fit in to their respective barrel and maintain the central accuracy. Tolerance required for lens mounts: 0.1 mm along the optical axis and 50m perpendicular to the optical axis.



Figure 9 : Lens Mount 2

c.4) main optics/ Collimated beam fold mirror This is a 100 mm diameter and 12 mm thick reflecting mirror that changes the plane of collimated beam. It is basically placed at 45 degree to the beam. So appropriate motion is required for this mirror mount. Fabrication of this part is completed for testing.

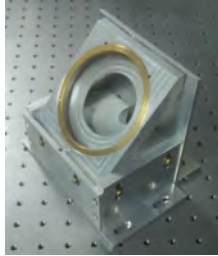


Figure 12

c.5) Motorized filter wheels Five different filters are to be fixed in to the filter wheel. This wheel is connected to a motor using a shaft with a support. Filter wheel is to be rotated at a required angle. There should only rotational motion any other kind of motion is not permitted. Fabrication of this part is completed for testing

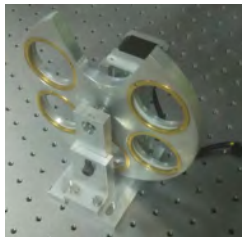


Figure 13

c.6) Motorized grating mount box Four different grating of size (68.5 x 68.5 x 9.5 mm³) is mounted on the 4 sides of the box. Box is then rotated using the stepper motor at required angle. Only rotational motion is required in the box any tip/tilt in grating cause the malfunction of system.. Fabrication of this part is completed for testing

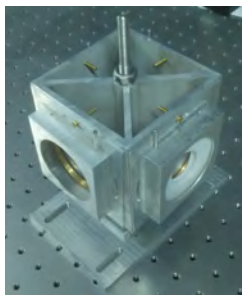


Figure 14

c.7) Calibration unit This unit contains an integrating sphere with several lamps and some lens. Lens are mounted in to the cage system using the mounts. Lens mount are fabricated for the testing. Fabrication concept of rest of part is under development.

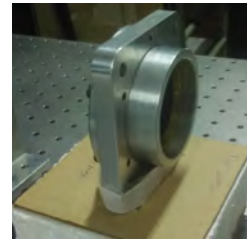


Figure 15



Figure 16 Collimator cage rod

Motorized Rotational Stage The main objective is to have the rotating sample for the desire use. For example the rotating sample are

1. Polarizer or wave plates: producing pulse for optical studies of material
2. Ground glass: scattering light for coherence studies,
3. Ruby rod: slow light studies etc. These all studies are going on in the lab.

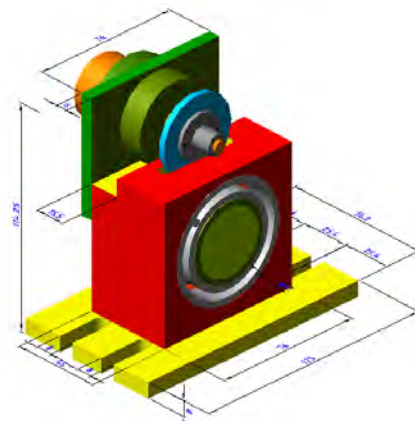


Figure 17 Motorized Rotational Stage

Motorized Rotational Stage includes parts like Rolling Bearing, Bearing Housing, and Single pair of 2 Gears, Holders for both Gears, Motor, Motor Bracket, Stopper and Mounting Base Plate. This system is designed to hold different types of optical components and provide precise, 360 rotation and used for automated positioning applications. Spur gear assembly perfectly matched to minimize play and back-lash is used as drive mechanism. Radial play is eliminated by the use of preloaded thrust bearings using balls as rolling elements. Stepper motor is used as the electrical actuator and is connected to the Spur Gear. Shaft of the stepper motor is connected to a rotating Gear as well for manual adjustments, whenever required. Top surface of the stage is provided with tapped holes and base with counter bored holes for mounting. The stage is manufactured in Aluminum as well as with required finish. Extra connecting holders are designed and manufactured to hold for different sizes in diameter of Optical components.

Filter Assembly for HIRISE System

A Filter Assembly has been made to house interference filters in the daytime multiwavelength high imaging spectrometer, a new optical technique for measuring daytime optical emissions for elucidating the method of analysis for retrieving the daytime airglow and auroral emissions using this instrument resolution and explain the procedure used to account for the Ring effect contribution. This Filter Assembly is at the image plane of the instrument and three filters of different wavelengths will be cut and put in it in a mosaic formation.

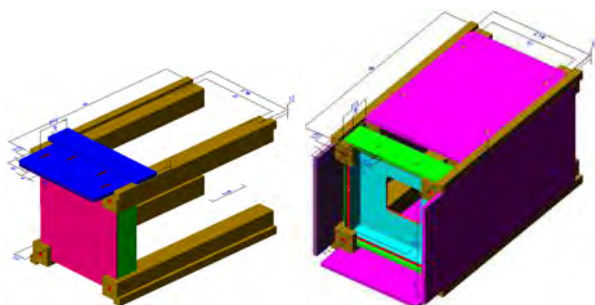


Figure 18 A & B: Filter Assembly for HIRISE System

An Assembly Comprised of Aluminum Holder, where at one side a different types of filters are to be place and on to the other side a Mirror has to be assemble. Care has to be taken at the time of manufacturing because of criticality and precision of the job.

Spatially Resolved Luminescence System

The system is meant to detect very faint luminescence light emitted by natural minerals like quartz and feldspar preserving the information about spatial distribution of luminescence on a surface. The spatial

distribution of luminescence light is recorded by means of EMCCD camera which is further used to estimate region specific dose and age. The system has significant application for dating of rock surfaces, fusion crust of meteorite, construction and destruction of building, to study luminescence light distribution and its characteristic, uniformity in preparation of phosphors etc. The mechanical design mainly includes housing for optical components, light stimulation unit, filter assembly coupled to EMCCD Camera. The assembly required several important scientific constraints along with flexibility of performing changes in assembly for different measurements.

The design of assembly required

1. Housing of achromatic doublet lenses such that image resolution is 1:1 with a flexibility of moving components for focusing.
2. Designing of LED assembly such that light from 30 LEDs can be focused on center at same point
3. Ease of sample removal and placement during repeated measurements.
4. Housing of electronics, and heating plate at center axis of lenses
5. Ease of changing filters without disturbing lens assembly.
6. Holding the heavy EMCCD camera on top resting plate. Coupled to rest of assembly.

The designing of assembly included several mechanical challenges. Total 43 parts are manufactured for the System in aluminum alloy and finished by black anodizing. The designed of Spatially Resolved Luminescence System is such that one can assembled or dismantled any part without disturbing other parts.

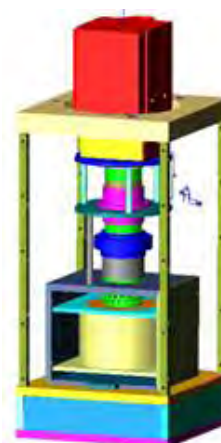


Figure 19: Spatially Resolved Luminescence System

Honorary Fellows

A. Hewish

J. E. Blamont

K. Kasturirangan

P. J. Crutzen

U. R. Rao

Honorary Faculty

A. Ambastha

A. Singal

A. C. Das

A. K. Singhvi
FNA, FASc, FNASc, FTWAS

A. R. Prasanna

A. S. Joshipura
FNA, FASc, FNASc

B. G. Anand Rao

D. P. Dewangan
FNASc

H. Chandra

H. O. Vats

H. S. S. Sinha

J. Banerji

J. N. Goswami
FNA, FASc, FNASc, FTWAS

M. M. Sarin
FNA, FASc, FNASc

N. Bhandari
FNA, FASc, FNASc, INSA Honorary Scientist

Ramesh R
FNA, FASc, FNASc

R. G. Rastogi
FNA, FASc, FNASc

Rengarajan R.

R. Sridharan
FASc, FNASc, NASI Senior Scientist

Rindani S. D
FASc, FNASc, NASI Senior Professor-H

Sarkar U.
FNA, FASc, FNASc

Shyam Lal
FNA, FASc, FNASc

S. K. Gupta
FNASc

S. P. Gupta

S. V. S. Murty
FASc

T. Chandrasekhar

U. C. Joshi

V. K. B. Kota

Y. B. Acharya

PRL Faculty

Sr. No.	Name	Designation	Specialization	Academic Qualification
1	Bhardwaj A. <i>FNA, FASc, FNASc</i>	Director	Planetary & Space Science	Ph.D., IIT,BHU (1992)
2	Acharyya K.	Reader	Astrochemistry	Ph.D., University of Calcutta (2008)
3	Baliyan K. S.	Professor	AGNs, Comets, Atomic Physics, Milky Way	Ph.D., Roorkee Univ. (1986)
4	Banerjee D.	Professor	Thermoluminescence & Planetary Physics	Ph.D., PRL, Gujarat Univ. (1997)
5	Banerjee D. P. K.	Senior Professor	Novae, Be Stars, Planetary Nebulae, IR and Optical Studies	Ph.D., PRL, Gujarat Univ. (1990)
6	Banerjee S. B.	Scientist - SE	Experimental Molecular Physics	Ph.D., Saurashtra Univ. (2011)
7	Basu Sarbadhikari A.	Scientist-SE	Petrology & Geochemistry	Ph.D., IIT, Khargpur (2006)
8	Bhatt J. R.	Professor	Astrophysics	Ph.D., IPR, M.S. Univ. (1992)
9	Bhattacharyya R.	Associate Professor	Plasma Physics	Ph.D., Jadavpur Univ. (2006)
10	Bhushan R.	Scientist-SG	Oceanography and Paleoclimatology	Ph.D., PRL, M.S. Univ. (2009)
11	Chakrabarty A.	Associate Professor	Extra-solar planets, Star Formation & Instrumentation	Ph.D., PRL, Gujarat Univ. (1999)
12	Chakrabarty D.	Associate Professor	Upper Atmosphere and Geomagnetic storm	Ph.D., PRL, M.L.S Univ.(2008)
13	Chauhan N.	Scientist-SD	Luminescence Dating and Luminescence Dosimetry	Ph.D. Gujarat University (2012)
14	Deshpande R. D.	Scientist-SG	Application of Environmental Tracers in Hydrology	Ph.D., PRL, M.S. Univ. (2007)
15	Dewangan. L. K.	Scientist-SD	Astrophysics	Ph.D., Gujarat Univ. (2011)

Sr. No.	Name	Designation	Specialization	Academic Qualification
16	Ganesh S.	Scientist-SF	Milky Way, Comets, AGN, Astronomical polarimetry	Ph.D., PRL, Gujarat Univ. (2010))
17	Gadhavi H.	Scientist-SE	Atmospheric Physics	Ph.D., PRL, Gujarat Univ. (2006))
18	Goswami S.	Professor	High Energy Physics	Ph.D., Calcutta Univ. (1998)
19	Guharay A.	Reader	Atmospheric Physics	Ph.D., Kumaun Univ. (2010)
20	Haider S.A. <i>FASc, FNA, FNASc</i>	Senior Professor	Planetary and Cometary Atmospheres	Ph.D., Banaras Univ. (1984)
21	Janardhan P.	Senior Professor	Solar Radio Astronomy & Space Weather	Ph.D., PRL, Gujarat Univ. (1991)
22	Joshi B.	Reader	Solar Physics, Astronomy	Ph.D., ARIES, Kumaun Univ. (2007)
23	Joshi V.	Scientist-SD	Observational Astronomy	Ph.D, Gujarat Univ. (2013)
24	Juyal N.	Scientist-SF	Quaternary Geology & Paleoclimate	Ph.D., PRL, M.S. Univ. of Baroda (2004)
25	Kushawaha R. K.	Scientist-SD	Atomic Physics	Ph.D., PRL, M.L.S. Univ. (2009)
26	Konar P.	Associate Professor	Particle Physics	Ph.D.,HRI, Allahabad Univ. (2005)
27	Kumar B.	Reader	Solar Physics	Ph.D., PRL, M.L.S Univ. (2007)
28	Kumar S.	Associate Professor	Aquatic and Terrestrial Biogeochemistry	Ph.D., PRL, M.S. Univ. of Baroda (2004)
29	Mahajan N.	Associate Professor	Particle Physics	Ph.D., Delhi Univ.(2004)
30	Marhas K. K.	Associate Professor	Solar System studies	Ph.D., PRL, D.A.V.V Indore (2001)
31	Mathew S. K.	Professor	Solar Magnetic & Velocity Fields	Ph.D., PRL, Gujarat Univ. (1999)
32	Mishra H.	Professor	Strong Interaction Physics & Nuclear Astrophysics	Ph.D., IOP, Utkal Univ. (1994)
33	Mohanty S.	Senior Professor	Astroparticle Physics	Ph.D., Wisconsin Univ. (1989)
34	Naik S.	Associate Professor	High Energy Astrophysics, X-ray Binaries	Ph.D., TIFR, Bombay Univ. (2003)
35	Pallamraju D.	Professor	Space Weather and Atmospheric coupling processes	Ph.D., PRL, D.A.V.V Indore (1997)
36	Rai V.	Associate Professor	Stable Isotope Cosmochemistry	Ph.D., PRL, M.S Univ. of Baroda (2001)
37	Rajpurohit A. S.	Scientist-SD	Astronomy & Astrophysics	Ph.D., Uni. de Franche-Comté, France (2013)
38	Ramachandran S.	Professor	Aerosols, Radiation & Chemistry-Climate Interactions	Ph.D., PRL, M.S Univ. of Baroda (1996)
39	Rangarajan R.	Professor	Particle Physics & Cosmology	Ph.D., Univ. of California, Santa Barbara (1994)

Sr. No.	Name	Designation	Specialization	Academic Qualification
40	Rastogi N.	Associate Professor	Atmospheric & Aerosol Chemistry	Ph.D., PRL, M.L.S Univ. (2005)
41	Ray J. S.	Professor	Isotope Geochemistry	Ph.D., PRL, M.S Univ. of Baroda (1998)
42	Ray D.	Scientist-SE	Marine Geology & Igneous Petrology	Ph.D., Jadavpur Univ. (2009)
43	Sahoo B. K.	Associate Professor	Atomic Physics	Ph.D., IIA, Mangalore Univ. (2006)
44	Sahu L. K.	Associate Professor	Atmospheric Science, Trace gases	Ph.D., PRL, M.L.S.Univ. (2005)
45	Samanta G. K.	Reader	Laser and Nonlinear optics	Ph.D., Universitat Politecnica de Catalunya Uni., Barcelona (2009)
46	Sarkar A.	Reader	MHD simulation & Solar Physics	Ph.D, University of Goettingen, Germany (2005)
47	Sekar R.	Senior Professor	Upper Atmospheric & Ionospheric Physics	Ph.D., PRL, Gujarat Univ. (1991)
48	Sharma S. K.	Associate Professor	Middle Atmosphere & Long Term Atmospheric Changes	Ph.D., PRL, Gujarat Univ. (2010)
49	Sheel V.	Associate Professor	Modelling of Lower Atmosphere	Ph.D., PRL, Gujarat Univ. (1996)
50	Shukla A. D.	Scientist-SE	Geochemistry & Cosmochemistry	Ph.D., PRL, M.S. Univ. (2012)
51	Singh A.	Reader	Ocean Biogeochemistry	Ph.D, MLSU Udaipur (2011)
52	Singh A. D.	Professor	Atomic Physics	Ph.D., IIA, Bangalore Univ. (1998)
53	Singh N.	Associate Professor	Theoretical condensed matter and Statistical Physics	Ph.D., RRI, Bangaluru (2006)
54	Singh R. P.	Professor	Laser Physics	Ph.D., J.N.U., New Delhi. (1994)
55	Singh S. K.	Professor	Isotope Geochemistry	Ph.D., PRL, M.S. Univ. of Baroda (1999)
56	Singh V.	Scientist-SD	Active Galactic Nuclei and evolution of galaxies	Ph.D., Calicut University (2011)
57	Sivaraman B.	Reader	Low Temperature Astrochemistry	Ph.D., The Open University, UK (2008)
58	Srivastava M.	Reader	Astronomical Instrumentation	Ph.D., Univ. of Pune (2012)
59	Srivastava Nandita	Professor	Solar Physics	Ph.D., PRL, Ravi Shankar Shukla Univ. (1994)
60	Srivastava Neeraj	Scientist SE	Planetary Remote Sensing	Ph.D., PRL, IIT, Roorkee. (2014)
61	Subramanian K. P.	Professor	Experimental Atomic and Molecular Physics	Ph.D., PRL, Gujarat Univ. (1987)
62	Vadawale S. V.	Associate Professor	High Energy Astrophysics and X-Ray Spectroscopy	Ph.D., TIFR, Bombay Univ. (2003)
63	Vijayan S.	Scientist-SD	Planetary Remote Sensing	Ph.D., Anna Univ. Chennai (2013)

Sr. No.	Name	Designation	Specialization	Academic Qualification
64	Yadava M. G.	Scientist-SG	Palaeoclimate, Radiocarbon dating and stable isotopes	Ph.D., PRL, DAVV, Indore (2003)
65	Mahirale V.K.	Engineer-SG	Civil Engg.	B.E., D.A.V.V., Indore (1982)
66	Adhyaru P. R.	Engineer-SF	Development of electronic sub systems for spectrometry	B.E., Gujarat Uni., (1991)
67	Bhavsar K.J.	Engineer-SE	Electrical Systems	B.E., Gujarat Uni. (1995)
68	Bayanna A. R.	Scientist-SE	Optical instrumentation & Solar Physics	Ph.D., PRL, MLSU-Udaipur (2015)
69	Jani R. A.	Scientist-SE	Paleoclimate and Application of Stable Isotopes in Hydrology	M.Sc., Gujarat Uni. (1988)
70	Mahajan R.R.	Scientist-SE	Noble gas isotopes, Meteorites	M. Sc. North Maharashtra Uni. Jalgaon (1994) M. Tech., D.A.V.V., Indore (1997)
71	Nishtha A.	Librarian-SE	Library & Information Sciences	Ph. D., M. S. Uni. of Baroda (2012)
72	Pabari J. P.	Engineer-SE	Planetary and Interplanetary Dust	Ph.D., PRL, IIT Bombay (2011)
73	Rajesh T. A.	Scientist-SE	Aerosol characterization and instrumentation	M.Sc., RDVV, Jabalpur (1998)
74	Rao D. K.	Scientist-SF	Isotope Studies of Methane	M.Sc., Andhra Uni. (1979)
75	Raval J.	Engineer-SE	IT/Cyber Security, Linux System Administration, Network Administration	M.Tech., Allahabad Agricultural Institute (2006)
76	Panda D.	Scientist-SE	Nuclear Instrumentation & Remote Sensing	M.Sc., Berhampur Uni. (1998)
77	Shah A. B.	Engineer-SG	Design and Development of Scientific instrumentation	B.E., Gujarat Univ. (1984)
78	Shah R. R.	Engineer-SG	Instrumentation & Control, Data Acquisition, Telescope	B.E., M.B.A.
79	Shanmugam M.	Engineer-SE	Space instrumentation, Semiconductor detectors and ASICs	Ph.D., PRL, D. D. Uni. (2016)
80	Singh R. P.	Scientist-SE	Mesosphere and Lower Thermosphere	M.Sc. (1998)
81	Sudheer A. K.	Scientist-SE	Chemistry	M.Sc., Calicut Uni. (1995)
82	Ubale G. P.	Engineer-SF	Design, Development, Production, Planning and Control of mechanical systems	B.E. (1987)
83	Vaghela H. R.	Engineer-SE	Mechanical Engineering and Finance	B.E. (1996), M.B.A. (2002)
84	Venkataraman V.	Scientist-SE	Infrared studies of evolved stars	Ph.D., PRL, MLSU, Udaipur (2015)
85	Venkataramani S.	Scientist-SF	Atmospheric Physics	M.Sc., Uni. of Madras (1986)
86	Wairagade S.	Engineer-SE	Civil Engg.	B.E., Nagpur Univ. (1993)

Audited Statement of Accounts

7th Floor, Heritage Chambers,
B/h. Bikanerwala, Off S.M. Road,
Nr. Azad Society, Nehru Nagar, Ahmedabad-380 015.
Phone : (B) 079 - 2647 2000 E mail : contact@mmsco.in
Website : www.mmsco.in

MUKESH M. SHAH & CO.

CHARTERED ACCOUNTANTS
AHMEDABAD • MUMBAI • BANGALORE

AUDITORS' REPORT

To
The Trustees
Physical Research Laboratory

1. We have audited the accompanying Financial Statements of the Physical Research Laboratory situated at Navrangpura, Ahmedabad having Registration No. E/1371 Ahmedabad for the year ended 31st March, 2017, which comprises the Balance Sheet as at 31st March, 2017, the Income & Expenditure Account for the year then ended and a summary of significant accounting policies and Notes forming part of accounts.
2. Management is responsible for the preparation of these financial statements that give a true and fair view of the financial position and financial performance of Physical Research Laboratory. This responsibility includes the design, implementation and maintenance of internal control relevant to the preparation and presentation of the financial statements that give a true and fair view and are free from material misstatement, whether due to fraud or error.
3. Our responsibility is to express an opinion on these financial statements based on our audit. We conducted our audit in accordance with the Standards on Auditing issued by the Institute of Chartered Accountants of India. Those Standards require that we comply with ethical requirements and plan and perform the audit to obtain reasonable assurance about whether the financial statements are free from material misstatement.

An audit involves performing procedures to obtain audit evidence about the amounts and disclosures in the financial statements. The procedures selected depend on the Auditor's judgment, including the assessment of the risks of material misstatement of the financial statements, whether due to fraud or error. In making those risk assessments, the auditor considers internal control relevant to the management's preparation and presentation of the financial statements that give a true and fair view in order to design audit procedures of the entity's internal control. An audit also includes evaluating the appropriateness of accounting policies used and the reasonableness of the accounting estimates made by the Management, as well as evaluating the overall presentation of the financial statements.

4. We believe that the audit evidence we have obtained is sufficient and appropriate to provide a basis for our audit opinion.



7th Floor, Heritage Chambers,
B/h. Bikanerwala, Off S.M. Road,
Nr. Azad Society, Nehru Nagar, Ahmedabad-380 015.
Phone : (B) 079 - 2647 2000 E mail : contact@mmsco.in
Website : www.mmsco.in

MUKESH M. SHAH & CO.

CHARTERED ACCOUNTANTS
AHMEDABAD • MUMBAI • BANGALORE

5. We report that:

- i. *As informed to us, value of movable and immovable assets as per physical verification last carried out in the financial year 2013-14, are subject to reconciliation with books of accounts including fixed assets. The loss which may arise due to non-making reconciliation between value of Fixed Assets (Movable) as per physical verification and value as disclosed in the books of Fixed Assets is not provided for.*

Further loss/gain which may arise on providing depreciation on WDV of each individual asset instead of providing depreciation on WDV of block of assets, which is not worked out and ascertained.

- ii. *The Trust has as required by the Prudent accounting policy not considered grants for the purpose of capital expenditure either while calculating depreciation or by way of amortization of grants to Income and Expenditure account. Except the grants Received during the year for specific purpose for Creation of Capital Assets. Cumulative Depreciation of ₹. 1,58,52,18,813/- is not charged to the Income & Expenditure account, however as per the consistent policy adopted by the Trust, the same is written off against the Corpus Fund.*

- iii. *None of the assets including Buildings of the trust except Vehicles are insured. Non-Insurance of Building is in violation of Rule 65 of The Bombay Public Trust (Gujarat) Rules, 1961.*

However, the policy adopted by PRL is in confirmation with the provision of Department's [Department of Space, Government of India] 'Book of Financial powers' as clarified vide letter No.28011/1/2014-V dated January 3, 2014.

- iv. *As informed to us the balances either Debit or Credit, stated under various advances to staff, deposits, receivables, advances to others and those under sundry creditors are subject to confirmation and reconciliation if any.*
- v. *The Loss due to carry forward deficit of ₹.1,64,31,122/- of PRL Employees Provident Fund shall be provided on getting Approval from Department of Space/Ministry of Finance for one Time grant to met with the Deficit.*
- vi. *The balances of various external projects being managed by the Trust are subject to confirmation, and are appended as Annexure 1 to the Notes of Accounts.*



7th Floor, Heritage Chambers,
B/h. Bikanerwala, Off S.M. Road,
Nr. Azad Society, Nehru Nagar, Ahmedabad-380 015.
Phone : (B) 079 - 2647 2000 E mail : contact@mmsco.in
Website : www.mmsco.in

MUKESH M. SHAH & CO.

CHARTERED ACCOUNTANTS
AHMEDABAD • MUMBAI • BANGALORE

6. **Subject to the matters stated in Para No. 5,** in our opinion and to the best of our information and according to the explanation given to us, the financial statements give a true and fair view in conformity with the accounting principles generally accepted in India:
- a) in the case of the Balance Sheet, of the state of affairs of the Trust as at March 31, 2017.
 - b) in the case of the Income and Expenditure Account, of the Deficit for the year ended on that date;
7. We further report that:
- a. Except for sanction and release of Grant for creating Capital Assets during the Finance Year **2013-14**, for other Capital Assets i.e., Fixed Assets are being purchased from the balances held from the grants (without having any specific directions) received by the Trust for the year prior to the current financial year.
 - b. As informed to us, the Trust has provided depreciation on its fixed assets for the first time in F.Y. 2008-2009 calculating retrospectively with effect from F.Y. 2001-2002, by estimating the same at 90% of opening Book Value of Fixed Assets for F.Y. 2001-2002. Then onwards for the subsequent additions and on the carried forward balances, depreciation is provided on the opening balance of fixed assets at the rates as prescribed under the Income Tax Act, 1961 by way of the written down value method. The Trust does not provide any depreciation on any additions / deletions in assets during the year.
 - c. The value of stores and medicines is taken as certified by the Management.
 - d. Reliance has been placed on Management for allocation of expenses amongst various external as well as internal projects including imprest at USO Udaipur and IFO Mt. Abu on account of the same being technical in nature. The expenses incurred are classified as capital or revenue by the Management as per policies and practices.
 - e. The accounts are maintained regularly and in accordance with the provision of the Bombay Public Trust Act, 1951 and the Bombay Public Trust (Gujarat) Rules, 1961.
 - f. Receipts and disbursements are properly and correctly shown in the accounts.
 - g. The cash balance and the vouchers were in the custody of the Accounts Officer on the date of audit and were in agreement with the accounts.



7th Floor, Heritage Chambers,
B/h. Bikanerwala, Off S.M. Road,
Nr. Azad Society, Nehru Nagar, Ahmedabad-380 015.
Phone : (B) 079 - 2647 2000 E mail : contact@mmsco.in
Website : www.mmsco.in

MUKESH M. SHAH & CO.

CHARTERED ACCOUNTANTS

AHMEDABAD • MUMBAI • BANGALORE

- h. The books, deeds, accounts, vouchers and other documents and records required for the purpose of Audit were produced before us.
- i. The registers of stock and inventories are certified by the Trustee, is maintained and updated on regular basis. However, register of movable and immovable properties is required to be reconciled with balances as stated in Financial Statements.
- j. The Registrar Prof. Jyotirnanjan S Ray and the Sr. Head Accounts & Internal Financial Adviser Shri Chavali V.R.G. Deekshitulu appeared before us and furnished the necessary information required by us.
- k. No property or fund of the Trust was applied for any objects or purposes other than for the objects or purposes of the trust.
- l. During the year under review there was no write off to Income & Expenditure account.
- m. Tenders were invited for repairs or construction for the expenditure exceeding Rs.5000/-.
- n. No money of the public trust has been invested contrary to the provisions of Section 35 of the Bombay Public Trust Act, 1951.
- o. No alienations of immovable property are noticed in contrary to the provision of Section 36 of the Bombay Public Trust Act, 1951.
- p. In view of the notification no. 51/2009 dated 25.06.2009 as issued by The Central Government, the Income of the Trust is eligible for exemption under Income tax law and hence no provision for income tax has been made in the books of accounts.

For Mukesh M Shah & Co.

Chartered Accountants

Firm Regn. No.106625W

C.S. Shah

CA Suvrat S Shah

Partner

Membership No.102651

Place: Ahmedabad

Date: 20/09/2017



PHYSICAL RESEARCH LABORATORY
Ahmedabad - 380 009
[Trust Regn. No. E/1371/Ahmedabad]
INCOME & EXPENDITURE ACCOUNT For the Year ended on 31st March, 2017
[Vide Schedule - IX, Rule 17(1) of The Bombay Public Trust (Gujarat) Rules, 1961]

EXPENDITURE	₹.	₹.	INCOME	₹.	₹.
EXPENDITURE IN RESPECT OF PROPERTIES (see Schedule No.1)			RENT (Realised) : (see Schedule No.4)		15,51,055
Rates, Taxes & Cesses	30,20,882		INTEREST (Accrued/Realised) :		
Repairs & Maintenance	1,42,25,157		On Vehicle/Computer Advance	40,844	
Salaries	-		On Interest (Miscellaneous)	1,307	
Insurance	-		On Interest (NPS Fund)	(16,730)	
Depreciation	-		On Bank FDs	3,53,29,874	3,53,55,295
Other Expenses	-	1,72,46,039			
ESTABLISHMENT EXPENSES : Remuneration (in case of a Math to the Head of a Math, including his household expenses if any.)		-	GRANTS (See Schedule No.3) :		87,37,90,000
LEGAL EXPENSES :		5,86,124	INCOME FROM OTHER SOURCES :		
AUDIT FEES : Statutory Audit Fees		1,80,450	Miscellaneous Income		
Contribution and fees :	-		(Sale of unserviceable/obsolete articles, discarded assets, Insurance Claim)	2,52,368	
AMOUNT WRITTEN OFF :			Income : Miscellaneous	1,801	
(a) Bad Debts & Store	-		(Loss of ID Cards, RTI fee,)		2,54,169
(b) Loan Scholarship	-				
(c) Irrecoverable Rent	-				
(d) Other Items	-				
(e) Irrecoverable Project Balance	-				



PHYSICAL RESEARCH LABORATORY
Ahmedabad - 380 009
[Trust Regn. No. E/1371/Ahmedabad]
INCOME & EXPENDITURE ACCOUNT For the Year ended on 31st March, 2017
[Vide Schedule - IX, Rule 17(1) of The Bombay Public Trust (Gujarat) Rules, 1961]

EXPENDITURE	₹.	₹.	INCOME	₹.	₹.
EXPENDITURE ON OBJECTS OF TRUST : Educational & Research (see Schedule No.2) Prior period Expenses			Prior Period Income		
			Other Income (Vehicle, Housing Adv. Int.)	-	
			Other Income (CISF Recovery)	-	
		98,21,33,747			
		1,64,91,805			
			Excess of Expenditure over Income during the Year : 2016-17		10,56,87,646
	TOTAL ₹	1,01,66,38,165		TOTAL ₹	1,01,66,38,165

As per our report of even date



Mukesh M. Shah & Co.,
Chartered Accountants
(F.R.N.: 106625W)
CS. Suvrat S Shah
CA Suvrat S Shah
Partner
Membership No. 102651

Ahmedabad
Date : 20/09/2017

For, Physical Research Laboratory

Kartikeya V Sarabhai
Kartikeya V Sarabhai
Trustee
P R L Council

Ahmedabad
Date : 20/09/2017

Sanjay S. Lalbhai
Sanjay S. Lalbhai
Trustee
P R L Council

PHYSICAL RESEARCH LABORATORY

Ahmedabad - 380 009

[Trust Regn. No. E/1371/Ahmedabad]

BALANCE SHEET as at 31st March, 2017

[Vide Schedule - VIII, Rule 17(1) of The Bombay Public Trust (Gujarat) Rules, 1961]

FUNDS & LIABILITIES	₹.	₹.	PROPERTY & ASSETS	₹.	₹.
TRUST FUND CORPUS			IMMOVABLE PROPERTIES		
Grant and contribution	3,91,02,83,135		[As per Schedule 'D' attached]	39,10,88,328	
[As per Schedule 'A' attached]			Less : Depreciation	13,30,24,685	25,80,63,643
Less : Depreciation	1,58,52,18,813	2,32,50,64,322	MOVABLE PROPERTIES		
OTHER EARMARKED FUNDS			Equipments, Furniture & Fixtures,		
[As per Schedule 'B' attached]	1,00,13,106	1,00,13,106	Dead Stock, Vehicles, Books & Journals	2,59,12,60,316	
			[As per Schedule 'F' attached]	1,45,21,94,128	1,13,90,66,188
			Less : Depreciation		
RESERVE FUND			INVESTMENTS (AT COST)		
Depreciation Fund	-	-	[As per Schedule 'E' attached]		58,90,84,677
Any Other Fund	-	-			
LOANS (SECURED OR UNSECURED)			Stock of Stores [At cost]	8,04,977	
From Trustees	-	-	Stock of Medicine [at cost]	18,138	
From Others	-	-	(As per inventory certified by the management)		8,23,115
PROJECTS BALANCES [GRANTS]			ADVANCES (SECURED)		
[As per Schedule 'C' attached]	5,13,28,021	5,13,28,021	Staff members		
			Vehicle/Computer Advance (Including accrued interest Rs. 37,355)	5,34,038	
CURRENT LIABILITIES			House Building Advance	4,11,199	9,45,237
[As per Schedule 'H' attached]					
For Expenses	68,72,317		CASH & BANK BALANCES		15,56,64,327
For Materials & Contracts	66,12,630		[As per Schedule 'G' attached]		
Miscellaneous Liabilities	1,64,47,696				
Other Deposits	2,85,65,837		ADVANCES (UNSECURED)		
New Pension Scheme	20,80,522		[As per Schedule 'I' attached]		
CHSS Retired Subscription	30,19,078	6,35,98,081	To Employees (including Rs. 1,15,304.00 More than one year and considered doubtful)	21,65,759	



PHYSICAL RESEARCH LABORATORY

Ahmedabad - 380 009

[Trust Regn. No. E/1371/Ahmedabad]

BALANCE SHEET as at 31st March, 2017

[Vide Schedule - VIII, Rule 17(1) of The Bombay Public Trust (Gujarat) Rules, 1961]

FUNDS & LIABILITIES	₹.	₹.	PROPERTY & ASSETS	₹.	₹.
INCOME & EXPENDITURE ACCOUNT			To Contractors & Suppliers	31,46,93,124	
Balance as per last Balance Sheet	16,89,55,036		To Others	2,39,72,370	34,08,31,253
Less : Excess Expenditure Over Income for the year	(10,56,87,646)	6,32,67,390	[As per Schedule 'I' attached] (including Rs.11059384 as Deposit)		
			ADVANCES (For CIVIL WORKS)		
			To Civil Engineering Division, DOS	55,20,044	
			To Civil Engineering SAC	1,34,69,632	1,89,89,676
			RECEIVABLES		
			Customs Duty Receivable	61,12,187	
			Forex Claim Receivable	1,93,974	
			SBI - ATM Rent Receivable	30,000	
			Interest Receivables on FDR	34,66,643	98,02,804
TOTAL ₹. ->		2,51,32,70,920	TOTAL ₹. ->		2,51,32,70,920

Schedules A to I are attached.
As per our report of even date



Mukesh M. Shah & Co.,
Chartered Accountants

(F.R.N.: 106625W)

CA Suvrat S Shah
Partner
Membership No. 102651

Ahmedabad
Date : 20/09/2017

For, Physical Research Laboratory

Kartikeya V Sarabhai
Trustee
P R L Council

Ahmedabad
Date : 20/09/2017

Sanjay S. Lalbhai
Trustee
P R L Council

PHYSICAL RESEARCH LABORATORY
NAVARANGPURA, AHMEDABAD – 380 009

**SIGNIFICANT ACCOUNTING POLICIES & NOTES FORMING PART OF ACCOUNTS FOR
FINANCIAL YEAR 2016-2017**

A. SIGNIFICANT ACCOUNTING POLICY

1. CONSTITUTION

Physical Research Laboratory (PRL) is a Trust registered under The Bombay Public Trust Act, 1950 and engaged in basic sciences research. PRL has not been carrying out any commercial activity.

2. ACCOUNTING METHOD

The trust has been following mercantile system of accounting *except* for the expenditure on retirement benefits since 01.04.2011 as per the recommendations of Comptroller and Auditor General of India and directions of the Department of Space vide letter dated 11.03.2002.

RECOGNITION OF INCOME AND EXPENDITURES

- i. In view of specific direction from the donor for the utilization of the 'Grant in Aid – Salaries' under Non Plan and 'Grant in Aid General' grants under Plan purpose, entire grant is credited to Income & Expenditure Account. The expenditure is also met against the respective object head under Plan and Non-Plan classification. The Grant in aid received during the financial year towards any capital component is taken to Corpus Fund for creation of specific Assets under Plan to the Balance Sheet; since objective head: Grants for creation of Capital Assets' and acquisition of assets thereto; shown separately in the books of accounts.

3. Fixed Assets

- i. Fixed Assets are stated at historical cost of acquisition less accumulated depreciation.



- ii. The assets to the extent identified by the Management for disposal are written off against its corpus till 31.03.2010, the amount realized from the sale of such Assets are credited to the Income & Expenditure Account. During the year under review the trust has not written off any assets. However, amount realized from the sale of such assets identified by the Management for disposal has been credited to Income & Expenditure account under the head Miscellaneous Income. The original cost less depreciation of the Assets sold/discarded is not deducted from the value of Assets and hence the value of Assets is overstated to that extent. Consequently the profit or loss on disposal of Assets is not accounted.
- iii. Books, periodicals and journals including digital journals are capitalized and the same are shown under Movable assets.
- iv. Fixed Assets including Equipments are valued at costs which are physically verified by an outside agency appointed by the Management and the same are subject to reconciliation with the Fixed Assets Register. Physical verification of Moveable Assets & Equipments has been carried out by the firm of Chartered Accountants upto the year 2013-14. Reconciliation of Fixed Assets physically available with the value as disclosed in the Books of Accounts is not ascertained and consequently loss which would arise due to difference in such values will be provided on ascertaining such loss. Depreciation on such Assets of Immovable and Moveable is worked out on the gross value of Assets less depreciation provided though depreciation on individual WDV of each asset is not worked out.

4. Depreciation

- i. The trust has worked out depreciation on its fixed assets for the first time in F.Y. 2008-2009 calculating retrospectively with effect from F.Y. 2001-2002, by estimating the same at 90% of opening Book Value of Fixed Assets for F.Y. 2001-2002. Then for the subsequent additions and on the carried forward balances, depreciation is provided on the opening balance of fixed assets at the rates as prescribed under the Income Tax Act, 1961 by way of written down value method. The trust does not work out any depreciation on any additions / deletions in assets during the year.
- ii. The Depreciation is not charged to the Income & Expenditure account, but it is shown as a deduction from Gross value of Fixed Assets and deduction from Corpus fund in the Balance Sheet. However, no accounting entries are passed for giving effect of such depreciation. The amount of such depreciation is



₹.16,18,86,969/- for current financial year and ₹. 1,58,52,18,813/- as the accumulated balance as on 31st March, 2017.

5. Investments

The trust consistently classifies Fixed Deposits under the head Investments. The fixed deposits are maintained in the custody of Accounts Officer and are physically verified by the Management or its authorized representative(s) periodically.

Surplus out of grants, those of endowment funds are maintained by way of Fixed Deposits and Savings Bank Accounts with Scheduled Banks.

6. Inventories

The stock of consumables and medicines are valued at cost which are physically verified by the Management and reconciled with the Stores records.

The stores item purchased and issued immediately to the department are treated as consumed.

7. Retirement Benefits

Retirement Benefits which include Gratuity, Leave Encashment and Pension are treated as payable in the year in which the retirement of employees takes place.

[As per actuarial valuations as on 31st March, 2017]:

Gratuity	: ₹.	13,28,79,235
Half Pay Leave encashment	: ₹.	1,44,27,490
Earned Leave encashment	: ₹.	10,77,30,267
Pension	: ₹.	2,58,57,62,925
Total	: ₹.	2,84,07,99,917

However, provision for the same is not made in the books of accounts.

8. Foreign Transaction

Foreign currency transactions are recorded at the exchange rate prevailing as on the date of the payment. Foreign Exchange fluctuation gain or loss is not booked for the payments outstanding as on 31st March, 2017.



B. Notes to Accounts

- 1 The trust has not quantified contingent liability in view of impending cases in various Courts.
- 2 In view of the notification no. 51/2009 dated 25.06.2009 as issued by The Central Government, the income of the trust is eligible for exemption under Income tax Law and hence no provision for income tax has been made in the books of account.
- 3 Expenditure incurred upto 2014-15 of ₹.13,26,99,700/- on additions/alterations to existing Buildings has not been appropriated to the respective building, but all such expenses have been clubbed under a separate head "Civil works, Additions, Alteration and Extension" shown in the Balance Sheet. Such expenditure incurred till the year 2016-17 stands.
- 4 The registers of stock and inventories are certified by the trustee, maintained and updated on regular basis. Register of stocks for movable properties is maintained for Assets acquired from 01.04.2004 (FY2004-05) which requires to be reconciled with balances as stated in Financial Statements, by making adjustments/ writing off untraceable items. However, register of immovable properties is required to be maintained including adjustment of expenditure stated in Para 3 above.
- 5 Balances stated either Debit or Credit under various advances to staff, deposits, receivables, advances to others and those under sundry creditors are subject to confirmation and reconciliation.
- 6 Project Leader Imprest comprising of cash and bank balance maintained by the project leader on account of the Trust, is stated under Cash and bank balance.
- 7 The rental agreement with State Bank of India not firmed up as on date hence rent receivable is not recognized.



- 8 Advance includes ₹. 61,12,187/- of customs duty receivable for which claim was rejected by the Customs Department and on further appeal made by the management, The Commissioner of Customs (Appeals-II) Mumbai passed order in favor of Trust. The Department went into further appeal, which the Customs, Excise & Service Tax Appellate Tribunal, West Zonal Bench –Mumbai dismissed vide order No. S/93425/16/CB and A/93426/16/CB dated 27.06.2016. Hence, no provision is made in the books of accounts.
- 9 A Fire took place in Seminar Hall Building in the year 2011-12 wherein furniture, electrical and Air-condition fixtures and fittings were destroyed. The original cost of item destroyed had not been identified and quantified and hence loss on account of this fire could not be written off.
- 10 The trust had initiated the new pension scheme as per Government guidelines. Some employees who had left the services hence their individual accounts could not be opened and data/funds could not be transferred to NPS Trust Fund due to lack of guidelines in this regard by PFDR, New Delhi. The non-transfer of such subscriptions to the NPS trust fund account, in the absence of guidelines of PFDR, held by PRL prior to the current financial year are invested in fixed deposits.
- 11 No fraud on or by the trust has been reported or recorded.
- 12 The trust is consistently not charging common institutional overheads on external projects.
- 13 The broad classification of expenses incurred and balances of Endowment / Earmarked funds adopted by the management construed as for the purpose of attainment of its objectives.
- 14 Transactions recorded in the books of accounts are supported by documentary evidences where such documentary evidence is not available; the entries in books of accounts have been taken as relied upon as authenticated by the Management.
- 15 The accounting for external projects managed by the Trust against specific mandate and funds received on reimbursement basis are segregated with effect from 01.04.2013 and



separate books of accounts and bank balances have been maintained. The activities are carried out as per mandate [directions from the donor agency] from the donor agencies and expenditures are met from the funds received from such donor agencies and interest earned from such unspent balance deposited in the bank account. The details of unspent grant of each donor agency and the bank balances are appended as per **Annexe- 1** to the notes to accounts.

- 16 The trust has not received any gifts or donations in kind or equipment on loan basis during the year under review as reported by the Management.
- 17 The current Liabilities include a balance amounting to ₹.27,36,045 in Gift under Will and its Codicil of Late Dr.Devendra Radhekrishna Lal Bank Savings bank account: Pension, NRI and PPF accounts shown in PRL's bank account. In addition, a Bunglow located in 20 Jayantilal Park, Makarba, Ahmedabad is also to be received under WILL for which application was made to the concerned revenue authorities on 09 May 2013. The transactions shall be accounted for on getting confirmation from the Mamaltadar for transfer of property in favour of Physical Research Laboratory, Ahmedabad.
- 18 The loss due to carry forward deficit of ₹.1,64,31,122/- of PRL Employees Provident Fund shall be accounted for on getting approval from Department of Space/Ministry of Finance for permission to write off and one time grant to be met the deficit. The grant amount as projected in the budget estimates amounting to ₹.1,69,00,000/- and claimed, funds have been received and kept as a separate TDR/FDR including Interest of ₹ 12,58,966 pending decision/approval in this regard by the Government.
- 19 The commitments for Purchase, both local and foreign and Works during 2016-17 are as below :

Purchase Commitment:

Consumables	: ₹.	2,56,86,239
Equipments	: ₹.	35,82,32,719

Stores Commitment:

Consumables	: ₹	2,01,13,139
Equipment	: ₹	30,84,66,633

Works Commitment:

Repairs and Maintenance	: ₹	Nil
Capital works	: ₹	Nil

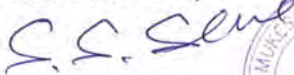


20 The following accounts heads include certain old outstanding debit (for more than one year) and credit balances (for more than one year) which need to be reconciled, adjusted or written off, as per Generally Accepted Accounting Principles (GAAP) by the management:

Accounts Head	Debit Balances		Credit Balances	
	NO. of Accounts	Amounts (Rs.)	NO. of Accounts	Amounts (Rs.)
Suppliers and Contractors	--	--	49	73,48,963
Advance to suppliers and Contractors	59	1,71,55,634	--	--
Traveling Advance	71	3,62,631	124	5,00,409
Staff Advance	62	1,27,292	44	1,28,344

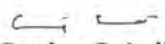
Mukesh M. Shah & Co.
Chartered Accountants
(F.R.N.: 106625W)

For Physical Research Laboratory


CA Suvrat S Shah
Partner
Membership No.102651




Kartikeya V Sarabhai
Trustee


Sanjay S. Lalbhai
Trustee

Place: Ahmedabad
Dated: 20/09/2017

PHYSICAL RESEARCH LABORATORY Ahmedabad- 380009

Annexe-1 to Note to Accounts - Project Balances [Liabilities] and Bank balances and other Assets.

2016-17

Account	Opening Balance	Additions		Deduction	Project Closed & balance Amount refunded	Closing Balance	Bank Balances
		Grants Received	Interest	Expenditure			
2108 DCS PLANT SCIENCE GRANT	-1,103	92,76,000	75,341	82,82,955		10,67,283	10,68,386
4900 ISROGBP AABG GRANT	78,90,101	-	3,15,086	-		82,05,197	82,05,197
5400 CSSTE AP M. TECH SAS-9 GRANT	14,99,317	25,00,000	39,970	39,36,783		1,02,504	8,182
7100 ISRO MLIT GRANT	71,604	-	2,859	-		74,463	74,463
7300 ISRO GBP-PRCCD/QMPPMR GRANT	23,00,941	-	1,07,964	(4,07,089.00)		28,15,994	27,87,299
7360 ISROGBP MCNC Fund	55,31,772	-	2,36,046	15,64,915		42,02,903	42,52,709
7350 ISROGBP PRS Fund	1,45,25,650	-	5,82,450	1,27,51,776		23,56,324	21,72,490
7460 ISRO GBP ARFI Grant	4,90,787	-	19,779	3,75,072		1,35,484	1,05,589
7870 MoES TEI in Indian Ocean Fund -SKS	2,73,98,506	-	10,70,678	99,21,006		1,85,48,178	1,44,46,361
7880 DST SDR - JC Bose Fellowship Grant	6,82,070	7,00,000	35,743	3,61,182		10,56,631	10,56,631
7891 ASJ - JC Bose Fellowship Grant	8,60,509	-	34,828	50,000		8,45,337	8,45,337
7907 DSL - JC Bose Fellowship Grant	-909	13,50,000	30,796	3,93,832		9,96,055	9,60,003
7910 JNG - JC Bose Fellowship Grant	6,87,860	-	45,338	4,75,099		2,58,099	2,33,050
7920 AKS - JC Bose Fellowship Grant	2,13,249	13,50,000	1,14,778	9,05,756		7,72,271	6,10,578
7930 PUS -JC Bose Fellowship Grant	9,36,814	-	21,753	1,08,308	8,50,259	-	-
7940 MMS -JC Bose Fellowship Grant	-29,158	15,00,000	14,902	3,67,024		11,18,720	11,41,867
7950 NASI - Fellowship Grant	2,48,086	6,66,914	5,819	6,20,348		3,01,471	3,16,471
7956 SERB-Women Excellence Award Grant - KKM	2,04,691	-	4,024	3,44,262		(1,35,547)	4,972
7961 SERB Women Excellence Award Grant-SVT	6,56,412	-	6,985	-	6,63,397	-	-
8450 Planex Chandrayaan II Payload Grant	95,67,820	-	3,82,010	-		99,49,830	98,25,336
8460 PLANEX - Ch-2 Devil/Experimental Fund	1,14,48,332	-	4,57,090	3,63,113		1,15,42,309	1,15,42,309
8470 Ch2 XSM Fund	2,33,00,475	-	9,31,809	70,12,467		1,72,19,817	1,60,50,549
8480 Ch2 APXS Fund	2,74,94,845	3,52,20,861	15,56,748	2,86,29,139		3,56,43,315	3,15,34,365
8570 MoES Annamox in NLAS Fund	7,06,081	-	28,311	-		7,37,392	7,37,392
8580 MoES POCEF from UAS-BoB Fund	-4,87,475	-	29	2,64,114		(7,51,560)	532
8590 MoES TEINIO from UAS-BoB Fund	3,10,153	-	10,981	3,86,669		(65,535)	-
8945 Grant from LEOS for SPROC facility at PRL(Mt. ABU)	79,691	1,04,00,000	91,951	1,06,31,866		(60,224)	2,14,488
9101 ISRO AT-CTM GRANT	3,17,64,744	-	12,35,292	1,36,29,166		1,93,70,870	1,93,27,143
9100 ISRO GBP TCG Grant	88,03,693	-	3,49,705	6,38,504		85,14,894	84,90,260
9760 SAC Study of Moon and Mars Analogues Fund	3,86,200	4,00,000	21,688	3,40,302		4,67,586	4,63,954
3217 INSA Grant/fellowship-MMS	39,109	3,75,301	2,572	3,75,572		41,410	31,760
7970 DST-INSPIRE Grant	7,91,453	-	32,405	1,18,380		7,05,468	7,09,468
8481 ASPEX Projects Fund	-	2,50,00,000	7,77,474	1,58,46,931		99,30,543	99,43,211
8586 INSA Grant/Fellowship-DSL	-	4,60,000	4,517	3,68,140		96,377	96,377
9200 Raja Ramana Fellowship-AKS-Grant	-	6,30,000	8,744	4,80,000		1,58,744	1,58,744
9220 NAM S&T RTF-DCS Scheme Grant	-	2,70,000	903	1,05,000		1,65,903	1,40,403
7990 SAH - JC Bose Fellowship Grant	-	5,00,000	-	39,393		4,61,607	4,61,607
9210 Raja Ramana Fellowship- ASJ- Grant	-	6,30,000	9,770	3,80,000		2,59,770	2,59,770
SUB- TOTAL (A) ₹	17,83,76,320	9,12,39,076	86,67,148	11,96,58,995	15,13,656	15,71,09,893	14,82,77,253

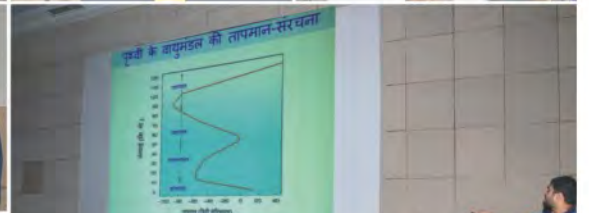


Account	Opening Balance	Additions		Deduction Exp. During the year	Project Closed & balance Amount refunded	Closing Balance	Bank Balances
		Grants Received	Interest				
Payable to PRL							
ISRO GBP TCG						3,524	
ISROGBP MCNC [957]						1,77,239	
MoES POCEF from UAS-BoB (Dr. R. Rangarajan)						7,24,578	
SB WEA KMK -7958						2,35,756	
MoES- TENIO from UAS-BoB (Dr.Ravi Bhushan)-8595						1,48,440	
IT on Contractor and Prof. Services & LWS-3208/3270/3277						1,67,384	
Electricity Charges						6,000	
SUB- TOTAL (1) ₹	-	-	-	-	-	14,62,921	-
Receivable from PRL							
ISRO GBP-PRCCDIQMPPMR - 7306						33,695	
8945 Grant from LEOS for SPROC facility at PRL (Mt. ABU)						4,00,000	
Ch2 XSM Payload						11,68,541	
Ch2 APXS Payload						40,75,156	
MoES TEI in Indian Ocean -SKS						41,54,868	
ISROGBP PRS						1,83,834	
ISRO GBP ARFI						34,481	
Guest House & DH Food						1,500	
SUB- TOTAL (2) ₹	-	-	-	-	-	1,00,52,075	
Total Payable to PRL [1-2] (B) ₹						(85,89,154)	
Liability							
Liability for expenses							
Misc. Liability - Labour Welfare						4,364	
Security Deposits- M/s HEC Infra Projects & M/s. Pranam Technologies							
Advance to staff						5,34,774	
SUB- TOTAL (C) ₹							8,93,914
Claim receivable from CSSTEAP (D)							
	-	-	-	-	-	5,39,138	8,93,914
							(1,11,290)
Capital Expenditure							
Project Grant received for acquisition of Capital Asset						1,84,60,810	1,84,60,810
Assets acquired from the Capital Grant for Projects							
SUB- TOTAL (E) ₹							
GRAND TOTAL (A+B+C+D+E) ₹	17,83,76,320	9,12,39,076	86,67,148	11,96,58,995	15,13,656	16,75,20,687	16,75,20,687





पी.आर.एल. में गतिविधियां Events at PRL





पी.आर.एल. में गतिविधियां Events at PRL



राष्ट्रीय विज्ञान दिवस समारोह
National Science Day Celebrations
भौतिक अनुसंधान प्रयोगशाला, अहमदाबाद



पी.आर.एल. में गतिविधियां Events at PRL



विक्रम जयंती Vikram Jayanti

विज्ञान और प्रौद्योगिकी के क्षेत्र में हाल पी.आर.एल. में नई पहल





पी.आर.एल. में गतिविधियां Events at PRL



